Characterization of Upward Vertical Gas – Liquid Flow (GLF) Using a Non-Intrusive Optical Infrared Sensor (NIOIRS)

by

Kwame Sarkodie

https://orcid.org/0000-0003-4689-4532

A thesis submitted in partial fulfillment of
the requirements for the award of
Doctor of Philosophy in Chemical, Process and Energy Engineering
PhD. Chemical Process and Energy Engineering

Chemical and Energy engineering department
School of Engineering
London South Bank University
November (2019)

Dedication

I want to dedicate the completion of this work to God Almighty, my wife Jemima, my daughter, Aveilla and my newborn son Avram Judah, you are my most treasured. Also, to Kwame Nkrumah University of science and technology for the provision of a study leave extension to be able to complete my studies.

Declaration

This dissertation is the result of my own work and includes nothing, which is the outcome of work done in collaboration except where specifically indicated in the text. It has not been previously submitted, in part or whole, to any university of institution for any degree, diploma, or other qualification.

Signed:

Date: 27/01/2020

Sarkodie, Kwame

Acknowledgements

I would like to express my profound gratitude to Dr. Andrew Fergusson-Rees my first supervisor and director of studies for his guidance, support, professionalism and supervision during this work. I would like also appreciate Dr Pedro Diaz my second supervisor, for the support on the rig build and constructive critique. My sincere thanks also to the technical staff of chemical engineering and electrical electronics lab for the guidance in the rig setups and sensor circuitry designs. I thank the laboratory technicians in lab 127, Hassan and Charles Coster and Medi for the instrumental support in the setup of equipment and software for signal analysis. Finally, to the post graduate research team for providing the scholarship that funded this work up until the end. Not to forget as well my close colleague, Nura Makwashi who collaborated with me on other flow assurance projects during my PhD journey.

Abstract

The pursuit to improve accuracy, cost effectiveness and safety in the operation of multiphase flow metering sums up the motivation for this work. Non-intrusive optical infrared sensors (NIOIRS) of 880 nm and 1480 nm wavelengths have been applied in this work for the objective identification of flow regimes, determination of phase fractions and ultimately for the measurement of phase volumetric flowrates in an upward vertical gas liquid flow. The sensing method detects flow structures based on the disparity of optical properties of each fluid. Air and water were used as working fluids to create GLF in vertical test and main rig setups with 0.018 m x 1 m and 0.0273 m x 5 m test section respectively under varied fluid flow rate combinations (0- 1.0 m/s of water and 0 - 13 m/s of air). Notable contributions were made in this work. These include (i) a derivation of a flow regime dependent phase fraction model, which accounts for interfacial scattering, hence improves phase fraction measurement (ii) A novel application of supervised learning methods to improve objective flow regime identification for a GLF (iii) Application of a modified calibration model to measure actual liquid velocities and flow rates in the absence of priori superficial velocities and slip ratio information (iv) a scheme to convert the NIOIRS into a GLF meter.

List of Figures

Chapter 2

Chapter 3

Chapter 4

Chapter 5

Chapter 6

Chapter 7

List of Tables

Chapter 2

Chapter 3

Chapter 4

Chapter 5

Chapter 6

Chapter 7

Nomenclature

Symbol	Description	units
Alphabetic symbols		
a	Attenuation coefficient	m^{-1}
A_C	Classification accuracy	%
A	Cross sectional area	m^2
A_g	Cross sectional area occupied by gas phase	m^2
A_l	Cross sectional area occupied by liquid phase	m^2
$\alpha_g(t)$	Temporal void fraction	Dimensionless
$\alpha_l(t)$	Temporal Liquid fraction	Dimensionless
$\bar{\alpha}_{sensor}$	Average void fraction from 880 nm sensor	Dimensionless
α_{sensor}	Average void fraction from 1480 nm sensor	Dimensionless
$\bar{\alpha}_{EB}$	Average entrained bubble fraction	Dimensionless
$\bar{\alpha}_{TB}$	Average Taylor bubble fraction	Dimensionless
$\bar{\alpha}_g$	Average void fraction	Dimensionless
α_s	Limiting slug void fraction	Dimensionless
α_{drift}	Drift flux model void fraction	Dimensionless
α_A	Amard model void fraction	Dimensionless
α_P	Differential pressure void fraction	Dimensionless
α_{level}	Swell level derived void fraction	Dimensionless
$\bar{\alpha}_{photo}$	Average void fraction from photos	Dimensionless
Co	Distribution coefficient	Dimensionless
D	Test section internal diameter	m
D_c	Critical bubble diameter	m
D_b	Bubble diameter	m
D_{ij}^2	Mahala Nobis Distance	-
$D_{ijPooled}^2$	Mahal nobis Distance	-
g	Acceleration due to gravity	m/s^2
f_{mix}	Mixture friction factor	Dimensionless
Fr	Froude number	Dimensionless

f_D	Bubble collision frequency	Hz
I_0	Initial light intensity	W/m^2
I	Attenuated light intensity	W/m^2
k	Ray vector	-
L	Length of test section	m
L_{su}	Slug unit length	m
L_s	Liquid slug length	m
L_{TB}	Taylor bubble length	m
L_w	Wake length	m
N_r	Number of detected rays	Dimensionless
N_e	Number of emitted rays	Dimensionless
ΔP_{gl}	Two phase flow pressure drop	Bar
ΔP_l	Liquid phase pressure drop	Bar
ΔP_g	Gas phase pressure drop	Bar
$P_{obs}(t)$	Instantaneous pressure reading	Bar
R	Radius of test section	m
R_b	Small bubble radius	m
R_{TB}	Taylor bubble radius	m
R_N	Nose radius of curvature of Taylor bubble	m
R_{12}	Cross correlation coefficient	Dimensionless
S_j	within-group covariance matrix for group *j*	
$S_{jPooled}$	pooled within – group covariance matrix for group j	
t	time	s
r^2	Reflection coefficient	Dimensionless
t^2	Transmission coefficient	Dimensionless
V_{air}	Sensor response to single phase air	Volts
V_{water}	Sensor response to single phase water	Volts
V_{int}	Sensor response to gas- liquid interface	Volts
$V_{obs}(t)$	Instantaneous observed sensor response	Volts
$\%V_{air}$	Percentage count of sensor response to air	%
$\%V_{water}$	Percentage count of sensor response to water	%
$\bar{V}_{obs}(t)$	Average sensor response	Volts
V_{TB}	Volume of Taylor bubble	m^3
v	Fluid velocity	m/s
v_{sg}	Gas superficial velocity	m/s
v_{sl}	Liquid superficial velocity	m/s
$v_{gsensor}$	Average actual sensor derived gas velocity	m/s
$v_{lsensor}$	Average actual sensor derived liquid velocity	m/s
$v_{ls}*$	Liquid superficial velocity derived from sensor calibration model	m/s
v_{mix}	Mixture velocity	m/s
v_{gu}	Drift flux velocity	m/s

v_∞	Bubble rise velocity	m/s
$\bar{v}$	Average fluctuating bubble velocity	m/s
v_N	Rise velocity at bubble nose	m/s
Q	Volumetric flow rate	l/min
Q_{sg}	Gas superficial volumetric flow rate	l/min
Q_{sl}	Liquid superficial volumetric flow rate	l/min
$Q_{gsensor}$	Actual volumetric gas flow rate from sensor	l/min
$Q_{lsensor}$	Actual volumetric liquid flow rate from sensor	l/min
qi	Posterior probability	Dimensionless
q	Ray position	-
s	Sensor spacing	m
S	Slip ratio	Dimensionless
We_{sg}	Weber number for gas phase	Dimensionless
We_{sl}	Weber number for liquid phase	Dimensionless
X_t	Training data set	-
x_i	Data input	-
x	Optical path	m

Greek symbols

δ_f	Liquid film thickness	m
α	Void fraction	Dimensionless
β	Homogenous gas fraction	Dimensionless
τ	Lag time	sec
τ^*	Average lag time from maximum cross correlation coefficient	s
ρ	Density	kg/m^3
σ	Surface tension	N/m
σ_{sensor}	Sensor response standard deviation	Volts
$\sigma_{predict}$	Predicted standard deviation	Volts

θ_I	Angle of incidence	Degrees
θ_R	Angle of reflection	Degrees
θ_T	Angle of refraction	Degrees
ω	Angular frequency	Hz
π	Prior probability	Dimensionless

Abbreviations

GLF	Gas Liquid Flow
NIOIRS	Non-Intrusive Optical Infrared Sensor
LDA	Linear Discriminant Analysis
QDA	Quadratic Discriminant Analysis
MPF	Multiphase Phase Flow
MPFM	Multiphase Phase flow meter
WMS	Wire Mesh Sensor
PCA	Principal Component Analysis
DAQ	Data Acquisition

Subscripts

Sensor	Optical sensor measurement
EB	entrained bubbles
f	Liquid film
TB	Taylor bubble
B	small bubble
sg	Superficial gas
sl	Superficial liquid
gu	Drift flux
g	actual gas
l	actual liquid
obs	observed response
air	air
int	air - water interface
water	water
mix	gas and liquid mixture
avg	Average

Publications

1. **Sarkodie, K**., Fergusson-Rees, A. and Diaz, P., 2018. A review of the application of non-intrusive infrared sensing for gas–liquid flow characterization. *The Journal of Computational Multiphase Flows*, *10*(1), pp.43-56.
2. **Sarkodie, K**., Fergusson-Rees, A., Makwashi, N. and Diaz, P., 2019, June. Slug Flow Monitoring in Pipes Using a Novel Non-Intrusive Optical Infrared Sensing Technology. In *SPE Europec featured at 81st EAGE Conference and Exhibition*. Society of Petroleum Engineers.
3. **Sarkodie, K**., Fergusson-Rees, A. and Diaz, P Flow regime identification via polynomial regression and probabilistic Linear and Quadratic discriminant analysis (Submitted)..
4. Makwashi, N., **Sarkodie, K**., Akubo, S., Zhao, D. and Diaz, P., 2019, June. Investigation of the Severity of Wax Deposition in Bend Pipes Under Subcooled Pipelines Conditions. In *SPE Europec featured at 81st EAGE Conference and Exhibition*. Society of Petroleum Engineers.
5. Makwashi, N., Barros, D.S.D., **Sarkodie, K.,** Zhao, D. and Diaz, P.A., 2019, September. Depositional Behaviour of Highly Macro-Crystalline Waxy Crude Oil Blended with Polymer Inhibitors in a Pipe with a 45-Degree Bend. In *SPE Offshore Europe Conference and Exhibition*. Society of Petroleum Engineers

Contents

Chapter 1

1. Introduction

1.1. Problem statement

The simultaneous flow of gas and liquid in a conduit constitutes a gas liquid flow condition. Gas - Liquid Flow (GLF) is experienced in equipment and components in the chemical, process and petroleum industries, specifically in reactors, pumps, wells and pipes. In focus, the presence of GLF in pipes however presents a challenge to industry due to the complex nature of the hydrodynamics induced by phase interactions. The effect of these interactions is physically evident from the geometric distributions of the flow mixture, referred to as flow regimes, within a range of phase fractions. In view of these phase interactions, there could be extremely poor accuracies in the measurement and monitoring of the flow stream of each phase. This leads to inadequate allocation and productivity challenges. In addition, gas and liquid build up in pipes presents safety hazards in pipes that require adequate monitoring in real time.

For instance, slugging in pipes is likely to exist in subsea flow lines, risers and wellbores. The severity of slugging in pipe lines as emphasized by key researchers over the years (see Malekzadeh, 2012; Taitel *et al.*, 1990) may lead to pipeline vibrations and inefficiency of receiving equipment. It is hence necessary to develop methods to monitor this flow assurance problem in real time. Currently, the design of slug catchers and homogenizer systems have been considered as antidotes to slugging, however, limited workspace and the extra cost of this equipment remain limiting considerations. In effect, these problems can only be solved with the pursuit of accurate characterization of GLF systems, which would improve prediction of the hydrodynamic behavior and phase flowrate measurements. It is worth noting that this pursuit still is a challenge for most design engineers and researchers worldwide (Van Dijk, 2005).

In the chemical and petroleum industry today, there are three approaches to measuring GLFs. These include: By separation, partial separation and inline multiphase flow (MPF) meters (TUV NEL, 2013). **Measurement by separation** requires the use of surface separators to isolate and measure single phase volumes via single phase flow meters. However, these are cumbersome and may become a problem when it comes to space in an offshore setting. In addition, there is no measurement of the local intrinsic characteristics of flows after the separation process.

Multiphase flow metering presents a new approach which uses various types of sensors such as hydraulic, electrical, gamma-ray, optical, acoustic etc. coupled with signal processing to measure local and average phase flow rates in the flow stream (Schreier, 2011). The third approach is by **partial separation** which combines the use of multiphase flow metering and smaller separators such as cyclones and test separators to measure phase flow rates with a higher gas to liquid ratio (≥ 95) (TUV NEL, 2013).

Among these approaches, use of MPF meters seems most convenient since they eliminate the need for large and cumbersome separators on site, especially for offshore operations. None the less, "the biggest obstacle to the successful implementation of multiphase metering is the general lack of understanding of the different flow regimes (controlled by phase fractions) present in the conduit (Falcone, 2009)". More so, MPF meters have been critiqued to be very expensive. A typical MP meter installation would cost in the range of US$100,000 – US$500,000 per well depending on the production location, the size of production and number of phases presents (Sheers and Noordhuis, 1999). Blaney and Yeung, (2007) also estimated that only 0.2% of hydrocarbon wells are instrumented with MPF meters because of cost.

The requirement of multiphase flow metering in pipes, which is growing in acceptance in industry, presents a solution especially in adding value of information when monitoring routines are incorporated. From a technical perspective, most of the MPF meters used today have limitations that include:

i. Intrusive designs, which mean that sensors are probed into the flow stream to obtain flow characteristics which present less accurate results in interpretation of phase distributions and phase fractions.
ii. A combination of different complementing sensor technologies that increases cost and further complicates the meter design.
iii. Safety implications that arise as a result of considering radioactive sensors.

In a nut shell, a triad problem of meeting cost, simplicity and technical performance of instruments to measure MPF characteristics, motivates this work. Mehdizadeh *et al.*, (2002), concluded that the industry is still in pursuit of better technological advancement in metering and monitoring of MPF characteristics. Bertani *et al.*,(2010) also emphasized that "ambitious goals remain for instrument developers such as; the development of simple to use low and high flow measuring techniques, High void fraction local and averaged density measurements, automated signal interpretation, and flow pattern identification". To improve confidence and accuracy of measurement and interpretation, research investigations into the use of non-intrusive methods of measurements of MPF have gained attention over the years.

The proposed solution to the triad problem can be achieved when a single sensing method is able to accurately determine MPF characteristics. The relevant research questions then arise as regards to GLF in pipes;

i. Can a single non-intrusive sensing technology be applied to meet the described triad problem?
ii. And if so, what would be the trade off in terms of accuracy of characteristics measured?

These questions form the motivation of this work to which are to be investigated.

1.2. Aim and objectives

The aim and objectives are hence shaped by the research questions. The aim of this work is to use a non-intrusive optical infrared sensor (NIOIRS) to characterize upward vertical GLF. The obtained characteristics are then combined to compute phase flow rates hence making the sensor operate as a gas liquid flow meter.

1.2.1. Specific objectives

To experimentally investigate upward vertical gas-liquid flow using two (2) designed fit for purpose flow rigs which incorporate a non-intrusive optical infrared sensor to:

i. Objectively identify flow regimes via statistical methods which includes sensor response distribution and supervised learning techniques such as polynomial regression and probabilistic linear and quadratic discriminant analysis (LDA and QDA respectively).
ii. Determine the temporal and average phase fractions via a derived flow regime dependent phase fraction model that corrects for interfacial scattering effects.
iii. Determine average structural characteristics of the GLF namely, liquid film thickness, the Taylor bubble void fraction, and entrained bubble void fraction.
iv. Determine the average actual gas velocity via cross correlation of sensor responses.
v. Compute the actual liquid velocity in combination with a modified calibration model correlation that accounts for the drift velocity of structures and flow separation.

vi. Determine the actual phase flow rate (gas and liquid) measurements computed from a combination of the derived flow characteristics.

1.3. Research Scope

Enumerated are the research boundaries that define the depth of investigation of this work.

i. Design and application of non-intrusive optical Infrared sensing for measurement and monitoring of air - water flow
ii. Concurrent upward flow (air – water)
iii. Two flow rig test sections of 0.0273-m pipe size ,5 m long (main rig) and 0.018 m, 1 m long (test rig).
iv. Flow ranges of water 0.01 –1.0 m/s and air of 0.01 –13.0 m/s for atmospheric conditions of flow.
v. Focus in on the attenuation of infrared light intensity and not heat absorbed by phases.
vi. Real time application as a potential two-phase flow meter.

1.4. Outline of thesis

Eight (8) chapters are presented in this thesis. This is categorized into 3 categories.

i. Background and approach chapters consist of two chapters.
ii. Results and discussion chapters consists of four chapters that address the objectives of this work and conclusion and Recommendations for future work.
iii. Closing chapter consists the conclusions and recommendations chapter.

1.4.1. Background and approach chapters

Chapter 1**-** Introduced the problem of the complexity nature of GLF measurement in relevant industry, which raised research questions and aims of this work. The boundaries of investigation for the scope and an outline of this thesis are detailed.

Chapter 2 – Details the theory and classic works from literature on the characteristics of two-phase flow in pipes that requires understanding for an accurate measurement to be achieved for an upward vertical GLF. These include flow regimes, phase fractions, phase velocities and other intrinsic characteristics which include entrained bubble fractions, liquid film thickness and the Taylor bubble fractions. A discussion of transition models for upward gas-liquid flow is made. The role of non-intrusive sensors and statistical and signal processing techniques for MPF characterization. A review of nonintrusive optical infrared sensing for gas-liquid flow, given design considerations with highlights of relevant gaps in research, finalizes this chapter.

Chapter 3 – The focus of this chapter is to delineate the key approaches and experimental facility and procedure which address the specific objectives of this work. These include an overview of the design and setup of two flow rig designs (test and main flow rigs) and design of the two optical sensors (880 nm and 1480 nm wavelengths). The range of experimental flow conditions and fluid property description is made for both flow rigs. The calibration results of each sensor setup are also presented. Also included is the approach to derivation of phase fraction models, identification of flow regimes and phase velocities. Relevant validation methods procedure for photography, image processing and swell level change methods are detailed.

1.4.2. The result and discussion chapters

Chapter 4 – This chapter focuses on preliminary work that uses the 880 nm optical sensor to identify flow regimes and phase fraction derived from the test rig set up. Further results and discussions of the infrared ray interaction with varied bubbles sizes is performed and compared with the experimental results of the sensor. Further validation results using photos, swell level change and correlations on the sensor performance is provided with recommendations made. Discussions on the performance of the sensor for real time application using LabVIEW is also presented.

Chapter 5 – Presents the details of the supervised learning approaches required to objectively identify flow regimes using the sensor response, derived from the 1480 nm NIORIS, installed on the main rig set up. A series of relevant steps that describe the application of polynomial regression, probabilistic linear discriminant and quadratic discriminant analysis for flow regime discrimination is presented. The results of the sensor response extracted were detailed with analysis of the adequate features required for the discrimination process under each supervised learning approach. Training and test performances of each method were analyzed based classification accuracies with recommendations for real time applications.

Chapter 6 – Using the main flow rig and 1480 nm NIOIRS sensor, this chapter focuses on the measurement of local and average and intrinsic structural characteristics of phase fractions under varied flow conditions. This is achieved using a flow regime dependent model that corrects for interfacial effects. A discussion of results that involves validation studies from experimental methods and correlations is detailed accordingly.

Chapter 7 – This chapter presents the results of the application of the 1480 nm optical sensor to determine phase velocities and phase volumetric flow rates. Results and discussions on the actual gas velocities using a cross correlation techniques and actual liquid velocity via calibration is presented for varied flow regimes detailed. Analysis of slip effect on variations in phase velocities and phase flow rates is also elucidated. Using readings from the flow meters (from the main rig) and data from literature the sensor performance is validated. Further discussions on a real time algorithm for GLF metering is proposed. This algorithm links the models from chapter 5 and 6 and 7.

1.4.3. Concluding chapter

Chapter 8 – The concluding chapter summarizes the findings of this work, highlighting the key results that meet the specific objectives. Recommendations for future work that include improvements on key areas is also discussed, with novel contributions to knowledge in the area of novel applications of non-intrusive optical sensing.

Appendix –This section presents further results of other characteristics that are investigated such as the average structural frequency derived from the optical sensor using power spectral density and. Other simulation work on the rise of bubbles in a vertical pipe was also presented. An error analysis approach is also presented which quantifies the uncertainty of the optical sensors considered in this work.

Chapter 2

2. Background and Literature

2.1. Introduction

This chapter provides a review of the background and literature of the concept of upward vertical GLF. An introduction to key terminologies that relate to the GLF context is presented, which include superficial and mixture velocities. Next a review of relevant characteristics for GLF metering is presented which includes typical flow regimes in the upward vertical GLF and their transitional criteria. A critical review of the phase fraction models is made with consideration of intrinsic characteristics and its relevance in GLF measurement given the existence of slip. A summary of existing technologies with focus on the application of non-intrusive optical infrared sensors for GLF characteristics is provided with relevant statistical and signal processing methods. Lastly, the gaps in application of non-intrusive sensing which unveils the novelty of this work are highlighted.

2.1.1. GLF in pipes concepts

Superficial velocity – is the velocity of the phase that occupies the full cross-sectional area of the pipe. It is also defined as the ratio of the phase superficial volumetric flow rate Q_{sg} , Q_{sl} to the cross-sectional area (A), which presumes a single phase is flowing through the pipe. Therefore, for a gas-liquid flow,

$$v_{sg} = Q_{sg}/A \tag{2.1}$$

$$v_{sl} = Q_{sl}/A \tag{2.2}$$

Mixture velocity -This is defined as the sum of superficial velocities of each phase in the pipe. This parameter is used in MPF models to represent mixture flow conditions.

$$v_{mix} = v_{sg} + v_{sl} \tag{2.3}$$

Actual phase velocity – This is defined as the flow rate of the phase over the actual flow area it occupies relative to the area occupied by other phases in the pipe. This means that for the same unit volume of flow, the cross-sectional area for flow is reduced which makes the magnitude of the velocities depend on the fraction of each phase in the pipe.

$$v_g = Q_g/A_g \tag{2.4}$$

and,

$$v_l = Q_l/A_l \tag{2.5}$$

It is therefore challenging to measure the actual liquid velocity in the pipe since a local variation of the instantaneous phase velocities exists. Thus, an average measure of the phase velocity is deemed adequate.

Phase fraction – Phase faction in a pipe refers to the fraction occupied by a phase (gas or liquid) relative to the total occupied by both phases. This could be chordal, cross sectional or volumetric reference. In this work, the phase fraction referred to, is a time – averaged cross-sectional phase fraction which approximates to a volumetric phase fraction under steady state conditions. The phase fraction in the gas phase referred herein as the void fraction, (α_g) and the liquid fraction $\alpha_l = (1 - \alpha_g)$ can be expressed as,

$$\alpha_g = \frac{1}{n}\sum_{t=0}^{T} \frac{A_g}{(A_g + A_l)} \tag{2.6}$$

And

$$\alpha_l = 1 - \left[\frac{1}{n}\sum_{t=0}^{T} \frac{A_g}{(A_g + A_l)}\right] \tag{2.7}$$

Where A_g and A_l are the cross-sectional areas occupied by the gas and liquid respectively, averaged over time *T* for *n* number of samples. For non-slip conditions, where the rise velocities of the gas phase and liquid are assumed equal, a homogeneous gas fraction β can be expressed as,

$$\beta = \frac{Q_{sg}}{Q_{sg} + Q_{sl}} = \frac{v_{sg}}{v_{sg} + v_{sl}} \tag{2.8}$$

Under the said homogenous condition, $\alpha_g = \beta$ which then follows that $\alpha_l = 1 - \beta$.

Slip ratio - In most upward vertical GLF situations, there exists a significant disparity between phase velocities due to a significant difference in phase densities. A slip ratio S is expressed as the ratio of the actual gas velocity to the actual liquid velocity. The slip is also a function of the of the actual phase flow rates and phase fractions expressed as,

$$S = \frac{v_g}{v_l} = \frac{Q_g A_l}{Q_l A_g} = \frac{Q_g \alpha_l}{Q_l \alpha_g} \tag{2.9}$$

Given that the slip condition is dominant for the upward flow case (Bratland, 2010), disparity in actual phase velocities complicates the estimation of the actual liquid velocities. Indeed, most GLF meters assume a homogenous condition which excludes the slip effects hence introduces further uncertainties in the measurement (TUV NEL, 2013). To include the slip effect, would require a cumbersome set up of instruments needed to measure separate flow characteristics which also increases cost of flow meters as previously discussed in chapter 1.

In this work, consideration is given to a calibration model that incorporates slip effects, which is expected to improve accuracy of phase flow rate measurement. Further discussion is presented on the GLF characteristics relevant for GLF metering.

2.2. Review of upward vertical Gas Liquid Characteristics

The key characteristics considered in this work for an upward vertical GLF include:

i. Flow Regimes
ii. Phase fractions
iii. Phase velocities

2.2.1. Upward Vertical Flow Regimes for GLF

Variations in the phase fraction in the pipe lead to the occurrence of varied geometrical distributions in the pipe referred to as flow regimes. Flow regimes have been observed to occur by the most researchers experimentally through transparent pipes. The defined regimes are still arguably subjective due to the mode of observation and description by investigators. This has led to a varied number of flow descriptions in the pipe. Figures 2.1 (a-d) present the most agreed upon descriptions of flow regimes for an upward flow in the order of increasing gas velocities, defined as bubble, slug, churn and annular flow regimes (see Hamilton, 2012; Harvel *et al.*, 1996; Mao and Dukler, 1991; Taitel *et al.*, 1980).

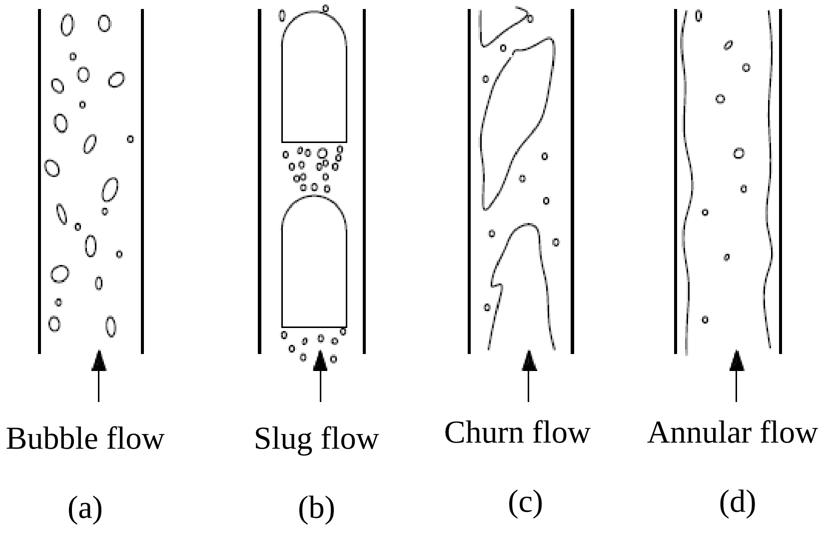

Figure 2.1: Upward vertical gas – liquid flow regimes (Modified from Brauner and Barnea, 1986) showing (a) bubble flow (b) slug flow (c) churn flow and (d) annular flow

For a gas-liquid flow in a pipe, **Bubble flow** (figure 2.1 (a)) occurs when there exist dispersed bubbles in the continuous liquid phase. These bubbles travel in a random motion with non-uniform sizes, (although approximated to be of spherical and ellipsoidal equivalence). Also, the distribution of bubbles could be concentrated at the center of the pipe, near the pipe walls which have been investigated as core peaking and wall peaking respectively by Isao and Mamoru, (1987).

Further increase in gas velocity increases the collision frequency of bubbles in the pipe. This increase in frequency, in turn, leads to increase in gas voidage that creates bubble coalescence to form larger bubbles. This large bubble termed as “Taylor bubble” is characterized to have a diameter that approaches that of the cross-section of the pipe, hence creates an intermittent flow of gas and liquid described as a **slug flow** in the pipe (see figure 2.1(b)). Liquid slugs have been observed to have entrained gas bubbles in them as well coupled with a downward flow of liquid film at the wall of the pipe.

Increases in the gas flowrates further increases the interfacial stress between the Taylor bubbles and the liquid film which creates a breakdown of the interface and hence an unstable elongated bubble. The mechanism is observed as the initiation of a **churn flow** (figure 2.1(c)). Further increases in the gas rate at constant liquid rate leads to formation of a to rising gas core at the center of the pipe with an upward rising liquid film referred to as as **annular flow** (figure 2.1

(d). The continuous gas core carries with it, entrained liquid droplets with a liquid film flowing upwards.

Theoretical flow regime transitions

A prediction of the shift from one flow regime to another based on operational conditions is vital for allocation of the appropriate models for GLF measurement. According to Wu et al, (2017) on assessing the transition criteria for vertical flow regimes, it was concluded that the following transition models were most reliable when compared based on an experimental database of 2500 data points. These models include:

i. Taitel et al. 1980, for bubble to slug flow,
ii. Barnea 1987, for slug to churn flow, and
iii. Mishima and Ishii 1984, for churn to annular flow regime transition.

Bubble to slug transition

The transition from bubble to slug flow is mainly driven by the bubble collision and coalescence (Biesheuvel and Gorissen, 1990). The frequency of bubble collision increases per their random motion. Moissis and Radovcich, (1962) considered a cubic lattice of bubbles and showed that bubble collision frequency f_D is proportional to,

$$f_D = \bar{v}/D_b[\left(\frac{0.74^{1/2}}{\alpha}\right) - 1] \qquad (2.10)$$

Where f_D is the dimensionless bubble collision frequency, $\bar{v}$ is the average fluctuating bubble velocity, D_b is the bubble diameter and α is the gas void fraction. The transitions are typically seen to occur at void fraction greater than 0.25 as suggested by Taitel *et al.*, (1980). Hence a relationship based on the bubble rise velocity relative to average liquid velocity describes the transition as,

$$v_{sl} = 3v_{sg} - 0.75v_\infty \qquad (2.11)$$

Where v_∞ is defined as the bubble rise velocity for large bubbles infinite to bubble size changes (Harmathy, 1960)

$$v_\infty = 1.53[{}^{g(\rho_l - \rho_g)\sigma}/_{\rho_l^2}]^{1/4} \qquad (2.12)$$

Slug to churn flow

There are four (4) possible mechanisms that could be responsible for slug to churn flow transition. These include the effects of entrance, flooding, wake and bubble coalescence mechanisms.

The entrance mechanism as proposed by Taitel (1986) is referred to as the effect of the entry length of gas and liquid into the pipe. They state the formation of a churn flow is due to an unstable short slug of liquids and Taylor bubbles formed at the entry length and with a more sufficient length downstream, the slugs could have formed. Thus, between the point of phase entry and stable slug formation is the proposed churn flow.

The **flooding mechanism** was proposed by McQuillan *et al.*, (1985). Flooding occurs under a flow reversal of gas and liquid and refers to the breakdown of the liquid film around the Taylor bubbles due to interfacial waves (Jayanti and Hewitt, 1992). They relate this occurrence strongly to churn flow and presented a model to evaluate the corresponding flooding velocities.

Ishii and Mishima, (1984) proposed the concept of the wake mechanism. It follows that the turbulence at the wake of Taylor bubbles leads to a churn flow. They propose a critical mean void fraction of the total slug region that exceeds the Taylor bubble region. Thus, a critical gas flow rate need to be determined to predict the transition from slug to churn flow. This mechanism has been questioned by a few investigators due to the inconsistent results during experimental validations.

The **bubble coalescence mechanism** was proposed by Barnea, (1987). They assumed that a slug to churn transition would occur when the bubbles entrained in the liquid slugs reach a void fraction of 0.52. The churn flow is evident when the entrained bubbles coalesce and break up the liquid slugs at the limiting void fraction. The expression of this limiting slug void fraction α_s is given by,

$$\alpha_s = 0.058[D_c({}^{2f_{mix}v_{mix}^3}/_{D})^{0.4}({}^{\rho_l}/_{\sigma})^{0.6} - 0.725\,]^2 \qquad (2.13)$$

Where f_{mix} and v_{mix} are the mixture friction factors and velocity.

D_c is the characteristic bubble size for a vertical flow and is defined by, Equation 2.14 as,

$$D_c = 2\sqrt{{}^{0.4\sigma}/_{g\Delta\rho}} \qquad (2.14)$$

Early and recent investigators have validated this model to be adequate for a range of flow rates (Owen, 1986; Wu et al.,2017). It is still a subject for debate as to what mechanism dominates the slug – churn transitions. In this work, it is anticipated that a fair contribution of each mechanism is likely given the varied flow configurations and gas injection set ups considered by the relevant investigators in literature. Costigan and Whalley, (1997) described the transition to be observed as unstable slug flow leading to Taylor bubble collapse. None the less, what is important in the context of tis work are the set of flow conditions that lead to a transition from a slug to churn flow.

Churn to annular flow

The transition from a churn flow to annular was inferred as a change in pressure gradient since it signifies a change of continuous phase of liquid to gas. Taitel *et al.* (1980), defined a minimum gas superficial velocity for churn to annular transition to occur. The proposed minimum gas velocity is required to carry liquid droplets up the pipe based on a balance between buoyancy and drag forces on the liquid droplets expressed as,

$$v_{sg} = 3.1\left[\frac{gD\left(\rho_l - \rho_g\right)}{\rho_g^2}\right]^{1/4}, \tag{2.15}$$

In addition, Kaichiro and Ishii, (1984) proposed that transition from churn to annular flow was based on superficial gas velocity that led to flow reversal of the liquid film around the large gas bubbles and the collapse of liquid slugs. Equation 2.16, expresses this velocity as,

$$v_{sg} = \sqrt{\frac{gD\left(\rho_l - \rho_g\right)}{\rho_g}} . (\alpha - 0.11), \tag{2.16}$$

It is worth highlighting that the churn to annular flow transition is observed as when a gas core is seen rising with variation in liquid film thickness induced by the gas core. Since the variation in liquid film thickness affect the GLF measurement via phase fractions, Further discussions on the dynamics of the liquid film thickness is presented in subsequent sections.

Flow maps for upward vertical GLF

The flow maps are mainly a representation of the theoretical and empirical models of transition that mark flow regime boundaries. Early researchers have developed flow maps for an upward two-phase flow, under varied flow conditions (Wallis ,1969, Hewitt and Roberts, 1969, Oshinowo and Charles, 1974, Taitel,1980 and, Barnea ,1987). The dependence of each flow regime on the two-phase flow properties and flow rates are combined to develop these flow maps.

A typical example of a flow map is presented in figure 2.2. The flow map indicates clear transition boundaries for variations in superficial velocities of gas and liquid in v_{sl} and v_{sg} respectively. For instance, at a low gas velocity and high liquid velocity a bubble regime is expected. Conversely, increases in the gas velocity for a low liquid velocity shifts the regime to a churn and annular regime. As of today, there are no universal flow maps that is applicable for all flow conditions. Thus, is it typical to use flow maps that apply to the range of flow conditions of interest.

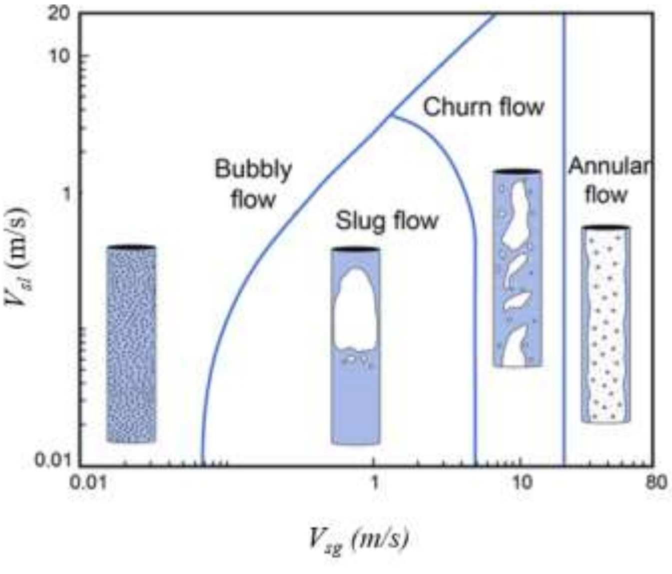

Figure 2.2 : Typical flow map used to identify upward vertical flow regimes of air and water at atmospheric conditions for a 72 mm pipe diameter according to the transition model of Taitel *et al.*, (1980) (modified from (Guet and Ooms, 2006))

Some investigators have attempted to use dimensionless numbers as coordinates to these maps to extend their applicability. The idea is to normalize the effect of the varied flow properties and flow configurations. Chen, (2006), considered the use of the Weber number of the gas and liquid phases (We_{sg}, We_{sl} ,) which includes the dominance of surface tension and interfacial forces for small pipe sizes (less than 5 mm). Rezkallah and Zhao, (1995), considered the use of the Reynolds number. Recent maps have also been modified under superficial flow conditions see (Agrawal, 2010; Chen *et al.*, 2005; Kelessidis and Dukler, 1989; Mao and Hibiki, 2017; Wu *et al.*, 2017).

2.2.2. Void Fraction correlations

According to Woldesemayat and Ghajar,(2007), there is a plethora of void fraction correlations available in literature. These have been grouped into three main categories namely, homogenous model, K-α model and the drift flux model (DFM) correlations.

The homogenous model computes the void fraction based on no- slip assumptions between each flowing phase. The derived void fraction, β, is already presented in equation 2.8 above. Albeit the non-slip assumption, the homogenous model has been reported to be useful for low flow conditions of gas and liquid where the effect of slip is not dominant.

The K-α model is a classic case of the empirical correlation with no theoretical basis. None the less, it represents a correction for the homogenous model. Adequate predictions have been observed using K-α model given that the model computes the void fraction as a fraction K of the homogenous void fraction

$$\alpha = k\beta, \tag{2.17}$$

A characteristic value for K is 0.83 derived from the investigations Armand, (1946) has proven to provide reasonable agreement with refence measurements. the Amard void fraction can be re written as,

$$\alpha_A = 0.83\beta, \tag{2.18}$$

DFM was first developed by Zuber and Findlay (1965) and later improved for radial void fractions and velocity profiles by Wallis (1969) and Ishii (1977). The drift-flux is defined as the relative motion of a less dense phase (gas) to that of the mixture of the two phases (gas and liquid). This drift velocity is related to the slip between gas and liquid velocities respectively as,

$$v_{gu} = v_g - v_{mix} \tag{2.19}$$

And

$$v_{lu} = v_l - v_{mix} \tag{2.20}$$

Based on a relative motion and non-homogenous flow, a distribution coefficient (*Co*) is included in the model, to correct for a flow regime variation and relates the homogenous void fraction (β) to the void fraction (α_{drift}),

$$\alpha_{drift} = {}^{\beta}\!/_{C_O} \tag{2.21}$$

The general expression for estimating the void fraction when combining equations 2.19 – 2. 21 is,

$$\alpha_{drift} = {}^{v_{sg}}\Big/_{(C_O v_{sg} + v_{gu})} \tag{2.20}$$

Table 2.1. presents *Co* and v_{gu} values for specific flow regimes of an upward vertical GLF. The derived average void fractions from these models would be compared with the that derived from in this work. The values for the churn flow regime are not given as no work in literature has provided a reliable range of values under this chaotic flow regime.

Table 2.1. Distribution coefficients and drift velocities corresponding to varied flow upwards vertical flow regimes.

Flow regime	*Co*	v_{gu} (m/s)	Investigators
Bubble flow	1.19	$1.53\left[\frac{\sigma g(\rho_l - \rho_g)}{\rho_l^2}\right]^{1/4}$	Zubar and Findlay, (1965) Wallis, (1969)
Slug flow	1.2	$0.35\left[\frac{g(\rho_l - \rho_g)D}{\rho_l^2}\right]^{1/2}$	Zubar and Findlay *et al.* (1967)
Annular flow	1.0	$23\left[\frac{\mu_l v_l}{\rho_g d}\right]\left[\frac{\rho_l - \rho_g}{\rho_l}\right]$	Ishii et al. (1976)

Other researchers have also presented modified versions of the DFM via experimental investigations within their scope of investigation (see, Wu *et al.*, 2017; Bhagwat and Ghajar, 2014; Isao and Mamoru, 1987; Lokanathan and Hibiki, 2016). They all suggested the robustness of the correlation in predicting phase fractions within acceptable error margins.

It is worth noting that three categories of correlations have been derived based on quasi steady state flow conditions. Therefore, a valid comparison with experimental results can only be made on this basis. This work compares the stabilized time for the measured phase fractions from the optical sensors with these correlations.

2.2.3. Structural Characteristics

Special attention is given to the characteristics of the slug flow regime, since it is geometrically representative of the structures that exist in other flow regimes. A typical slug unit (presented in figure 2.3) of length L_{su}, is unique with a Taylor bubble of length, L_{TB} and Radius R_{TB} close to the pipe diameter 2R. This bubble shape is described as an elongated bullet shape hence having a close to hemispherical nose of curvature radius R_N. The bubble tail, though, simplified in figure 2.3, has been observed by investigators to be characterized as an unstable zone with a varying profile (Nigmatulin and Bonetto, 1997).

This instability has been reported to be due to the downward velocity of the liquid film around the Taylor bubble which in turn enhances shedding of the bubble tail. A wake zone, with length L_w is formed as a result, which has been described to be a zone of velocity profile recovery of the bubble tail (Barnea and Taitel, 1993). Within the zone are entrained bubbles in the liquid slug which coalesce with the rising bubble, hence creating a longer bubble through time. A stable liquid slug then exists for lengths L_S greater than the wake length. Typical ranges of stable slug lengths for vertical upward flows have been reported to be around 8-25 pipe diameters (Xia *et al.*, 2009).

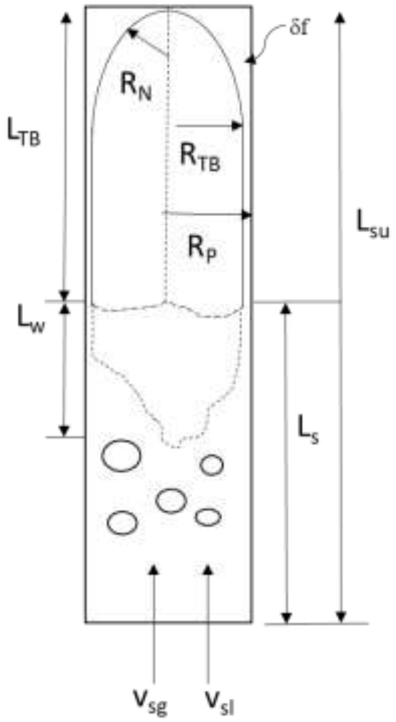

Figure 2.3**:** Typical slug unit in an upward vertical flow showing key features

Various aspects of the hydrodynamics of slug flows for varied pipe configurations and flow conditions have been studied such as slug length, wake length and bubble lengths distributions (Griffith and Wallis, 1961; Nicklin, 1962; Nigmatulin and Bonetto, 1997; Polonsky et al., 1999a, 1999b. However, the hydrodynamics of flow remains a probabilistic problem. Typical intrinsic structural characteristics that require further consideration include the Taylor bubble void fraction α_{TB}, entrained bubbles void fraction α_{EB} and the liquid film thickness δ_f. In the context of GLF metering, a better understanding of these intrinsic characteristics is expected to improve the accuracy of the average phase fractions, under the slug flow regime and can be extended to other flow regimes. Equation 2.21 presents closure relationship between the average void fraction $\bar{\alpha}_g$, average Taylor bubble fraction $\bar{\alpha}_{TB}$ and entrained bubble fraction $\bar{\alpha}_{EB}$ for a slug flow regime.

$$\bar{\alpha}_g = \bar{\alpha}_{TB} + \bar{\alpha}_{EB} \tag{2.21}$$

According to Fernandes *et al.*(1983) and Xue *et al.*(2015) an average liquid film thickness $\overline{\delta_f}$ can be expressed based on the average Taylor bubble void fraction $\bar{\alpha}_{TB}$ as shown in equation 2.22,

$$\bar{\delta_f} = \frac{D}{2}(1 - \sqrt{\bar{\alpha}_{TB}}) \tag{2.22}$$

The expression in equation 2.22 was derived from a geometrical interpretation of concentric cylinders. Assumptions such as a uniform liquid film and minimal effect of the Taylor bubble nose shape were made. Equation can be similar applied to the churn flow regime, since it is represented by unstable Taylor bubbles. For the annular flow regime in this work $\bar{\alpha}_{TB}$ in equation 2.22 can be substituted by $\bar{\alpha}_g$ (see equation 2.23),

$$\bar{\delta_f} = \frac{D}{2}(1 - \sqrt{\bar{\alpha}_g}) \tag{2.23}$$

The application of equation 2.22 for the churn flow has not been considered yet, given the literature search. It is thus, worthwhile to validate the accuracy of equations 2.22. and 2.23 using image processing technique discussed in chapter 3. Even though researchers have studied numerical models in relation to the complexity of the liquid film, (Yu *et al.*, 1996; Häber *et al.*, 2015), the models were still could not account a varying liquid film, especially for non-intrusive measurements.

2.2.4. Phase velocity correlations

Phase velocities (i.e., the actual gas and liquid velocities) under prevailing flow regime require investigation especially for cases where the slip condition is prevalent, as is mostly the case. Relevant correlations that relate the phase velocities are discussed with bearings on GLF metering.

Actual gas velocity

The actual gas velocities have been studied mostly in the slug flow regime which mainly constitutes the Taylor bubble velocities. The classic works which are still relevant today are the study of the rise velocity of an air Taylor bubble through a vertical pipe of stagnant liquid water by Dumitrescu (1943) and Davies and Taylor (1950). They derived a relationship between the rise velocity at the bubble nose to the pipe diameter and buoyancy force given as,

$$v_N = F_r\sqrt{gD} \tag{2.24}$$

Where F_r is a dimensionless number denoted as the Froude number typically in the range of 0.32- 0.351 and v_N is the terminal velocity at the bubble nose. The drift velocity v_{gu} is assumed to be equivalent to v_N for a terminal velocity condition, hence can be used herein as a substitute. Nicklin (1962) later correlated (see equation 2.25) the rise velocity of Taylor bubbles as the sum of the mixture velocity for flowing liquid of a single rising Taylor bubble with rise or drift velocity. Their experiments were for an air water flow in a 26 mm diameter vertical pipe. The slope of the trend was equivalent to the distribution parameter from the DFM C_o, as 1.2.

$$v_g = C_o v_{mix} + v_{gu} \tag{2.25}$$

Fernandes *et al.* (1983) and Mao and Dukler (1985a) showed that the upward motion of a continuous train of Taylor bubbles in a flowing liquid presents higher rise velocities of bubbles due to the effect of leading Taylor bubbles and the entrained bubble dynamics in the liquid slug. Fernandes *et al.* (1983) hence obtained a higher Co as 1.29 with a consistent drift velocity based on a Fr of 0.35. Other investigators have also considered the effect of surface tension, viscosity and entrained bubbles on the motion of Taylor bubbles in a vertical pipe , with consistent results that agreed with earlier works of Nicklin (1962), Fernandes *et al.* (1983) and Mao and Dukler (1985a) (see Abdulkadir *et al.*, 2014b; Bhusan *et al.*, 2009; 1991; Polonsky *et al.*, 1999; Shemer *et al.*, 2007). In context, equation 2.25 provides a consistent explanation for the rise of Taylor bubbles for the slug regime and can be considered as a validation for the actual gas velocity measurement.

For the bubble flow regime, the rise velocity of bubbles characterized as equivalently spherical, ellipsoidal and possibly bubble caps (spherical caps) has been studied by the most notable works of Harmathy (1960), Mendelson (1967), Lehrer (1976) and Davies and Taylor (1950).The aforementioned researchers proposed correlations that delineate the independence of bubble rise velocity with pipe diameter, given that there is no contact with the pipe wall, unlike the Tayler bubbles. Table 2.2. summarizes the bubble rise correlations that describe the terminal velocities of small bubbles in the bubble flow regime for most fluid systems.

The random motion of bubbles even under terminal velocity conditions creates variations in the bubble velocities depending on the bubble equivalent diameter and shape. For instance ,

Figure 2.4, presents typical trends expected for the rise velocities of small bubbles in a stagnant pure or contaminated liquid as adapted from the critical review of Kulkarni and Joshi, (2005). A general increase in bubble velocity in the spherical bubble regime is observed for increases in bubble diameter, with an undulating trend in the ellipsoidal regime. Further increases in bubble diameter greater than 10 mm bubbles shows increases in the bubble velocity even in the spherical cap regime (bubble cap). This explained behavior of smaller bubbles further complicates the metering accuracy in terms of determination of an average actual gas velocity.

Table 2. 2. Correlations for small bubble rise velocities for Newtonian and Non-Newtonian fluids systems

Investigator	Fluid system	Correlation	Applicability
Harmathy (1960)	Pure and contaminated Air – water	$1.53\left(\frac{g\Delta\rho\sigma}{\rho_l^2}\right)^{1/4}$	Slightly distorted ellipsoidal bubbles
Mendelson (1967)	Most fluid systems	$\left(\frac{\sigma}{R_B\rho_l}+gR_B\right)^{1/2}$	for bubble sizes >2 mm
Lehrer (1976)	Most fluid systems	$\left(\frac{3\sigma}{2R_B\rho_l}+\frac{2R_Bg\Delta\rho}{\rho_l^2}\right)^{1/2}$	For spherical and ellipsoidal bubble sizes
Davies and Taylor (1950)	Most fluid systems	$0.71\left(\frac{g\Delta\rho D}{\rho_l}\right)^{1/2}$	Bubble caps with length <1.5D

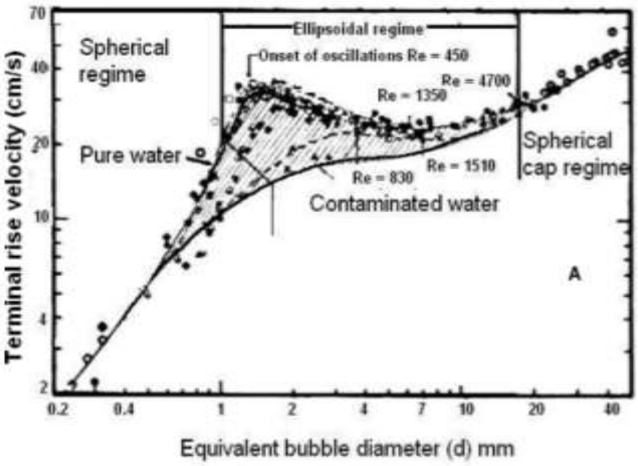

Figure 2.4: Typical trends in rise velocity with bubble size for pure and contaminated liquids (adapted from Kulkarni and Joshi, (2005))

Actual liquid velocity

Determination of the actual liquid velocity is one of the most challenging tasks encountered in the measurement of GLFs. Most of the correlations used to determine the actual liquid velocity either require priori knowledge of the slip ratio or the superficial phase velocities. More so, occurrence of a slip condition further complicates the accuracy of the measurement in that, it is dependent on the phase fraction, mixture density and mass fractions. According to Shaban and Tavoularis (2015), the Nicklin type of correlation combined with an adequate sensing technique is capable of providing reasonable actual liquid velocity determination . In other words, the actual liquid velocity is a secondary parameter derived from other parameters, such as the phase fraction and drift velocity of the gas phase and actual gas velocity with a known flow regime condition.

It is therefore useful to consider a modified correlation, combined with sensor measurements to determine the actual liquid velocity. This is expected to meet the compromise amongst cost effectiveness, technical requirement and safety. Details to relevant measurement techniques and the application of NIOIRS for GLF characterization discussed in sections 2.3 and 2.4.

2.3. GLF Measurement Technologies

There are several notable technologies applied to measure and monitor GLFs directly or indirectly based on the inherent property disparities of each phase. These include (not exhaustive):

i. Electrical Impedance (resistive, conductive, capacitance),
ii. Optical (Infrared, Laser)
iii. Magnetic Resonance
iv. Radioactive (X-rays, Gamma Ray),
v. Acoustic (ultrasonic)
vi. Pressure (differential /gauge)
vii. High-Speed Video and photo imaging
viii. Tomography (Electrical, Radioactive)

Generally, each of these technologies can be installed intrusively or non-intrusively on a pipe section, depending on the value of information required from the flow stream. Figure 2.5 presents the differences between the intrusive and non-intrusive installation of sensors along test section pipe wall. In the context of this work, non-intrusive installation refers to non-invasive and non-intrusive installation of the sensor head (s) at the outer wall of the pipe.

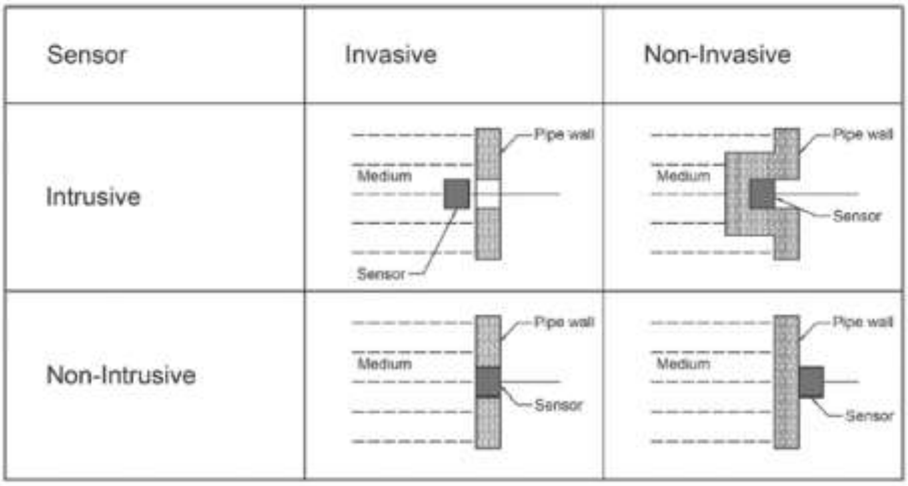

Figure 2.5: Description of intrusive and non-intrusive installations on pipe (Adapted from Wahab *et al.*, 2015).

2.3.1. Intrusive sensing technologies for GLF

The monitoring of local and temporal flow characteristics such as void fractions and radial velocity distribution in the pipe of interest has been achieved with intrusive probes designs of any of the technologies. Local phase fractions have been investigated using forms of resistive, and conductive intrusive probes in pipes for varied flow configurations.

Intrusive optical probes which operate based on disparities in refractive indices were also used to study local void fractions with reasonable degrees of accuracy (Abuaf *et al.*, 1978). The sensor responses are analyzed to calculate a time averaged phase fraction based on reference responses of the probes to each phase. However, accuracy of these methods strongly depends on the geometry of the probes, the area of contact, de-wetting conditions of bubbles and so on (Barrau *et al.*, (1999) further categorized the main sources of errors as blinding effect, crawling effect and bubble drifting effect.

Electrical sensing in the form of wire mesh sensors (WMS) installed intrusively across the pipe cross section has been applied to measure actual gas velocity , identify flow regime and estimate void fraction by quite a number of investigators (Nuryadin *et al.*, 2015; Olerni *et al.*, 2013; Shaban and Tavoularis, 2016; Velasco Peña and Rodriguez, 2015; Zhai *et al.*, 2014). In all of these investigations, the limitations due to significant distortion of flow regimes, observed as bubble fragmentation and pressure losses occurs which decreases the range of applicabiity and confidence in the accuracy of measurment.

2.3.2. Non-Intrusive Sensing technologies for GLF

The term non-intrusive sensing techniques, as used in the context of this work, refers to the method of measurement where a sensor setup is positioned at the outer wall of a pipe or conduit to detect and relay signal or visual information without having physical contact with the flow within the pipe (Figure 2.6). These techniques comprise (a) the sensing component and (b) the signal analysis components. The sensing components are the actual sensors (based on similar technologies as intrusive sensors) that provide raw signal or visual data to be analysed. The signal analysis component includes spectral, statistical and image processing techniques used in the analysis of the raw signals for inferential interpretation.

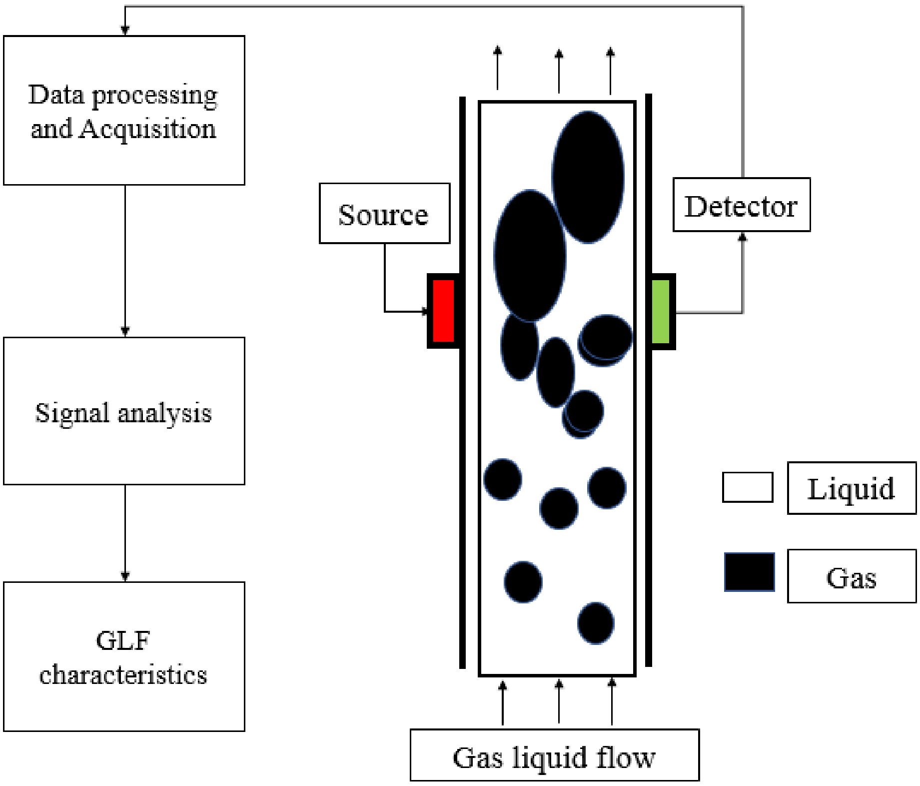

Figure 2.6: A general schematic of a non-intrusive sensing setup for GLF measurement.

A reasonable number of non-intrusive techniques are available. These include radioactive, electrical, acoustic and videometry technologies (Thorn *et al*., 1999). The use of non-intrusive radioactive techniques has been considered for phase fraction estimation and flow regimes identification (S A Abouelwafa and J M Kendall, 2000). The sensing components consists of a radioactive source and detector. This source emits a penetrating beam of particles which interacts with the fluids in the pipe. A radiation attenuation is observed due to the preferential absorption of each phase in the pipe. The unabsorbed energy is detected and transmitted for inferential interpretation which could be a temporal signal or tomographic information. Investigators have considered the use x-rays (Jones and Zuber, 1975), photon and neutron set ups (Heindel, 2011; Harvel *et al.*, 1996; Gardner, 2008).
Accurate results have been reported however, high cost of dedicated setups and critical safety concerns are key limitations using these technologies (Banowski *et al.*, 2017). The cost estimates of a typical radioactive setup for MPF metering as reported by Falcone *et al.*, (2008) are in the range of $50,00-400,000 and $1-4 million for subsea special applications.

In recent years, tomographic technologies have been investigated for GLF characterization due to low cost and high temporal resolution in image capture. One common form of this technology is electrical impedance tomography (with variations in forms of conductance, inductance or capacitance) which discriminate between gas and liquid interfaces based on disparities in resistance, permittivity and dielectric properties (Sardeshpande *et al.*, 2015).

Non-intrusive electrical sensing involves electric fields generated by sensor electrodes which are preferentially distorted based on the spatial distribution of each phase. The phase fractions and flow regimes can then be inferred via signal analysis or image reconstruction techniques. Accuracy of the aforementioned technology depends on the design of electrode configuration which has been reported to be challenging (Ji *et al.*, 2014). This challenge is primarily because the electrode geometries define the uniformity of the electrical field distribution.

Most investigators have sort to develop various geometries that would minimize the distortion of electric field by varying electrode shape, surface area and lengths. For instance, Xie *et al.*, (1999), considered concave electrodes which were designed to reduce sensitivity to axial flow distributions. Andreussi *et al.*, (1988) designed a ring electrode to achieve a uniform electric field around the pipe. Other documented electrode designs include helical, rotating and multiple electrode arrangements (Jones and Zuber, 1975; Merilo *et al.*, 1977).dos Reis and da Silva Cunha, (2014) compared the performances of the above electrode geometries and concluded that the ring electrode gave the best performance in determining phase fractions for a GLF. Similar comparisons were made by Salehi *et al.*, (2017) for flow regime identification, they concluded that the concave electrode gave a good agreement with photos from high speed camera. Albeit these efforts to improve accuracy, the problem of configuration superiority for varied flow conditions remains, hence limiting the range of applicability to low void fractions.

Non-intrusive acoustic technologies have also been investigated by a few researchers(Huang *et al.*, 2013b). Al-lababidi *et al*. (2012), investigated the performance of acoustic emissions for GLF using ultrasonic sensors. They correlated the acoustic emission energies with gas void fractions and phase velocity for a horizontal flow case. They concluded that the acoustic sensors needed additional testing for higher flow velocities. Ultrasonic Doppler Velocity measurement was studied under MPF conditions (Huang *et al.*, 2013a). The aim was to measure a reliable bulk velocity of phases for determination of phase flow rates. The investigators concluded that the results on bulk velocity was not reliable because of gas bubbles in the liquid phase, thus limiting the interrogation depth of the ultrasonic wave to a shallow liquid region near the pipe wall.

Videometry techniques also present non-intrusive options especially for cross validation of results from other techniques. It involves the use of cameras used to visualize flow regimes directly and capture images for phase fraction estimation using image processing techniques. For high flow rates, the use high speed cameras which incorporate image processing presents a more objective method of identifying flow regimes and phase fractions. Recent investigators have considered this technique for characterizing slug lengths and interfacial velocities (Al-Kayiem *et al.*, 2017; Amaral *et al.*, 2013).In addition, the estimation of bubble flow characteristics using videometry such as bubble size distribution, and liquid film thickness for annular flows were reported to be in good agreement with flow models (Lau *et al.*, 2013 ; Bonilla Riaño *et al.*, 2015).

Videomerty is however limited to only transparent or clear pipes and could be expensive in the case of high speed imaging. It is also only applicable to controlled laboratory conditions were adequate lighting for quality imaging is required. Uncertainties exist in detecting bubble overlaps when two or more bubble or slugs overlap in the field of view (De Oliveira *et al.*, 2015), hence further image processing may be required to improve accuracy of measurement.

Signals from pressure sensors have been used to infer flow regimes (see, Bin *et al.*, 2006; Elperin and Klochko, 2002; Matsui, 1984; Shaban and Tavoularis, 2014) and most recently void fractions (Han *et al.*, 2016; Jia *et al.*, 2015). Jia *et al.*(2015) proposed a method that estimates void fractions of a gas liquid flow from differential pressure derived from two pressure transducers. They derived an expression from the Bernoulli equation which shows a relationship between the void fraction, measured pressure differential using two static pressure transducers and calculated friction factor (Fanning friction factor). They compared their results to wire mesh sensor (WMS) and Electrical Resistance Tomography (ERT).

Their model used the actual liquid velocity derived from a liquid flow meter reading, while the fanning friction factor was derived based on the laminar and turbulent correlations of the Reynolds number. Furthermore, their assumption of a negligible air density further introduced an error of 0.12 % to the void fraction measurement. The error thereafter excludes other sources of errors in their work. Shaban and Tavoularis, (2014) also presented a simpler void fraction model (equation 2.26) based on responses from a pair of pressure sensors, the void fraction α_P ,was computed based on the hydrostatic pressure drop of the liquid ΔP_{gl}, and hydrostatic pressure drop relative to the two phase flow system ΔP_{gl} . The model hence assumes the dominance of the gravitational pressure drop and a negligible frictional pressure drop. They therefore considered only low flow rates in their work

$$\alpha_P = 1 - \frac{\Delta P_{gl}}{\Delta P_l} \tag{2.26}$$

In this work, comparative studies between the void fraction derived from NIOIRS and that from differential pressure is considered.

2.3.3. Non-intrusive Optical Infrared Sensor (NIOIRS)

Optical infrared sensors emit and detect infrared radiation or light in the range of 700 – 1mm wavelength. More so, the consideration of a non-intrusive installation of these sensors affords significant advantages such as elimination of flow distortion which leads to no pressure losses, no corrosion or erosion of sensor heads. According to Arunkumar *et al.*(2016), optical infrared sensors are preferred to other sensing methods due to the following:

i. Low sensor power requirement
ii. Simple design
iii. Reduced noise to signal output
iv. Low cost

A sensor response from NIOIRS is converted into temporal electrical signals which could be processed and interpreted to characterize GLFs via direct observation or signal analysis techniques. The sensing component mainly include an emitter such as light emitting diode (LED) and a detector called a photodiode. LEDs are semiconductor devices that convert electrical energy to light energy and are operated in the forward bias mode. The Photodiode detectors are also semiconductor devices that convert light absorbed as photons into electrical voltage or electric current and is operated in the reversed biased mode.

The sensor pair arrangement could be transmissive or reflective. Transmissive NIORIS as can be seen in figure 2.7(a) are designed to transmit the ray of light through a path from source to the detector, where the detector is positioned at the opposite end of the pipe section. When an object crosses this ray path, there is an interruption of the beam of light which changes the intensity of detected radiation. For reflective NIOIRS, the sensor arrangement has the emitter to the detector to be adjacent to each other as shown in figure 2.7(b), such that the reflection of the incident rays from any object in the domain of radiation is detected by the photodetector; hence leading to a variation of measured intensity.

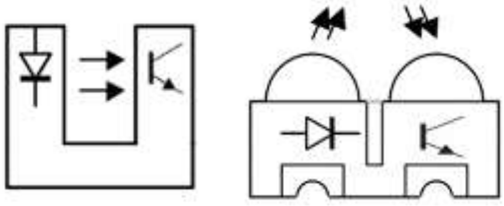

(a) (b)

Figure 2.7: Infrared Sensor – detector arrangements (a)Transmissive type (b) Reflective type

Theory of operation

The theory of operation of the NIOIRS typically involves the emission of light of a specific wavelength within the infrared range from the LED. The light is attenuated based on disparity in refractive index and absorbance coefficients between the phases when it travels through the pipe. The phase interfaces could lead to light scattering, refraction, absorption or a combination, which depends on the bubble sizes of gas in the liquid.

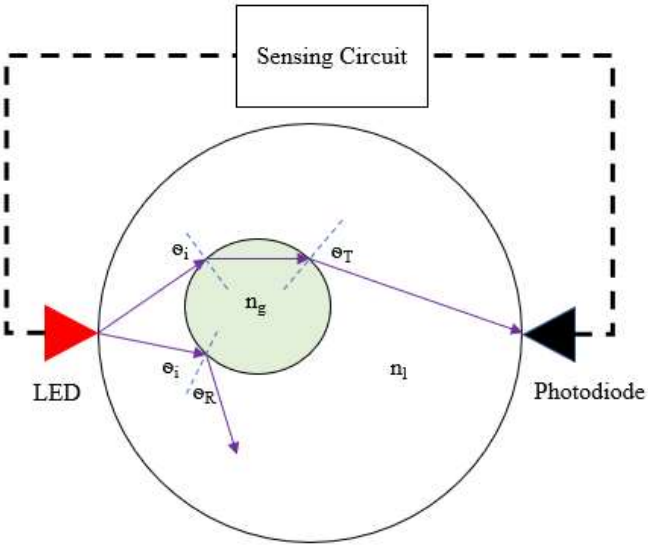

Figure 2.8: Schematic of a typical NIORIS set up showing emitted rays from an LED transmitted rays towards the photodiode (blue dashed liens are imaginary normal lines at phase interface)

The governing laws that define the IR light propagation are described by equations (2.27 – 2.30)

Law of reflection $\theta_I = \theta_R$ (2.27)

Snell's law for refraction $n_1 sin\theta_I = n_2 sin\theta_T$ (2.28)

Where θ_I ,θ_R and θ_T are the angles of incidence, reflection and refraction respectively, n_1 and n_2 are the refractive indices of the first and second phases respectively.

Fresnel's law defines the percentage of light transmitted to reflected light. Based on a relationship for reflection r^{2} and transmission coefficient t^{2}, in a parallel and perpendicular axis.

$$r^2 + t^2 \frac{n_1 cos\theta_T}{n_2 cos\theta_i} = 1 \tag{2.29}$$

The interaction could lead to an attenuation of light intensity (from I_o to I) and can be modelled as an exponential decay which depends on the attenuation coefficients (a) across the thickness of the medium (x) based on the Beer lamberts relation as defined by equation (2.30)

$$I = I_o e^{-ax} \tag{2.30}$$

The emergent light is then received by a photodiode which converts light to electrical signals over time which are processed and analysed for GLF characteristics. Technically, a linear relationship between the attenuated light and bubble sizes for a specific wavelength makes the optical technique a viable candidate for understanding flow regimes and phase fractions. (Berthold *et al.*, 1994).

NIORIS setup considerations

To ensure accuracy in monitoring and detection of GLF, it is important to design the IR sensing circuit to (a) handle global and local measurements, (b) minimize ray divergence and (c) compensate for changes in temperature and ambient light. The impacts of each consideration on the design are detailed below.

i. Global and local measurements

To be able to detect local and global characteristics of GLF, IR sensor pair arrangements need to be installed on at least two points along the pipe. A practical solution is to design an optical sensor setup that emits a consistent beam through the transparent pipe with more than one detector system at the appropriate spacing on the test section to give an improved representation of flow in the pipe. Signals from each detector are correlated and used to determine flow characteristics. Also, the use of an appropriate sampling rate by a data logger is required to capture temporal information flow structures of interest. Furthermore, the choice of sensor spacing between sensor pairs along the pipe needs to be optimized to ensure accurate cross-correlation between sensor signals. It is a rule of thumb to optimally space sensors according to Nyquist sampling theorem as 3+5 times smaller than the characteristic dimension of the flow structure of interest (Azzopardi, Hills, Fabre, Brauner, Bertola, Celata, Mariani, Marchioli, Picciotto, 2003).

ii. Ray divergence

The divergence of the incident beam due to the refractive index of the pipe wall should be minimized to improve transmittance of the IR light across the pipe section. A recent publication by Li *et al.*, (2016) on the characterization of GLF for a horizontal flow, details the design of a multi-array optical sensor setup as shown in figure 2.9. This uses an extender lens with slits to minimize beam divergence and to create parallel beams. More so, to minimize Ray scattering effects at the pipe wall, Lau *et al.*, (2013) made use of fluorinated ethylene propylene (FEP) pipes, which has a refractive index close to that of water. The effect of divergence can be ignored with angle is less than 10 degrees.

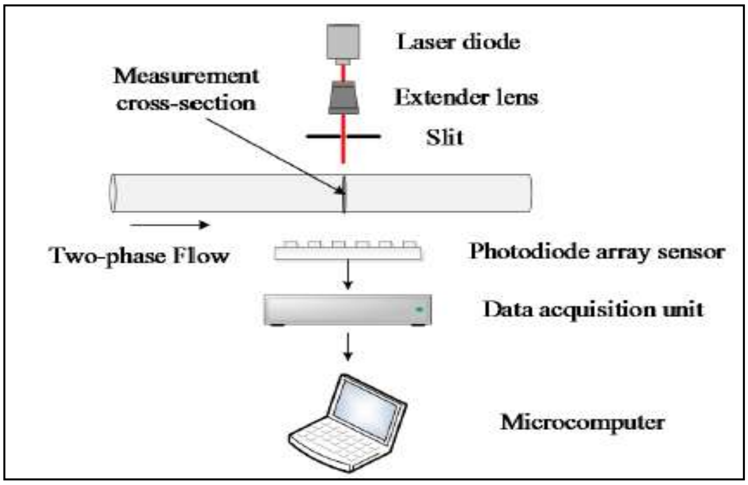

Figure 2.9: Multi-array IR sensor set up for a focused laser beam

(Adapted from (Li et al., 2016).

iii. Ambient light

The interference of ambient light could affect the incident and transmitted light intensity penetrating the test section. For instance, an exposure of the photodetector to ambient light could saturate the signal output and increase signal output. This situation causes misinterpretation of results and frequent recalibration of the sensor. It is therefore advised to cover the sensor pairs with an opaque material which prevents ambient light from affecting results. Furthermore, a reduction in the aperture size reduces exposure of the photodetector to ambient light (Semiconductors and Drawings, 2010). Importantly, further minimization of the ambient light interference could be achieved the photodiode is chosen have a narrow band of detectible wavelengths (TT electronics plc, 2016). This work compares the performances two photodiodes of different detectible wavelength bands.

iv. Temperature variations

Ambient temperature variations also affect absorption coefficient of the pipe wall and fluid mixtures and thus would alter the reference output signals detected by the photodetector. To compensate for these changes, appropriate monitoring techniques must be employed to alter the circuity parameters. For instance, a temperature decrease could be compensated by increasing the output power of the LED and decreasing the sensitivity of the photodetector. This measure assists in keeping the overall signal constant as temperature changes.

2.4. Review of signal and statistical analysis techniques

A direct interpretation of GLF characteristics has been made performed already in literature from raw NORIS Reponses. However, this has been applicable for only small size or capillary tubes (Coleman and Garimella, 1999 Xiaoming *et al.*, 2004,Ji *et al.*, 2014).

Arunkumar *et al*. (2016) made direct inferences from NIOIRS responses for the identification of flow regimes in a 4.8 mm pipe. They compared their results with CFD and photographs from a high-speed camera as shown in figure 2.10 (a-c).

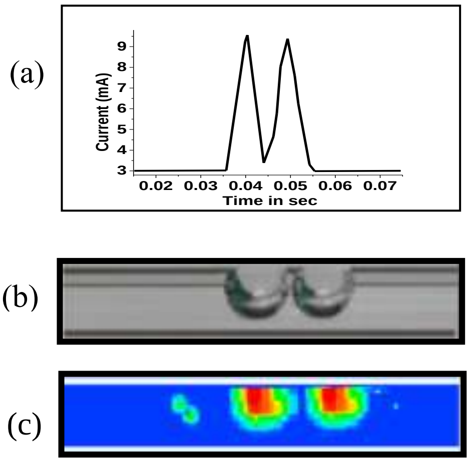

Figure 2.10 : A comparison of an identified bubble flow regime from (a) current signals derived from IR sensing with (b) high speed photographs and (c) CFD simulation

(modified from, Arunkumar *et al.* 2016)).

For larger pipe sizes, it is difficult to make direct interpretations of GLF characteristics since the distribution of flow structures in the pipe may not be homogenous. Therefore, the delineation is made vibrant via the application of signal and statistical analysis techniques. These methods of analysis enable sensor interpretation to be performed in real time. The most prominent methods considered in literature with regards to NIORS for GLF characterization include,

i. Probability Distribution Function (PDF)
ii. Cumulative Probability Distribution Function (CPDF)
iii. Cross Correlation
iv. Power Spectral Density (PSD)
v. Machine learning methods

2.4.1. Probability Distribution Function (PDF)

The PDF represents the likelihood that a sensor response (in voltage or current) would occur at a certain range. Generally, the PDF is defined mathematically as the ratio of the frequency of co-occurrence of the samples f_s in each range to the Total number of samples, N_s

$$P(N) = \frac{f_s}{N_s} \tag{2.31}$$

This distribution is therefore a representation of a function of the amplitude of the signal response, thus converting the time domain signal to an amplitude domain. It has been observed by several investigators that the PDFs derived from sensor signals is useful discrimination tools for identifying flow regimes of GLF, (Keska and BE, 1999; Omebere-Iyari and Azzopardi, 2007 iIsmail and Ahmed, 2008). For many samples, a PDF approximates a histogram distribution as would be used interchangeably in the rest of this thesis. Typical signatures of the PDF or histograms for flow regime identification is presented as (see figure 2.11),

i. Bubbly flow exhibits a characteristic single peak for signals corresponding to low void fractions,
ii. Slug flow is seen as a bimodal peak for low and high void fractions, corresponding to the liquid slugs and Taylor Bubbles respectively
iii. Churn flow is interpreted as a local peak and global peak distribution of void fractions
iv. Annular flow represents a single peak skewed to the opposite end as compared to the bubble flow distribution

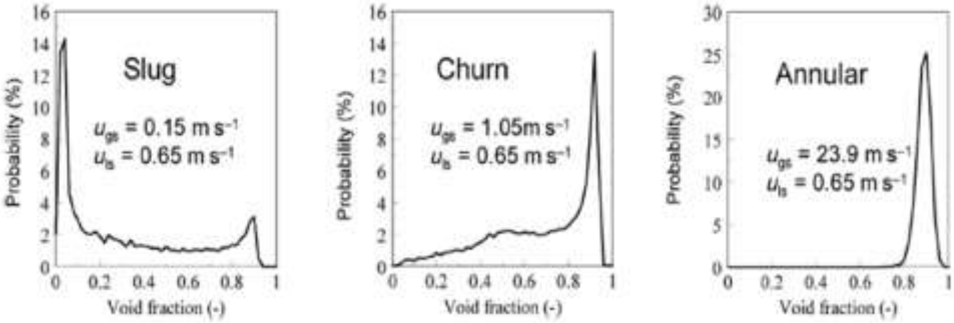

Figure 2. 11: Shapes of PDF identifying (a)Slug flow (b)Churn flow (c) Annular flow (Adapted from Omebere- Iyari and Azzopardi, 2007)

A novel application of the PDF in GLF characterization is the estimation of entrained bubble and Taylor bubble void fractions in a slug flow regime. This method has only been performed using non-intrusive electrical sensors by Abdulkadir *et al.* (2014b) for an upward flow of air and oil in a vertical riser. It is therefore worth considering this method in this work.

2.4.2. Cumulative Probability Distribution Function (CPDF)

The CPDF represents the sum of PDF based on the total probability distribution. According to Ruixi *et al.* (2013)the CPDF is expressed mathematically as

$$CPDF = \sum_{i=1}^{n} PDF \tag{2.32}$$

Where *i* represents the number of PDF from each range of amplitude values. The changes in slope or turning points using CPDF curves are key indicators of flow regime transitions. Ruixi *et al.* (2013), illustrates the change of slope at a CPDF, representing a transition from to bubble flow at the reference velocities as shown in figure 2.12. Keska and BE, (1999) made use of the amplitude value (derived from infrared sensors) range at a CPDF of 0.5 criterion to identify flow regime in a vertical upward flow of air and water.

As objective discriminators, the moments and turning points of the PDFs and CPDFs respectively have not shown a global consistency in flow regime discrimination, especially for the churn and annular flow regimes. Keska and BE, (1999) concluded that there was no clear transition distinction between the slug – churn and churn – annular transitions from their optical sensors due to the clustering of curves.

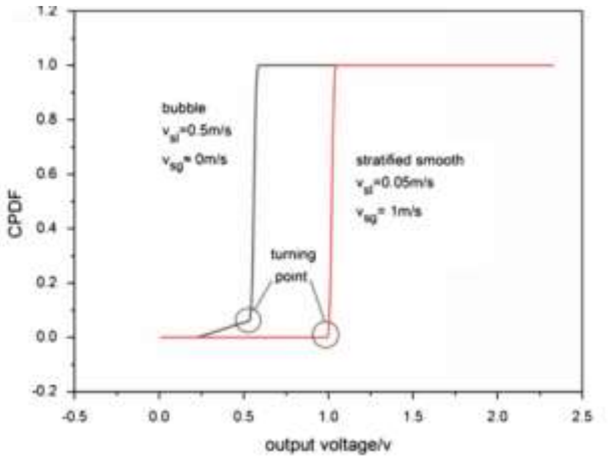

Figure 2.12: Interpretation of CPDF for flow regime discrimination (Ruixi et al., 2013)

2.4.3. Cross-correlation function

When two temporal signals are derived from similar sensors; upstream (1) and downstream (2) spaced at a distance along the pipe d, the measure of similarity of the signals S_1 and S_2 are described by the cross-correlation function. From the mathematical standpoint a cross correlation coefficient is derived as a result of the function described as,

$$R_{12}(\tau) = \frac{1}{T}\int_0^T S_1(t)S_2(t+\tau)dt \qquad (2.33)$$

A time lag between $\tau *$ or delay each sensor pair is then obtained as the argument of the maximum cross correlation coefficient as,

$$\tau * = argmax(R_{12}(\tau)) \qquad (2.34)$$

Figure 2.13, shows the cross-correlation of two signals containing the same square pulse at different times: R_{12} shows a maximum at $\tau *$ (representing the lag between signals) with a known spacing between sensor pairs then the structure velocity can be calculated as:

$$v = {}^{S}/_{\tau *} \qquad (2.35)$$

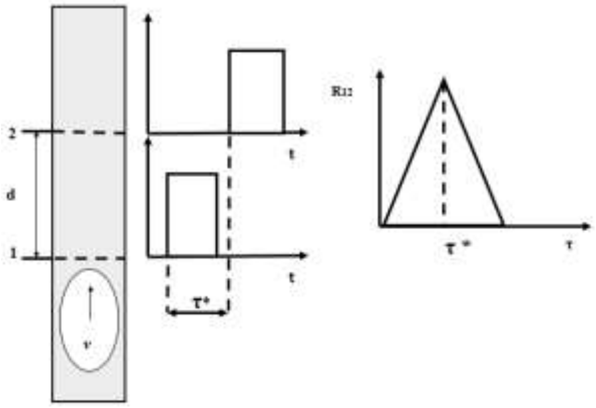

Figure 2.13: Gas velocity measurement using cross correlation technique

(modified from (Azzopardi, Hills, Fabre, Brauner, Bertola, Celata, Mariani, Marchioli, Picciotto, 2003)

The accuracy of the cross-correlation technique is dependent on a steady interface such as te presence of a gas-liquid mixture which creates the disparity in sensor response. It is important to space sensors apart appropriately to capture the passing flow structures but not too close to prevent errors in the correlation technique. Also, a high sampling rate is required to capture the flow structures. A few invesitgators have applied cross correlation for gas velocity determination using the NIORIS responses (Wolffenbuttel *et al.* 2002). It is therefore worthy to investigate the accuracy of the cross-correlation method over the varied flow regimes in the upward vertical GLF.

2.4.4. Power Spectral Density (PSD)

The PSD analysis converts the temporal signal from a time domain to a Frequency domain. This information is useful in delineating a fundamental frequency that corresponds to a specific flow regime. The PSD is computed using the Fast Fourier Transform F(x^2) as defined by,

$$PSD(x) = |F(x^2)| \tag{2.36}$$

The spectral analysis also represents the unsteady nature of the gas-liquid flow. It was first used as a noise frequency identifier can be related to the randomness of bubble motion. As a flow regime discriminator, the PSD of the measured the sensor is represented by three key features: a wide-band low-amplitude spectrum associated with bubbly flows, a low-frequency peak of large amplitude corresponding to the characteristic frequency of slug flow, and a medium-width band spectrum for annular flow (Rocha and Simões-Moreira, 2008). Although this method as not considered in achieving the specific objectives of this work, the PSD was applied to determine average structural frequencies in all flow regime with relevant validation and comparison with existing work in literature. Find results in appendix G of this thesis.

2.4.5. Machine learning methods

The aim of machine learning (ML) is to apply data to train an algorithm which becomes a predictor of certain characteristics. Figure 2.14 presents two broad categories of ML methods. These include supervised and unsupervised learning. Supervised learning is based on developing algorithms derived from input and output data while unsupervised learning methods develop algorithms that group and interpret data based on only the input data. A comprehensive review on the subject of ML for fluid characterization can be found in Brunton *et al.,* (2019)

ML as a branch of soft computing is currently leading in pattern recognition and is suitable for online recognition for a large range of flow regimes in pipes without knowledge of the flow rates. These developed algorithms use features derived from statistical and spectral methods to solve classification problems. Low error rates (up to 5%) of misclassification have been reported by investigators (Yan *et al.,* 2004; Shaban and Tavoularis, 2014b). Examples of these include, recurrence analysis, artificial neural network (ANN), cluster analysis, support vector machines (SVM) and least square methods.

However, the challenge of sample insufficiency for training algorithms, coupled with the requirement for numerous extracted input features, complexity of hidden layers in assigning classes and optimization of fitting parameters remains. Dimensionality reduction methods such as principal component analysis (PCA), have been considered in reducing the numerous features into feature spaces where further analysis can be carried out on the classification (Nnabuife *et al.,* 2019). This increases computational time in the context of real time monitoring and hence the need for simpler and more efficient classifiers.

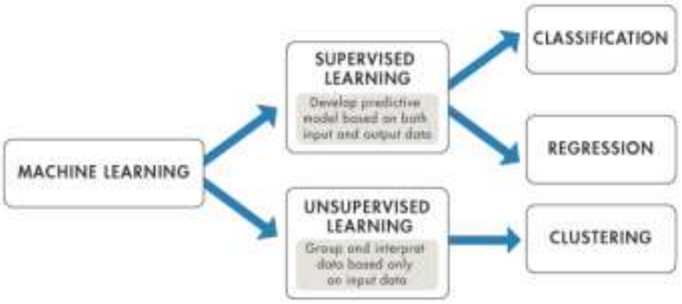

Figure 2.14: A general classification of machine learning methods

Given the setbacks, ML is a growing area and still requires investigations focused on less feature generation which may suffice for an adequate prediction model.

It is therefore proposed that focus on supervised learning methods, which support reinforced learning can suffice to bridge the less feature generation gap. Figure 2.15 presents a general framework applied to supervised learning methods. First, relevant data from a sensor response is labelled with known characteristics, then relevant features are extracted to be used to develop a learning algorithm. The algorithm then predicts the known characteristic, given that an adequate training is achieved. Lastly, the performance of the model is assessed based on the accuracy prediction of the correct label. Types of supervised learning such as Polynomial regression and Probabilistic Discriminant analysis of the linear discriminant function and Quadratic functions are new areas applied to objective discrimination of flow regimes.

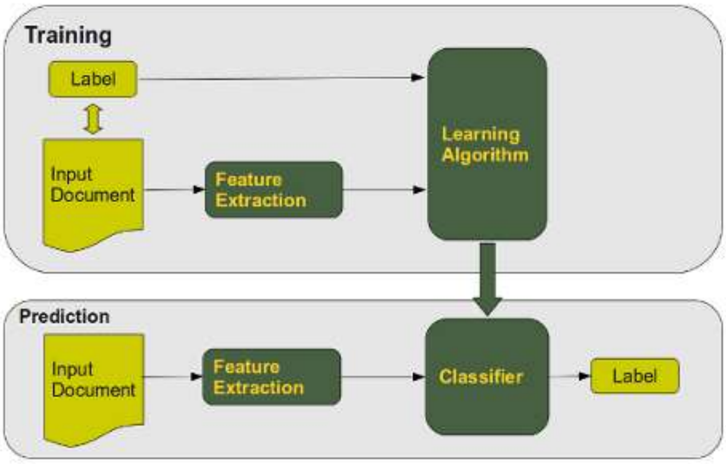

Figure 2.15: Typical framework used in supervised learning methods

Polynomial regression

Polynomial regression analysis is a well-known method that has been applied in numerous disciplines. Regression techniques predict continuous responses which makes them suitable for analysis of the sensor response in real time. It requires a minimum of two features (extracted from the sensor response) which may suffice for defining the decision boundaries based on representative fitting data. The derived functions provide a linear combination of fitting coefficients which aide faster decision making where real time applications remain a priority. However, the predictive performance of the regression fit relies on the most appropriate feature selection which largely possess strong dependence on the prevailing flow conditions in the pipe.

More so, in the case of challenging classification problems, where overlapping of features or variables occurs, the regression is however limited and avoided by most researchers. The severity of overlapping or clustering of boundaries is expected to worsen for flow regimes with similar structural characteristics. However, this clustering is expected to be minimized by high resolution sensor response acquired from the proposed NIOIRS.

Discriminant analysis

Discriminant analysis (DA) encompasses methods for classification (Duda *et al.*, 2012; Hastie *et al.*, 2005). and dimensionality reduction (Zhu and Hastie, 2003). Most commonly considered is the linear discrimination analysis (LDA). The LDA can either be applied based on Fishers approach or the Bayes probabilities approach. Fisher's approach (also Fishers discriminant analysis, FDA) tends to find the linear combination of features which maximize the between - class variance relative to the within class variance. Various researchers have considered FDA in other fields of study (Hiraoka *et al.*, 2001; Tharwat, 2016; Tharwat *et al.*, 2017). However, few have applied FDA to multiphase flow studies. Ameel *et al.*(2012) used FDA to reduce dimensionality of various features extracted from video footages of gas liquid flow in a pipe. Li *et al.*(2016) used the FDA to identify flow regimes using the average and standard deviation of responses from an array of optical sensors. The flow regime identification results were used to allocate valid void fraction models which were computed using SVM, where a maximum error of 7 % was realized.

The second interpretation is a probabilistic view, which uses Bayes rule to determine a maximum posterior probability that discriminates between classes or groups, in this case flow regimes based on priori probabilities of a training set. Wu *et al.*(1996) mentioned that use of probabilities as a classification criterion provides details about the separation distance of groups compared to the discrete classification accuracies from the normal LDA. On their work on online facial recognition, Ioffe, (2006) pointed out that the probabilistic approach has the advantage of making inferences about the likelihood of classifying new members into groups. This provides a better understanding of the level of confidence associated with the classification accuracy of the model.

The probabilistic interpretation of DA has not been applied to multiphase flow classification based on literature search, especially in the area of gas liquid flow regime identification from non-intrusive optical sensors. The probabilistic approach can also be applied to Quadratic discriminant analysis (QDA), which is termed as another variant of LDA. It is applied to cases where the covariances between groups are unequal. Although, QDA computes more terms in the discriminant function, incremental classification accuracies have been recorded for larger data sets compared to the LDA. Tharwat, (2016) details the comparison between the LDA and QDA.

2.5. Summary of research gaps

Table 2.3. below summarizes investigations carryout in literature with regards to the application of NIOIRS for GLF characterization. Presented are highlights of test section dimensions, orientation of flow section material, flow conditions, fluid systems and characteristic investigation.

Table 2.3. Summary of previous work on the application of NIOIRS for GLF characterization with the current work

Investigators	**Test section diameter/ length (m)**	**Orientation/ Material**	**v_{sl}, v_{sg} (m/s)**	**Fluids**	**IR setup**	**Investigation**
Ruixi *et al.*, (2013)	0.05, 20	Horizontal, PPMA pipe	0.1 1.1, 0.1- 8.0	Air, water	Coaxial double pair	Flow-regimes using CPDFs
Keska, (1999)	0.035, ***	Upward Vertical, Plexi-glass	0.1 -0.5 0.1 - 10	Air, water	Single pair, Laser	Flow regimes using PDF and CPDFs
Arunkumar *et al.*, (2016)	0.0048, 1	Horizontal, Glass	0.01-1.1 0.1-8.0	Air, water	Single pair	Flow regimes Direct observation

,Wolffenbuttel *et al.*, (2002)	0.002, 1	Downward Vertical, Plexiglass	0.2-1.0 0.1 – 5.0	Air, decane, water	Spaced Double pair	Slug velocity and length, direct observation
Vaitsis *et al.*, (2004)	0.005, 2	Downward flow, Plexiglass	0.01– 1.0 0.1-1.0	Nitrogen, Water	Single pair	Bubble, slug length, slug velocity by direct observation
Nguyen and Truong, (2005)	0.0024, 0.2	silicone tube horizontal	***	Air- water	Double pair	Single Flow rate measurement
Berthold *et al.*, (1994)	0.0068, 3	Glass tube vertical	1.2 – 5.6 0.01, 0.5	Nitrogen – water	3 pairs of fiber optics	Void fraction. Use of Beer lamberts relationship
Mithran and Venkatesan, (2017)	0.0025, 0.3	Horizontal, borosilicate glass tube	***	Air – water	90^{o} and 50^{0} pair	Liquid film thickness, simulation work in
Sulthana *et al.*, (2018)	0.002, 0.15	Horizontal square Channel, borosilicate glass.	***	Air - water	Single pair	slug-bubble train scattering simulation work
Dutra *et al.*, (2017)	0.0012, 0.1	Curvette Optical window borosilicate glass, vertical	0.046 0.058	Air – crude oil	IR lamp emitter and array detector	Bubble size effects on IR intensity and flow visualization,
Keerthi Vasan and Venkatesan, (2017)	0.0047,0.3	Borosilicate Glass, horizontal	0.3 -1.5 0.2 - 0.4	Air- water	Laser based pointer (660nm)	Liquid film thickness
Adhavan *et al.*, (2017)	0.0048, 1	Borosilicate Glass, horizontal	0.2 -1.5 0.2 0.4	Air -water	Sing pair	Slug velocity and length
Arunaganesan *et al.*, (2017)	0.0018 0.00314 0.00468, 0.3(length)	Borosilicate Glass, horizontal	****	Air-water, oil-water	Laser- 3 pairs photodiode pair+ camera	Flow regimes, slug velocity photodiode arrangement
Ide *et al.*, (2007)	0.0001, 0.065	fused silica capillary tubing Horizontal,	0.2- 0.4 0-5	Air – water	Double spaced / Fiber optic emitter and IR photodiode	void fraction, gas and liquid slug lengths,

Current work	0.018, 1 0.0273, 5	Upward vertical flow, PVC clear	0-2.0.61 0.001-13	Air, Water	Spaced Double pairs, Dual wavelength	Flow regimes, phase fraction, phase velocities Taylor bubble and entrained bubble fractions, Liquid film thickness, Gas and liquid flow rate. Real time application

In comparison with the current work, it is evident from table 2.3, that most investigators considered small and short test sections, except for Ruixi et al. (2013) and Keska, (1999) who considered pipe sizes of 0.05 m and 0.035 m. However, they investigated flow regimes using PDFs and CDFs, hence no objective prediction of flow regimes was proposed.

Most investigations that considered phase fractions reported less accurate measurements due to the measurement of residence time of bubbles observed on the sensor response. For instance, the presence of spherical or ellipsoidal bubbles has been reported to cause random signal scattering. Dutra *et al.*, (2017) reported this form of scattering as a lensing effect which leads to errors in the phase fractions computed. Berthold *et al.*, (1994) reported a compensation method for the effect of bubble scattering on a developed fiber optic sensor response. They used two LEDs of different wavelengths (835 nm and 1300 nm). The 835 nm wavelength allowed no absorption of light of either phase of water or nitrogen. This formed a reference wavelength when compared to the 1300 nm emitter. Hence, a modification to the beer lamberts law in relation to the sensor response was developed with known fluid absorption coefficients, however they obtained a +/- 10 % error void fraction, even for the small pipe size of 6.8 mm considered in their work. The error was attributed to the effects of flow regime transitions on the phase fraction model.

Most notably, this work considers a novel application of the NIORIS for determination of flow regime-dependent phase fraction, which is modified for interfacial scattering, structural characteristics such as liquid film, void fractions of Taylor and entrained bubbles in the slug flow regime, phase velocity measurement and two-phase flow rates.

In addition, none of the investigations in literature have applied supervised learning methods such as polynomial regression and probabilistic discriminant analysis of LDA and QDA as signal analysis to the NIOIRS response. Finally, real time applications in identifying flow regime and phase fraction measurements further extend the boundaries of knowledge with regards to the capabilities of the NIORIS.

Chapter 3.

3. Experimental Facility and Methods

3.1. Introduction

This chapter presents details on the key experimental facilities and a methodological approach to achieve the specific objective earlier presented in chapter 1. The following areas are discussed as follows, (i) the description and operation of two experimental flow rigs with other flow conditions and properties for the investigation of upward vertical GLF (ii) the design and setup of two NIOIRS setups. (iii) relevant data analysis approaches and validation methods considered for result verification from the designed non-intrusive optical sensors. A justification of methods is also discussed further discussed.

3.2. Experimental flow rigs

Measurement techniques (direct or indirect) need to be developed to make accurate measurements and monitoring of GLF possible. Experimental investigations using flow rigs have made meaningful contributions to the study of multiphase flows (Bello *et al.*, 2007b; Falcone *et al.*, 2008). Contributions leading to the developments of models and testing of MPF meters have been achieved. These flow rigs study multiphase flow for various flow configurations and scales. Bello *et al.*, (2007), gave a detailed review of existing flow loops worldwide.

Generally, the design of these rigs enables the circulation of multiple phase fluids upstream of the pipe test section and separation of phases downstream of the section. The flow mixture is then characterized in the test section pipe. The test section is fitted with instruments which measure and relay information to a data acquisition system (DAQ) and are analyzed on a computer.

In this work, a test and main flow rig were designed and setup in the Chemical and Petroleum Engineering laboratory at London South bank University (Lab 127), to investigate the characteristics of an upward vertical GLF. The test rig was set up to initially study the response of a NIOIRS to upward GLF and too understand the effect of interfacial scattering on the sensor response. The main rig was setup to further analyse the performance of the NIOIRS for extended flow conditions to achieve a full range of stable flow regimes and improved confidence in the characterization and measurement results from the test rig. A description of setup and operational procedure is detailed below for both flow rigs.

3.2.1. Test rig set up and operation.

The test section (TS) was a transparent PVCu pipe of length 1m and 0.018 m internal diameter (equivalent to L/D = 58) with a wall thickness of 0. 0015m. The test section was transparent which gave optical access for the capture of flow regimes and measurement of bubble lengths in the pipe. The dimensions of the test section were also sufficient for the development of mainly bubble and the slug flow regimes. Air was supplied from a compressed air cylinder (CAC) at 0.5 bar gauge pressure into the bottom of the TS via an injection pipe of 0.004 m diameter (as shown in figures 3.1)

Tap water was also supplied to the bottom of the TS at a steady rate from a sump (SP) using the variable speed pump (PU) from Liquid Port (2 bar rating). The air flowmeter (AF) valve controlled the airflow rate, while the speed pump controlled the water flowrate coupled with the water rotameter (WF) up to maximum flow rates of 2 l /min and 120 l/hr for air and water respectively. The two-phase system was circuited up the TS with air released to the atmosphere. The typical procedure for a run of experiment was to fill the pipe with water at constant velocity while increasing the gas flow rate. A meter rule was setup parallel to the TS to provide a measuring reference when the video camera VC captured high-speed photographs and videos. The infrared sensor (IRS) was installed at 45D to capture the flow events in their optical path cross sectionally in real-time with information logged by the DAQ or processed in real time and displayed by the computer (PC).

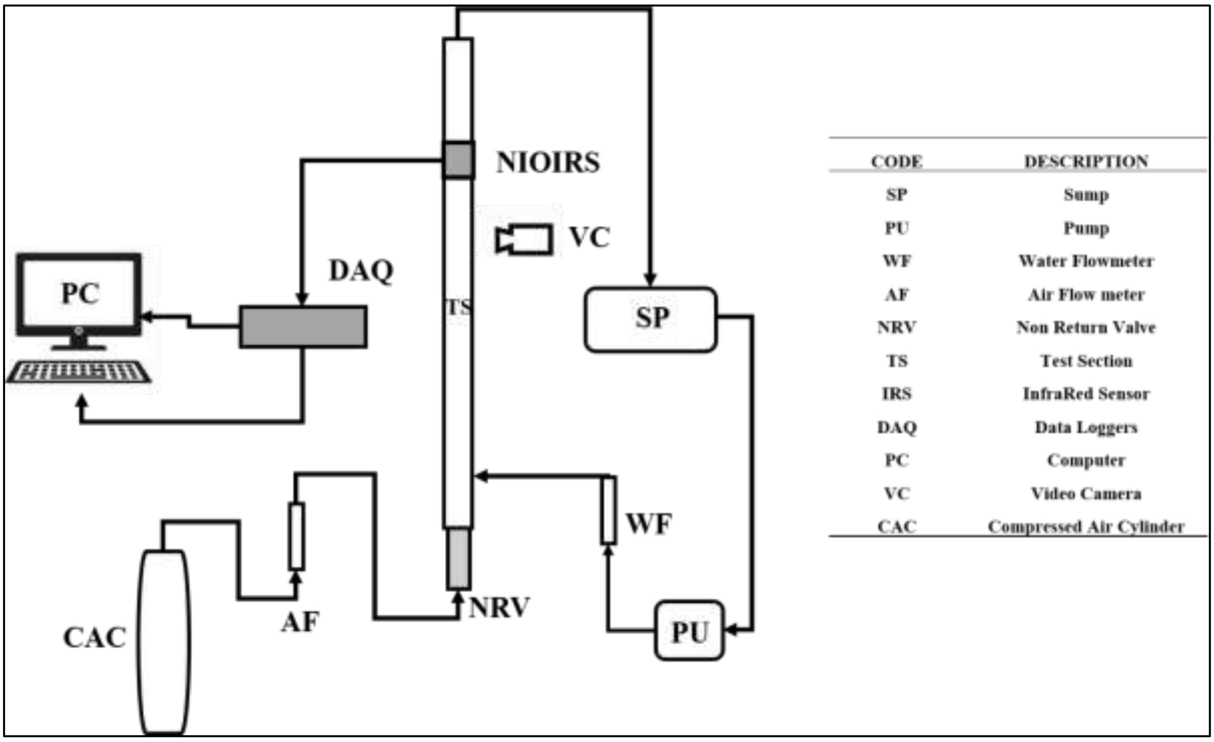

Figure 3.1: Schematic of the test rig

3.2.2. Main rig set up and operation.

Figure 3.2 shows the schematic of the main rig setup, purposely designed and setup for the purpose of the vertical upward flow of air and water studies and instrumentation. This consists of a test section (TS), of 27.3 mm internal diameter, wall thickness of 1.5 mm and 5 m long transparent PVCu pipe (to aid visual observation of flow regimes). The air was delivered by a compressed air supply at discharge pressure of 6 bar, while the water was circulated from a water tank (WT) (from Enduraxx, 300 litres) using an inline single variable speed booster set (from Lowara LPL10/10SV07). Water was circulated at atmospheric conditions with low flow (2 – 20 l/min) and high flow (19 – 190 l/min) ranges.

A rotameter (from Omega, FL-2080-V) and turbine flow meter (from pipe stock) were used to control the low and high flow rates respectively when the three-way valve (TWV) was used to select the desired flow path. The compressed air was also metered at low and high flow rate ranges using two rotameters and HAF (both from Omega, FL-2017-SS, 5 - 100 l/min and FL-2075-V, 100 - 1400 l /min) respectively. Measurement uncertainties of air and water were at +/-1.25 % of full-scale measurements.

Water is then injected from side of the tee mixer (AWM) with air injected from the bottom of the TS through a pipe of size 4mm fitted with a non-return valve to prevent the injected water from entering airline. The two-phase flow mixes and develops into a stable flow regime towards the top section of the TS. The Infrared sensor pair (NIOIRS) was installed at 180 D from the bottom of the TS (more details in figure 3). This was to ensure well developed flow regimes were formed before approaching the sensing area and not too close to the top to prevent bubble break up effects at the top bend of the TS. Data from the NIOIRS is pre- treated by the sensor circuit and captured by the data logger DAQ, and finally stored on a computer (COM) for further analysis.

To measure differential pressure along the TS, three (3) similar pressure transducers PT_1, PT_2 and PT_3 (from omni PI605R series) of pressure Range 0 - 6 bars and corresponding output of 0.5 - 4.5V were installed on the TS. Each pressure transducer (or sensor) had a combined error < 0.25% of the full-scale reading. PT_1 was installed at the base of the TS, PT_2 and PT_3 were installed at each end of the sensing section of the TS spaced at 1.25 m. Calibration information of the pressure sensors was provided by the manufacturer, which was based a linear interpolation that enabled the voltage reading to be converted to pressure readings (in bars).

$$P_{obs}(t) = 1.5(V_{obs}(t)) \tag{3.1}$$

Where, $P_{obs}(t)$ a pressure value taken at a sample interval and $V_{obs}(t)$ is the instantaneous reading of the obtained from the pressure sensor.

The high-speed camera (VC) (from NIKON, D300) was set to capture videos and photographs (at 5 frames per second) of the flow regimes at around 190D of the test section. It provided a cross validation of the sensor response to desired GLF characteristics. The two-phase flow is circulated through the test section and via the horizontal section (HS), where air is expelled to the via a separator, with water returning through the vertical return line (VRL) for recirculation. The equivalent superficial velocities of each phase v_{sl} and v_{sg} were calculated as the ratio of the flowrates to the entry diameter of the test section at ambient conditions.

$$v_{sl} = \frac{Q_{sl}}{A} \tag{3.2}$$

$$v_{sg} = \frac{Q_{sg}}{A} \tag{3.3}$$

A metre rule (not shown in figure 3.2) was also set up from the top of the test section within the sensing area to provide reference measurements for captured structures by the VC. A 15DC volt power box was also installed which connects all sensors from the top to the base of the rig where, they are all linked to the computer via a 5 m USB booster cables. Booster cables were used to minimize the noise to signal outputs of each sensor pair.

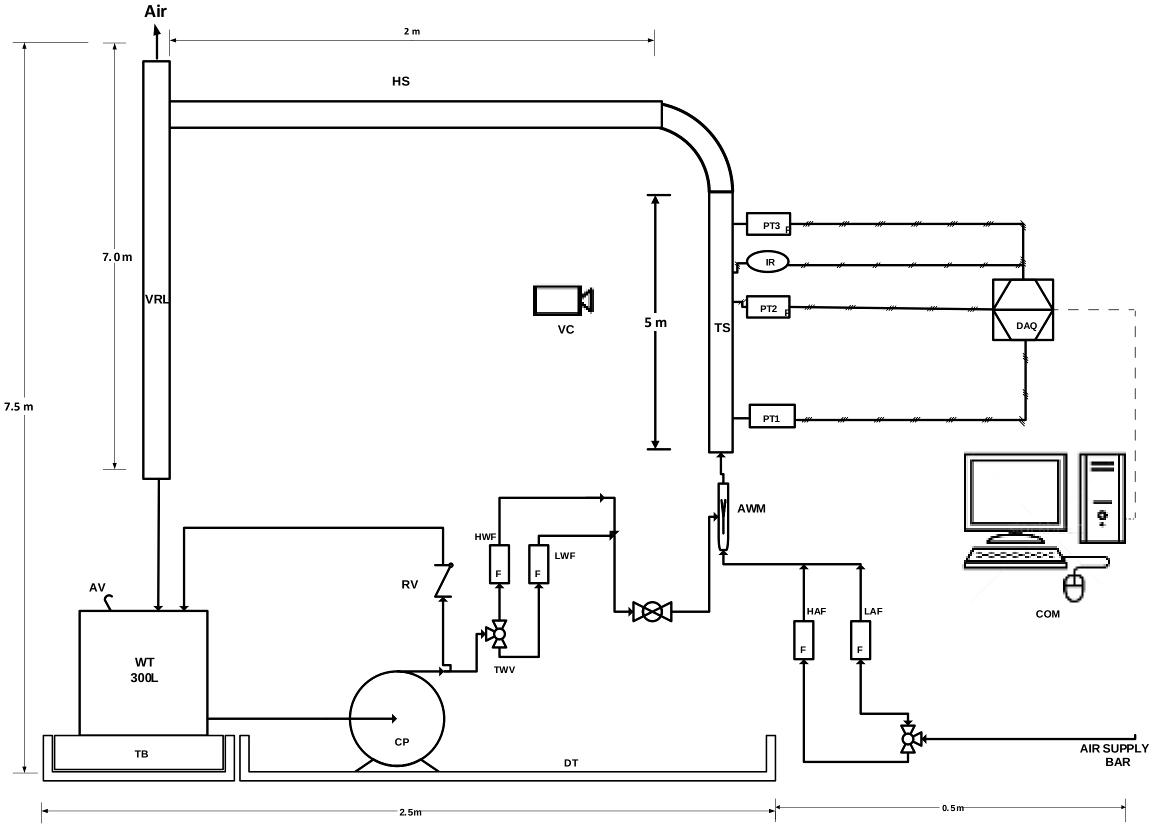

Figure 3.2: Schematic of experimental flow rig air water flow rig showing key component

WT - Water Tank, CP -Variable speed pump, HWF-High Water Flowmeter, LWF - Low Water Flowmeter, AWM - Air Water Mixer, NRV - Non-Return Valve, HAF - High Air Flow meter, LAF - Low Air flow meter, TS - Test Section, HS - Horizontal Section, VRL - Vertical Return Line, TB - Tank Bund, RV - Return Valve, TWV - Three Way Valve,PT1,2,3 - Pressure Transducers, DAQ - Data logger ,VC - Video Camera, COM – Computer, IR1,2 - NIORIS sensor head.

3.2.3. Fluid properties and data matrix

Table 3.1. summarizes the key fluid properties and range of superficial velocities considered for this work for both flow rigs. It is important to note that the properties of air and water were obtained from literature given the ambient conditions of 18 ^{0} C and atmospheric pressure of 1 bar. More so, through the period of experimentation, care was taken to ensure that the viscosity of water stored in the sump (test rig) and tank (main rig) was not affected accumulation of debris or biotic activity. This was done by regular circulation of water and periodical replacement of the volumes of water required for the experiments.

Table 3.1. Summary of fluid properties and flow conditions for the test and main rig.

					Test rig	Main rig
Fluid	Density (kg/m^3)	Viscosity (cp)	Refractive index ([-])	Surface tension (N/m)	superficial velocities (m/s)	superficial velocity (m/s)
Water	998	1	1.33	0.0728	0 - 0.131	0 – 1.00
Air	1.204	0.018	1	-	0 - 0.161	0- 13.00

Figures 3.3 (a) and (b) present the range of flow conditions expressed in superficial velocities of air and water performed using the test rig and the main rig respectively. In order to achieve a range of flow regimes, each rig was operated at a constant liquid superficial velocity with an increasing interval of gas superficial velocities per run.

(a)

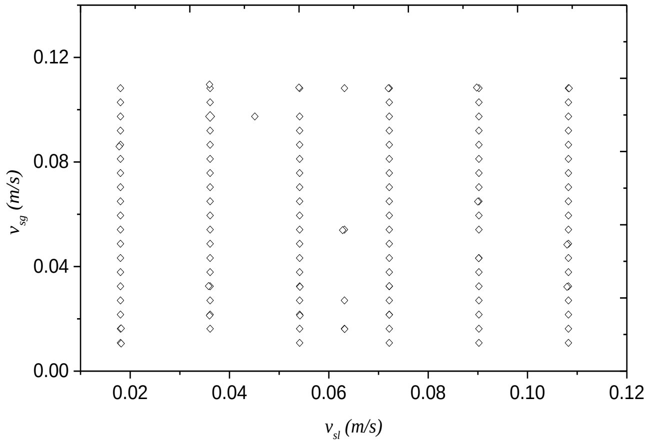

(b)

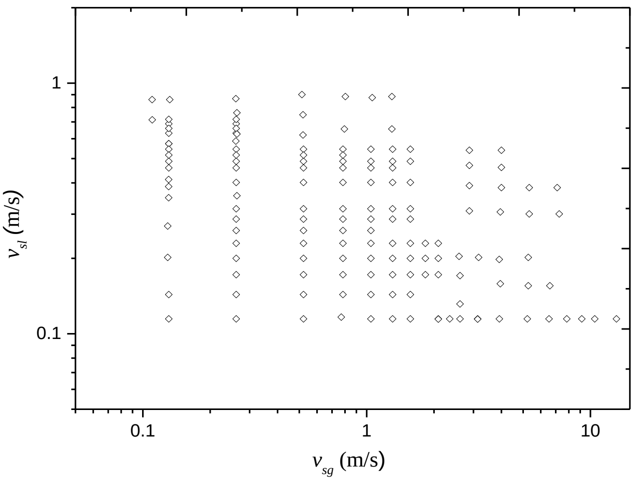

Figure 3.3: Experimental data matrix for the main rig

3.3. NIOIRS design and setups

In this work, it was interesting to investigate the performances of a NIOIRS given variation in wavelengths. Therefore, two One of the sensors has an 880 nm wavelength pair of optical sensors. At this wavelength, emitted infrared light travels through liquid water and is attenuated by the passage of air – water interface in the form of varied structures. The 1480 nm NIOIRS was also considered, given that water has a higher absorption coefficient in the 1480 nm wavelength, it was expected to have a higher sensitivity for water than air. Thus, its installation on the main rig was considered, as it was is conceivable to be robust in detection of chaotic structures that exist in the churn and annular flow regimes such as liquid droplets varying liquid films churning mixtures. The next sub - sections describe the design and setup of each NIOIRS.

3.3.1. 880 nm NOIRS design and Set up

The set up as shown in figure 3.4 consists of two sensor pairs designated as bottom (BS) and top (TS) sensor. Each pair consist of a light emitting diode LED and photodiode sensor. Each component was inserted opposite the other into an opaque pipe and covered to prevent effect of ambient light on the photosensitive diodes. The LED emits light at a wavelength of 880 nm (the near infrared region), while the photodiode received the light at the similar wavelength and converts the intensity of light into an electrical response. Figure 3.4(a) presents the linkage of components that make up the set up.

A processing circuit (figure 3.4(b)) provided a direct current to power each sensor pair. This circuit also provided signal conditioning to improve the quality of the sensor response. Conditioning included signal denoising from capacitors (C1 and C2) and amplification from amplifiers (LM324a and LM324a) for each sensor pair. Figure 3(a) indicates the link between each component of the NIOIRS. The sensor responses were collected via a two channelled data logger (Pico scope 2204) set to a logging rate of 164 µs per sample. Hence the Pico scope was able to capture $3x10^4$ samples per 5 second frame. Measurement times were set to 60 seconds for all test runs. Results were displayed on computer where further signal analysis was performed to extract flow characteristics and real time measurement. Table 3.1 summarises the properties of the sensors used for the investigation.

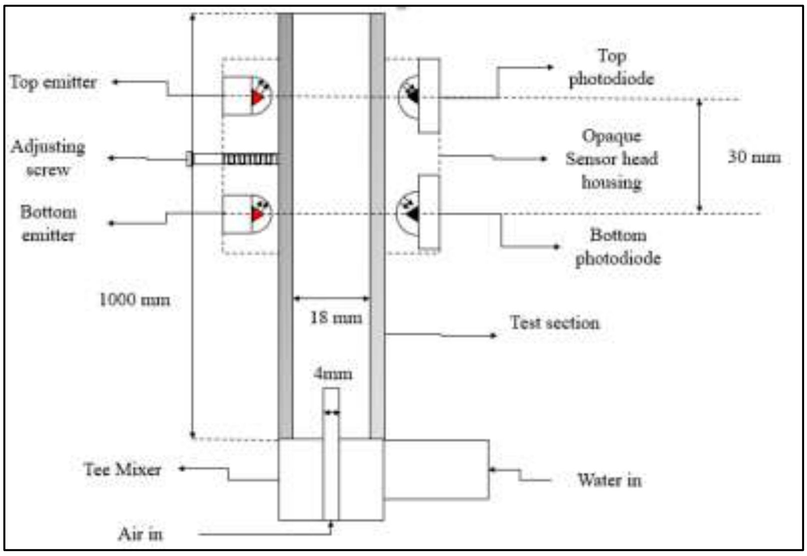

Figure 3.4: Schematic of installed 880nm set up on the test rig test section

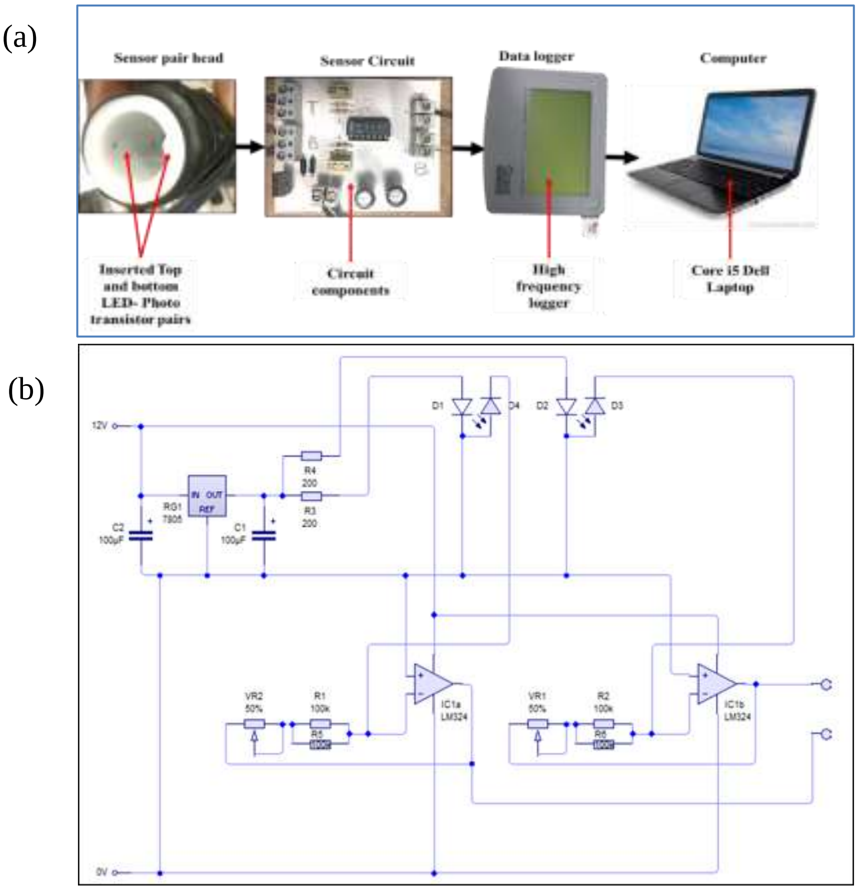

Figure 3.5: Schematics of the (a) sensor components set up and (b) circuit design for the 880 nm NIOIRS

Table 3.2. Summary of sensor head specification

Component	Type	Wavelength	Plastic window	Composition	Forward current (mA)
Source	IR diode	880	3	AlGaAs	20
Receiver	Photodiode	880	4	Silicon	1.5

Calibration of the 880 nm NIOIRS

Calibration of the NIOIRS was performed under static and dynamic conditions. The static testing conditions were for an air-filled pipe ($\beta = 1$) and water filled pipe ($\beta = 0$). Results showed that the response in air V_{air}, was lower than that of the response in V_{water}. This can be explained by the lower refractive index of air causing the emitted ray path to be more dispersed from the photodiode compared to that of water with a high refractive index. These results were similar to that of Keska and BE, (1999). It is also interesting to note that water has a low absorbance in the 880 nm IR range, hence higher intensity of light is received by the photodiode.

For dynamic testing conditions, the effect of increasing air bubble sizes on the sensor response was investigated by injection of air into the vertical column of stagnant water and flowing in the TS. Bubble sizes were controlled using the AF valve. For increasing bubble sizes, varied shapes were observed in the form of spherical, ellipsoidal, bubble caps and Taylor bubbles. The presence of spherical and ellipsoidal bubbles was observed to be stable for size ranges of 2 mm - 8 mm. Equivalent bubble diameters were measured using the high-speed camera (details of image processing can be seen in section 3.8). They behaved as lenses which scattered light in their path, hence attenuating the received light. Dutra *et al. (*2017) referenced to the scattering as the lensing effect.

Figure 3.6(a) presents a time series for the typical sensor response to the passage of a Taylor bubble and entrained bubbles trailing it. Drops in signal from V_{water} to a response below the V_{air} response is observed due to the bubble nose and tail. These parts of the bubble represent an air – water interface which is designated V_{int} response. Figure 3.6(b) is a validating photograph from the VC. Table 3 Summarizes the calibration responses of both sensor pairs. The sensor has sufficient sensitivity range to capture each flow structure in its path.

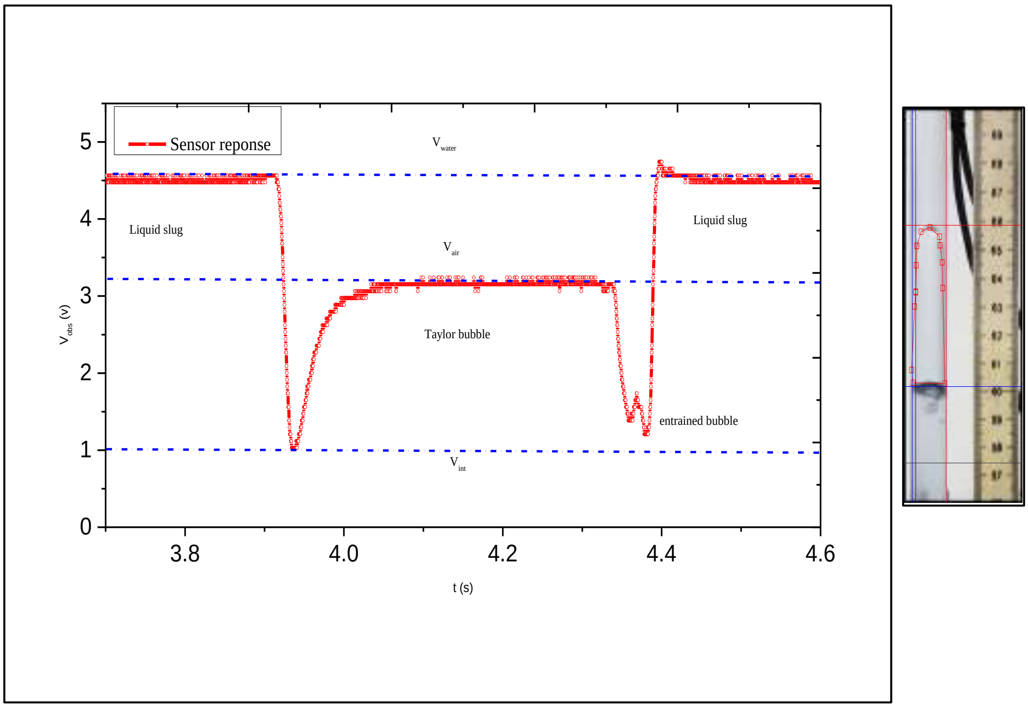

Figure 3.6: (a) Typical calibration response of the sensor in the presence of water (V_{water}), air (V_{air}) and air - water interface (V_{int}) (b) corresponding photograph of the slug flow

Table 3.3. Summary of sensor response for water, air and inter-facial detection

Response (V_{obs}) (V)	**Top Sensor (TS)**	**Bottom Sensor (BS)**	**Average response**
V_{water}	4.45	4.65	4.5
V_{air}	3	3.2	3.1
V_{int}	0.9	1.1	1.08
Sensitivity range	3.55	3.55	3.55
Deviation σ (+/-V)	0.001	0.001	0.001

3.3.2. 1480 nm NIORS set up

Figure 3.7 presents a schematic of the 1480 nm NIOIRS set up and its non-intrusive installation on the test section. A sensor head made up of two pairs of light emitting diode (LED)and light receiver photodiode (from Balluf, BOH TJ-Q06-001-01-S49F) was embedded in a 33 mm diameter opaque casing. Each sensor pair was spaced at 40 mm. The LED emits infrared light at a wavelength of 1480 nm which is received by the photodiode. The received light is transmitted to the circuit as current signal for signal conditioning and amplification via two signal amplifiers (from Balluf, BAE SA-OH-038-UA-DV02) into voltage signals for each sensor pair respectively.

The output sensor responses were aquired using a two channelled oscilloscope (from Pico scope model 2204), up to a rate of 3000 Hz which was sufficient to capture high velocity flow structures in the sensing area of the test section for periods of 60 seconds per flow condition.The sensor response is then viewed in real time and stored for further analysis on the computer.

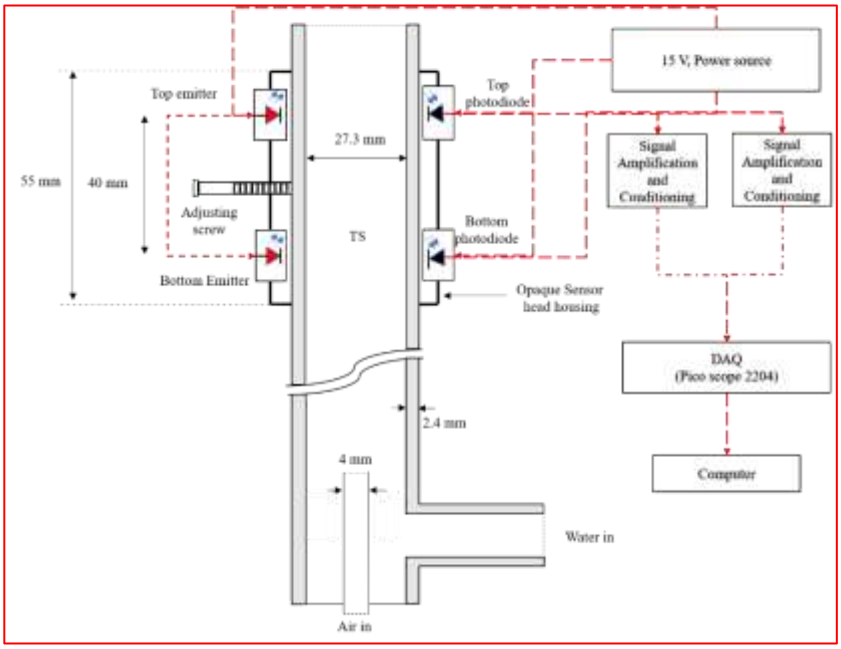

Figure 3.7: The basic set up of the Non-intrusive Optical infrared sensor (NIOIRS), showing the link between the sensor head, sensor circuit, data logger and display computer.

It should be noted that the 1480 nm sensor setup was not designed but rather acquired off the shelf from Balluf suppliers. The only modifications made to the 1480 nm sensor were the addition of a designed integral 15 DC volts, power box that was used to supply power to each sensor pair and the opaque casing used to hold and fit each sensor piece on to the test section non intrusively with an adjusting screw. Figure 3.8 presents the schematics with dimensions of the single pair of the 1480 nm considered in this work.

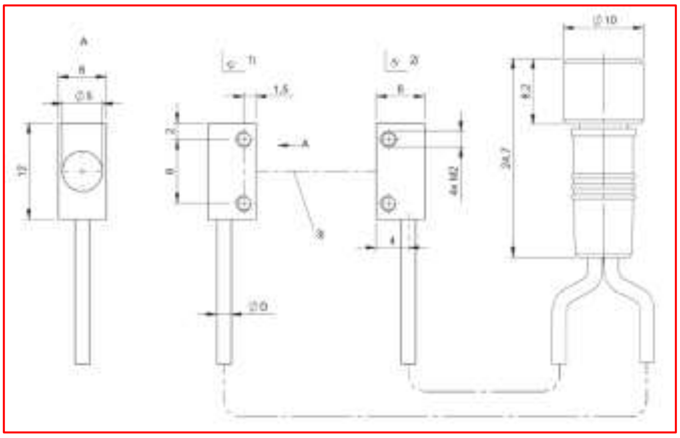

Figure 3. 8 :Schematic of a typical 1480 nm sensor pair showing dimensions of each sensor piece from Balluf suppliers.

Calibration of the 1480 nm NIOIRS

The test section was initially air filled with water injected at a low rate creating air- water interface moving up the test section. The calibration results (figure 3.9) show that lower responses were captured in the presence of a water filled pipe (V_{water}) compared to the higher responses for the presence of the air-filled pipe (V_{air}). This disparity in response relates to the absorption of emitted light at the wavelength of 1480 nm. These results hence present an adequate detection for the presence of water and air. The effect of air - water interface on the sensor response was considered.

Figure 3.9 shows the drop from V_{air} to a steady V_{water}. This drop was evidently due to the moving interface in the sensing area of each sensor pair. The interface acted as a barrier or mirror, which scattered the emitted light, and hence a low response, V_{int}. Table 3.4 summarizes the responses for both sensor pairs after the calibration process.

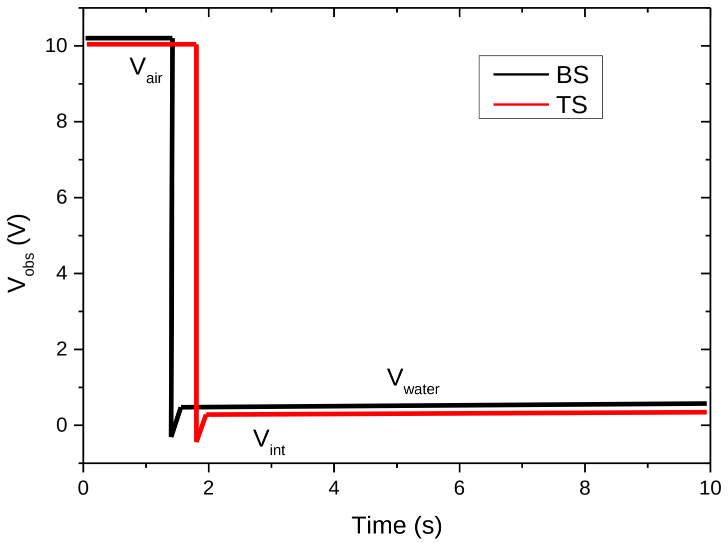

Figure 3.9: Sensor calibration showing typical bottom sensor (BS) and top sensor (TS) responses to the presence of air and water filled test section including the effect of the air-water interfaces

Table 3.4. Summary of sensor response to water, air and interface

Response (V_{obs})	**Bottom Sensor (BS)**	**Top Sensor (TS)**
V_{water}	1.17679	0.6769
V_{air}	10.25239	10.19562
V_{int}	-0.06836	-0.02869
Deviation σ (+/-)	0.001	0.001

3.4. Data analysis approach

A general approach to achieve all the set objectives of this work is summarized in the flow chart below figure 3.10. The flow chart shows that the sensor response is analysed based on the relevant techniques to identify flow regimes, phase fractions and phase flow rate measurements.

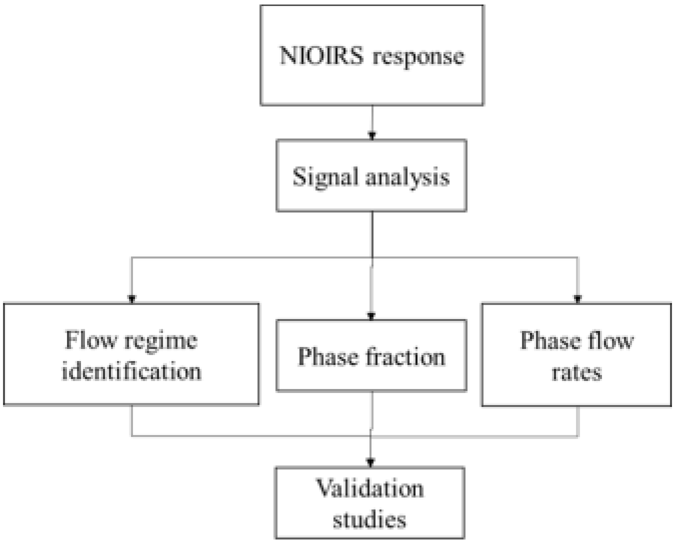

Figure 3.10: Flow chart, showing simplistic sequence of methodology

3.4.1. Flow regime identification

Test rig

On the test rig, the flow regime identification process is detailed in chapter 4, The application of histograms derived from the sensor response, computes count of sensor calibrated response of air, water and interface. The 880 nm NIORIS response is under on the test rig. Typical signatures of the histogram are utilized to discriminate the prevailing flow regimes in the test section. Refer to section 2.41 in chapter 2 for the mathematical detail on determination of histograms. It is important to note that the choice of the unit samples must adequate to capture the trends in each flow condition. These unit samples are referred to as bin sizes (Objectives, 2011). Flow regimes were inferred using histograms binned at intervals that were equivalent to the sampling rate from the DAQ system. This is adequate to ensure all features in the flow are captured. Focus was on identification of bubble and slug flow regimes as the test rig not fully dedicated for the formation of churn and annual flow regimes due to the short length of the test section

Main rig

In chapter 5, the use of supervised learning methods derived from the 1480 nm NIOIRS installed on the main rig is carried out. The application of polynomial regression and probabilistic LDA and QDA were considered. Details of the mathematical background of these methods are provided in chapter 5. These methods make of extracted relevant features from the sensor response which provide unique discriminatory information about each flow regime. The flow regimes discriminated are the main four regimes which include bubble, slug, churn and annular flow regimes.

For sake of simplicity, the transition between each stable flow regime was considered as an abrupt shift between flow regimes in the data labelling process. The simple assumption infers that, the bubble – slug flow, characterized as bubble caps is considered as the initiation of the slug flow regime. The slug – chum transition which is observed as unstable Taylor bubbles is marked as the churn flow and finally the churn-annular flow transition is considered as the development of an annular flow regime. Therefore, extracted features in the vicinity of the transition zones may lead to misclassifications for broad and chaotic transitions such as that the annular. The assumption is however reasonable since from previous tests during the sensor calibration, that small bubbles quickly coalesce to form bubble caps, hence creating a narrower transition compared to the slug- churn flow regime. Details are presented in chapter 5. Further real time application of flow regime identification model using LabVIEW software is demonstrated.

3.4.2. Phase fraction determination

The approach to determine phase fractions for both NIOIRS categories is to propose a linear relationship between the sensor response and the volume fractions in the sensing area. Therefore, the calibration responses for both NIOIRS were combine as a linear interpolation relationship. The model accounts for interfacial effect where the concept of similar geometries can be used to correct for interfacial scattering. The models derived were based on linear interpolation of the calibrated responses with respect to either the 880 nm NIOIRS (in chapter 4) or the 1490 nm sensors (in chapter 6).

3.4.3. Average Structural characteristics

Consideration of the average structural characteristics previously discussed in section 2.2.3 of chapter 2. was necessary, since these characteristics provide understanding of the intrinsic behavior of the GLF. Analysis of the 1480 nm NIOIRS response installed the main rig is considered in the determination of the entrained Taylor bubble void fraction, Taylor bubble void fraction and the liquid film thickness of the slug flow regime. The 880 nm NIORS sensor was not considered due to the lesser sensitivity detect water as already mentioned.

Under the slug flow regime, the average Taylor bubble void fraction, is determined from a % count distribution or histogram of the temporal void fraction series derived from the 1480 nm NIORS. It is expected that two dominant peaks of high and low void fractions in turn corresponds to the presence of Taylor bubbles and the presence of liquid respectively. Therefore, based on the closure relationship presented in equation 2.21 the entrained bubble void fraction can be computed as

$$\bar{\alpha}_{EB} = \bar{\alpha}_{g} - \bar{\alpha}_{TB} \tag{3.1}$$

Azzopardi *et al.*, (2015) and Abdulkadir *et al.*, (2014b) introduced this form of signal analysis when they considered analyzed an ECT sensor. The accuracy of their method was however dependent on the choice of an obituary threshold void fraction. Further to this, they only validated the entrainment using empirical correlations. In this work, there is a better validation of the entrainment using image processing techniques (discussed in later subsections ,3.5.2). The average liquid film thickness can easily be determined by equation 2.22 for the slug flow regime and equation 2.23 for the churn and annular flow regimes.

3.4.4. Average actual gas velocity

By applying equations 2.33 – 2.35 to the temporal void fraction from the two pairs of the 1480 nm NIORS, the average actual gas velocity then be determined. The sensor spacing considerations have been considered where 40 mm spacing is considered adequate for the application of the cross-correlation function in equation 2.33. It is also interesting to consider the effect of flow regimes on the accuracy of the cross-correlation method which is validated from photographic frames Results are detailed in chapter 7 of this work.

3.4.5. Average actual liquid velocity

As already mentioned in chapter 2, the average liquid velocity presents the most challenging of characteristics to determine, given the dominance of slip in upward GLF. therefore, it was deemed fit to combine a modified calibration model derived from the Nicklin type correlation with the average phase fraction and derived actual gas velocity to obtain an adequate estimate for the actual liquid velocity. Validation is performed using the readings from the single-phase flow meters given when the modified calibration model is re- written to determine a superficial liquid velocity, given the absence of another multiphase flow meter. . Results are presented in chapter 7 of this work. Details of the derivation is given in chapter 7 of this work.

3.4.6. Actual volumetric phase flow rates

The actual volumetric gas and liquid flowrates can be then bae determined based on the phase velocities, phase fraction (void fraction and liquid fractions) and cross section areas of the test section.

3.5. Experimental validation methods

This work considered two main experimental validation methods for the GLF characteristics derived from the NIOIRS. The methods include a swell level for phase fraction validation under low flow conditions and high-speed photographic methods for all GLF characteristics considered given both rigs.

3.5.1. The swell level method

The swell level involved the determination of void fractions based on an observed rise in air/water interface when a Taylor bubble gas bubble is injected into the test section via the air control valve. The test section was filled with water to 0.8L (for both rigs) just above the NIOIRS positions for each test run to prevent the effect of flow structure back flow on the final level to be read. For a constant cross section, this rise in liquid level is proportional to the volume of bubble V_{TB} rising in the test section. Hence, the void fraction α_{level} is then calculated as,

$$\alpha_{level} = \frac{l_2 - l_1}{l_1} \tag{3.2}$$

l_1 and l_2 are the initial and final levels of the air- water interface. The levels were recorded from the meter rule mounted parallel to the test section. All experimental runs were carried out under static water conditions to minimize disturbances in interface hence improving accuracy of observations. The swell level method has been applied adequately by other investigators under similar flow conditions, especially for the rise of Taylor bubbles (Azzopardi *et al.*, 2015; Costigan and Whalley, 1997). The fact that entrained bubbles or small bubbles are not able to cause a clear rise in the liquid level makes it limited only to Taylor bubble injection. None the less the swell level change remains reliable under the said flow conditions. It should also be noted that the visual observation of the level rise was complimented by the video recordings.

3.5.2. High speed photography method

The main validation tool for this study is the use of high-speed photographic frames taken by the video camera under similar flow conditions as the sensors. Each photo is further processed according to the characteristic to be measured or determined. The processing of these photos was executed with the use of Origin Pro imaging tool for dimensional extraction and J image software for image conversion and percentage area measurement. The following below delineates the varied applications of the high-speed photos method for respective characteristic measurements.

Void fraction validation procedure (test rig)

The derived void fractions α_{Photo} were determined by processing high speed photographs taken by a video camera at 6 frames per second. Bubbles were injected into the test section similar to the swell level method. However, the spherical, ellipsoidal and Taylor bubbles were injected separately in order to assess the performance of each proposed phase fraction model. Bubble volume computation was performed via the extraction of bubble length, L_{TB} and Radius R_b from photo frames using an image digitizing tool in Origin Pro imaging software. The Taylor bubble volume (V_{TB}) was then computed based on hemispherical and cylindrical geometries of the bubble nose and body regions respectively, authors concede to the described Taylor bubble shape (Barrau *et al.*, 1999; Shaban, 2015; Thome, 2007):

$$V_{TB} = \frac{2}{3}\pi R_b^3 + \pi R_b^2 (L_{TB} - R_b) \tag{3.3.}$$

The volumes of spherical and ellipsoidal bubbles, Vb were computed using an average bubble radius $R_{b\ avg}$ derived from the axial and longitudinal radii of these bubbles. This averaging was performed to account for variations in bubble curvature. A spherical volume relationship was then computed as

$$V_b = \frac{4}{3}\pi R_{b\ avg}^3 \tag{3.4}$$

The considered control volume V_P was a cylindrical volume (equation 3.5) computed based on the internal pipe radius (R_p) and pipe length section (L) equivalent to the distance travelled by the target bubble from the bottom of the test section through to the top of the sensing section at 0.84 m,

$$V_p = \pi R_p^2 L \tag{3.5}$$

Hence, based on the computed bubble volumes (V_{TB}, V_b) and designated pipe volume, (V_p) the average void fraction was determined using equation (3.6) for the Taylor bubbles and equation (3.7) for the smaller bubbles injected separately from the bottom of the test section:

$$\bar{\alpha}_{Photo} = \frac{\sum V_{TB}}{V_P} \tag{3.6}$$

$$\bar{\alpha}_{Photo} = \frac{\sum V_b}{V_P} \tag{3.7}$$

single rising ellipsoidal bubbles were also measured using similar methods, diameters were measured more accurately using an image digitization tool in origin lab software. The images were imported into the software and digitized with reference measurements from the known pipe diameter (32 mm, outside diameter), and measurement from the meter rule as axial reference.

Figure 3.11: Image processing for the extraction of bubble diameter and Taylor bubble length required for volume calculation.

Image processing procedure for void fraction measurement (main rig)

On the main rig, where higher mixture velocities exist, bubbles tend to significantly distort thus creates the need for further imaging processing techniques to improve accuracy of measurement. Image processing techniques were performed to each flow structure of interest captured by the video camera in the measurement section. Taylor bubbles lengths and diameter, liquid film thickness, and entrained bubble area were measured with good accuracy using the technique in ImageJ, image processing software (open source software). The key steps common for all measurements except for the entrained bubble area includes:

Pre processing

i. The saved video footages from the video camera are converted to photographic frames for each flow condition using Windows Photo application, on a computer.

ii. The photo frame of interest was cropped to view only the test section and flow structures.

iii. Photos are adjusted using the auto correct for improving features of the capture flow.

Image conversion

i. Image conversion using the PROCESS tab. From RGB to Grey scale conversion

ii. The grey scale image is processed using an FFT band pass filter (Huang model) to optimize visibility of the entrained bubbles by supressing the liquid slug background.

iii. Using the threshold tab, the enhanced grey scale image is then converted to a binary scale image

Edge detection

i. The binary image is calibrated using the ANALYZE tab, for the global measurement scale from the SET SCALE sub- tab.

ii. The MEASURE sub tab is then used to detect edges and measure area, lengths of the identified structures

Post processing

i. Results are exported to Microsoft Excel where the bubble distribution is plotted as for analysis of the percentage area occupied by the binary colours. The area fraction derived from image processing from colour to binary scale is performed using image j processing software.

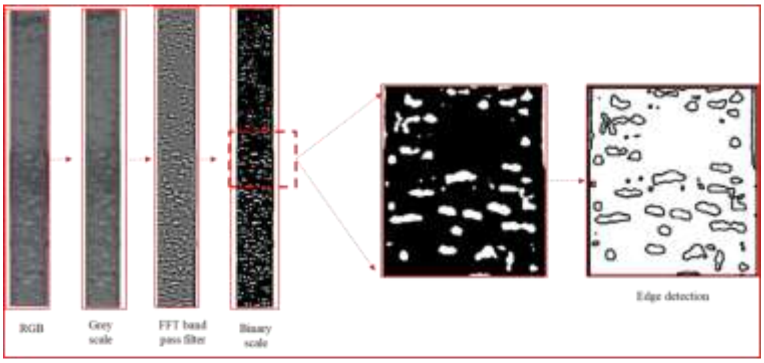

Figure 3.12: Example of extracting entrained bubble fraction from a liquid slug using image processing which includes, image conversion from colour (RGB), to binary scale.

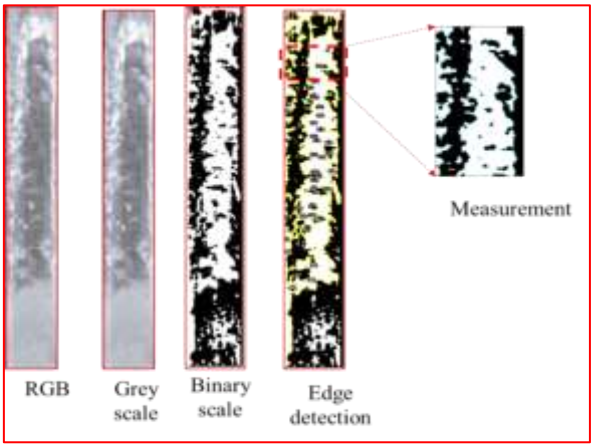

Figure 3.13: Liquid film thickness measurement via image binarization, edge detection and percentage area measurement

Image validation of structural velocities

Photographic frames were taken at 5 frames per second with a length reference to measure the distance travelled by bubbles and corresponding to the time-base between each photographic frame.

Figure 3.14: Measurement of bubble velocity from photographic frames derived from high speed camera

3.5.3. Numerical simulation studies

Given the fact that scattering complicates the sensor response and leads to limited performance of most optical sensors as described by Barrau *et al.*, 1999. attention was further given to interfacial scattering simulation over varied bubble sizes. Interaction of bubble interfaces with the emitted light and that received by the photo - diodes can be modeled in COMSOL Multiphysics software notably few investigators have considered this area. For instance , Sulthana *et al.*, (2018) carried out a simulation work on the interaction of a bubble -slug train of air and water with infrared light using an IR single pair setup for a pipe in COMSOL. Their results indicated that IR light scattering effects were evident as reduced fractions of photons at the detectors. (Dutra *et al.*, 2017) also emphasized on the effect of bubble sizes on the way emitted rays interact in terms of reflection, transition and absorption. They found that there was a critical bubble diameter above which scattering is minimized. It then adds to the understanding that small bubbles are likely to lens or scatter light more than larger bubbles, hence corrections are required to improve NIOIRS response interpretation. Results of the effect of bubble size is also detailed in chapter 4 of this work.

3.5.4. Error analysis

The error analysis approach employed in this work is mainly based on the use of parity plots. The parity plot is a scatter plot that compares reference data with experimental data. A reference or parity line is drawn, which is defined as y= x is drawn to compare both data sets. In the case where the experimental data falls on the reference line or parity line, then it is interpreted as a perfect match, indicating there is no error between the data sets, if it falls below or above the parity line it is an underestimation, similar an overestimation is inferred when the data is above the parity line.

Outliers may not be included in the error margin given the extreme deviation from the cluster of data in the experimental results. The error margin or deviation from parity margin is hence determined based in the maximum deviation of points from the parity line. The error margin is the standard deviation scaled according to the maximum value of the data sets. It is also referred to as the root mean square error (RMSE) between the reference and experimental data sets. Equation H.1 gives the formulas as,

$$RMSE = \sqrt{\frac{\sum_{i=1}^{n}(x_i - y_i)^2}{n}} \qquad (3.8)$$

The resulting RMSE error is then obtained +/- absolute value that defines the error margin lines in dashed blue. More so a percentage of the RMSE can be computed based on the maximum scale from the data set.

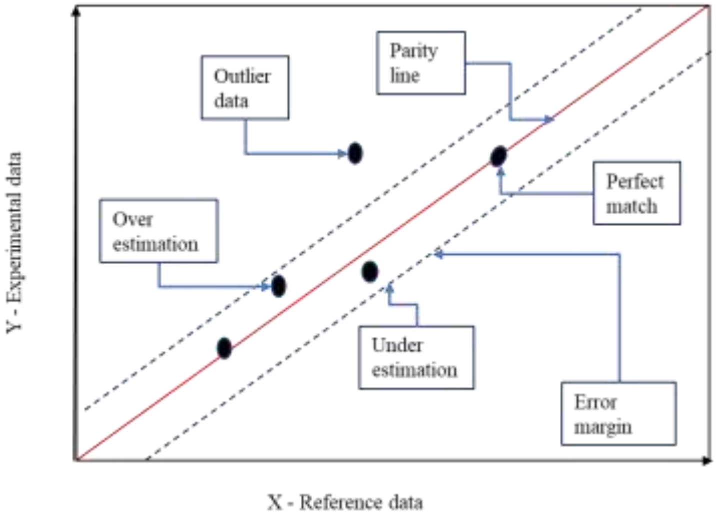

Figure 3.15: A typical parity plot with features for error analysis

Chapter 4

4. Preliminary Studies - Flow Regime and Phase Fraction Determination

4.1. Introduction

The primary aim of this chapter is to provide preliminary results from the 880 nm NIOIRS for flow regime identification, phase fraction determination, and to confirm the effects of interfacial scattering on the accuracy of sensor response. Experiments were performed using the test rig (see description in chapter 3). Finally, a real time monitoring of the gas liquid flow is demonstrated via an algorithm that incorporates a derived model phase fraction model and a threshold for the discrimination of bubble and slug flow regimes executed in LabVIEW. The results show the capabilities of NIOIRS for monitoring slug flow development.

4.2. Sensor modelling

The interaction of bubbles with the emitted light, the effect of bubble size and position was investigated using a 2D numerical ray propagation model. The ray propagation is based on the first order differential equations of the governing laws of light interaction as described in the earlier section. Also incorporated was the ray tracking feature defined as ray position q, wave vector k and angular frequency, ω,

$$\frac{dq}{dt} = \frac{d\omega}{dk} \tag{4.1}$$

$$\frac{dk}{dt} = -\frac{d\omega}{dq} \tag{4.2}$$

The model had similar dimensions as the sensing area of the test flow rig used. The test section was modelled as filled with water and bubbles were made of air. A pair of emitters and photodiodes represented the source and detectors of the rays, since each pair was expected to produce similar response. Emitted number of rays was set at 10 to aid observation of bubble effect on the emitted and received rays. The sensor response was computed as the ratio of number of received rays at the detector (N_r) to the number of emitted rays (N_e) from the emitter. Based on earlier experimental observation typical bubbles sizes and shapes rising through the mid-section of the test section were considered. The emitter is modelled as a release feature from the left and the photodiode as an accumulator of rays on the right. To simulate the effect of a moving bubble in the path of the emitted ray, varied bubble sizes set at nose, body and tail positions were introduced in the path of the emitted ray.

Figure 4.1 (a – c) and 4.1 (d - f) shows simulation results of a 1mm and 8 mm spherical bubble. It was observed that the bubble behaved as a light scatterer at all positions hence a reduced ratio of received to emitted number of rays was computed. Increasing spherical bubble size to 8 mm (figure 4.1 (d - f)) and 15 mm ellipsoidal, figure 4.1 (g - i) at nose and tail positions showed similar lensing effects due to the curved interfaces. However, the dominance of refraction of the transmitted light was observed for the passage of each bubble at the body positions. Since bubble sizes approach the pipe diameter enough air media is formed to allow light through to the photodiode. Similar results were observed for the bubble cap of 17 mm size (figure 4.1 (j-l)). Results were similar to that of Mithran and Venkatesan, (2017) and Sulthana *et al.*, (2018).

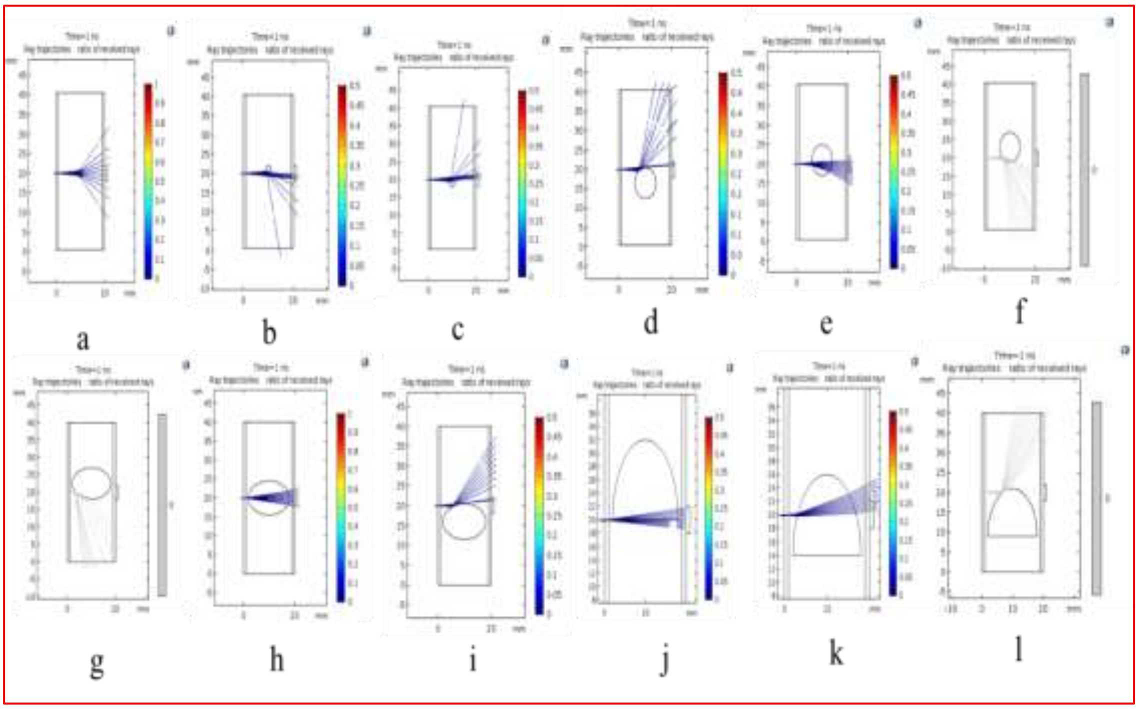

Figure 4.1: Sensor modelling with 2D ray path, showing the nose, body and tail effects of: (a-c) spherical bubbles of 1 mm; (d-f) spherical bubbles of 8mm; (g-i) ellipsoidal of 15 mm (j-l) bubble cap of 17 mm.

The derived understanding of the critical interactions of bubble shapes and sizes enables an enhanced confidence for interpreting the response from the NIOIRS. Hence, comparison of the sensor response with the ratio of received to emitted rays was performed. Figure 4.2 shows a comparison of a typical Taylor bubble (L_{TB} = 20 mm) detection from the normalized sensor response with the numerical model at varied positions from the nose to the tail. At the bubble nose and tail a decrease in response occurs for the experimental and model. The sensor still received some amount of light at nose and tail positions since these interfaces behave as lenses. The model shows no reception of light at nose and tail positions. Therefore, a disparity of 0.1 between the experimental and model is observed. This could be due to the number of rays used in the model, hence changes in the probability of rays arriving at the detectors. A similar offset in results was observed in the bubble body positions, where a plateau trend was evident for both experiment and model. Overall the trends in comparison can summarized as adequate. An improvement in the model would be to use a larger number of emitted rays improving the probability of the rays arriving at the photodiode even in the presence of an interface.

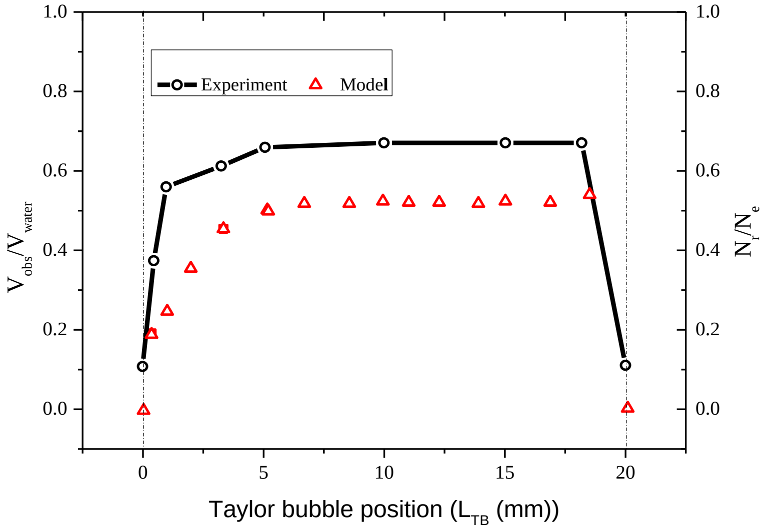

Figure 4.2: Comparison of the experimental sensor response with the ratio of received rays from ray propagation simulation at varied Taylor bubble positions in the path of emitted light.

4.3. Signal analysis

Based on the 880nm NIOIRS calibration results (chapter 3) and numerical simulation (figure 4.1 and 4.2), the NIOIRS capability to differentiate between air and water has been proven to be valid. Therefore, the sensor response was analyzed for flow regime identification and phase fraction determination. The analysis for flow regime identification was executed by converting the sensor response to a signal distribution. This was in the form of a calculated histogram derived over the measurement time. At every experimental run, a total of 29944 samples were used in the analysis over each measurement time frame (detailed in the sensor setup section).

A class width for the histogram was chosen as 0.2V. This was based on the calibrated responses for air and water. The derived histograms were used as flow regime discriminators, based on the percentages of counts around the calibrated sensor responses V_{water}, V_{air} and V_{int}. This method can be compared to the use of probability distribution functions (PDFs) which have been used by several investigators (Keska et al., 1999, Jones et al, 1975, etc.). The difference between the approach presented here is that a direct response is used compared to a phase fraction-derived response used by other investigators for the signal distribution PDFs. A propagation of error derived from the phase fraction estimation could affect the flow regime analysis.

The proposed models in this work are based on the time averaged observed sensor response ($\overline{V_{obs}}$), combined with the calibrated responses $V_{air,}$ V_{water} and V_{int} from each sensor pair. The time averaged phase fractions (void fractions and liquid fractions) $\bar{\alpha}_{sensor}$ for varied flow rates (equivalent to v_{sl} and v_{sg}) are determined from a proposed linear model for the bubble flow (equation (4.3)) and slug flow regimes (equation (4.4)

$$\bar{\alpha}_{sensor} = 1 - \left[\frac{\overline{V_{obs}} - V_{int}}{V_{water} - V_{int}}\right] \tag{4.3}$$

$$\bar{\alpha}_{sensor} = 1 - \left[\frac{\overline{V_{obs}} - V_{air}}{V_{water} - V_{air}}\right] \tag{4.4}$$

Where

$$\overline{V_{obs}} = \sum_{t=0}^{t=t} \frac{V_{obs} t_i}{t} \tag{4.5}$$

The accuracy of the proposed models is assessed by comparing the instantaneous void fractions, which represents the void fraction per observed response (V_{obs}).

4.4. Results and discussion

A total of 25 flow conditions varying v_{sg} (0 – 0.16 m/s) and v_{sl} (0 - 0.131 m/s) are presented and analyzed. Each experimental run was repeated three times to improve the quality of results. Representative results are presented and discussed in relation to the performance of the NIOIRS technology for monitoring two phase flow from the flow rig.

4.4.1. Flow regime identification

Results in figure 4.3 shows a stack of 6 sensor response traces with corresponding photographs each captured at v_{sl} = 0.0361 m/s for increasing v_{sg} conditions, at 0.005 m/s, 0.0108 m/s, 0.0541 m/s, 0.081m/s, 0.108 m/s and 0.161 m/s. Figure 4.3 (a) shows the photograph of a bubble flow regime in the TS, at v_{sg} = 0.005 m/s. This was categorized by the presence of ellipsoidal and spherical bubbles rising upwards in the TS. The corresponding sensor response with a low gas fraction (β = 0.12), indicates signal attenuation from V_{water} (4.5 V) to a minimum V_{int} (1.0 V) and then to V_{water}. The variation in attenuation is related to the sizes of bubble sand shapes as well. Spherical bubbles led to scattering of the signal above the V_{int} response, while ellipsoidal bubbles (larger bubbles) led to larger drops in response closer or equal to the V_{int} response.

At v_{sg} = 0.0108 m/s (equivalent to β = 0.22), initiation of a transition from bubble flow to a slug flow regime was visualized as the growth of bubbles into bubble caps. These caps increased in diameter as bubbles rose to the top of the test section (photograph from figure 4.3(b). The presence of a bubble cap could be inferred from the corresponding variation in sensor response in figure 4.3(b) shown over the time interval of 2.8 s – 2.9 s. The sequence of response variation is a drop from V_{water} to V_{int} due to the bubble cap nose and a rise to V_{air} (3V) due to the presence of a larger cross section to enable light refraction. As the cap moves past the sensing area, the response increases to V_{water}.

The development of a stable slug flow regime can be observed from the photographs in figure 4.3(c), 4.3(d) and 4.3(e) for increasing gas fractions (v_{sg} = 0.0541 m/s , v_{sg} = 0.081 m/s and v_{sg} = 0.108 m/s). This flow is characterized by the upward flow of Taylor bubbles ranging from sizes of 2D - 23D in the test section, with entrained bubbles in the liquid slugs. For increasing gas velocities, increase in the average Taylor bubble lengths is observed. These increases have been attributed to the increase in kinetic energy of injected bubbles from the bottom of the test section, hence a collision to coalescence mechanism creates longer bubbles forming the observed Taylor bubbles. The corresponding signal responses (as presented in figure 4.3(c), 4.3(d) and 4.3(e)) for each Taylor bubble are similar to that of the bubble caps. However, the key difference is the stabilization of the response at V_{air}, due to the elongated lengths of each passing Taylor bubble in the sensing area. The inference of entrained bubbles in the liquid slug can be seen as signal attenuations trailing the Taylor bubbles.

A further increase in superficial gas velocity (v_{sg} = 0.161 m/s) equivalent to β = 0.81, for the same liquid flow (v_{sl} = 0.036 m/s) was observed to create a churn flow regime. Figure 4.3(f) shows a photograph of the churn flow regime effect. For the length of test section an entrance effect of the high gas fraction seemed to be the cause of the elongated bubble instability. This observation marks the slug – churn flow regime transition for the set of flow conditions considered. The mechanism leading to the churn flow regime has been argued by most researchers to be due to either the entrance effect, coalescence or bubble breakup mechanisms. However, the mechanism, the description of the churn floe regime seems to be unified. This was characterized by varying liquid film with a flow reversal due to flooding in the test section. Figure 4.3(f) presents a typical sensor response to the churn flow regime. It is inferred from the time frame of around 4.2 s – 4.6 s that a churn effect occurs. This presents an unstable elongated bubble collapsing as a result and carried up the pipe with the rising liquid slug (time interval 4.6 s – 4.9 s) behind it.

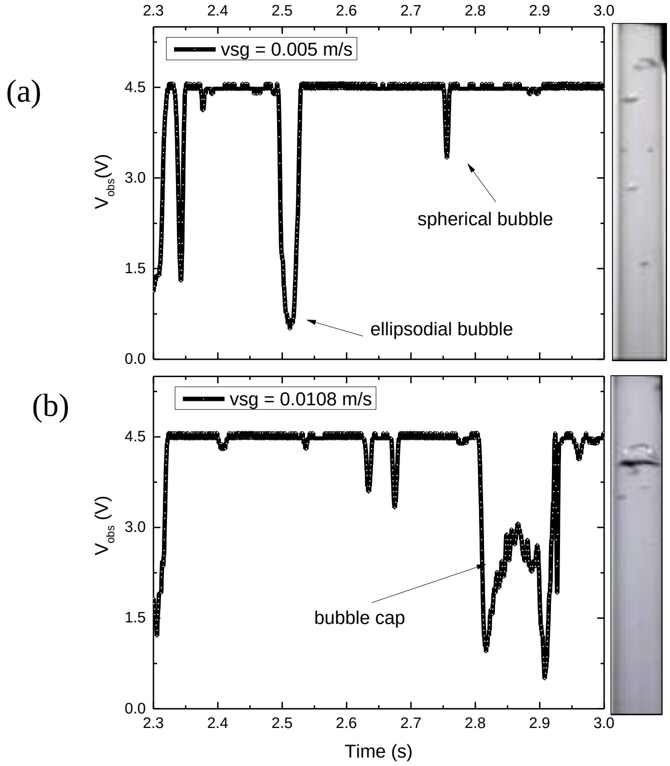

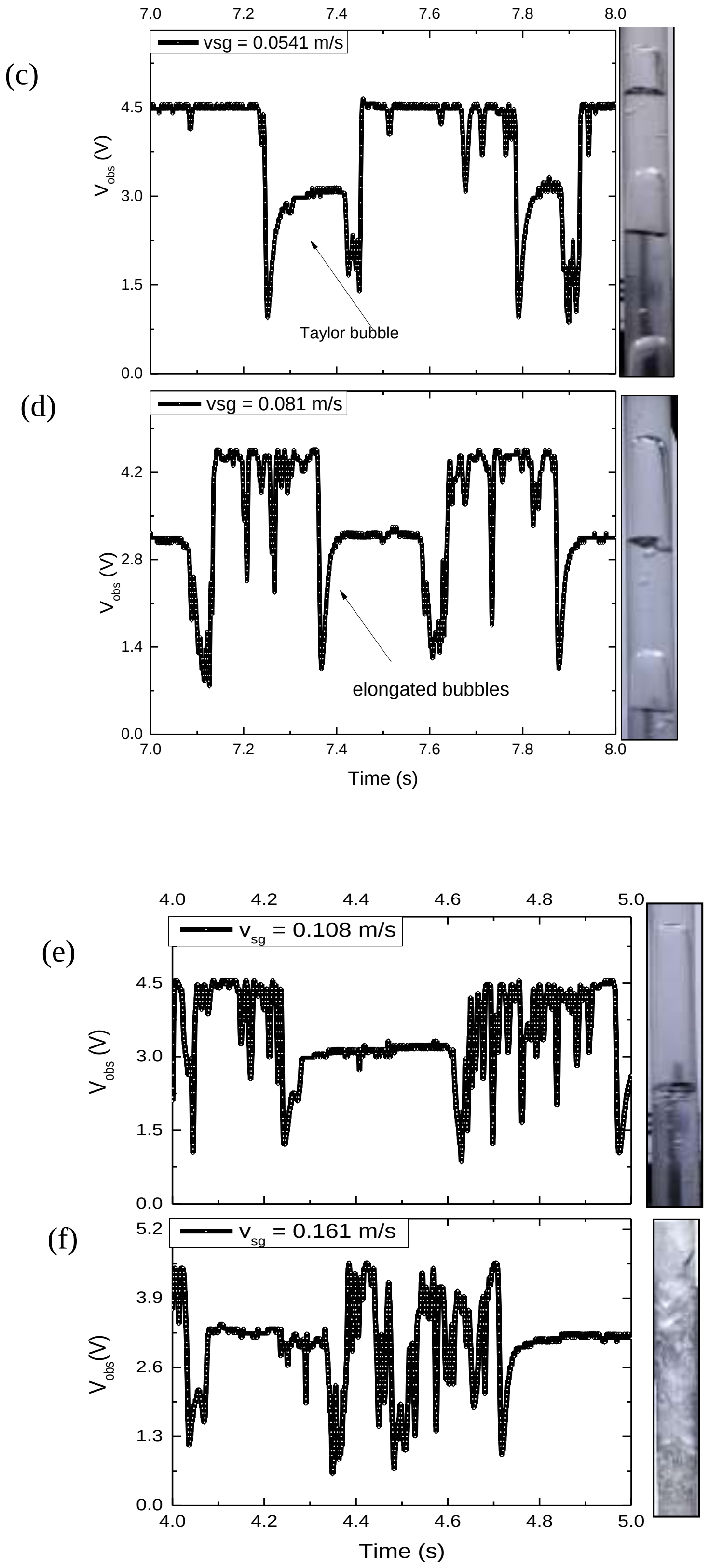

Figure 4.3**:** Sensor responses and observed photographs of flow regimes at constant superficial liquid velocity (v_{sl}= 0.0360 m/s) and increasing gas velocities at (a) 0.005 m/s (b) 0.0108 m/s (c) 0.054 m/s (d) 0.081 m/s (e) 0.108 m/s (f) 0.161 m/s

Observation of the sensor response is adequate for identifying flow structures based on the variation in calibrated responses. However, further analysis of the sensor response is necessary to aide a real-time identification of flow regimes. In view of this, the consideration of a flow regime discrimination method was performed using histograms composed of the sensor response and count percentage. The percentage count was computed based on the total sample count of 29944 captured over a period of 10 seconds for each sensor pair. Figure 4.4 shows a group of histograms, derived for the same flow conditions (i.e. $v_{sl} = 0.0361$ m/s and varying gas velocities) as described in figure 4.3. Figure 4.4(a) presents a typical histogram derived for the bubble flow regime (at vsg = 0.0051 m/s).

The shape of the histogram is characterized by a high count of around 60% at the V_{water} response (representing the single peak). This represents the presence of a high fraction of liquid in the test section. The spread of the remaining counts is attributed to the interfacial scattering of the bubbles rising in the sensing area. A 5% count around the V_{int} response shows evidence of this scattering caused by the presence of ellipsoidal bubbles. The presence of smaller spherical bubbles contributes to scattering leading to counts between the V_{water} and V_{air} responses. Owing to the dominance of the scattering effect, there exists a minimal count around the V_{air} response as indicated in figure 4.4(a).

For increasing gas velocities and constant liquid velocity (i.e., higher gas fractions), the percentage of counts around the V_{air} response begins to increase. This is due to the presence of bubbles large enough to create refraction of light at their body lengths. The bubble – slug flow transition in figure 4.4(b) shows evidence of this increase around the V_{air} response (at $v_{sg} = 0.0108$ m/s, $\beta = 0.22$) compared to figure 4.4(a). This transition criteria agrees with that of Taite*l et al, (1975*). It is interesting to note that the % count around the V_{water} and V_{int} responses remains similar to the of bubble flow histogram in figure 4.4(a). This is due to the presence of a continuous liquid and ellipsoidal bubbles still trailing the growing bubble caps. Further increase in gas velocity above the bubble – slug transition, leads to significant increase around the % count of the V_{air} response and a corresponding decrease in the % count at V_{water} due to the presence growing Taylor bubbles. This development of two local peaks on the histogram infers a developing slug flow regime as shown in figures 4.4(c), 4.4(d) and 4.4(e). A threshold of 10 % count around the V_{air} response was chosen for a fully developed slug flow regime over all flow conditions run.

Figure 4.4(c) presents a typical 10 % criteria around the V_{air} response, represented by the presence of Taylor bubbles. A reduction in the V_{water} response also indicates a reduction in the fraction of liquid slug in the test section. Further reductions in V_{water} and increases in V_{air} can be observed as gas fractions increase in figure 4.4(d) and 4.4(e). The transition from the slug flow to churn flow is expected to occur when a minimal % count of V_{water} exists, hence indicating the absence of a continuous liquid phase or rather an unstable liquid film forming at the walls of the test section. Figure 4.4(f) shows the shift from right to left of the distribution due to significant counts between the V_{air} and V_{int} responses. This is expected due to the collapse of elongated slugs and variations in gas liquid interface. The transient nature of the signal distribution and computed histograms reflects the changes that occur in the test section for all flow conditions considered proving to be an adequate statistical tool for identifying flow regimes.

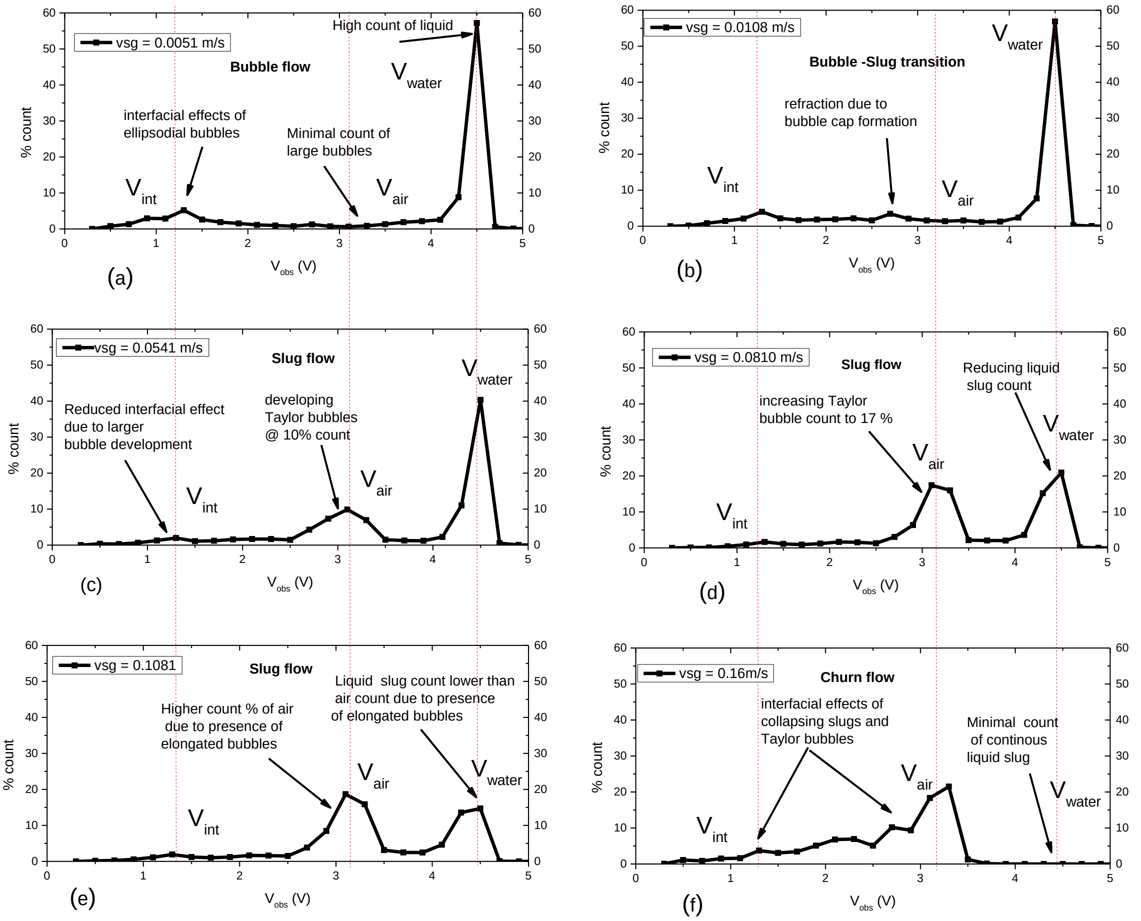

Figure 4.4**:** Sensor derived histograms inferring the development of flow regimes at constant v_{sl} = 0.0361 m/s for increasing gas fractions at v_{sg} (a) 0.0051 m/s (b) 0.0108 m/s (c) 0.0541 m/s (d) 0.081 m/s (e) 0.1081 m/s (f) 0.16 m/s

4.4.2. Flow regime effects on average response

The relationship between the average sensor response ($\overline{V_{obs}}$) for each sensor pair and increasing gas fraction over varied superficial liquid velocities is presented. Figure 4.5 shows that for increasing gas fractions, there is a relative decrease in ($\overline{V_{obs}}$). This decrease is again due to the increased scattering and refraction of the emitted light with increasing gas fractions. Moreover, flow regime boundaries are defined for the range of responses from each sensor pair based on the results of observed flow from the histograms (figure 4.4). In figure 4.5, the flow regime boundaries are presented as bounding dash boxes with transitions occurring at the meeting points of each bound. It is worth stressing that the bubble – slug flow transition was observed to be gradual and hence is presented in figure 4.5 as a bounded region. The slug – churn transition occurred relatively abruptly in the present investigations, though further investigation may define this transition region. Overall, based on the current flow conditions, results infer a desirable sensor sensitivity to detect any prevailing flow regime. Therefore, a calibrated sensor flow map coupled with the count percentage information can be developed to fully identify the flow regimes in the pipe in real time.

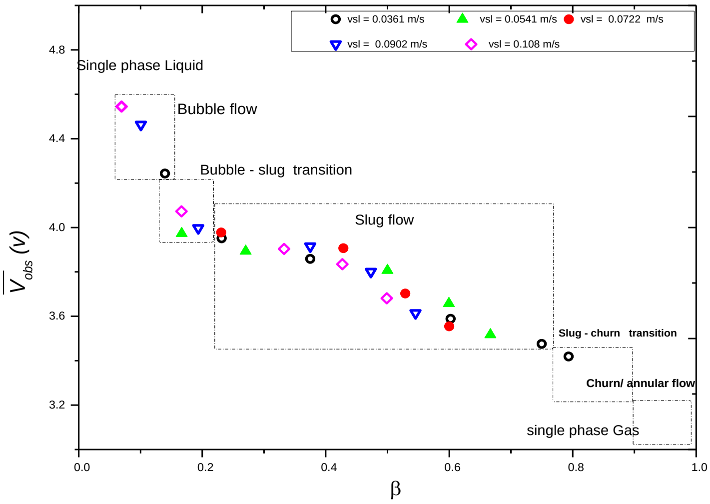

Figure 4.5**:** The Effect of increasing gas fraction on the average sensor response ($\overline{V_{obs}}$) at v_{sl} = 0.0361 m/s, 0.0541 m/s , 0.0722 m/s, 0.0902 m/s, 0.108 m/s.

4.4.3. Instantaneous phase fraction

In order to assess the validity of the proposed phase fraction models presented as equation 4.3 and 4.4, instantaneous void fractions due to the presence of bubbles was computed over the temporal sensor response. Figure 4.6 presents the void fraction results computed from the proposed bubble flow model (equation 4.3) (LHS) with a corresponding photograph (RHS). Over the time interval considered (2 s- 3.5 s). The lowest V_{obs} response (close to the V_{int} response) at 2.7 seconds indicates the presence of an ellipsoidal bubble of size approaching the pipe diameter. This leads to the largest scattering of light; corresponding to a void fraction close to one. Moreover, the presence of smaller bubbles with corresponding levels of scattering far less than the V_{int} response are directly proportional to the computed void fraction using the bubble model.

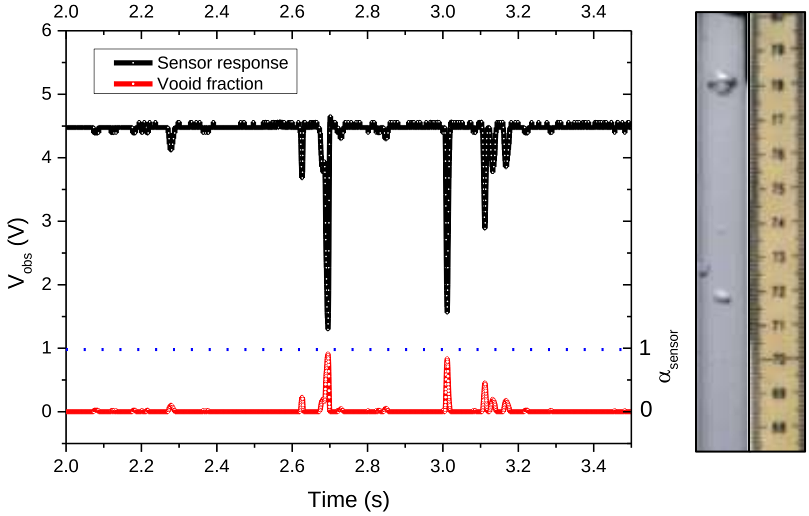

Figure 4.6: Comparison of the sensor response with instantaneous void fraction of bubbles computed using the proposed bubble flow model

Figure 4.7 (a) and 4.7 (b) show the instantaneous void fraction α_{sensor} calculated by the linear slug model (equation 4.4), corresponding with the sensor response of Taylor bubbles of 5.5 cm and 23 cm respectively. The predicted liquid fraction of zero in the presence of the liquid slugs is accurate for the time traces in both cases. The mid-section of the Taylor bubble is also accurately predicted to be have a fraction around one. However, the model shows a limitation in calculating the fractions at the air -water interface located at the nose and tails of the bubble. This leads to the prediction of unrealistic void fractions above one. Therefore, the model tends to overestimate the void fraction. Other investigators have considered binary filtering to eliminate the interfacial responses. However, this method would tend to eliminate other flow structure effects on the sensor response. A correction to the slug flow model is hence proposed to eliminate this interfacial effect around the bubble nose and tail.

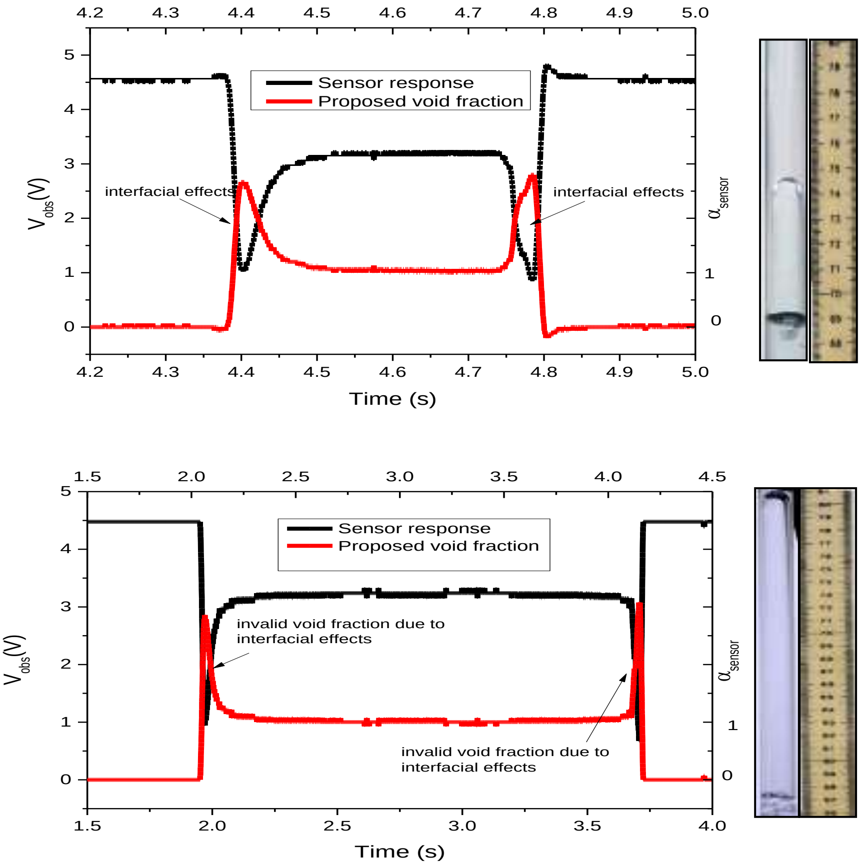

Figure 4.7: Comparison of sensor response and corresponding photograph with computed instantaneous void fractions for a (a) 5.5 cm Taylor bubble and, (b) 23 cm Taylor bubble

Based on the results from figure 4.7 (a) and 4.7(b), the observed sensor responses V_{obs} which are less than the V_{air} response leads to the invalid computation of the α_{sensor} at each point in time. These invalid results become increasingly severe up as V_{obs} approaches the V_{int} response. A typical example is found in figure 4.7 (a) where the α_{sensor} is equal to 2.3. This represents more than 200 % deviation from the expected void fraction of zero. Therefore, a correction factor (CF) is applied to modify the void fraction model for responses V_{obs} between the V_{air} and V_{int} using:

$$CF = \left[\frac{V_{obs} - V_{int}}{V_{air} - V_{int}}\right] \tag{4.6}$$

Hence the corrected instantaneous slug void fraction in equation 4.7 is derived by multiplying equation 4.4, by the correction factor from equation 4.6.

$$\alpha_{sensor} = \left[1 - \left[\frac{V_{obs} - V_{air}}{V_{water} - V_{air}}\right]\right] \cdot \left[\frac{V_{obs} - V_{int}}{V_{air} - V_{int}}\right], for\ V_{int} \le V_{obs} < V_{air} \tag{4.7}$$

Figure 4.8 (a) and 4.8 (b) show results of the corrected void fraction for the same Taylor bubbles as described in figure 4.7. The elimination of interfacial effects is evident at 4.4 s and 4.8 s in figure 4.8 (a) and 2.0 s and 3.7s in figure 4.8(b), where α_{sensor} is computed as zero at the V_{int} response. Following the results presented, the corrected model makes valid computations of the phase fraction over time averaged conditions. However, an error occurs at the nose and tail of each bubble when the CF is applied, due the fall and rise times that cause a transition from V_{water} to V_{int} at the nose and vice versa at the tail of each bubble.

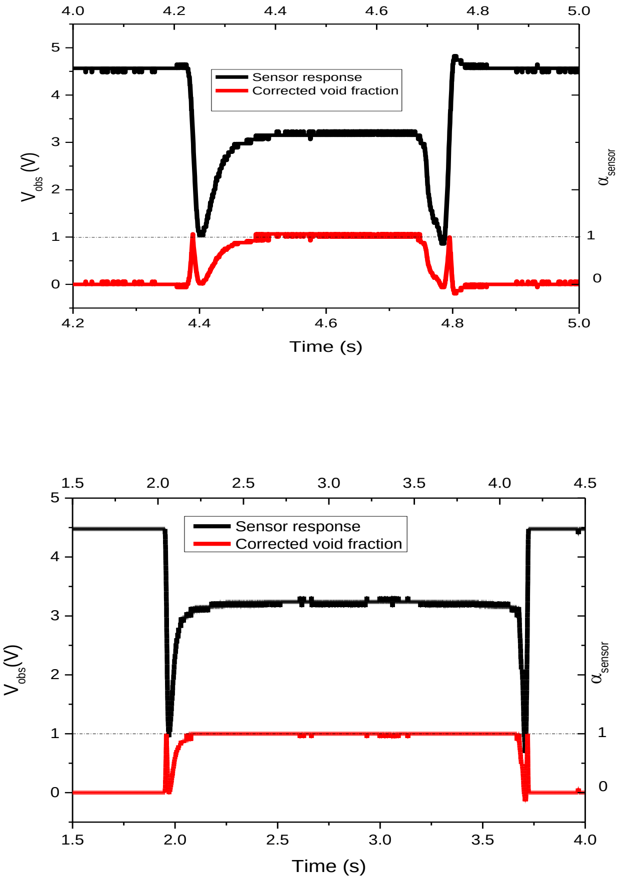

Figure 4.8: Corrected void fractions for interfacial effects (a) 5.5 cm Taylor bubble (b) 23cm Taylor bubble

A general formulation for the averaged sensor void fraction $\bar{\alpha}_{sensor}$ for the bubble and slug flow, over an averaged observed response $\overline{V_{obs}}$ is hence summarized in table 4.1

Table 4.1. Summary of the 880 nm sensor time-averaged void fraction $\bar{\alpha}_{sensor}$ models

Flow regime	**Model**	**Domain of validity**
Bubble flow	$\left[1-\left[\frac{\overline{V_{obs}}-V_{int}}{V_{water}-V_{int}}\right]\right]$	$V_{int} \leq \overline{V_{obs}} \leq V_{water}$
Slug flow	$\left[1-\left[\frac{\overline{V_{obs}}-V_{air}}{V_{water}-V_{air}}\right]\right].\left[\frac{\overline{V_{obs}}-V_{int}}{V_{air}-V_{int}}\right]$	$V_{int} \leq \overline{V_{obs}} < V_{air}$
Slug flow	$\left[1-\left[\frac{\overline{V_{obs}}-V_{air}}{V_{water}-V_{air}}\right]\right]$	$V_{air} \leq \overline{V_{obs}} \leq V_{water}$

4.4.4. Data acquisition stability

To understand the temporal effect on the sensor void fraction, a minimum time of measurement is required to capture the global event of flow in the pipe as is a requirement for real time monitoring. Hence for varying gas superficial velocities, the effect of the data acquisition time on the accuracy of the sensor void fraction over increasing gas fractions was investigated for cumulative periods ranging from 0.5 -10.0 s. Results show in figure 4.9, the unsteady nature of the flow at early times, typically from 0.5s to around 2s for the considered flow conditions. At shorter measurement times, the sensor tends to capture a local void fraction, since fewer bubbles would have enough time to be captured by the sensors. To attain the most appropriate timing for a global measurement, the relative velocities and frequencies of flow events in the test section need to be determined. The stabilization in void fraction beyond 5 seconds is an indication of a constant average velocity and flow frequency.

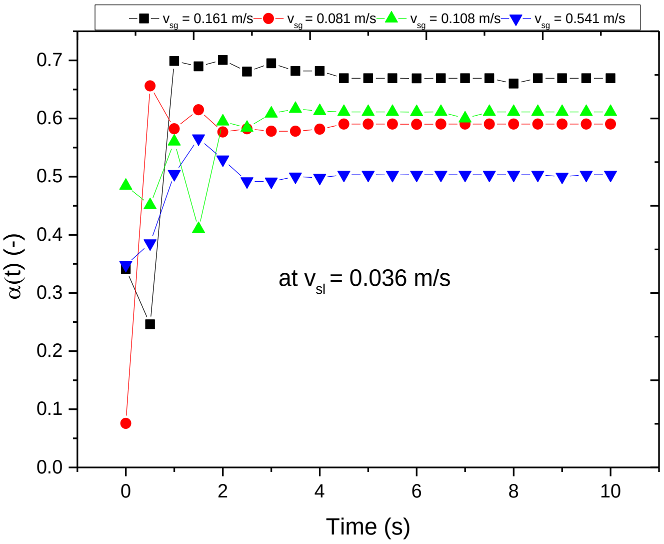

Figure 4.9**:** Variation of average sensor void fraction calculated over cumulative time (data acquisition time) from 0 to 10 seconds for varied gas fractions

4.4.5. Calibration curve

Based on the calibration studies, the information for the identification of flow regimes and phase fraction determination are combined and are presented as a calibration curve in figure 4.10. The calibration curve presents the direct relationship between the phase fractions flow regimes, transition boundaries and average sensor response for the NIOIRS. This curve can then be used in a real time application for monitoring slug flow in a pipe.

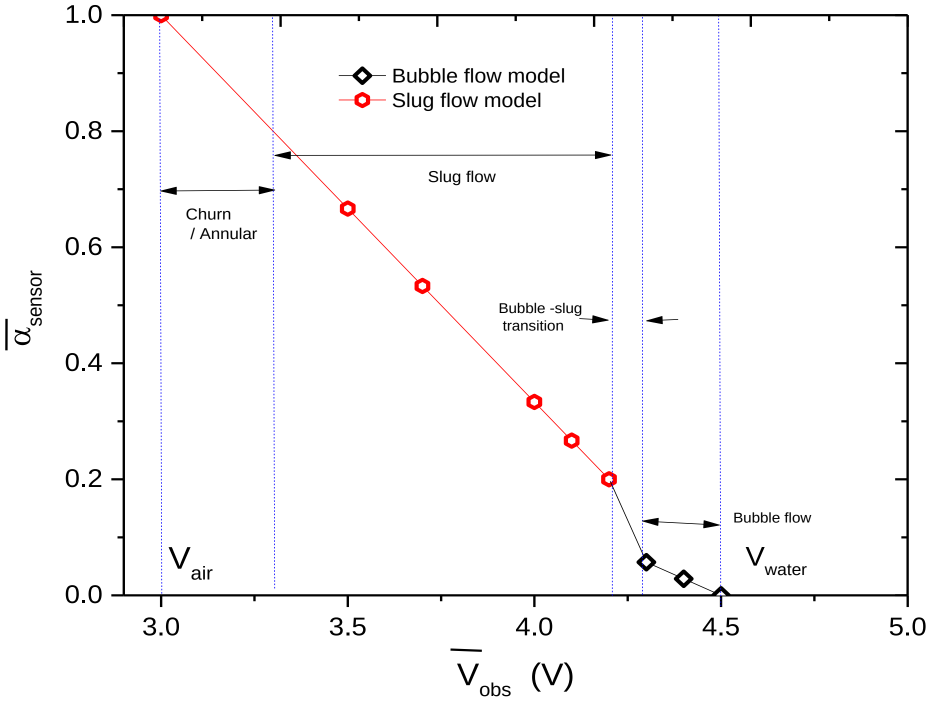

Figure 4.10**:** Calibration curve for the average void fraction based on the averaged sensor response from the 880 nm NIOIRS

4.4.6. Model validation

Figure 4.11 shows the parity between the swell level method and the sensor derived void fraction under low flow conditions. The parity line (red line) shows a good agreement between the $\bar{\alpha}_{\text{sensor}}$ and $\bar{\alpha}_{\text{level}}$ with a +/- 0.5 % error margin of the maximum void fraction considered. A contributing source of error could be the uncertainty of +/- 0.5 mm obtained when reading the meter rule for measuring changes in level of the liquid.

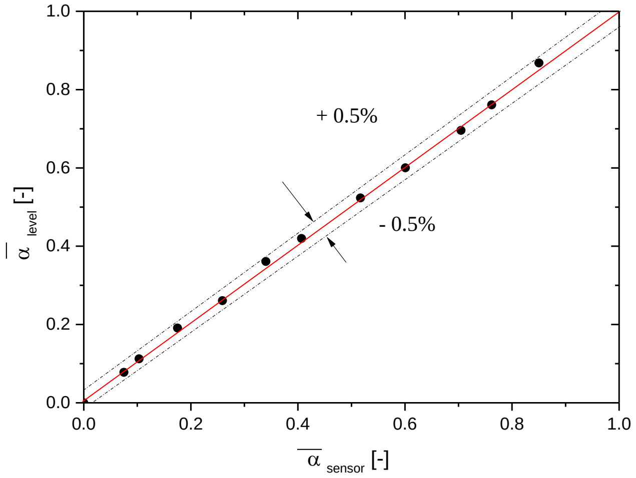

Figure 4.11**:** Validation of the sensor void fraction determination with swell level method

Figure 4.12 shows results of the parity between the average sensor void fraction and derived void fraction from photos. Results from the photographs show good agreement with the sensor void fraction for the range of void fractions considered based on an error of +/- 0.3 % (relative to the maximum void fraction considered). However, slight disparity was observed at higher void fractions (above 0.6). At this range, bubbles were injected at higher gas velocities leading to instability of the bubble nose and tail, hence leading to bubble shape distortions. This increased the uncertainty in the bubble dimensions that was extracted from the photographs.

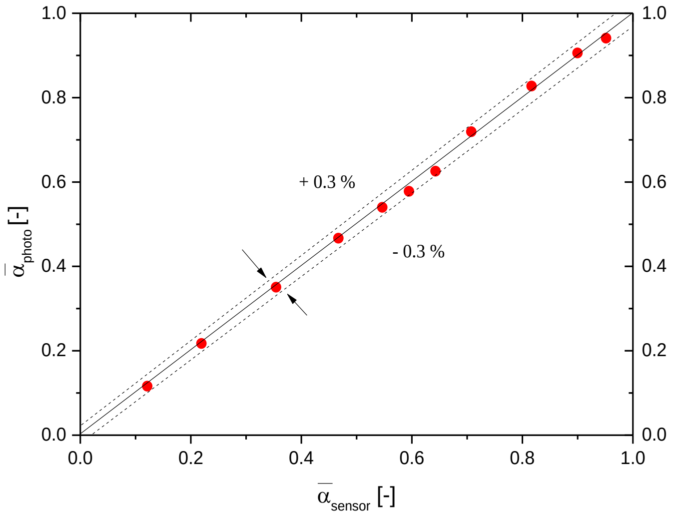

Figure 4.12: Validation of sensor void fraction determination with void fraction derived from photograph

Figure 4.13 presents the parity between the averaged sensor void fraction and the homogenous void fraction and drift flux correlation. For the homogeneous model, good agreement was observed for void fractions less than 0.6, above which a deviation from parity is evident. The converse is true for the performance of the Drift flux correlation, which includes the concept of slip between the gas phase and liquid phases, where a significant deviation is observed at low void fractions (below 0.6) and a good agreement at higher void fraction (above 0.6). This disparity between both correlations compared to the $\bar{\alpha}_{\text{sensor}}$ is indicative of the effect of a slip condition for the flow velocities considered.

The dominance of the slip effect for gas-liquid flow measurement was also observed by Oliveira *et al.*, (2009), above a void fraction of 0.7, for the same flow velocities considered in this work. Overall, the agreement with parity and error margin of +/- 0.3 % and 0.5 % from figure 15 and 16 respectively, suggests that the signal error shown in figure 12, for V_{obs}, can be considered negligible and the determination of the sensor void fraction to be valid. Overall, the performance of the 880 nm NIOIRS is considered adequate for all flow conditions considered for the test rig in this work.

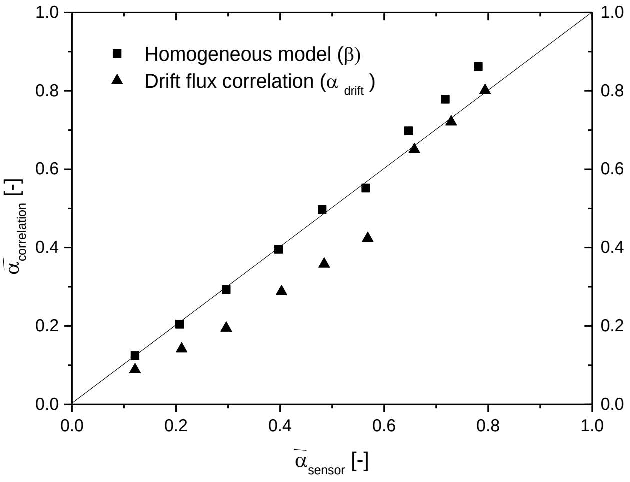

Figure 4.13**:** Comparison of average sensor void fraction with homogenous and Drift flux correlation

4.4.7. Real time Application

The execution of an algorithm in identifying flow regimes and phase fractions in real time was carried out using National instruments LabVIEW software. The real time analysis provides dynamic local flow regimes and void fractions and also global measurement via a voltage time average of the sensor response from both sensor pairs. The Pico scope was linked with LabVIEW using a development kit known as Pico scope SDK conversion code. A simple description of the algorithm used to achieve this can be seen in figure 4.14. The block diagram where the algorithm is executed is shown in figure 4.15(a) and 4.15(b).

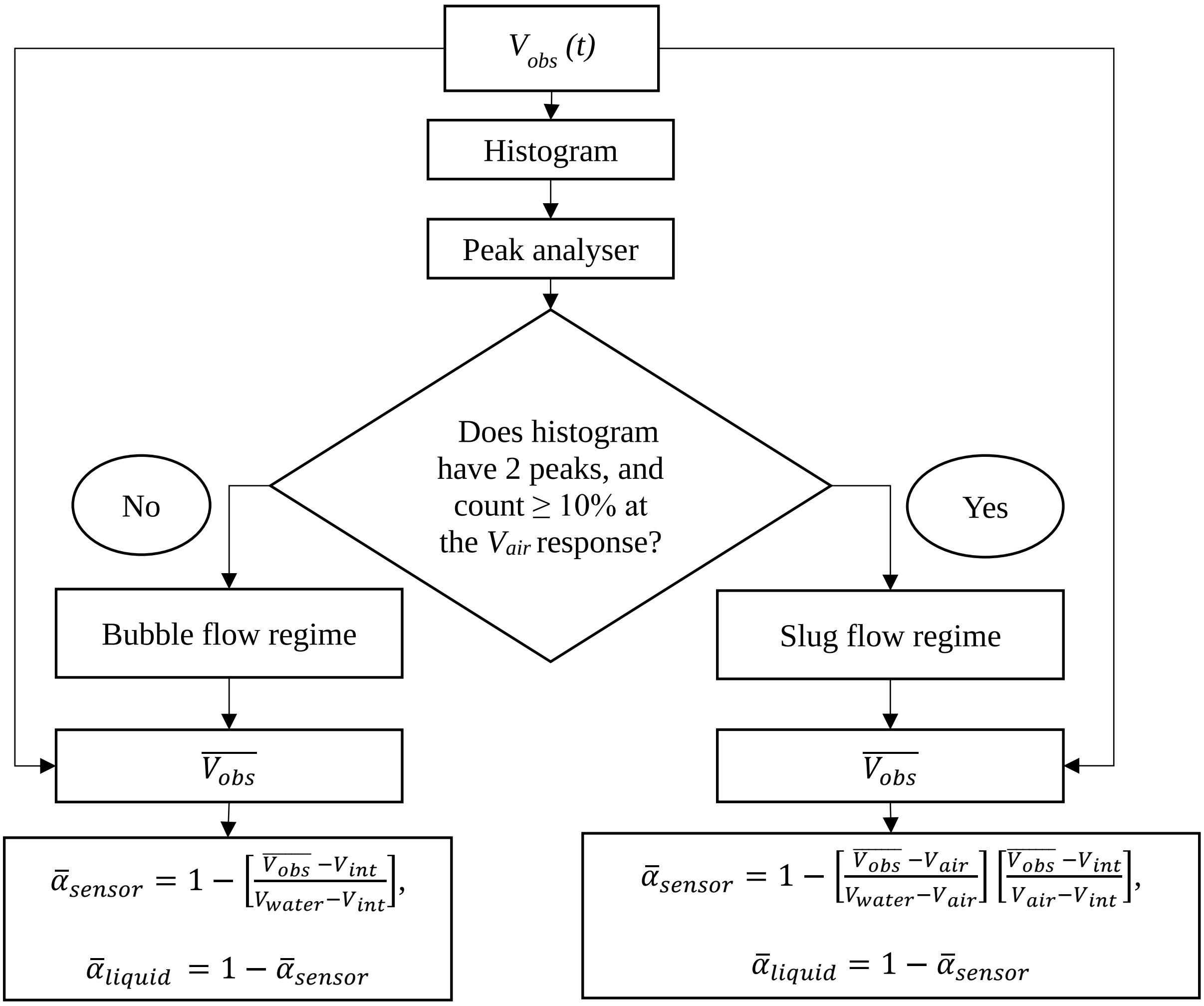

Figure 4.14: Flow chart showing the algorithm the for real time identification of flow regimes and phase fraction determination of gas liquid flow

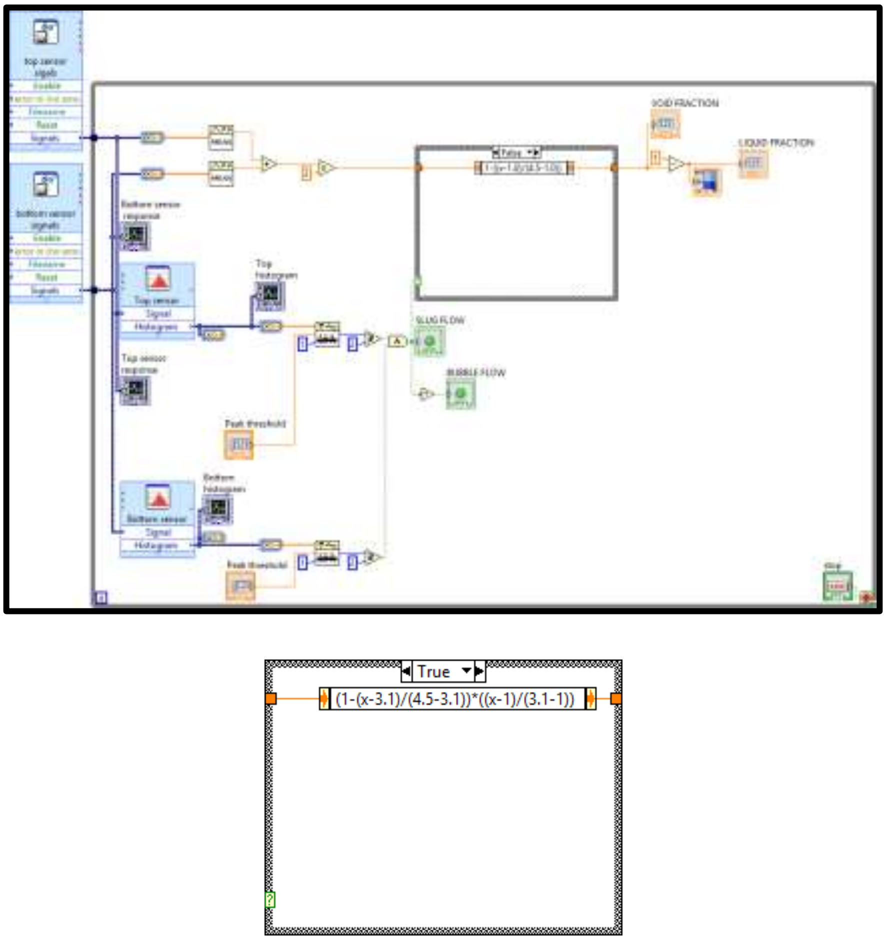

Figure 4.15: Block diagram for the executed algorithm showing (a) all links from data phase fraction determination (b) showing the true event expression for the slug flow model

A minimum measurement time of 5 sec is considered sufficient to provide valid flow regime identification based on figure 4.10. The single peaked histogram indicates a bubble flow and a double peak histogram indicates slug flow, with a threshold value of 10% of the signal count used to recognize the presence of the second peak. A true or false event tool is then linked to the flow regime identification scheme to designate the appropriate phase fraction model, since the phase fraction ($\bar{\alpha}_{sensor}$) is dependent on the prevailing flow regime. Results from the front panel as shown in the figure 4.16 (a), show a typical case of a single peaked histogram, which infers the presence of a bubble flow regime in the pipe with the corresponding void fraction and liquid fractions. Figure 4.16 (b) shows front panel results of an identified slug flow regime based on the double peaked histogram above the V_{air} count threshold of 10 %.

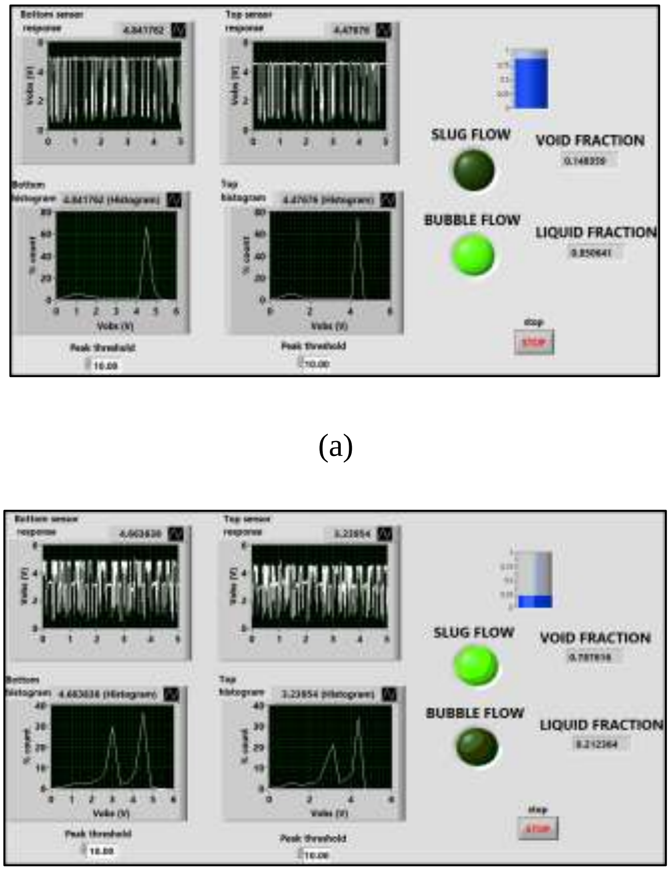

VOID FRACTION 0.148359
LIQUID FRACTION 0.850641
Peak threshold 10.00

(a)

VOID FRACTION 0.787636
LIQUID FRACTION 0.212364
Peak threshold 10.00

(b)

Figure 4.16: User front panel showing flow regime identification and phase fraction results for the (a) bubble flow and (b) slug flow

4.5. Summary

The modelling and application of the 880 nm NIOIRS for the monitoring of the slug flow regime in vertical upward flow is presented. Flow regimes identified via statistical analysis of the 880 nm NIOIRS response showed that a consistent threshold can be chosen to discriminate the bubble and slug flow regimes, however extended work is required to consider discrimination of the churn and annular flow regimes. A composite flow regime dependent phase fraction model is proposed and validated with photographs and the swell level method with relative error bands of +/- 0.3% and +/- 0.5% respectively. Validation with the homogenous and DFM correlations gave an indication of the slip condition of the gas liquid flow. Results from the real time analysis have proven that the NIOIRS system has the potential to be used as a flow regime and phase fraction meter for gas liquid- flow. Extension of this work in chapter 4 to other flow regimes, a larger pipe size and incorporation of phase velocity measurement for phase flow rate determination will be considered using the high liquid absorbance wavelength NIOIRS (typically 1480 nm).

Chapter 5

5. Flow Regime Identification Via Polynomial Regression and Probabilistic Linear and Quadratic Discriminant Analysis

5.1. Introduction

Given that the use of the percentage count distribution as applied in chapter 4, may not be reliable for more chaotic flow regimes under the upward vertical GLFs, an improved method of analysis is required. The specific objective of this chapter is to focus on the signal analysis of the 1480 nm NIORS response using polynomial regression and discriminant analysis (DA) methods for objective discrimination of flow regimes. The experiments were performed on the main rig (see description of rig set up in chapter 3).

5.2. Flow regime identification approach

The flow regime identification approach considered in this work, follows four (4) key steps of developing classification models and assessment of their performances (Hiraoka *et al.*, 2001; Tharwat *et al.*, 2017, Duda *et al*, 2012).These steps are explained below and summarized in figure 5.1.

a. Data acquisition and labelling: Acquisition of voltage to time response referred to as the sensor response was performed for a total of 145 flow conditions (v_{sl} ; 0 – 1.0 m/s and v_{sg} ; 0 – 12.0 m/s). Each flow condition was assigned according to the four stable flow regimes (bubble, slug, churn and annular flow regimes) by inspecting the sensor response validated using photographs and a flow map from literature. Training and test data sets: The labelled data sets were divided into two categories as 105 training and 40 test data sets. The training data set was used to fit and train the models while the test data category was chosen to assess the validity and the robustness of each model. Both data sets covered the full range of flow regimes produced in the test section: bubble, slug, churn and annular flow regimes.
b. Feature extraction and selection: Features were extracted via statistical analysis of the sensor response for each data set. Relevant features were then selected based on their relationship with changes in gas fraction and observed flow regimes.
c. Model fitting: The selected features extracted from the training set were used for the development of the regression model and training of the discriminant functions (LDA

and QDA). Each model is developed using appropriate algorithm discussed in sections 5.2.1. and 5.2.2. respectively).

d. Performance Assessment: The performance of each model was assessed based on the accuracy of classification and sensitivity to each predicted flow regime on the training and test data sets.

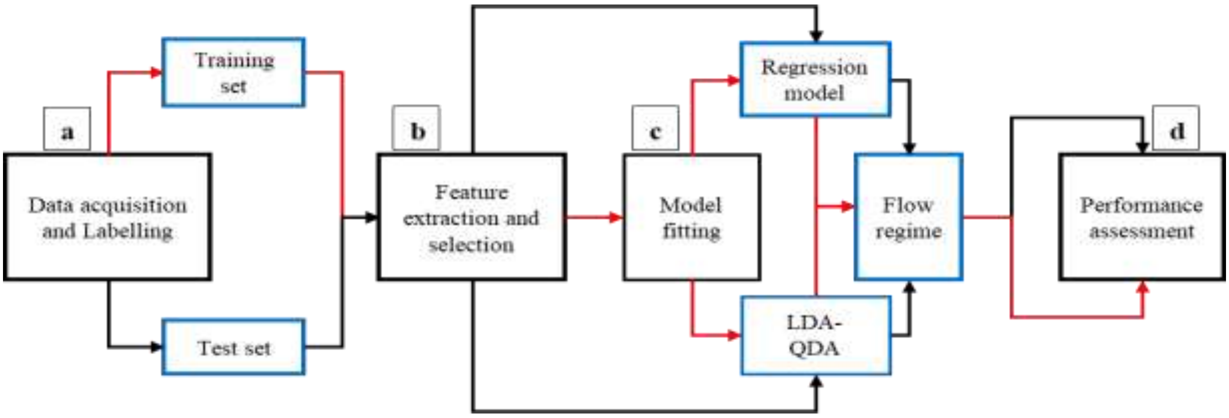

Figure 5.1: Flow chart of signal analysis method for objective flow regime identification approach using the 1480 nm NIORIS response

5.2.1. Regression analysis

Polynomial regression analysis is used to find the relationship between variables. The derived regression model is expected to explain the variability which aides an improved prediction for a classification problem. For a data set of independent and dependent variables, x and y , the regression fits the following model:

$$y = a_0 + a_1x_1 + a_2x_1^2 + a_3x_1^3 \dots\dots + a_nx_1^n + \varepsilon \qquad (5.1)$$

Where a_i represents the regression coefficients of the fit, n represents the order or degree of the polynomial fit. ε is the error term that allows for the complex variation between the independent and dependent variable. The error term is assumed be independent, random and normally distributed such that, (N (0, σ^2). The fitting process is defined by an iterative process that computes a residual y_{resi},

$$y_{resi} = y_i - (a_0 + a_1x_1 + a_2x_1^2 + a_3x_1^3 \dots\dots + a_nx_1^n) \qquad (5.2)$$

y_{resi} is assumed to be normally distributed such that, (N (0, σ_i^2), where a minimization of Chi square ($\mathcal{X}^2$) is used to compute the most likely estimates of a_i , for a given observed value y_i and predicted value $\hat{y}_i$.

$$\mathcal{X}^2 = \sum_{i=1}^{n} \frac{(y_i - \hat{y}_i)^2}{\sigma_i^2} \tag{5.3}$$

In order to avoid overfitting, the model, the choice of the highest degree of the regression model is justified for its significance on the dependent variable, using the analysis of variance (ANOVA). A 95% confidence level is computed based on standard error with a 5% significance level which follows a null hypothesis that assumes a zero correlation between variables.

5.2.2. Discriminant analysis (DA)

DA as a form of supervised learning is used to derive a function which allocates observation to groups of a new set of data (i.e. test data set) based on a training data set with priori classifications. Tharwat, (2016) provided details of the development of the LDA and QDA.

Let X_t be the training data set with n observations and p features on n_g flow regime groups. x_j is a row vector of the sample mean for the jth group, n_j is the number of observations for the jth group. The within-group covariance matrix for group j can be expressed as:

$$S_j = \frac{1}{n_j - 1} . \left(X_t - \bar{x}_j\right)^T (X_t - \bar{x}_j) \tag{5.4}$$

The pooled within – group covariance matrix

$$S_{jPooled} = \frac{1}{n_j - 1} . \sum_{j=1}^{n_g} \left(X_t - \bar{x}_j\right)^T (X_t - \bar{x}_j) \tag{5.5}$$

Mahalanobis distance is the distance of an observation from a group. The within group covariance matrix is defined as:

$$D_{ij}^2 = (x_i - \bar{x}_j) S_j^{-1} (x_i - \bar{x}_j)^T \tag{5.6}$$

The pooled within group covariance matrix defined as,

$$D^2_{ijpooled} = (x_i - \bar{x}_j)S^{-1}(x_i - \bar{x}_j)^T \tag{5.7}$$

The assigned prior probability π_j refers to the known probability of occurrence of an observation i.e. the flow regime in a given class. For data sets with equal size of observations the prior probability is computed using,

$$\pi_j = \frac{1}{n_g} \tag{5.8}$$

While unequal group size observations are calculated proportional to the group size as,

$$\pi_j = \frac{n_j}{n} \tag{5.9}$$

On the assumption that the chosen features p are normally distributed with a mean μ_j, and covariance matrix of $\sum j$, given that the probability of observing x_i from the *jth* group is $p((j|x_i, \mu_j, \sum j)$, the defining parameter which discriminates between groups is defined by the posterior probability :

$$q_j = p((j|x_i, \mu_j, \textstyle\sum j) \propto p(x_i|\mu_j, \textstyle\sum j)\pi_j \tag{5.10}$$

The posterior probability can be expressed in form of the **linear discriminant function** when an equal covariance matrix is assumed between groups as,

$$\ln(q_j) = -\frac{1}{2}D^2_{ijpooled} + \ln(\pi_j) + c_o \tag{5.11}$$

For unequal covariance matrix, the **quadratic discriminant function** in equation (5.12), defines the appropriate posterior probability for allocation of observation x_i to the j^{th} group,

$$\ln(q_j) = -\frac{1}{2}D^2_{ij} + \ln(\pi_j) - \frac{1}{2}\ln|S_j| + c_o \tag{5.12}$$

The trained models are assessed by comparing observed group membership and predicted group membership. The classification accuracy rate is hence calculated by the percentage of correctly classified observations weighted by the prior probabilities of groups. Equation (5.13) presents the classification rate A_C as,

$$A_C = 1 - \sum_{j=1}^{n_g} e_j \pi_j \tag{5.13}$$

Where e_j is the percentage of misclassification for each j^{th} group. The test data set can then be classified to the group with the highest posterior probability.

5.3. Results and discussion

5.3.1. Acquired sensor response

A total of 145 data sets of varying water and air flow rates within 0.01 – 2 m/s and 0.01 – 13 m/s respectively were acquired. The sensor responses over time captured the presence of the bubble, slug, churn and annular flow regimes and their transitions in the sensing area validated by photographs. The effect of increasing gas fraction on typical sensor response for flow regime identification is discussed.

Bubble flow

The presence of a bubble flow as presented in the photograph figure 5.2 (a) (at $\beta = 0.13$, v_{sl} = 0.86 m/s and v_{sg} = 0.13 m/s) is characterized by the presence of spherical (around 4 mm) and ellipsoidal (4mm – 10 mm) bubbles dispersed in the liquid. Aoyama *et al.*, (2016) reported that formation of ellipsoidal bubbles in vertical flows is due to the balance of forces of drag, gravity and buoyancy given the rise velocity. It is no surprise to have observed this shape at low gas fractions in this work. The corresponding sensor response (figure 5.2 (a)), is characterized by two levels of signal scattering created by the gas liquid interfaces. The first is scattering within the V_{water} and V_{int} responses due to the smaller spherical bubbles. The second is scattering between V_{int} and V_{air} responses due to larger ellipsoidal bubbles. The ellipsoidal bubbles tend to admit a higher intensity of light to be received by the photodiode, hence the increase in response from V_{int} to V_{air}. Dutra *et al.*, (2017) observed similar responses and termed it the lensing effect.

Bubble – slug transition

Further increase of the gas fraction ($\beta > 0.27$), produces a transition from bubble to slug flow regime. This was observed by the coalescence of ellipsoidal bubbles into larger bubble caps with diameter, approaching that of the pipe (figure 5.2 (b) photograph). This coalescence mechanism was reported by Guet *et al.*, (2002) to be significantly dependent on the initial bubble size and agreed with the criterion of Taitel *et al.*, (1980). The sensor response from

Figure 5.2 (b) (β = 0.29, v_{sl} = 0.69 m/s and v_{sg} = 0.26 m/s) indicates variations between calibrated responses (i.e. V_{int}, V_{water} *and* V_{air}), however, the increase in the residence time of the V_{air} response representing the short lengths of the bubble caps (equivalent to pipe diameter) can be observed.

Slug flow regime

The photograph in figure 5.2 (c) (β = 0.61, for v_{sl} =0.49 m/s and v_{sg} = 0.78 m/s) shows the presence of a slug flow regime, characterized by the presence of rising Taylor bubbles with diameters close to that of the pipe and lengths increasing to a maximum of 10 D. The bubbles were separated by liquid slugs which had entrained spherical bubbles in the wake of the Taylor bubbles, hence forming an intermittent pattern of flow. The corresponding signal response in figure 5.2 (c) shows longer residence times for V_{air} compared to the bubble caps detected in figure 5.2 (b), representing longer bubble length. Hence a stable response of V_{air} and V_{water} infers Taylor bubble and liquid slug lengths respectively. Signal scattering between V_{int} and V_{water} indicates the presence of the entrained bubbles in the liquid slug.

Furthermore, the sensor response in figure 5.2(c) interestingly shows signal attenuations along the inferred elongated Taylor bubbles at 1 and 4 s. This attenuation was as a result of variations in liquid film thickness around newly formed Taylor bubbles following a merging process. During the process, the collision of the accelerating Taylor bubble in the wake of the preceding bubbles causes a disturbance wave to propagate upwards along the bubble length thereby producing a wavy liquid film with amplitudes high enough to be captured by the sensors. Thickness. Shemer *et al.*, (2007) suggested that the merging process is typical of a slug flow regime, causing a reduction in slug frequency, increase in bubble lengths and overall slug unit lengths.

Slug – churn transition

A transition from slug flow to churn flow was observed to mostly occur at β > 0.8. The underlining consequence of the higher gas fraction led to the reduction of the liquid slugs separating the Taylor bubbles. This further lead to Taylor bubble instability since the entrained bubbles in the liquid slug coalesced hence destroying the liquid slugs and Taylor bubble noses. Brauner and Barnea, (1986) described this mechanism as the coalesce effect. Costigan and Whalley, (1997) also observed similar instability of bubbles at high gas fractions and referred to this as an unstable slug flow. Figure 5.2 (d) (at β = 0.83, v_{sl} = 0.20 m/s, v_{sg} = 1.04 m/s) shows an unstable Taylor bubble with corresponding its corresponding sensor response which shows bubble break up and reduced residence time for the V_{water} response, which infers a reduction of the liquid slug. Response variations at 0 – 0.5 s and 2.5 – 3s indicate turbulence of entrained bubbles which tend to break up the liquid slugs.

Churn flow regime

Beyond the observed slug to churn transition, a chaotic flow termed the churn effect by many researchers was observed (photograph in figure 5.2 (e), at $\beta = 0.89$, $v_{sl} = 0.23$ m/s $v_{sg} = 1.83$ m/s). This occurred at higher gas fractions where the breakdown of the liquid slug prevented the formation of Taylor bubbles. The corresponding sensor response in figure 5.2 (e) further shows significant scattering compared to the response in figure 5.2 (d). This indicates turbulence due to bubble break up and interfacial effects.

Annular flow regime

At gas fraction of 0.98, ($v_{sl} = 0.11$ m/s, $v_{sg} = 5.22$ m/s), figure 5.2 (f), shows a typical sensor response for annular flow in the test section. A steady response around V_{air} can be observed with minimal interfacial effects of a rising liquid film thickness, leading to drops in response around V_{int}. More so, the presence of entrained liquid droplets is inferred from the same figure as attenuations within the $V_{air} < V_{obs} < V_{water}$ responses; given the fact that droplets are not large enough to be captured as V_{water} responses. Researchers (Ashwood *et al.*, 2014; Xue *et al.*, 2015; Zhao *et al.*, 2013) have attributed the formation of a rising liquid film and droplet entrainments to the shearing effect of the rising gas core at the center of the test section. which causes a flow reversal condition on the liquid film and discharges the liquid droplets from the film. The photograph in figure 5.2 (f) shows the wavy liquid film, with a continuous gas core at the center of the test section though not clearly captured in the photograph.

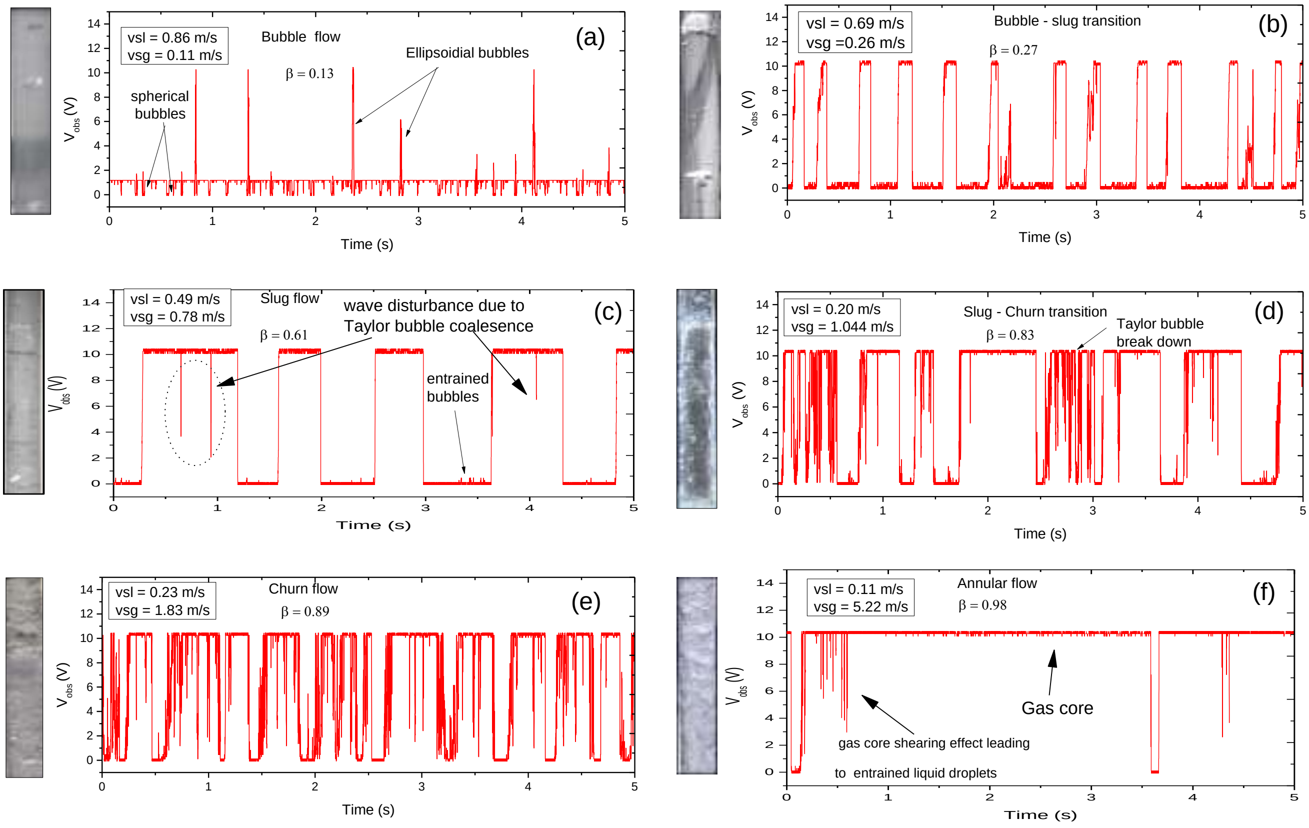

Figure 5.2: Typical sensor responses with corresponding photos for (a) bubble flow at β = 0.13 (b) bubble – slug transition at β = 0.27 (c) slug flow at β = 0.61 (d) slug – churn transition at β = 0.83 (e) churn flow at β = 0.89 and (f) annular flow at β = 0.98

5.3.2. Data set labelling

Based on the results of the sensor response and validating photographs, flow regimes were assigned to each of the 145 flow conditions (see table 5.1). A total of 105 was considered for model fitting and training , in accordance with the sample sufficiency criterion of 100 (Bray *et al.*, 1985), leaving 40 flow conditions for testing of the models.

Figure 5.3, presents results of further comparison of the assigned flow regimes with a composite upward vertical flow map derived from thirteen investigators as cited by Wu *et al.*, (2017). The assigned flow regimes agreed with the flow map boundaries in figure 5.3 for all 145 flow conditions. The agreement of the labelled data with the flow map is understandable given the fact that transitions were assumed to be abrupt as discussed in chapter 3.

Table 5.1. Summary of data set and assigned flow regimes for the training and test sets

Identified flow regime	Training data set		Test data set	
	Observations	Data range	Observations	Data range
Bubble	15	1-15	10	1-10
Slug	61	16 -76	10	11-20
Churn	19	77 - 95	10	21- 30
Annular	10	96 - 105	10	31 - 40

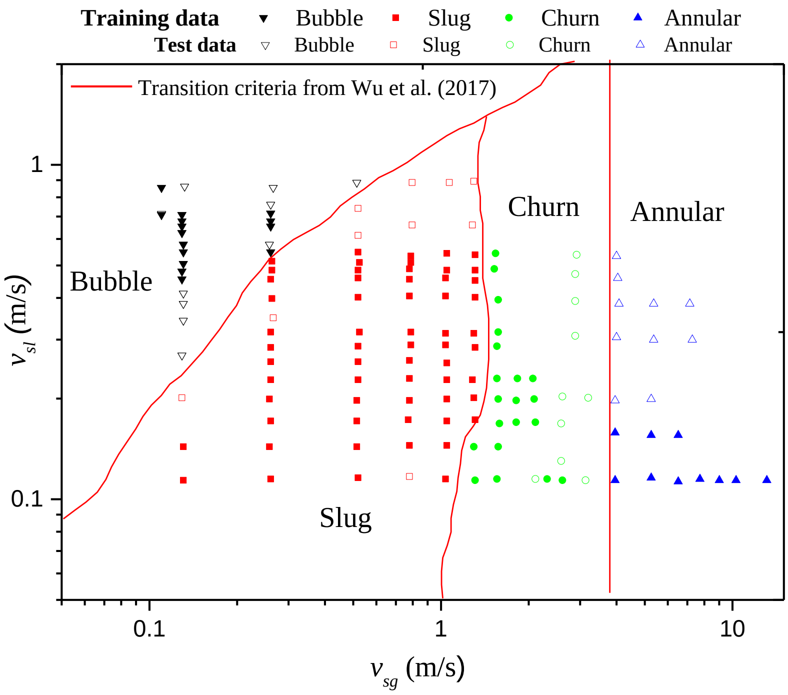

Figure 5.3: Comparison of the assigned flow regimes of the training and test data sets, showing agreement with the modified flow map cited by Wu *et al.*, (2017)

5.3.3. Feature extraction and selection

From the acquired sensor response ($V_{obs}(t)$), the extraction of five features that are expected to provide unique information in classifying flow regimes was performed. These features include the average sensor response $\overline{V}_{obs}$, standard deviation, σ_{sensor}, the percentage count of the calibrated sensor responses $\%V_{water}$, $\% V_{air}$ and $\%V_{int}$ respectively.

The average sensor response $\overline{V}_{obs}$, and standard deviation σ_{sensor} were computed based on a time average for each of the 145 flow conditions using equation (5.14) and (5.15) respectively,

$$\overline{V}_{obs} = \frac{1}{N}\sum_{i=1}^{N} V_{obs}\,(t) \tag{5.14}$$

$$\sigma_{sensor} = \sqrt{\frac{1}{N-1}\sum_{i=1}^{N}(V_{obs}(t) - \overline{V}_{obs})^2} \tag{5.15}$$

The percentage counts of calibrated responses (V_{air}, V_{water} and V_{int},) were computed as a percentage of the number of captured calibrated sensor responses (N_{water}, N_{air}, N_{int}) to the total number of data points N, captured by the NIORS setup.

$$\%\, V_{calibrated\ response} = \frac{1}{N}\sum_{i=1}^{N} N_{calibrated\ response} \tag{5.16}$$

The considered features were then screened for selection based on their relationship with changes in gas fraction and observed flow regimes. According to Maugis *et al.*(2011) adequate feature selection involves the choice of useful features that provide unique discriminatory information hence, eliminating noisy features which provide unexplainable variance in the model.

Feature extraction results

i. Average sensor response

Figure 5.4 presents the result of the effect of gas fraction β on the average sensor response $\overline{V}_{obs}$ for the training data set. The results show a general linear trend for most of the data points corresponding to the slug flow regime. This trend is due to increases in Taylor bubble lengths causing an increase in light received by the sensor. For the bubble flow regime, increases in β, produced a slight variation of $\overline{V}_{obs}$ within 1.1V, which is indicative of the presence of smaller bubble (spherical and ellipsoidal bubble) interfacial scattering.

It also follows that the smaller bubbles did not coalesce within this region, but rather formed clusters which produced varied levels of scattering, hence the variation in $\overline{V}_{obs}$. Around β = 0.27, The abrupt transition from bubble to slug flow is indicative of the sudden formation of bubble caps by the clustering smaller bubbles. At higher average sensor responses beyond (6.9V) and β = 0.8, A deviation from the apparent linear slug Trend can be observed due to the slug - churn flow transition. The decreases in average sensor response is simply due to interfacial scattering and bubble break down hence the decreases in light transmission. At higher gas fractions greater than 0.9, a general increase in $\overline{V}_{obs}$ is observed in the annular region due to less scattering effects attributed to variations in liquid films thickness and presence of entrained liquid droplets in the gas core.

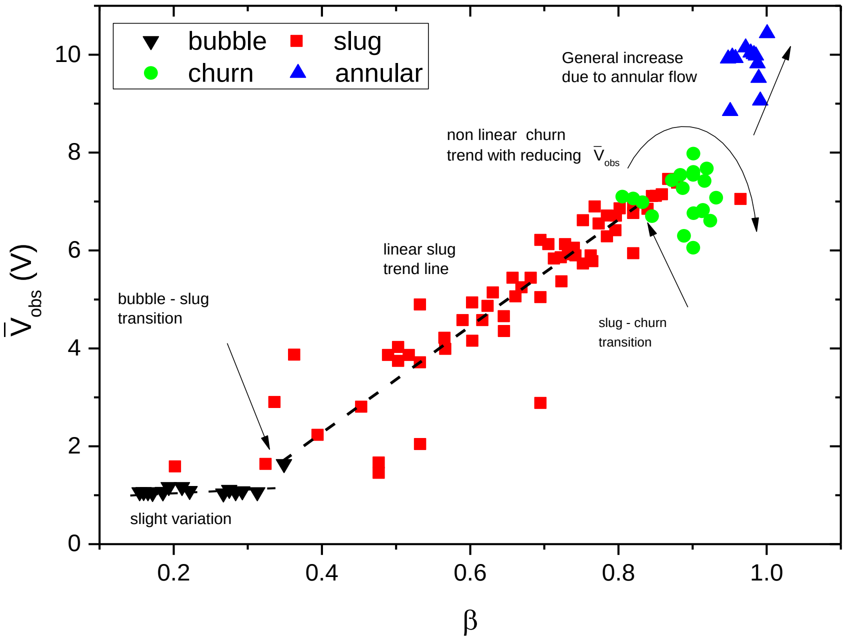

Figure 5.4: The effect of gas fraction and corresponding flow regimes on (a) the average sensor response and (b) sensor standard deviation

ii. Sensor standard deviation

The σ_{sensor} is considered as a feature to represent fluctuations in the sensor response caused by flow structures in a given flow regime. Figure 5.5 presents results of the effects of β on the σ_{sensor}. At β < 0.27, i.e., the bubble flow regime, an undulating trend in σ_{sensor} infers fluctuation in the sensor response due to bubble scattering effects similar to that observed in figure 7. However, the variation is amplified using the standard deviation thus providing unique discriminatory information. In the range of, 0.27 < β < 0.55, a general increase in σ_{sensor} can be observed corresponding to a bubble – slug transition (bubble cap formation) and the slug flow development (Taylor bubble formation). A decrease in rate of increase of in σ_{sensor} as β approaches 0.6 infers the formation of the maximum stable bubble length which corresponds to the maximum fluctuation in response equal to 5 V.

Further increases in the gas fraction (0.6 > β > 0.88) led to a decreasing trend in response fluctuation indicative of bubble breakdown and churn flow transition. The formation of annular flow regime at for such as the annular flow regimes and single-phase flow of air.

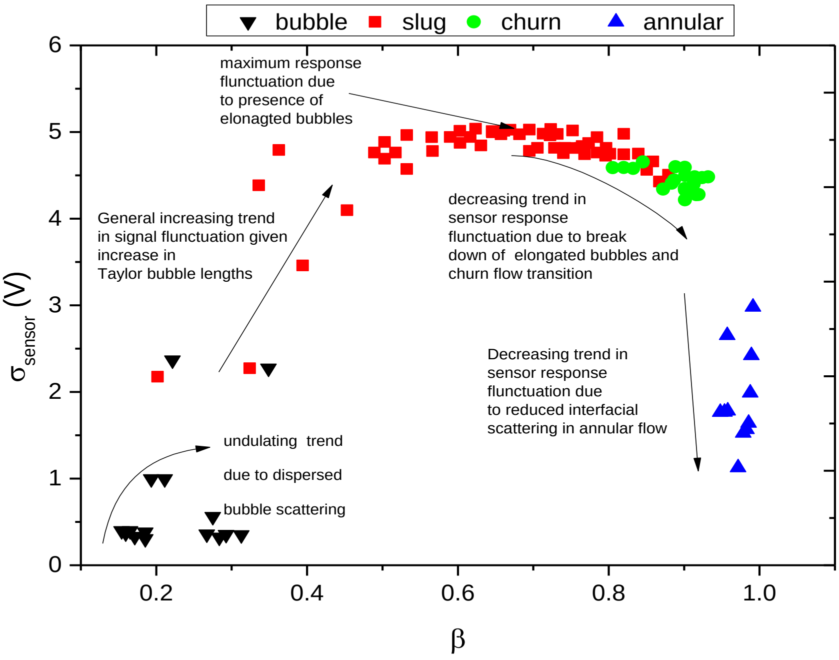

Figure 5.5: The effect of gas fraction and corresponding flow regimes on (a) the average sensor response and (b) sensor standard deviation

iii. Percentage counts of calibrated responses

Figure 5.6 shows the plots of the sensor histogram based on the sensor response V_{obs} and % counts. A general skew from left to right of the histogram for increasing gas fractions can be observed. Figure 5.6 (a) shows results of the histogram of a single-phase liquid at $\beta = 0$, a single peak around at 100 % of V_{water} indicates the presence of only water in sensing area. Figure 5.6(b) shows a bubble flow histogram at $\beta = 0.13$ with a significant 9 % count of V_{int} response due to the effect of interfacial scattering of bubbles with a reduction in the count of V_{water} to 90 %.

A typical slug flow regime in figure 5.6 (c) (at $\beta = 0.34$) shows two global peaks at the V_{int} and V_{air} responses with a significant drop in % V_{water}. The increase in % V_{air} is due to the increase in gas fraction leading to a corresponding reduction in % V_{water} . The increase in % V_{int} is mainly due to the lensing effect by a cluster of entrained bubbles dispersed in the liquid slug. Increasing gas fractions further, then leads to the churn flow regime (in figure 5.6 (d)) where a reduction in % V_{air} can be observed. This reduction is as a result of the turbulent nature of the churn flow for which infrared light was scattered by the collapsing and rising gas liquid interfaces. More so, the interfacial scattering is evident with a significant $\%V_{int}$ and apparent absence of a significant $\%V_{water}$,

At very high gas fraction beyond the churn flow, the histogram in figure 5.6(e) shows a single peak around the % V_{air} response with minimal variations at the V_{int} response, hence indicating an annular flow regime. Figure 5.6(f) shows a complete skew to the right representing a single-phase air flow where 100 % V_{air} was observed. In general, trends from the histogram were in agreement with PDFs results considered by other researchers (Azzopardi *et al.*, 2015; Chakrabarti *et al.*, 2007; Jones and Zuber, 1975; Shaban and Tavoularis, 2014a).

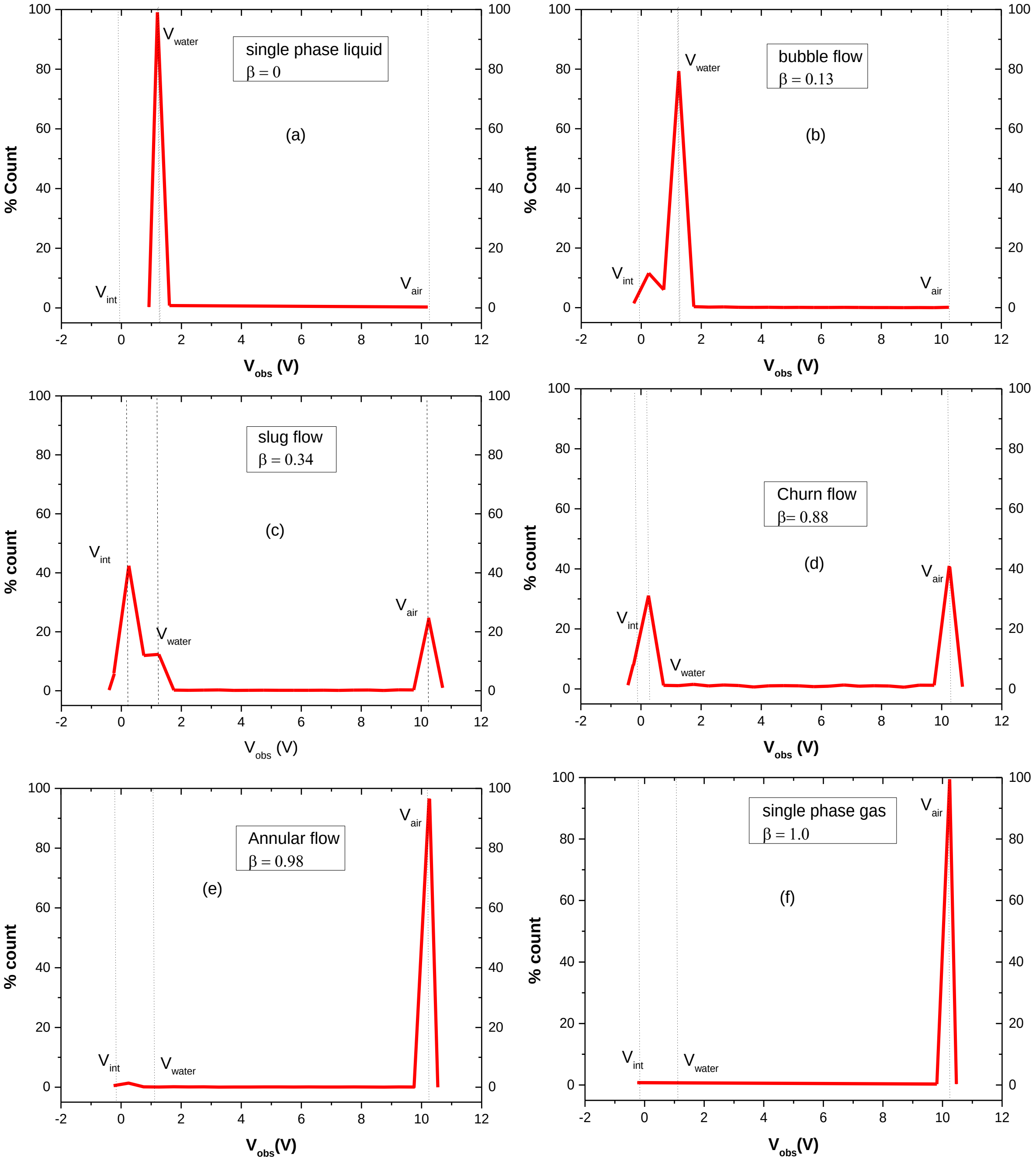

Figure 5.6**:** Typical histograms for (a) single liquid phase at β = 0 (b) bubble flow regime at β = 0.13, (c) slug flow regime at β = 0.34 (d) churn flow regime at β = 0.88 (e) annular flow at β = 0.98 (f) single phase liquid, at β = 1.0

A summary of the relationships between gas fraction and the percentage count responses is presented in figures 5.7 (a), (b) and (c). The % V_{water} plot in figure 5.7(a) shows a general reduction for increasing gas fraction as a result of increasing gas fractions. An unclear trend in bubble- slug transition is indicative of variations in light scattering from bubble cap formation with entrained bubbles for the bubble flow regime. The % V_{water} drops remarkably in the annular flow regime due the presence of thin liquid film. The % V_{air} also in figure 5.7 (b) shows an inverse trend compared to the V_{water} for increases in gas fraction. The % V_{int} response is presented in figure 5.7 (c) shows a nonlinear trend for increases in gas fraction. Moreover, interfacial scattering exists for all flow regimes from small bubbles (in bubble flow), Taylor bubbles and entrained bubbles (in slug flow), unstable bubbles (in churn flow), wavy liquid film and liquid droplets (in the annular flows). Table 5.2 summarizes the effect flow regime mechanisms on each extracted feature.

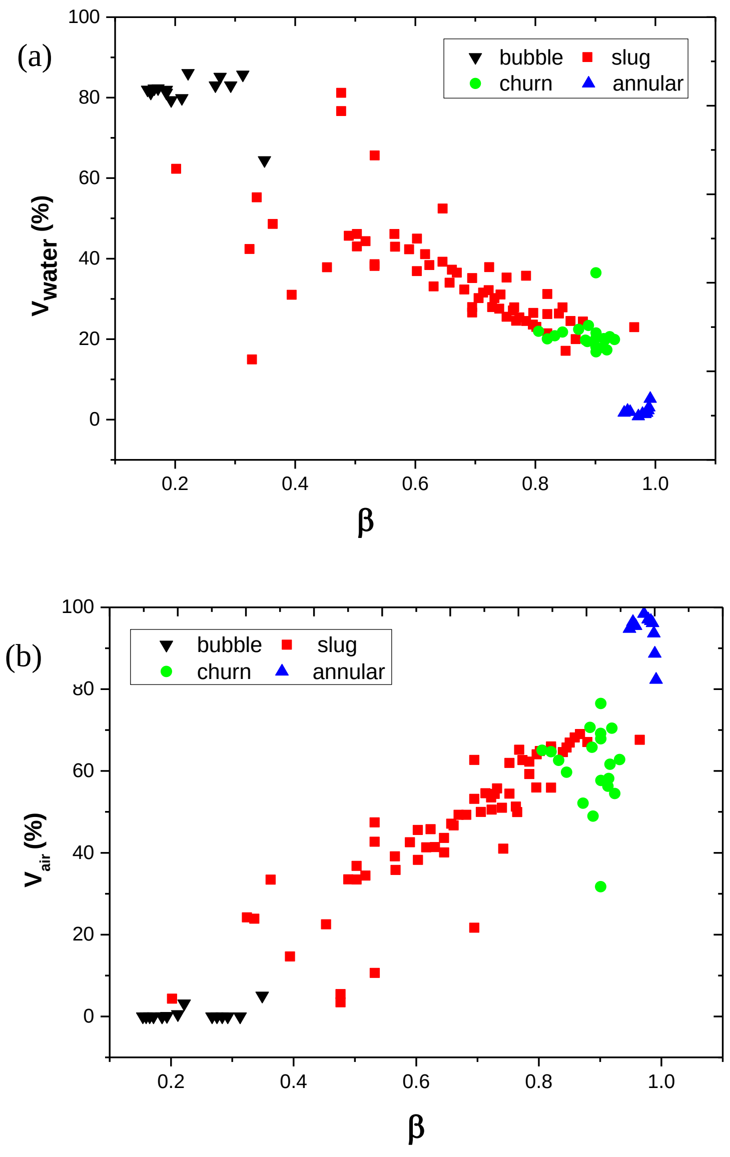

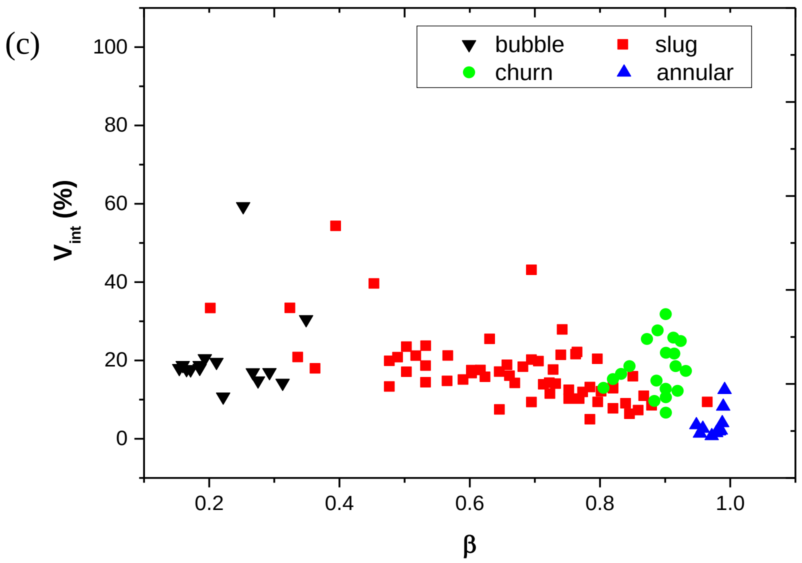

Figure 5.7: Plots of extracted features from the sensor response of the training data set showing the effect of gas fractions and flow regimes on the (a) percentage count of V_{water} (b) percentage count V_{air} (c) percentage count of V_{int}.

Table 5.2. Summary of the effect of the observed flow regimes on each extracted feature from the sensor response

Flow regime	**Extracted Features**					
	Dominant Mechanism	$\overline{V}_{obs}$	σ_{sensor}	$\%V_{water}$	$\%V_{air}$	$\%V_{int}$
Bubble	Bubble cluster formation	Slight variation	Larger undulating variation	Slight variation	Slight variation	Nonlinear Variations
Slug	Taylor Bubble formation and length increase	Increases	Increases	Decreases	Increases	Nonlinear Variations
Churn	Bubble collapse and turbulence	Nonlinear variation	Gradual decrease	Decreases	Increase	Nonlinear Variations
Annular	Gas core with liquid film formation hence less scattering	Increases	Decreases	Decreases	Increases	Slight decrease

Feature selection

Based on the analysis of results in figures 5.4 – 5.7, the average sensor response, and standard deviation were selected as the key features for developing the regression and DA models, given the fact they provided unique discriminatory information indicative of variations in flow regimes. Combining both features is heron termed feature group 1. Feature group 2 is selected by combining feature group1 with $\% V_{air}$ and $\% V_{water}$. The $\% V_{int}$ feature is not selected since it did not provide clear trends, unique to each flow regime therefore may reduce feature redundancy. Table 5.3 summarizes the selected feature groups required for the polynomial regression and training of the LDA and QDA models.

Table 5.3**:** Selected feature groups for each identification model

Group	Feature	Model
1	$\bar{V}_{obs}$ and σ_{sensor}	Polynomial Regression, LDA, QDA
2	$\bar{V}_{obs}$, σ_{sensor} , %, V_{water} and $\% V_{air}$	LDA, and QDA

5.3.4. Polynomial Regression analysis

The average response (independent variable) and the standard deviation (dependent variable) of the sensor were chosen as the features for developing the regression model using the training data set. A clear polynomial relationship between both features can be observed in figure 5.8. For bubble flow regime, a relative increase in both features can be observed until the slug flow regime is transitioned, where a deviation from the trend occurs until a maximum standard deviation of 5V. Beyond this point a transition from slug to churn flow is observed with decreasing variation in the response which has been explained as scattering effects. The variation in response continues to decrease as the average response approaches the V_{air} response, this indicates the stabilization from churn to an annular flow regime.

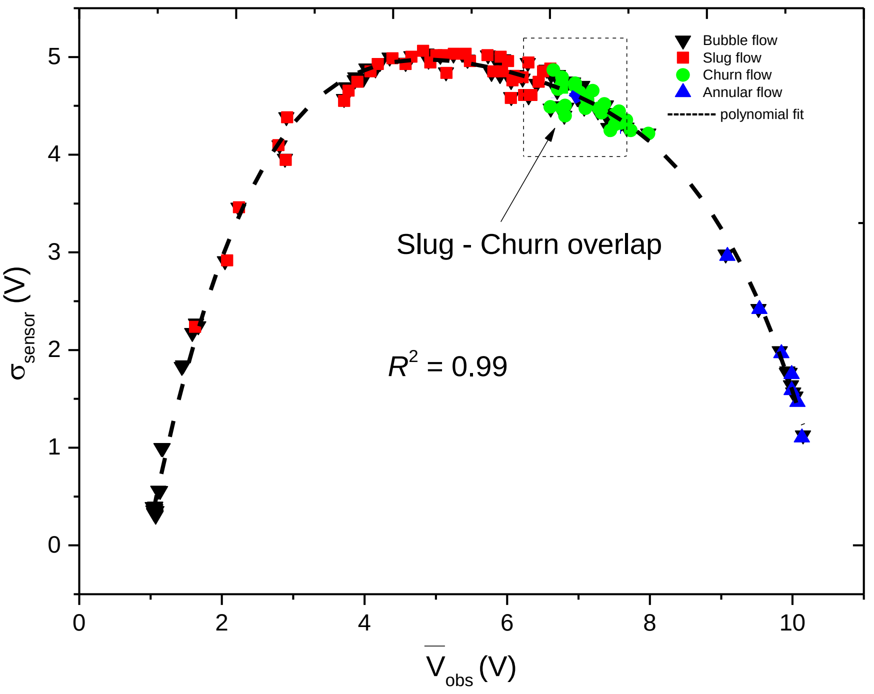

Figure 5.8: Relationship between the average sensor, $\bar{V}_{obs}$ and standard deviation , σ_{sensor} showing a model fit derived from the polynomial regression analysis.

The fitted model is hence described as a 4th order polynomial for the optimal fit of $R^2 = 0.99$.

$$\sigma_{predicted} = a_0 + a_1\bar{V}_{obs} + a_2\bar{V}_{obs}^2 + a_3\bar{V}_{obs}^3 + a_4\bar{V}_{obs}^4 \tag{5.17}$$

Table 5.4 summarizes the fitting parameters of the polynomial model. The coefficients of the regression, standard errors together with the 95% confidence levels were computed. According to the ANOVA, results of the test of significance of each coefficient (in table 5.4) show probabilities of zero for which the computed test statistics would be higher than the critical value. This implies that all coefficients are significant up to the highest order of the polynomial model. This test was computed for a 5% significance level.

Table 5.4. Fitting parameters for the polynomial regression model

Coefficients	Value	Standard Error	t-Value	Prob> |t|	95% LCL	95% UCL
a_0	-4.54643	0.1444	-31.48525	0	-4.83295	-4.25992
a_1	6.02771	0.17555	34.33652	0	5.67939	6.37604
a_2	-1.41653	0.06148	-23.0397	0	-1.53852	-1.29453
a_3	0.14917	0.00824	18.09404	0	0.13281	0.16553
a_4	-0.00617	3.72E-04	-16.56306	0	-0.00691	-0.00543

Figure 5.9 (a) presents the results of the computed residuals over the independent variable, i.e. $\bar{V}_{obs}$. Over the full range of $\bar{V}_{obs}$, ,the variation of residuals was close to zero, which further suggests that an adequate estimate of regression coefficients was computed. Figure 5.9 (b) also shows a plot of a slightly asymmetric normal distribution of the residuals which satisfies the conditions of normality and hence an acceptable solution of regression coefficients.

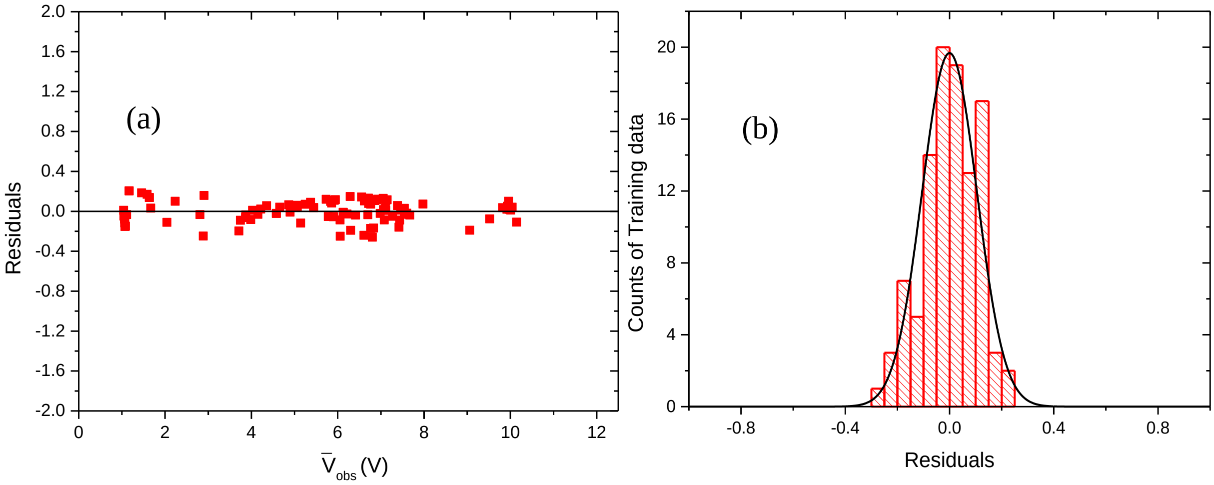

Figure 5. 9: (a) The residuals of the regression model (b) Normality of the residuals

To use the polynomial regression model as a predictor of flow regimes under any prevailing flow conditions in the pipe; objective boundaries are marked based on the derived polynomial model. Table 5.5 summarizes the domains and ranges of validity for each flow regime encountered during the experiment.

Table 5.5. Objective boundary identification from the polynomial regression model equation (5.17)

Flow regime	Average sensor response (V)	Sensor standard deviation (V)
Liquid flow	$\bar{V}_{obs} = V_{water}$	$\sigma_{predicted} < 0.01$
Bubble flow	$0 < \bar{V}_{obs} < 1.45, \neq V_{water}$	$0.01 < \sigma_{predicted} < 1.85$
Slug flow	$1.45 \leq \bar{V}_{obs} < 7.01$	$1.85 \leq \sigma_{predicted} < 5.01$
Churn	$7.01 \leq \bar{V}_{obs} < 9.06$	$3.01 \leq \sigma_{predicted} < 4.58$
Annular	$9.06 \leq \bar{V}_{obs} < V_{air}$	$0.001 < \sigma_{predicted} < 3.01$
Gas flow	$\bar{V}_{obs} = V_{air}$	$\sigma_{predicted} < 0.01$

For a practical application of the model, $\bar{V}_{obs}$ can be extracted from the sensor response and used to compute $\sigma_{predicted}$. A flow regime is then identified according to the defined boundaries. The σ_{sensor} , can also be compared with the $\sigma_{predicted}$ to ensure validity of the model.

Performance of the regression model

The performance of the regression model was assessed using the test data set (40 flow conditions) which comprises of $\bar{V}_{obs}$, and σ_{sensor} ,(feature group 1). Figure 5.10 (a) shows a plot of the test data on the polynomial regression model to show the prediction fit. According to the flow regime boundaries (shown as dashed boxes), most of the test data points are within the prediction band of the polynomial regression model. However, close to the objective boundaries, an error of classification of a churn flow for a slug flow was observed at $\bar{V}_{obs} = 6.97\, V$, $\sigma_{predicted} =$ 4.58 V. Misclassifications have often been reported to occur around these boundaries due to the unstable nature of the transitions between flow regimes .

It is therefore a challenge to accurately predict the instabilities around these boundaries. A practical solution is to define a standoff between transition boundaries hence defining transition zones of instability. This could minimize the severity of the problem, but not eliminate it.

According to the misclassification error, an average classification accuracy of 97.5 % was derived from regression model. Further comparison of the sensor and predicted standard deviations is presented in figure 5.10 (b). The parity plot shows an average error of +/-7 % of the maximum standard deviation value, largely due to overestimations of the predicted standard deviations for the bubble flow conditions. Further evidence of this could be observed in the computed residuals in figure 5.9 (a) where the highest residuals were at low average sensor responses corresponding to the bubble flow regime. Despite this overestimation, all the bubble flow conditions were accurately identified according to the marked boundaries of the regression model, hence highlighting its robustness. This further suggests that the average sensor response ($\bar{V}_{obs}$) can be used as the sole discriminating feature specific to the bubble flow and annular flow regimes. However, the slug and churn flow regimes require both features as a result of the polynomial relationship.

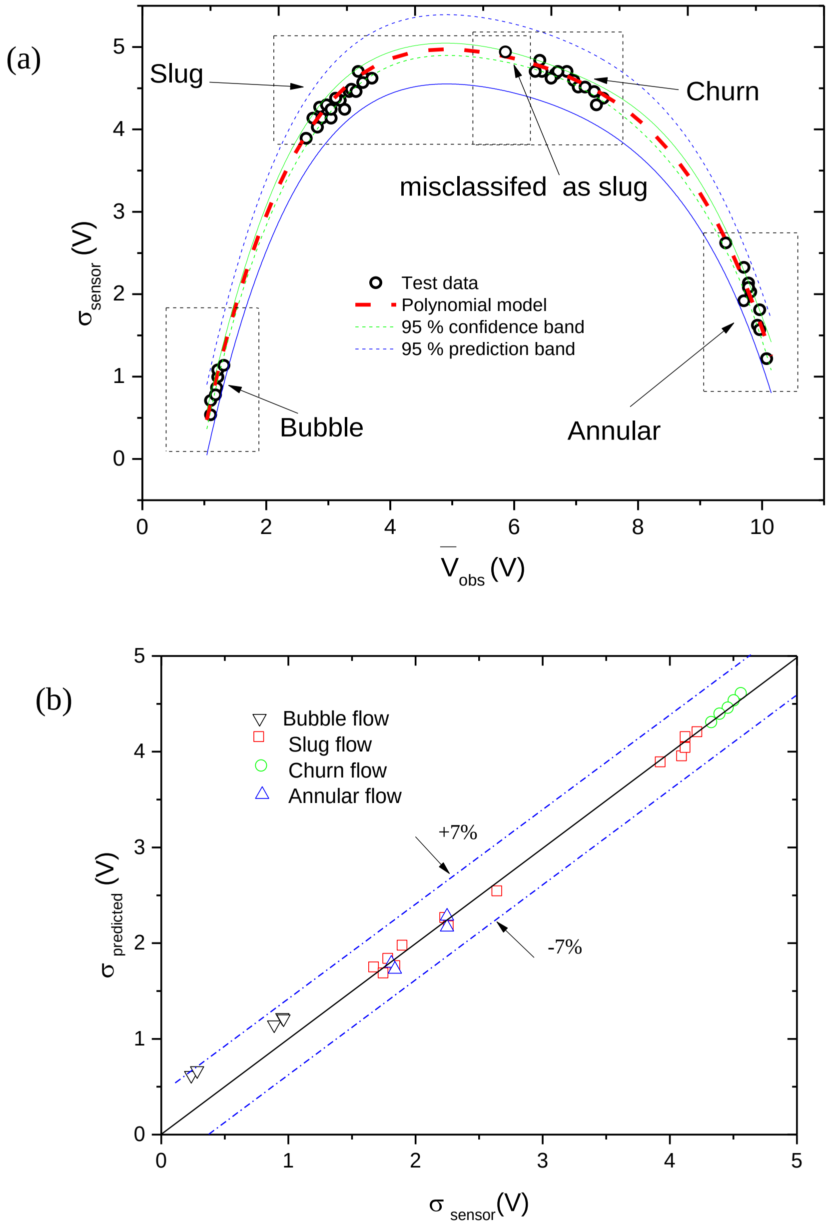

Figure 5.10 : Performance of the polynomial regression model on the test data showing (a) flow regime prediction of the test data and (b) parity plot of the sensor standard deviation with the predicted standard deviation for each flow regime group

5.3.5. Discriminant analysis (DA) results

Based on the selected features extracted from the optical sensor, discriminant functions were derived from the training set to compute posterior probabilities qi, using the Mahala Nobis distances, D_{ij}^2 (equation 5.6) , $D_{ijpooled}^2$ (equation 5.7) and the priori probabilities π_j, (equation 5.10). Each observation vector was then allocated to the flow regime group with the highest q_i under each LDA and QDA feature group case. The prediction of the test data can be assessed for each case.

DA training posterior probabilities

Figure 5.11 (a-d) presents results of the posterior probabilities from the training data set for each case of the LDA and QDA feature groups (105 data points). An inspection of the results at the assigned bubble flow data (1- 15) and annular flow data (96 – 105) in all cases, show that the posterior probabilities were equal to one. This is an indication of an absolute certainty that the bubble, and annular flows occur at the assigned features. A good discrimination is thus expected, since the bubble and annular flows have contrasting dispersive structures as clearly captured by the optical sensor. The q_i for the slug and churn flows at similar data points were close to zero, hence a good discrimination for all cases within the aforementioned data ranges.

For the data range of 16 – 76, in figures 5.11 (a-d), clustering of probabilities between the assigned slug and churn flow regimes can be observed. The clustering is indicative of the uncertainty in correctly discriminating between these flow regimes. The structural similarities between slug and churn flow especially for flow conditions around the slug – churn transition, such as the intermittent characteristics of elongated, entrained bubbles and variations in liquid film are primary causes of the probability variations. As compared to the assigned slug flow regime, the posterior probabilities for the assigned churn flow data range of 77 - 95, show a better separation of posterior probabilities between the churn flow and other regimes for all cases in figure 5.11.

In general, the QDA feature groups of figures 5.11(c) and 5.11 (d) show better separation of posterior probabilities than the LDA feature groups of figures 5.11 (a) and 5.11 (b). The QDA computed Mahala Nobis distances D_{ij}^2 combined with the within group covariances S_j from represents the main contributing factors to the observed improvement in separation. The QDA has been reported to present a better fit for large training data since it has nonlinear flexibility. Wu *et al.*(1996) observed similar superiority of the QDA when they used a large training set to train models for classification of near infrared spectra data.

The effect of the feature groups on the computed posterior probabilities can also be observed. Inclusion of the percentage counts of V_{air} and V_{water} in feature group 2 influenced a better separation of probabilities, given the fact that each feature adds a unique discriminatory dimension to the models. This is observed by the comparison of the LDA feature groups 1 and 2 (figure 5.11 (a) and (b)) respectively and QDA feature groups 1 and 2 (figure 5.11 (c) and (d)) respectively. Results of the model classification accuracies are discussed in the next subsection.

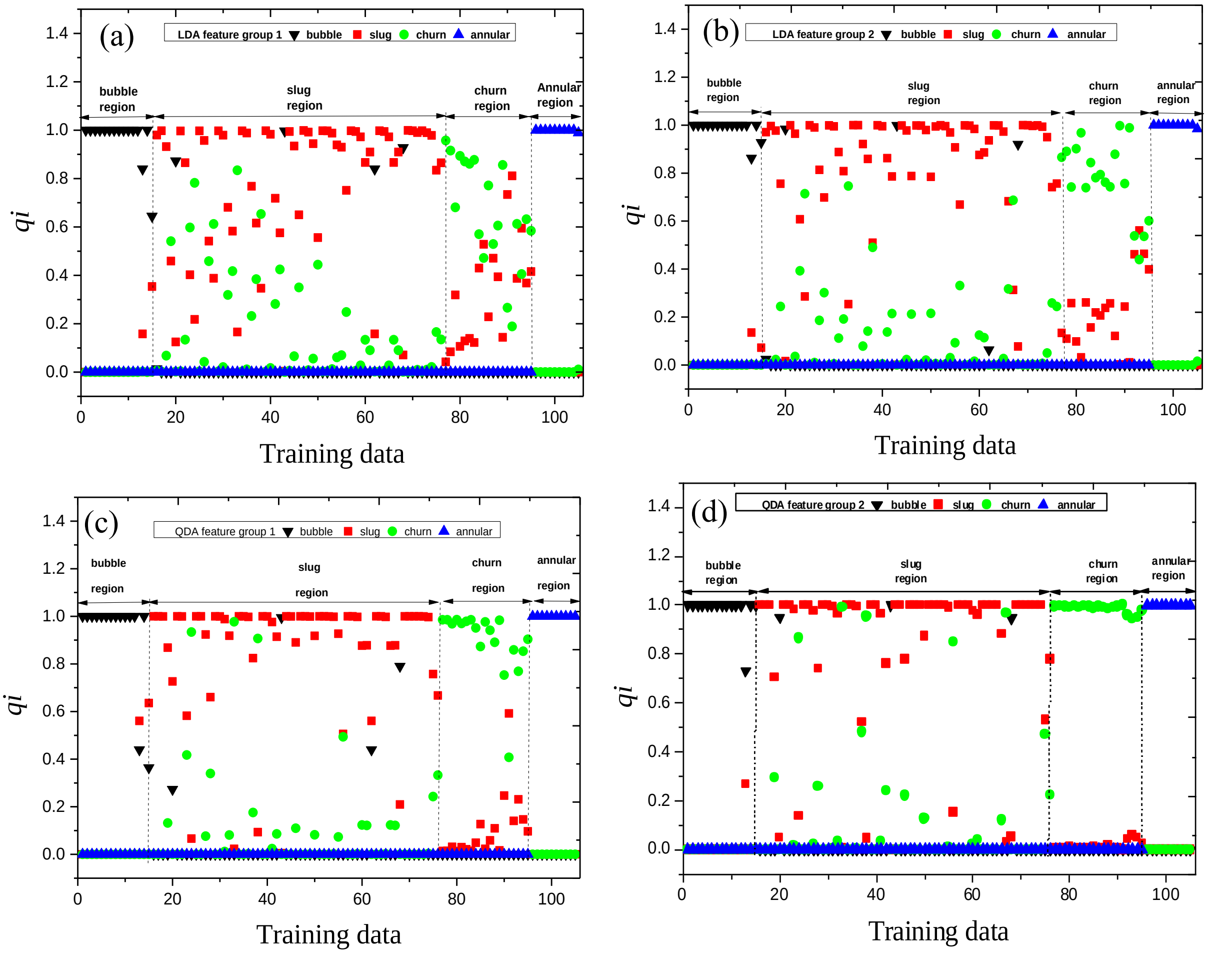

Figure 5.11: Computed posterior probabilities for each flow regime group for (a) LDA feature group 1 (b) LDA feature group 2 (c) QDA feature group 1 (d) QDA feature group 2.

DA training performance

A summary of the classification performance of each DA case is presented in the confusion matrix tables 5.6 – 5.9. The tables present the error and classification accuracies associated with identifying each flow regime for each case. The rows represent counts of the observed flow regime groups and the columns are the predicted flow regime groups by the discriminant functions for each case. Values in the diagonal of the matrix represent the correct classification of each flow regime. The LDA feature group 1 from table 9, shows an average error 13.33 %. This average error is due to the misclassification of the slug flow at 16.39 % and churn flow at 21.05 %, with no misclassification for the bubble and annular flow regimes. An error rate of 6.67 % which corresponds to a 50% reduction in the error rate from LDA feature group 1 to LDA feature group 2 (table 5.9) further indicates the relevance of including the count percentages of the V_{air} and V_{water} as features. The error rates specific to the bubble and annular flows remained at 0 %.

Results from both QDA feature groups 1 and 2 of tables 11 and 12 respectively, show similar average error rates of 7.62 %. However, performance varied specific to each flow regime. QDA feature group 1 , showed error rates for the bubble flow regime at 13.33%, 8.20 % for the slug flow , 5.26 % for the churn and 0 % for the annular flows. QDA feature group 2 shows 0 % error rates for bubble, churn and annular flow, with a 13.33 % error rate for the slug flow regime.

It can be concluded that most of the error rates of misclassification are due to the proximity of data points to flow regime transition boundaries. For instance, the structural similarity of unstable elongated bubbles (labelled as slug flow) with the commencement of their collapse (labelled as churn flow) provides almost similar feature combinations. The similarities then lead to almost equal Mahal Nobis distances from the grouped means of each flow regime. This ultimately leads to equal posterior probabilities hence the misclassification.

Table 5.6**.** Confusion matrix for the LDA feature group 1

Observed group	**Predicted group**				
	bubble	slug	churn	annular	*Total
bubble	**15** **100.00%**	0 0.00%	0 0.00%	0 0.00%	15 100.00%
slug	4 6.56%	**51** **83.61%**	6 9.84%	0 0.00%	61 100.00%
churn	0 0.00%	4 21.05%	**15** **78.95%**	0 0.00%	19 100.00%
annular	0 0.00%	0 0.00%	0 0.00%	**10** **100.00%**	10 100.00%
Total	19 18.10%	55 52.38%	21 20.00%	10 9.52%	105 100.00%
e_j	**0.00%**	**16.39%**	**21.05%**	**0.00%**	**13.33%**
A_c	**100%**	**83.61%**	**78.95%**	**100%**	**86.67%**

Table 5.7.Confusion matrix for the LDA feature group 2

Observed group	**Predicted Group**				
	bubble	slug	churn	annular	Total
bubble	**15** **100.00%**	0 0.00%	0 0.00%	0 0.00%	15 100.00%
slug	3 4.92%	**55** **90.16%**	3 4.92%	0 0.00%	61 100.00%
churn	0 0.00%	1 5.26%	**18** **94.74%**	0 0.00%	19 100.00%
annular	0 0.00%	0 0.00%	0 0.00%	**10** **100.00%**	10 100.00%
Total	18 17.14%	56 53.33%	21 20.0%	10 9.52%	105 100.00%
e_j	**0.00%**	**9.84%**	**5.26%**	**0.00%**	**6.67%**
A_c	**100%**	**90.16%**	**94.74%**	**100%**	**93.33%**

Table 5.8.Confusion matrix table for the QDA feature group 1

Observed group	**Predicted group**				
	bubble	slug	churn	annular	Total
bubble	**13**	2	0	0	15
	86.67%	13.33%	0.00%	0.00%	100.00%
slug	2	**56**	3	0	61
	3.28%	**91.80%**	4.92%	0.00%	100.00%
churn	0	1	**18**	0	19
	0.00%	5.26%	**94.74%**	0.00%	100.00%
annular	0	0	0	**10**	10
	0.00%	0.00%	0.00%	**100.00%**	100.00%
Total	15	59	21	10	105
	14.29%	56.19%	20.00%	9.52%	100.00%
e_j	**13.33%**	**8.20%**	**5.26%**	**0.00%**	**7.62%**
A_c	**86.67%**	**91.8%**	**94.74%**	**100%**	**92.38%**

Table 5.9.Confusion matrix for the QDA feature group 2

Observed group	**Predicted group**				
	bubble	slug	churn	annular	*Total
bubble	**15**	0	0	0	15
	100.00%	0.00%	0.00%	0.00%	100.00%
slug	3	**53**	5	0	61
	4.92%	**86.89%**	8.20%	0.00%	100.00%
churn	0	0	**19**	0	19
	0.00%	0.00%	**100.00%**	0.00%	100.00%
annular	0	0	0	**10**	10
	0.00%	0.00%	0.00%	**100.00%**	100.00%
Total	18	53	24	10	105
	17.14%	50.48%	22.86%	9.52%	100.00%
e_j	**0.00%**	**13.11%**	**0.00%**	**0.00%**	**7.62%**
A_c	**100%**	**86.67%**	**100%**	**100%**	**92.38%**

According to the classification accuracy specific to each flow regime for the training data, the QDA feature group 2 is chosen as the best performing case at 92.38% and significant error rate of misclassifying only the slug flow regime at 13.11 %. According to the average accuracy of classification the LDA feature group 2 is chosen as the best performing model. With an average classification accuracy of 93.38 %. Although, its error rate of misclassification of the slug and churn flow regimes at 9.84 % and 5.26 % respectively remains a significant downside. Depending on the degree of accuracy required in characterizing multiphase flows, the LDA and QDA feature groups 2 can be recommended. More so, a test performance of each case is required to solidify this claim. Overall, general training performances of the DA cases were adequate and in an acceptable range compared to other investigations (Ameel *et al.,* 2012; Tharwat, 2016; Tharwat *et al.*, 2017; Yanjun, 2015).

DA Test performance

Validation of the trained DA cases was carried out using the test data summarized in table 4. Figure 5.12 (a-d) presents results of the computed posterior probabilities of each observation from the training data set.

The LDA feature group 1 case (figure 5.12 (a)) indicates acceptable separation across all assigned flow regimes, though variations in the posterior probabilities between the assigned churn flow and slug flow exist, for the data range 21-30. The LDA feature group 2 (figure 5.12 (b)) shows improvement of the separation as expected, following the inclusion of non-redundant features as discussed earlier in section 5.3.3.

Figure 5.12 (c) of the QDA feature group 1 case, gives superior separation for all assigned flow regimes. For the assigned annular flow data range of 31 – 40 in figure 5.12 (d), the QDA feature group 2 misclassified three (3) flow conditions as slug flow regimes. Among the misclassified points are two slug flow predictions which are equiprobable with the annular flow. This equiprobable situation infers the existence of a transition from slug to annular flow which, is not in accordance with the physics of flow regime development for the vertical upward flow. Therefore, it is evident that the QDA feature groups 2 has been overfitted with the training data since it fails to explain the physics of GLF development. Over fitting of the training data was initiated by the inclusion of the percentage counts of V_{air} and V_{water} as features.

Wu *et al.,* (1996) observed similar results and alluded to the fact that quadratic functions tended to reduce bias of fit and hence increase variance of prediction for a test condition. The included features can be described as redundant in this case, since their inclusion created a degradation in classification potential of the QDA feature group 2.The potential of linear functions to handle variations in test data given a tradeoff between bias and variance, explains the improved separation of the LDA feature group 2 (figure 5.12 (b)) compared to the QDA feature group 2 (figure 5.12 (d)). Therefore, the LDA affords the flexibility to better predict variations due to a new data set. In effect, increasing the number of relevant features as input to the LDA provides a better fit for both training and test variations. A careful selection of features for the QDA is also necessary, which focuses on optimizing the bias to variance tradeoff.

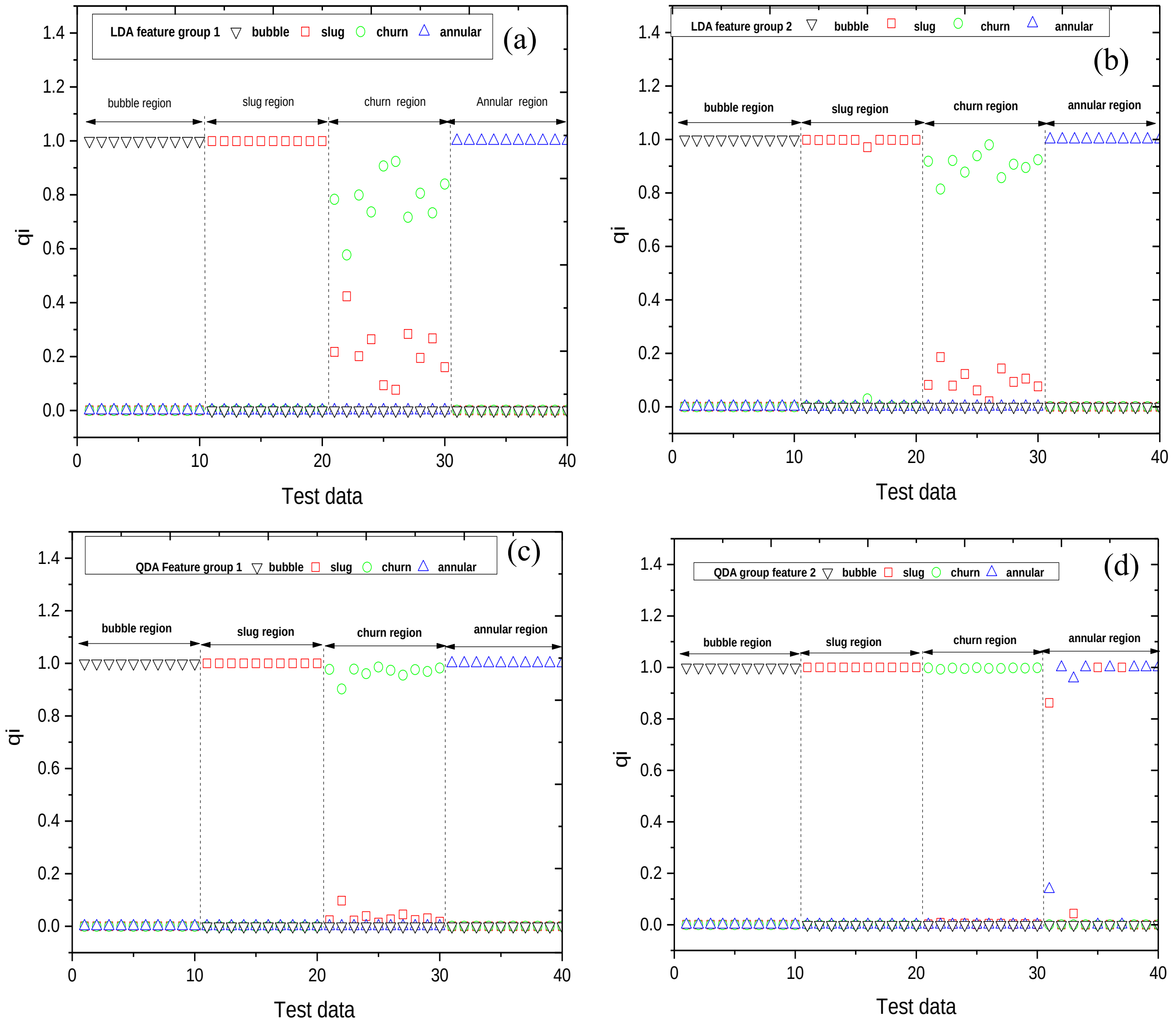

Figure 5.12: Computed posterior probabilities for classification of test data for (a) LDA feature group 1 (b) LDA feature group 1 (c) QDA feature group 1 (d) QDA feature group 2

The classification accuracies for three cases of the DA performed at 100 % accuracy i.e. all 40 test conditions were correctly identified with no associated error rates. An exception was the QDA feature group 2 case, with an accuracy of 92.5 %. This was due to misclassification of the assigned annular flow predicted as slug flow regimes. In summary, the probabilistic approach of the DA has been applied to flow regime identification for gas liquid. The computed posterior probability provides both discrimination of the data and provided understanding of the quality of fit of the LDA and QDA.

Comparison of regression and DA model performances

The classification accuracies of the polynomial regression and DA models are summarized in table 13. The polynomial regression model performed at 97.5% accuracy with a misclassification of one test condition. All the DA cases performed at a 100 % accuracy, except for the QDA feature group 2 performing at 92.5 % due over fitting by redundant features. The resolution of the 1480 nm NIOIRS response aided the selection of a maximum of 4 features ($\bar{V}_{obs}$, σ_{sensor}, %, V_{water} *and %* V_{air}*)* which was sufficient for the analysis, hence eliminating the need for further feature extraction methods.

Table 5.10.A comparison of percentage classification accuracy of the test data for the polynomial model, LDA and QDA

Flow regime	Polynomial Regression Model	LDA feature group 1	LDA feature group 2	QDA feature group 1	QDA feature group 2
Bubble	100%	100%	100%	100%	100%
Slug	100%	100%	100%	100%	100%
Churn	90%	100%	100%	100%	100%
Annular	100%	100%	100%	100%	70%
A_C	**97.5%**	**100%**	**100%**	**100%**	**92.5%**

5.4. Real time application

Given the fact that the observed sensor response V_{obs} (t) is within the limits of the air - water interfacial response, V_{int} and response to air V_{air} , the derived models are expected to handle an interpolation rather than extrapolation problem. So far, the models were tested under static conditions. i.e. the data sets were acquired from the 1480 nm NIOIRS and analyzed offline. The feasibility of each model for real time applications, can be considered under the following criteria:

i. expected time of computation
ii. knowledge of the priori probabilities, πj of each flow regime group

The computational time required by the regression model is expected to be fast and require less computing memory, since there is a 1-1 feature input and prediction (see equations 23). However, the DA groups require a matrix computation according to the number of features to determine the posterior probabilities for each flow condition for flow regime prediction. More so, the QDA has more terms to compute such as the covariances of each group S_j and the Mahala Nobis distances, hence becoming a limitation in meeting the time scales. Other variants of the LDA, can be used to transform the matrix computation into a linear combination of linear discriminant coefficients and selected features as variable inputs. The result of the transformation is similar to the Fisher discriminant functions as applied by (Li *et al.*, 2016)

Albeit the prescribed suitability of the LDA, a key setback in using the DA models is the inability to apply the correct prior probability , πj, for each flow regime given that the data streams are unassigned . Tharwat, (2016), investigated the effect of varying πj, for the LDA given a set of data with different πjs. They observed that the change in slope of each discriminant function was insignificant when they assumed equal πj. However, the derived biases were greatly deviant from the expected, which induced erroneous results in classification. In effect, the regression model is thus considered for real time application as a result of meeting the prescribed conditions.

5.4.1. Real time set up and conditions

An attempt to implement the regression model for real time flow regime identification was carried out. The real time identification involves the continuous processing of a moving length of the sensor response in voltage over time (Nsefik et al, 2019). In order to implement the real time identification process, LabVIEW (from national instruments) was linked to the oscilloscope using an allocated fast streaming template in the software development kit (SDK) from Pico scope. This enabled the live stream of data from the 1480 nm NIOIRS captured by the oscilloscope to be visualized in the LabVIEW environment on the computer. At a constant liquid rate and increasing gas rates, six (6) flow conditions (figure 5.13) were run using the flow rig. The flow conditions were specifically chosen to close to the flow regime boundaries or transitions to test the robustness of the regression model. The flow map adapted from Wu *et al.*, (2017) in figure 5.13 indicates the expected flow regime of each chosen flow condition.

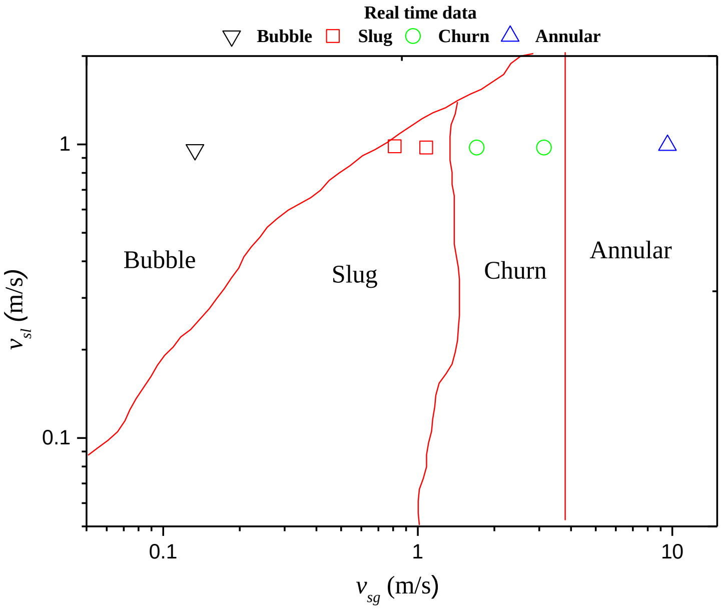

Figure 5.13: Summary of the six (6) real time flow conditions superposed on the composite flow map adapted from (Wu *et al.*, 2017).

5.4.2. The implemented algorithm

The implemented algorithm is shown in figure 5.14. At each streaming flow condition, the sensor response is captured at 300 Hz over the period of testing. The algorithm is implemented after a time delay of 10 seconds which was sufficient to identify stable flow regimes based on the static test results. The average sensor response $\bar{V}_{obs}$, (using equation 5.14) and sensor standard deviation σ_{sensor} (using equation 5.15) are then computed from the sensor response. The average sensor response is inputted into the regression model (equation 5.17), to compute the predicted standard deviation, $\sigma_{predict}$.

According to static test results, an error threshold of +/-7 % between the predicted and sensor standard deviations was chosen to cross validate the model i.e. to account for variations between the predicted standard deviation and the actual sensor standard deviation. Within this threshold, the regression model prediction is assumed to be valid and hence used to identify the prevailing flow regimes within the time frame, using table 7. However, if the error threshold is exceeded, the model is recommended for a review using an indicator tool in LabVIEW. The results of the identified flow regimes were visualized using indicators allocated by appropriate Booleans and later compared with the composite flow map and photos. Figure 5.15 shows the block diagram of the implemented algorithm in LabVIEW.

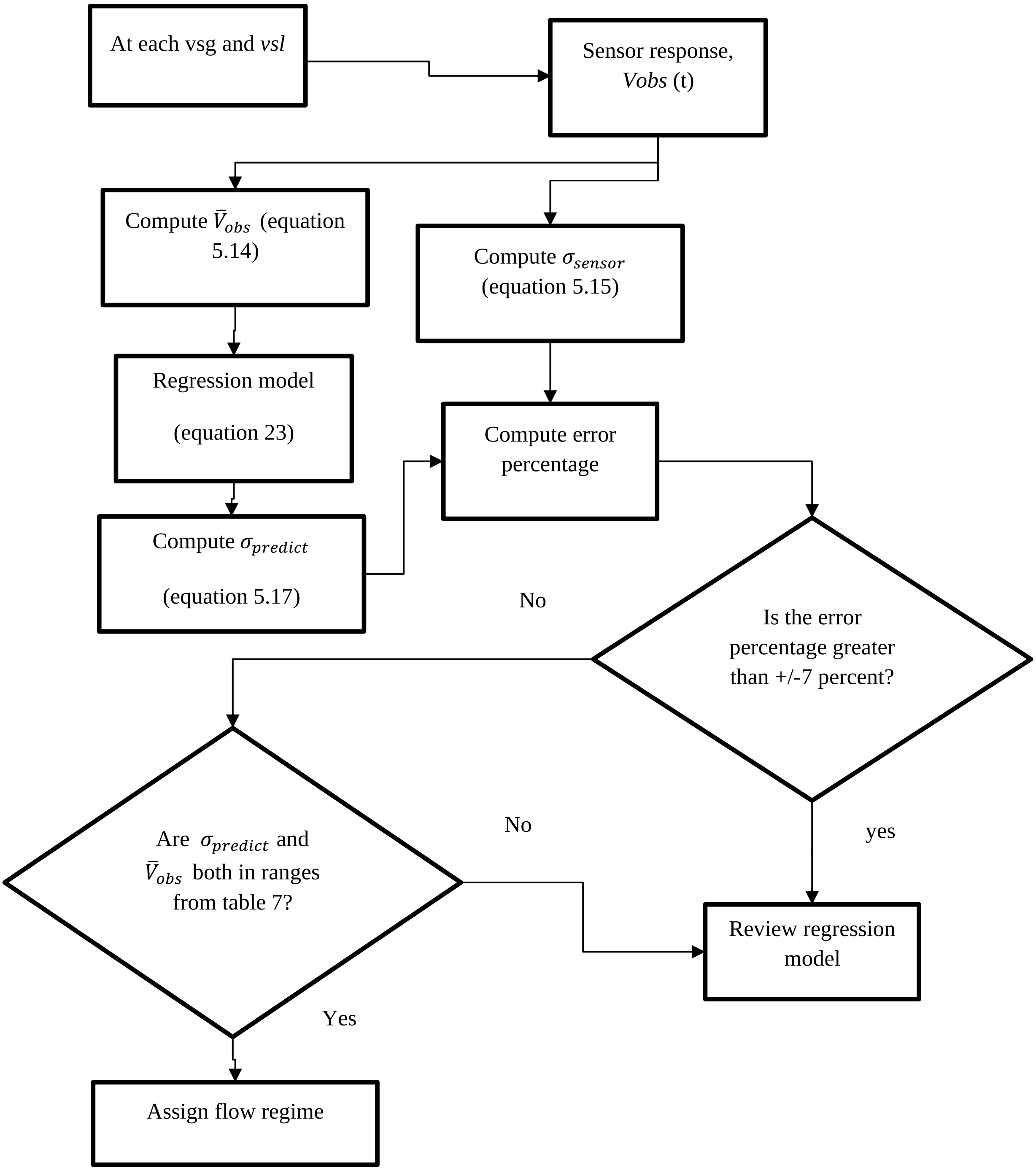

Figure 5.14: Flow chart of the Implemented algorithm in LabVIEW for the real time capture of processing of 10 seconds of streaming data (sensor response)

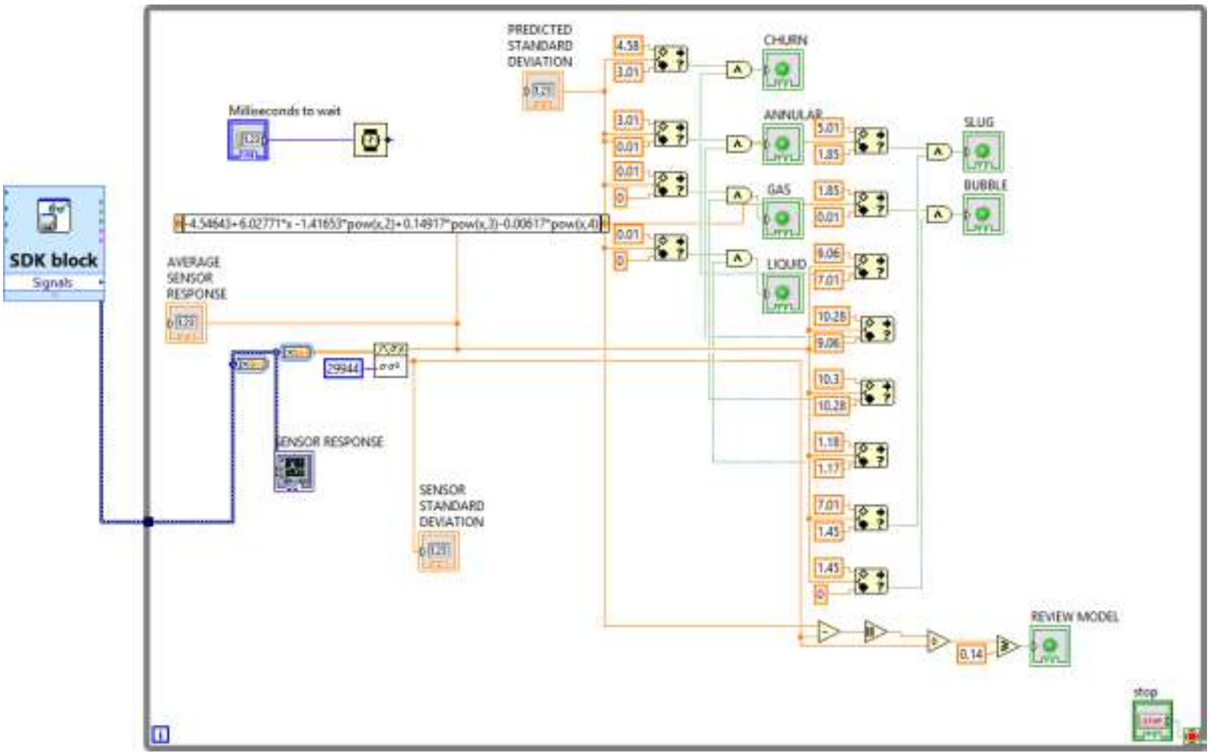

```
-4.54643+6.02771*x -1.41653*pow(x,2)+0.14917*pow(x,3)-0.00617*pow(x,4)
```

Figure 5.15: The block diagram showing the implemented algorithm in LabVIEW, with data received from the SDK block

5.4.3. Real time results

The results using the regression model showed excellent response to the prevailing flow regimes in the pipe for all 6 flow conditions, hence a 100 % accuracy. Figure 5.16 (a- d) presents results from the front panel user interface, showing the identified flow regimes of the four flow regimes, computed average responses, predicted and computed standard deviations for corresponding flow conditions over the 10 seconds capture. The prediction of the standard deviation was observed to be within the threshold of +/- 7 %, except for the bubble flow at around 40 % and the annular that came to close to 6.7 %. There was however no review prompt, at these flow regimes since the average sensor response was used as the sole features in the identification process. Table 5.11 summarizes the real time results.

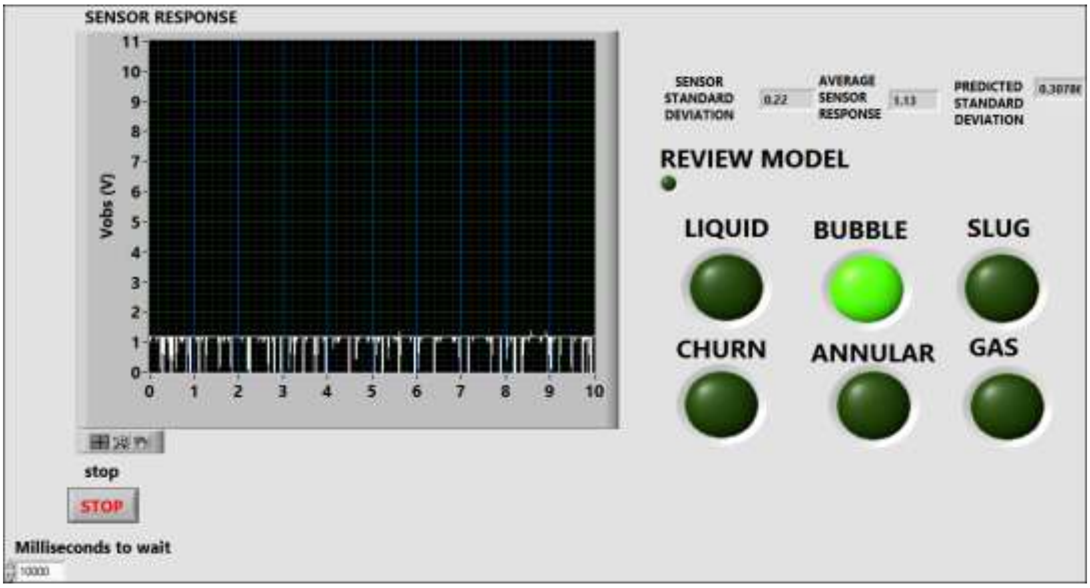

SENSOR STANDARD DEVIATION 0.22

AVERAGE SENSOR RESPONSE 1.13

PREDICTED STANDARD DEVIATION 0.3078

Milliseconds to wait 10000

(a)

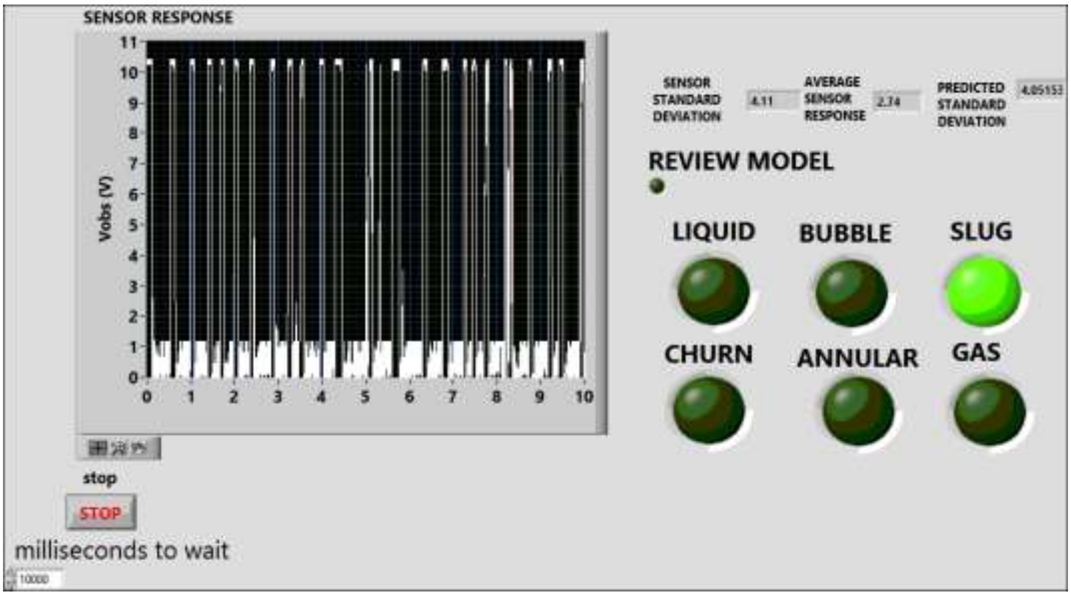

SENSOR STANDARD DEVIATION 4.11

AVERAGE SENSOR RESPONSE 2.74

PREDICTED STANDARD DEVIATION 4.05153

milliseconds to wait 10000

(b)

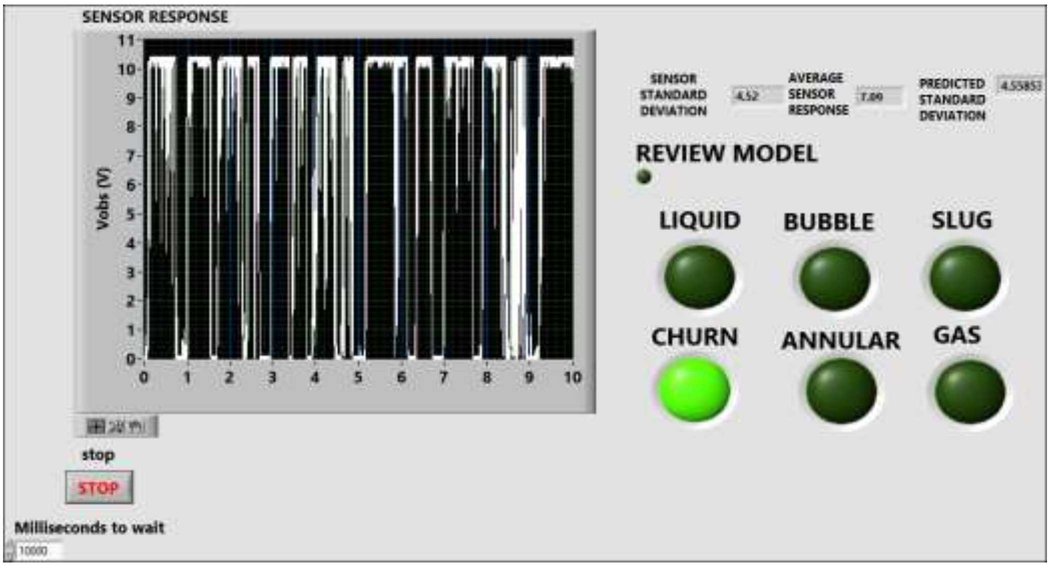

SENSOR STANDARD DEVIATION 4.52
AVERAGE SENSOR RESPONSE 7.09
PREDICTED STANDARD DEVIATION 4.55853
Milliseconds to wait 10000

(c)

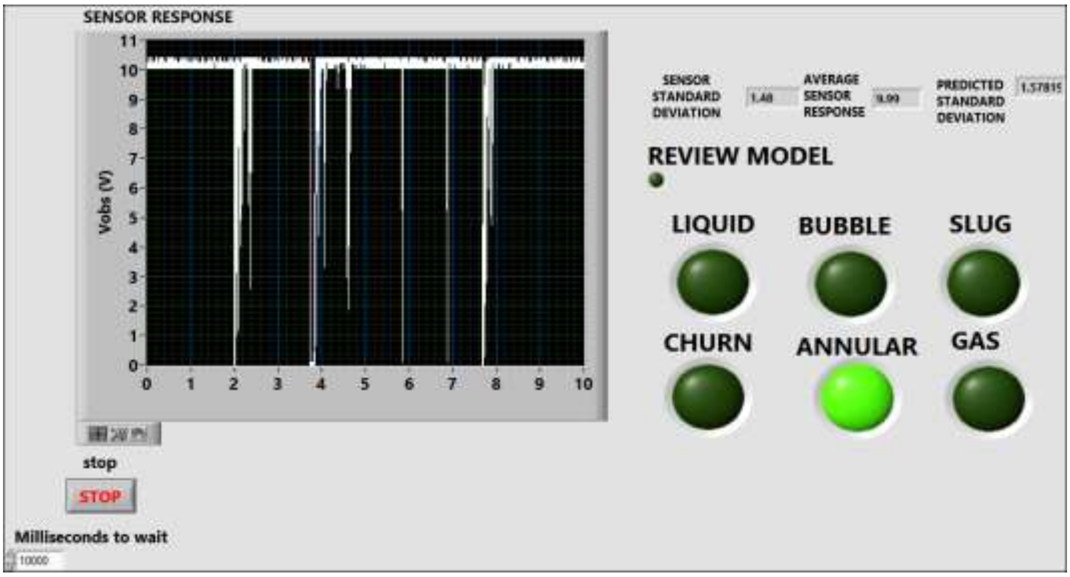

SENSOR STANDARD DEVIATION 1.48
AVERAGE SENSOR RESPONSE 9.99
PREDICTED STANDARD DEVIATION 1.5781
Milliseconds to wait 10000

(d)

Figure 5.16 : Designed front panel of the LabVIEW environment, showing the captured sensor response, computed average sensor response, predicted standard deviation, computed sensor standard deviation and prediction of (a) bubble flow condition at v_{sl} = 0.98 m/s and v_{sg} = 0.14 m/s (b) slug flow condition at v_{sl} = 0.98 m/s and vsg = 0.7 m/s (c) churn flow condition at vsl = 0.98 m/s and v_{sg} = 1.53 m/s (d) annular flow condition at vsl = 0.98 m/s and vsg = 10 m/s

Table 5.11. Summary of real time results of the regression model

v_{sl} (m/s)	v_{sg} (m/s)	V_{obs} (V)	σ_{sensor} (V)	$\sigma_{predicted}$ (V)	error (%)	Assigned	Predicted
0.98	0.14	1.13	0.22	0.31	0.409091	bubble	bubble
0.98	0.7	2.74	4.11	4.05	-0.0146	slug	slug
0.98	1.00	4.65	4.42	4.46	0.00905	slug	slug
0.98	1.53	7.09	4.52	4.56	0.00885	churn	churn
0.98	3.10	8.06	3.55	3.53	-0.00563	churn	churn
0.98	10.0	9.99	1.48	1.58	0.067568	annular	annular

At the end of the investigation, the aim of the combining NIOIRS response with signal analysis via regression and probabilistic discriminant analysis has been achieved to improve identification of gas liquid flow regimes under static conditions. The sensor response has afforded the use of regression analysis to provide adequate results. Moreover, the poor prediction of the standard deviation around the bubble and annular flow did not affect the identification accuracy of the regression model.

A cross validation of the regression model for static conditions could be carried out using the discriminant methods given the fact that the test performances of the DA analysis (LDA group 1 and 2 and QDA group 1) gave 100 % accuracy in predicting the bubble and annular flows. In the real time application, the regression model was suitable with excellent results. Changes to the flow configuration such as the pipe diameter, fluid properties and pipe orientation may yield unreliable results of the derived models and would require a review of the model. However, the methods applied remain unchanged. It is also interesting to note that the need for several features in the analysis of the DA is not necessary as the sufficiency of a maximum of 4 features has proven valid in the flow regime identification process.

5.5. Summary

The identification of flow regimes based on the visual inspection of the acquired sensor response was discussed with the existing limitations on identifying flow regimes beyond the slug flow regime. Feature extraction was then performed using statistical analysis of the sensor response acquired over 145 flow conditions, with adequate selection of relevant features based on respective variations over gas fractions. The relevant features which include, the average sensor response $\bar{V}_{obs}$, sensor standard deviation σ_{sensor} and calibrated percentage counts of water and air %, V_{water} *and %* V_{air} respectively were categorized into two feature groups. The average sensor response and standard deviation (both in feature group 1) proved to suffice as independent and dependent variables respectively, for the objective identification process via a fitted polynomial regression model in orders of 4.

Two feature groups were considered in training the linear and quadratic discrimination methods, with improvement in training performance of QDA over the LDA due to disparity in the covariance matrix computed from the same data set. Results were expressed as posterior probabilities, which gave more detail about the likelihood of each model to discriminate flow regimes. The test performance of the polynomial regression fit was comparable with the DA methods with an accuracy rate of 97.5 %, compared to the DA groups performing at 100 % accuracy of classification except for the QDA feature group 2 with accuracy of 92.5 %. This performance was due to an over fitting problem. Furthermore, real time results using the regression model surprisingly gave a 100 % classification accuracy for new test data. The results of this work have shown that the analysis of the non-intrusive optical sensor response combined with supervised learning approach can provide accurate identification of flow regimes and proven useful for multiphase flow studies.

In future studies, the derived polynomial regression model can be used in a real time application to allocate valid phase fraction models required ultimately for phase flow rate measurement. LDA can be extended to real time monitoring using the coefficients of a canonical analysis and FDA. The performance of combining the 1480 nm NIOIRS with unsupervised learning for flow regime identification is also worth considering.

Chapter 6

6. Measurement of Phase Fraction and Structural characteristics

6.1. Introduction

This chapter presents results of the specific objective of phase fraction measurement and other structural characteristics for an upward flow of air and water, via the 1480 nm NIOIRS, using the main flow rig setup. Figure 6.1 presents a flow chart that summarizes two sections (a) and (b) that were investigated. Section (a), summarizes the development of the phase fraction model with validation from experimental methods which includes, photography and swell level change methods. Further comparisons with existing correlations (Homogenous, Drift flux and Armard model) and other sensors (the 880 nm NIOIRS from and pressure sensor technique) were performed. Section (b) focuses on the extraction of structural flow characteristics from the validated temporal void fraction response α(t), of the 1480 nm optical sensor, with capabilities of a real time application using adequate statistical and signal processing methods. A cross validation of the analysis of results is also discussed.

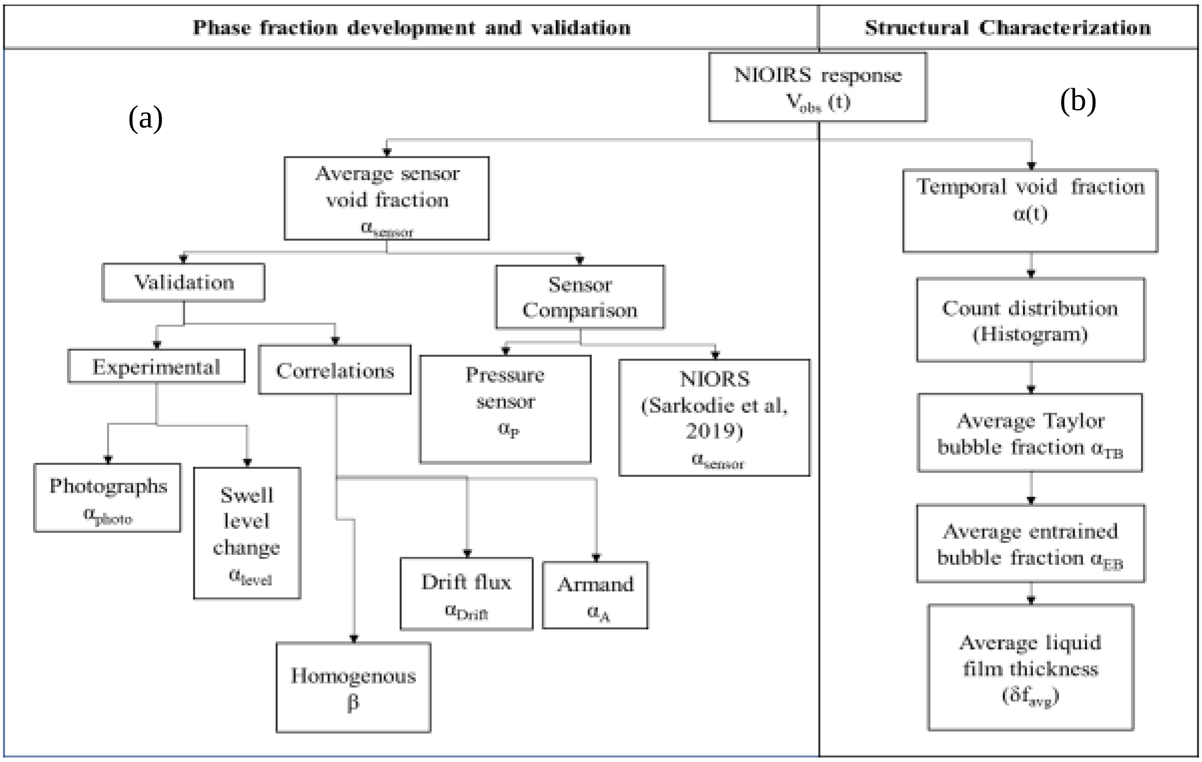

Figure 6.1: A flow chart showing a summary of the two sections of considered in this chapter. phase fraction determination and validation methods

6.2. Phase fraction determination

This section presents the analysis of the sensor response, V_{obs} *(t)* for measuring local or temporal and average phase fractions over varied flow rates of water and air (conditions presented in chapter 3). The time dependence of flow stability relative to the observed flow regimes as investigated in chapter 4, is considered in this chapter for the 1480 nm sensor. The effect of superficial gas velocities on the average void fraction is also discussed with comparative results.

6.2.1. The phase fraction model

It is already known that NIOIRS is sensitive to bubble shape and sizes, however it is important to understand the threshold response for specific categories of bubble sizes; in developing valid phase fraction models. Figures 6.2 (a), (b) and (c) present results of the sensor response V_{obs}, in the presence of varied bubble sizes and shapes. Figure 6.2 (a) shows a typical sensor response of two ellipsoidal bubbles with an equivalent diameter (validated from photos) of 9 mm and 8 mm respectively. The dominance of light scattering by the bubble noses and tails is evident (in figure 6.2 (a)) given the observed attenuation of the sensor response over their residence times Δt_{res}.

The corresponding drop in response increases with bubble size as observed at t = 5.465s (9 mm bubble) and 5.485 s (8 mm bubble) due to the lensing effect as earlier highlighted in chapter 5. This scattering effect was observed for small bubbles less than 9 mm, where attenuation varied between the V_{water} and V_{int} responses. Figure 6.2 (b) presents a typical sensor response of a bubble cap formed from ellipsoidal bubble clusters. The effect of the cap nose and tail led to attenuation of the response to V_{int} due to interfacial scattering effects. A response peak greater the V_{water} observed as V_{obs} = 3V indicates the transmission of light (refraction) through the cap body.

Taylor bubbles (i.e. greater than 0.35D) as captured in figure 6.2(c) show a longer residence time Δt_{res}, compared to responses of figure 6.2(a) and (b). Response attenuation from V_{water} *t*o V_{air} response infers an increase in bubble diameter close to the pipe internal diameter. The effect of the liquid film around the Taylor bubble indicates responses close to V_{air} response. This further indicates the sensitivity of the optical sensor to the liquid film given the fact that emitted light travel through the liquid layer of thickness, the bubble cross section, liquid film again and finally approaches the photodiodes. A similar interfacial effect due to the bubble nose and tail is observed as a V_{int} response. The entrained bubble also captured which is characterized by a similar response as the small bubbles in figure 6.2 (a).

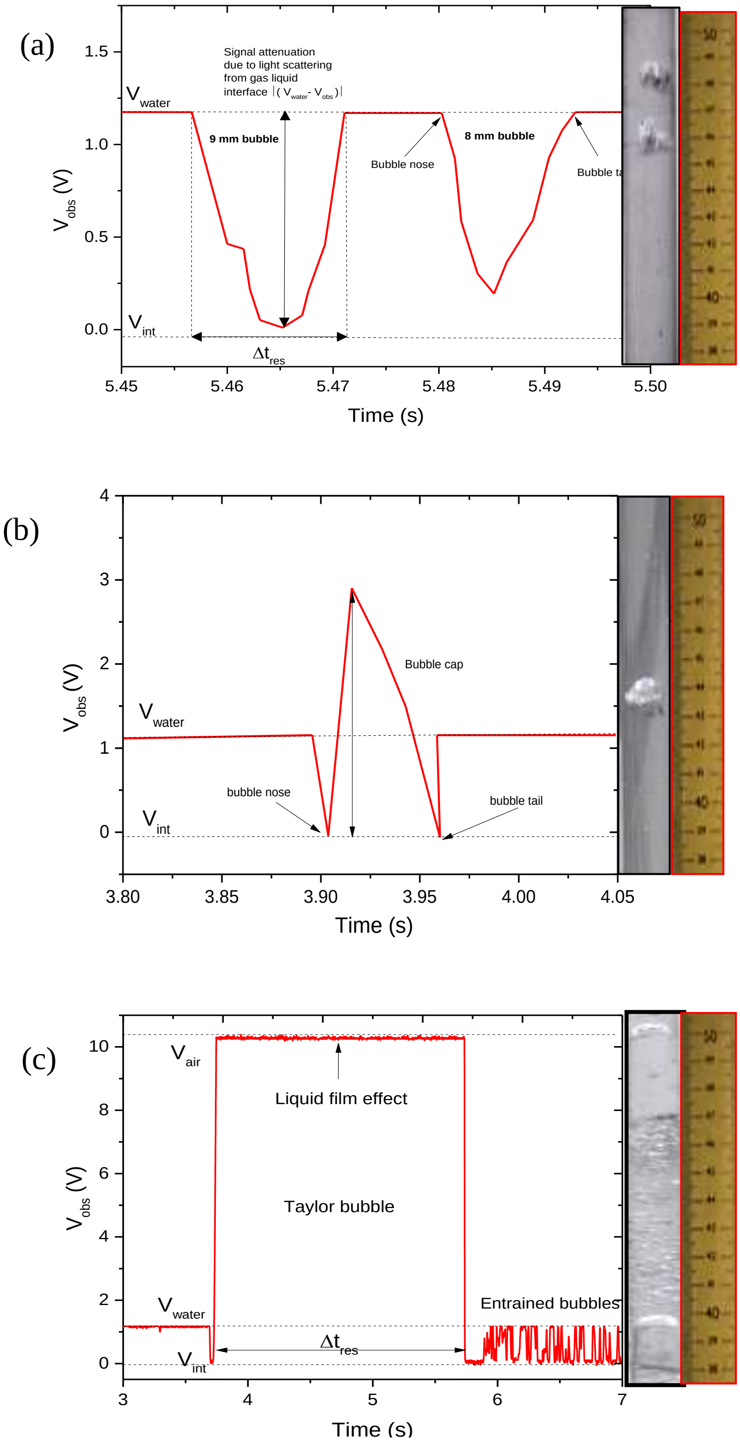

Figure 6.2: Typical variations in sensor response and residence times due to the effect of (a) 9 mm and 8 mm ellipsoidal bubbles (b) a bubble cap, and (c) Taylor bubble.

(*Note that there is an enlargement of the traces presented in figure 6.2 (a) and (b), so as to aide clarity in the variations of sensor response*)

It follows that at $V_{obs}(t) = V_{water}$ and $V_{obs}(t) = V_{air}$ the void fractions are set as 0 and 1 respectively. For the sensor response range, $V_{int} < V_{obs}(t) < V_{air}$, a linear interpolation of the calibrated sensor responses is proposed to determine phase fraction between 0 and 1. However, based on the variations in sensor response to bubble sizes discussed above, two interpolation models were required to account for small spherical and ellipsoidal bubbles that correspond to $V_{int} \leq V_{obs}(t) \leq V_{water}$ and larger bubbles (bubble caps and Taylor bubbles), that correspond to $V_{water} \leq V_{obs}(t) \leq V_{air}$.

Model 1 ($V_{int} \leq V_{obs}(t) \leq V_{water}$)

According to photographic evidence, bubble sizes up to 9.5 mm in equivalent diameter led to a maximum attenuation between the response range, $V_{int} \leq V_{obs}$ (t) $\leq V_{water}$. This corresponds to a cross sectional void fraction of 12 % based on the bubble diameter and internal diameter of the test section. Therefore, the presence of bubbles of less than 0.35 D, led to increases in sensor response attenuation in proportion to the cross-sectional variation in bubble size captured in the sensing area. This bubble size criteria also agrees with the analytical model described by The bubble model can then be derived as the temporal void fraction, $\alpha_g(t)$ for, $V_{int} \leq V_{obs}(t) \leq V_{water}$, expressed in equation 6.1,

$$\alpha_g(t) = \left(1 - \left(\frac{V_{obs}(t) - V_{int}}{V_{water} - V_{int}}\right)\right) . \left(\frac{V_{water} - V_{int}}{V_{air} - V_{int}}\right) \tag{6.1}$$

The model computes for a maximum $\alpha(t) =$ 12 % which corresponds to the bubble diameter that creates a V_{int} response.

Where $\left(1 - \left(\frac{V_{obs}(t) - V_{int}}{V_{water} - V_{int}}\right)\right)$ is the void fraction scaled using the expression, $\left(\frac{V_{water} - V_{int}}{V_{air} - V_{int}}\right)$ that adjusts for the fraction of the overall sensor response. Further Simplification of the equation gives the final model in expressed by equation 6.2,

$$\alpha_g(t) = \left(\frac{V_{water} - V_{obs}(t)}{V_{air} - V_{int}}\right) \tag{6.2}$$

Including the temporal liquid hold up $\alpha_l(t)$ computed by equation 6.3;

$$\alpha_l(t) = 1 - \left(\frac{V_{water} - V_{obs}(t)}{V_{air} - V_{int}}\right) \tag{6.3}$$

Model 2 ($\boldsymbol{V_{water} \leq V_{obs}(t) \leq V_{air}}$)

The presence of bubble sizes greater than *0.35D* corresponds to sensor responses in the range $V_{water} \leq V_{obs}(t) \leq V_{air}$. Therefore, the $\alpha_g(t)$ can be computed using equation 6.4,

$$\alpha_g(t) = \left(\frac{V_{obs}(t) - V_{water}}{V_{air} - V_{water}}\right).\left(\frac{V_{air} - V_{water}}{V_{air} - V_{int}}\right) \tag{6.4}$$

Equation 6.4, can then be simplified and can be expressed as in equation 6.5

$$\alpha_g(t) = \frac{V_{obs}(t) - V_{water}}{V_{air} - V_{int}} \tag{6.5}$$

The liquid fraction can also be written as in equation 6.6.

$$\alpha_l(t) = 1 - \frac{V_{obs}(t) - V_{water}}{V_{air} - V_{int}} \tag{6.6}$$

When $V_{obs}(t) < V_{water}$, corresponding to interfacial effect of Larger bubbles, equation 6.5 computes $\alpha_g(t) < 0$, which is invalid. To correct for this effect at the nose and tails of such bubbles, $\alpha_g(t)$ is set to zero. Table 6.1. Summarizes the local void and liquid fraction models based on the bubble size categories and related sensor ranges derived from the sensor.

Table 6.1. Summary of the local phase fraction model based on bubble sizes and corresponding sensor response ranges

Bubble size, D_b	Sensor range	Local void fraction, $\alpha_g(t)$	Local liquid fraction $\alpha_l(t)$
$D_b \le 0.35D$	$V_{int} \le V_{obs}(t) \le V_{water}$	$\frac{V_{water} - V_{obs}(t)}{V_{air} - V_{int}}$	$\alpha_l(t) = 1 - \alpha_g(t)$
$D_b > 0.35D$	$V_{water} \le V_{obs}(t) < V_{air}$	$\frac{V_{obs}(t) - V_{water}}{V_{air} - V_{int}}$	
	$V_{int} \le V_{obs}(t) \le V_{water}$	0	
	$V_{obs}(t) = V_{air}$	1	

The average sensor void fraction α_{sensor} can expressed based on the time average of the sensor response $\bar{V}_{obs}$, which can be substituted for the local response $V_{obs}(t)$ of each model. This is also equivalent to the time average of the local void fraction $\alpha_g(t)$ based on the number of samples captured n, (equation 6.7),

$$\alpha_{sensor} = \frac{1}{n}\sum \alpha_g(t) \tag{6.7}$$

6.2.2. Local void fraction

Figure 6.3(a) presents results of the sensor response for a Taylor and entrained bubbles with the corresponding local void fraction in figure 6.3(b), derived from the proposed phase fraction model (equation 6.5). The model corrected for the interfacial effect at the Taylor bubble nose and tail, where the V_{int} responses were set to a void fraction of zero. A maximum local void fraction around 88 % infers the presence of a liquid film around the Taylor bubble as observed in figure 6.3- (b). Moreover, the entrained bubbles fraction as a component of the void fraction is also computed according to equation 6.2, with a maximum void fraction approximately 12 %, indicating the presence of small bubbles. The results indicate an adequate execution of the proposed model fraction relative to the sensor response.

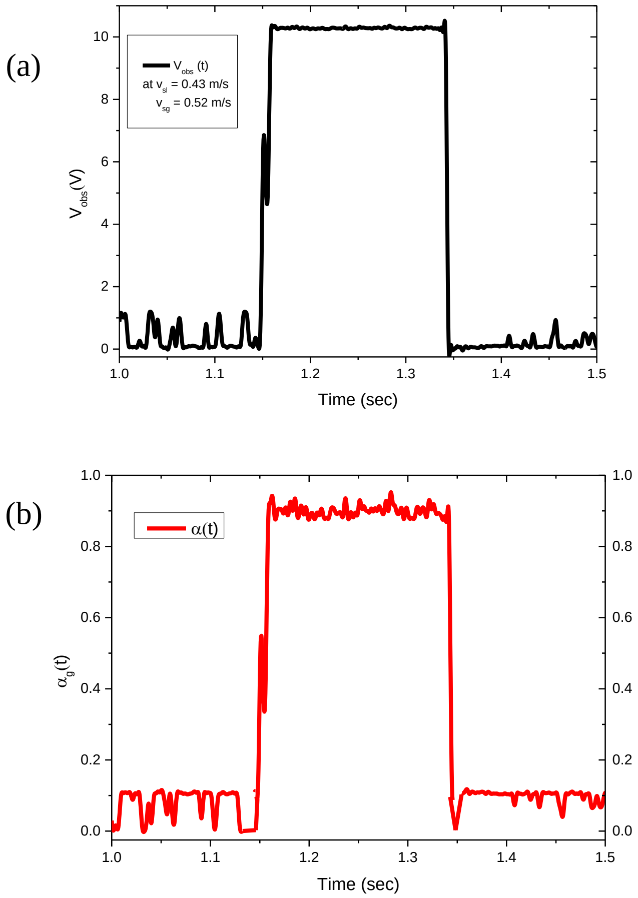

Figure 6.3 : Comparison between the (a) sensor response of a Taylor bubble and entrained bubbles and (b) temporal void fractions

6.2.3. Time dependent void fraction

Figure 6.4 presents the effect of integral times on the average void fraction (computed from equation 6.7). Void fraction was averaged over incremental times under a 2.5 s interval over period of 60 seconds under a constant liquid superficial velocity and varied gas superficial velocities. For the bubble flow condition, (v_{sl} = 0.47 m/s and v_{sg} =0.13 m/s), a stabilized averaged void fraction was reached at an integral time of 12.5 s, while average void fraction corresponding to a slug flow regime (v_{sl} = 0.47 m/s and v_{sg} = 0.52 m/s), stabilized at 22.5 seconds. The void fractions at the churn and annular flow conditions a fair stability at 35 and 30 s respectively.

According to results in figure 6.4, it can be inferred that the observed increases in integral time for void fractions stability under increasing gas fractions is related to the increases in structural lengths (i.e. bubbles lengths) for the bubble and slug flow conditions. Therefore, at lower gas fractions, the presence of smaller bubbles in the bubble flow regime approach shorter residence times which in turn leads to higher frequencies of intermittence, hence the earlier stabilization at 12.5 s, compared to the longer Taylor bubbles formed for the slug flow regimes. The integral time of 35 s for the annular flow condition was observed due to the persistence of the disturbance waves, which lead to increases in amplitudes created by the liquid film thickness. The longest integral time required for void fraction stability was observed for the churn flow condition given its unsteady nature and inconsistences in structural intermittence.

Understanding time scales may therefore aide the validation of volumetric void fraction studies. Furthermore, the integral time is useful in the execution of online measurement algorithms, given the variations in interpretation of flow regimes and phase fractions under varied time scales. The effect of pipe length and size on the flow stability is also worth a mention. An integral time of 5 s was reported by Sarkodie *et al.*(2019) (discussed in chapter 4) for a smaller pipe diameter of 0.018m and 1 m length. In comparison with the current study, it can be concluded that flow stability is reached earlier for smaller pipe sizes. It is important to note that the average void fraction used in the rest of this work is computed based on the stabilized integral times with respect to the flow regimes.

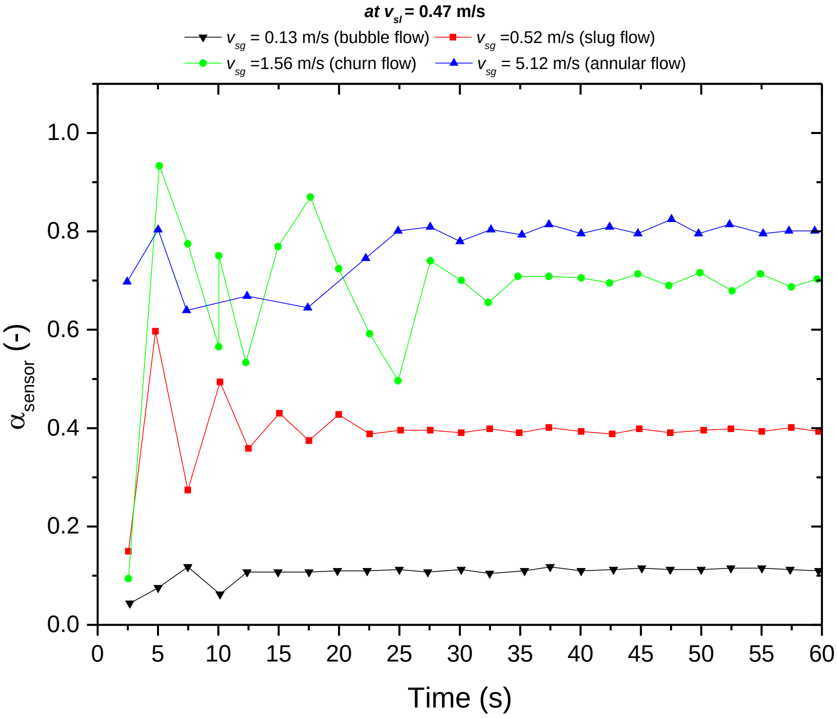

Figure 6.4: Effect of integral time measurements on the derived sensor average void fraction measured at constant vsl = 0.47 m/s and corresponding vsg = 0.13 m/s (bubble flow), 0.52 m/s (slug flow), 1.56 m/s (churn flow) and 5.12 m/s (annular flow).

6.2.4. Relationship between gas velocity and average void fraction

The relationship between gas velocities and the average void fraction is presented in figure 6.5, for constant superficial liquid velocities (0.11 m/s - 0.98m/s), and superficial gas velocities (0.13 m/s – 9.2 m/s). For increases in the superficial gas velocities, general increases were observed in the average void fraction as expected. However, variations in the rates of increase occurred due to flow regime transitions effects. For most of the superficial liquid velocities that correspond with 0.13 $m/s \leq v_{sg} \leq$ 1.25 m/s, a steep increase corresponding to $0 \geq \alpha_{sensor} \leq 0.72$, can be observed. This was due to increasing bubble lengths in the bubble and slug flow regimes. The slight decreases in average void fraction at $1.25 m/s \leq v_{sg} \leq 2 m/s$ were mainly due to the deformations of elongated Taylor bubbles in the slug flow regime which formed unstable slugs of a churn flow regime and ultimately causing a drop in the average void fraction. Beyond the churn flow regime, further increases in the superficial gas velocity $(2.0\, m/s \leq v_{sg} \leq 9.2\ m/s)$ follows a lower slope in the average void fraction corresponding to $0.53 \geq \alpha_{sensor} \leq 0.89$ due to the development of a steady gas core at the center of the pipe and variations in liquid film thickness for the annular flow regime.

Abdulkadir *et al.*, (2014) suggested in their work on air and silicone oil flow, that the relationship between the average void fraction and superficial gas velocity follows an exponential trend, given as $\alpha_{sensor} = Cv_{sg}^{x}$, where *x* describes the exponent that defines the linearity between the variables and C is the base parameter that defines the exponential increase. They highlighted that $x \approx 1$(linear relationship) for the bubble and slug flow condition and $x \approx 0.8$ (nonlinear relationship), for the churn and annular flow conditions. Similar trends can be deduced from the results of figure 6.5, however, the slight decrease in α_{sensor} related to the transition from slug to churn transition was not evident in the work of Abdulkadir *et al.*, (2014) due to the disparity in working fluid used (i.e.. density and viscosity).

Cioncolini and Thome, (2012) further described the relationship as growing and saturating, defined mathematically as $\frac{d\alpha_{sensor}}{dv_{sg}} > 0$ and $\frac{d^2\alpha_{sensor}}{dv_{sg}^2} < 0$ respectively. They proposed the Hill function, (Hill, 1910) as the fit model for the defined trend between the void fraction and gas mass fractions. Overall, figure 6.5 presents a similar trend which has been reported by investigators under varied flow configurations for air and water flow (see, Almabrok *et al.*, 2018; Azzopardi *et al.*, 2015; Omebere-Iyari and Azzopardi, 2007). The trend similarity provides an apparent validation of the derived phase fraction derived from the optical sensor in this work.

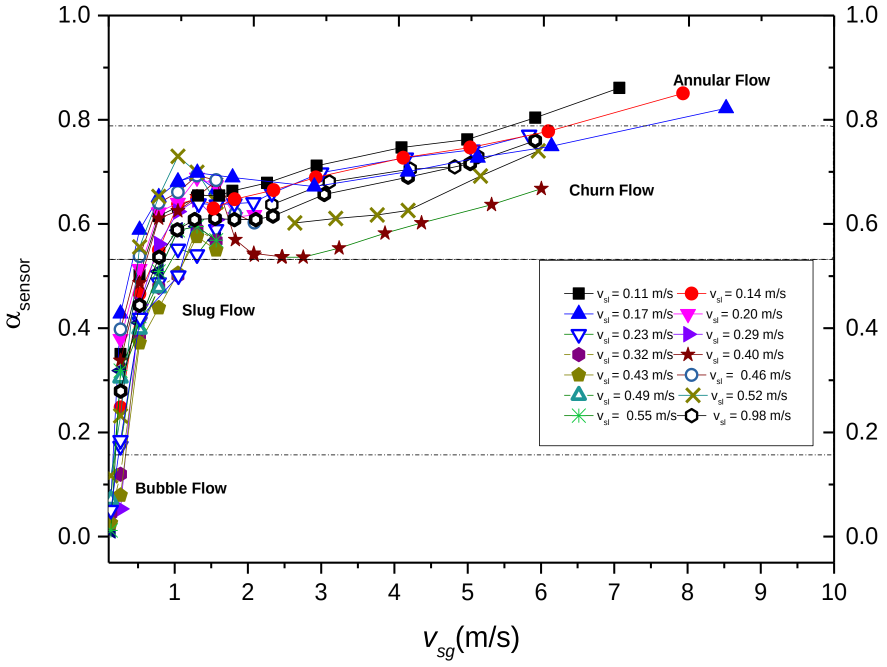

Figure 6.5: Relationship between the superficial gas velocities and the average sensor void fraction at constant liquid superficial velocities indicating flow regime zones (dashed lines) designated based on visual observations

6.3. Model validation

Results of the experimental validation of the derived sensor phase fraction model are discussed. These include validation from photography and the swell level change methods.

6.3.1. Photography

The average void fraction model of equation 6.7, $\alpha_{sensor,}$ was validated with the void fraction derived from photography α_{Photo} under similar flow conditions. As already described in chapter 3, the extraction of equivalent bubble size, Taylor bubble radius and lengths from photos were performed via image processing techniques to determine α_{Photo}. The parity plot in figure 6.6, presents an overall deviation of +/- 1.25 % of the maximum void fraction value of the $\alpha_{sensor,}$ relative to the $\alpha_{photo.}$ An underestimation of α_{photo} for most runs in the bubble flow regime is due to disparities in the bubble shapes during the sensing and image capture process. The distortion of rising bubbles creates irregular surfaces that scatter the emitted light and hence creates reductions in the instantaneous sensor response, $V_{obs}(t)$, and ultimately computes, lower values of the void fraction. Turbulence effects are responsible for these distortions thus creating a wobbling motion as described by Ziegenhein *et al.*, (2018)

The α_{sensor} at slug flow conditions show good agreement with the α_{Photo}. This was due to the stability of Taylor bubbles geometries within 25D lengths (stable Tyalor bubble lengths invesitgated by Batchelor, 1987). However, slight variations from parity occurred due to the presence of entrained bubbles in the wake of each Taylor bubble. A significant deviation from parity due to slug to churn flow transition and turbulence in the churn flow regimes can also be observed from the figure 6.6 at higher void fractions. This deviation significantly contributes to the overall deviation from parity. The annular flow conditions present a better agreement as compared to the churn flow regime, given the development of a defined gas core and liquid film thickness.

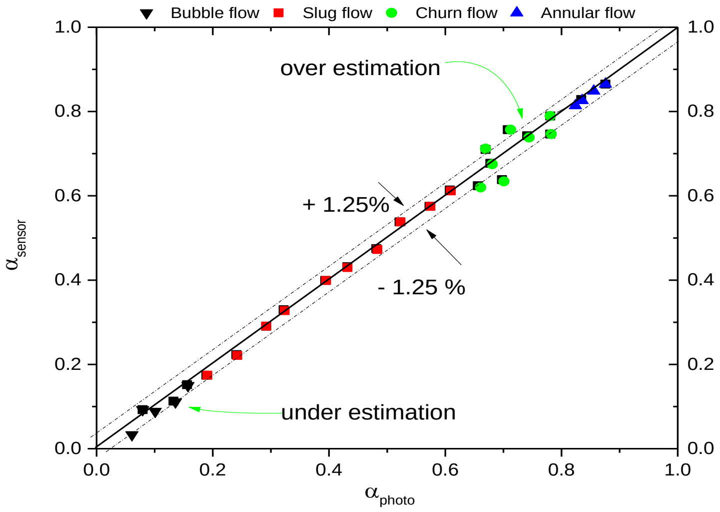

Figure 6.6: Validation of sensor average void fraction model (equation 6.7) from photography. A deviation from parity of +/- 1.25 % of void fraction for all flow regimes considered.

6.3.2. Swell level method

The swell level method was also used to validate the sensor average void fraction for conditions corresponding to the slug flow regime. The slug regime was considered solely because of the visibility of swell changes in the liquid level for bubble lengths greater than 1.5D. Figure 6.7 presents the results of the comparison showing a good agreement within a +/- 2 % deviation relative to the maximum measured void fraction. For 50 percent of the plotted data, there are higher values of the α_{sensor} compared to the swell level void fraction, α_{level}. This was due to the inclusion of void fraction of entrained bubbles in the wake of the rising Taylor bubbles captured by the sensor. Given the fact that a swell in the liquid level is dominated by the rise larger Taylor bubbles, the rising entrained bubbles did not provide significant contribution to the liquid swell effect, that could be measurable by the meter rule. None the less the overall accuracy of the void fraction measurements according to results has proven to be accurate for the flow conditions considered.

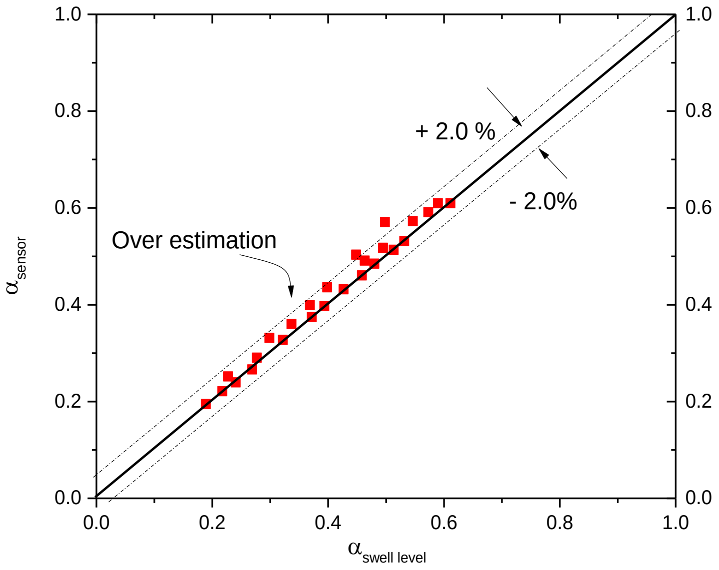

Figure 6.7: Comparison between the swell level change void fraction and sensor average void fraction for slug flow conditions showing a +/- 2% deviation.

6.4. Model comparisons

Based on the adequate validations of the phase fraction model, this section discusses results of the comparisons between the derived sensor phase fraction model with existing void fraction correlations and sensors. Comparisons were based on the average sensor response relationship, effect of gas velocity and error analysis relative to sensor void fraction. To ensure consistency of results, the sensor void fraction was time- averaged over 35 seconds according to results from figure 6.4.

6.4.1. Comparison with correlations

Average sensor response with void fraction

Figure 6.8 presents results of the correlation between the average sensor response, $\bar{V}_{obs}$ and void fractions derived from the sensor, α_{sensor} homogenous, β (equation 2.8), Drift flux, α_{Drift} (equation 2.20) and Armard correlations, α_A (equation 2.18) for the 145 flow conditions summarized in chapter 3. The regions of observed flow regimes are indicated by the dashed boxes which corresponds to the void fraction of each model. It is observed that for increases in $\bar{V}_{obs}$, all models show a general increase in void fraction as expected. This trend indicates a positive correlation between the $\bar{V}_{obs}$, and the void fraction a. However, deviations from the trend occur in the bubble flow and bubble cap dominated flows corresponding to $0.5\,V \leq \bar{V}_{obs} \leq 3.5V$. This deviation becomes less severe reaching the slug flow regime. Void fractions for all correlations also show an apparent flattening in the churn and annular flow regimes. This trend corresponds to the spatial distribution of the fluctuating liquid film and turbulence nature of gas core rising high velocities. It can also be pointed out that the homogenous model provides higher estimates of void fractions while the drift flux lower estimates of the void fraction relative to the sensor void fraction. Armads correlation which is 83% of the β, seems to be in closer agreement with the α_{sensor}.

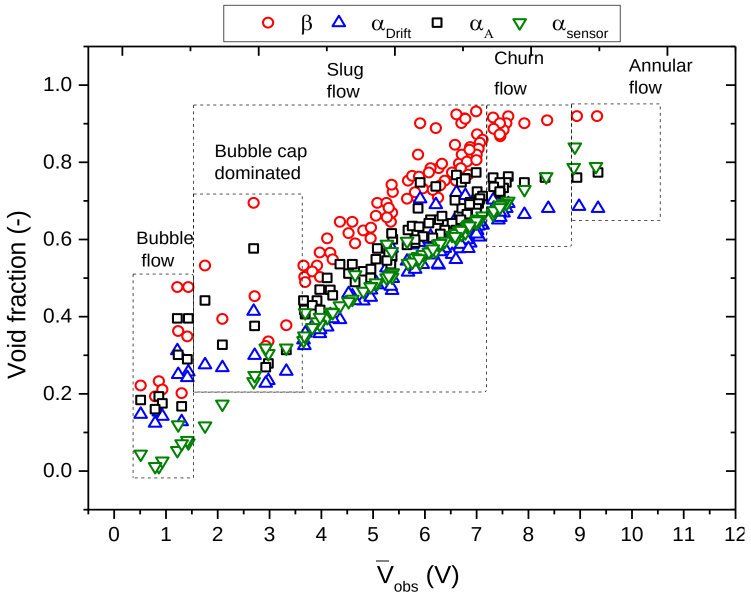

Figure 6.8: Relationship between the average sensor response and void fractions derived from the sensor, homogenous, Drift flux and Amard correlation

Comparison of the effect of gas velocities

Figure 6.9 - (a-d) present the comparison of the effect of gas superficial velocities (0.13m/s ≤ v_{sg} ≤ 1.60 m/s) at varied liquid superficial velocities (v_{sl} = 0.11 m/s, 0.22 m/s, 0.43 m/s and 0.55 m/s), on derived void fractions from the sensor, homogenous, Drift flux and Amard correlations. The results from figure 6.9 show that increases in v_{sg}, lead to increases in void fractions for all correlations, however growing, with a saturation trend observed for higher gas

velocities. Specifically, the β correlation obtained the highest estimates of void fractions relative to that of the sensor for all flow conditions considered. This was expected due to the no slip assumption. The Drift flux correlation on the other hand, includes the concept of a slip assumption , where the inclusion of respective C_o and v_{gu} parameters lowers the upper limit void fraction derived from the homogenous correlation (Cioncolini and Thome, 2012). These lower estimates for all cases in figure 6.9, is the reason for a better agreement with the sensor void fraction. The Armand correlation also agreed with the sensor void fraction for all cases, given the fact that it is defined as an 83% of the homogenous void fraction.

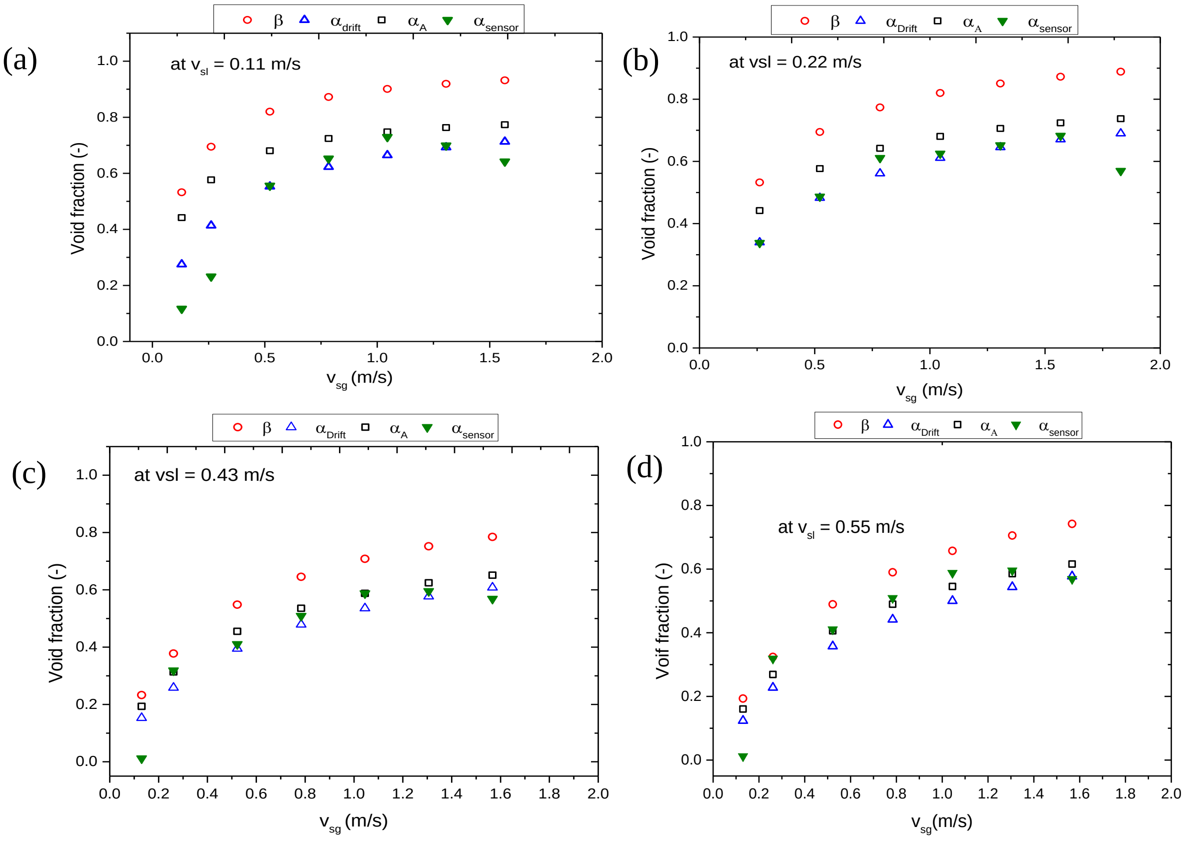

Figure 6.9: Comparison of the effect of superficial gas velocities (v_{sg}) on derived void fractions from the sensor, Homogenous, drift flux, Armards correlations at superficial liquid velocities (v_{sl}) of (a) 0.11 m/s (b) 0.22 m/s (c) 0.43 m/s and (d) 0.55 m/s

The results of the error margins relative to the maximum void fractions measured are presented between α_{sensor} and β (figure 6.10 (a)), the α_{Drift} (figure 6.10 (b)) and α_A (figure 6.10 (c)). The data points are based on the145 flow conditions described in chapter 3. Figure 6.10 (a) shows that β was in +20 % and -0.5% error margin, for about 85% of the data points relative to the α_{sensor}. This clearly indicates an overestimation of the void fractions derived from the homogenous model. The Root Mean Squared Error (RMSE) is obtained as +/- 20.5%. Figure 6.10 (b) shows a +/- 8.5 % error margin or deviation of the α_{Drift} from parity with the α_{sensor} for 90 % of the data points, with a corresponding RMSE of +/- 6.8%. Figure 6.10 (c) for the Amard correlation predicted 87% of the data points within a +/- 10 % error margin and a RMSE of +/-10.3 % of all data points relative to the α_{sensor}.

Given the acceptable agreements from each correlation, there are however poor predictions made by all correlations at lower void fractions, for $0.01 < \alpha < 0.3$ (corresponding to the bubble flow and bubble cap dominated flows). This poor performance has been reported to be due to instabilities in the structural distributions of dispersed phases, i.e. the small bubbles. The Drift flux correlation shows the best prediction of void fractions and in parity with the sensor void fraction for $0.3 < \alpha < 0.75$, which corresponds mostly to slug flow regime conditions. Amard correlation however , in the same range of void fractions shows an overestimation relative to the sensor's measurement, although presented as a good agreement overall. Sowiński *et al.*(2009) reported a similar agreement of the Amard correlation relative to a sensor measurement highlighting the variations in the multiplier of the β to be variant of the fluid properties. Therefore, Amard correlation prediction can be improved when the 0.83 multiplier is corrected to match the sensor void fraction results, specific to each flow regime.

For $0.75 < \alpha < 1$ which corresponds to churn and annular flow regimes, an overestimation of the measured void fraction was obtained by all correlations. None the less, based on the degree of accuracy required by the investigator in determining void fraction, the choice of the best performing correlation relative to that of the sensor is the drift correlation. The discussed prediction performance of the Drift flux correlation has also been supported by comparative studies in literature (see Thome, (2005)).

s

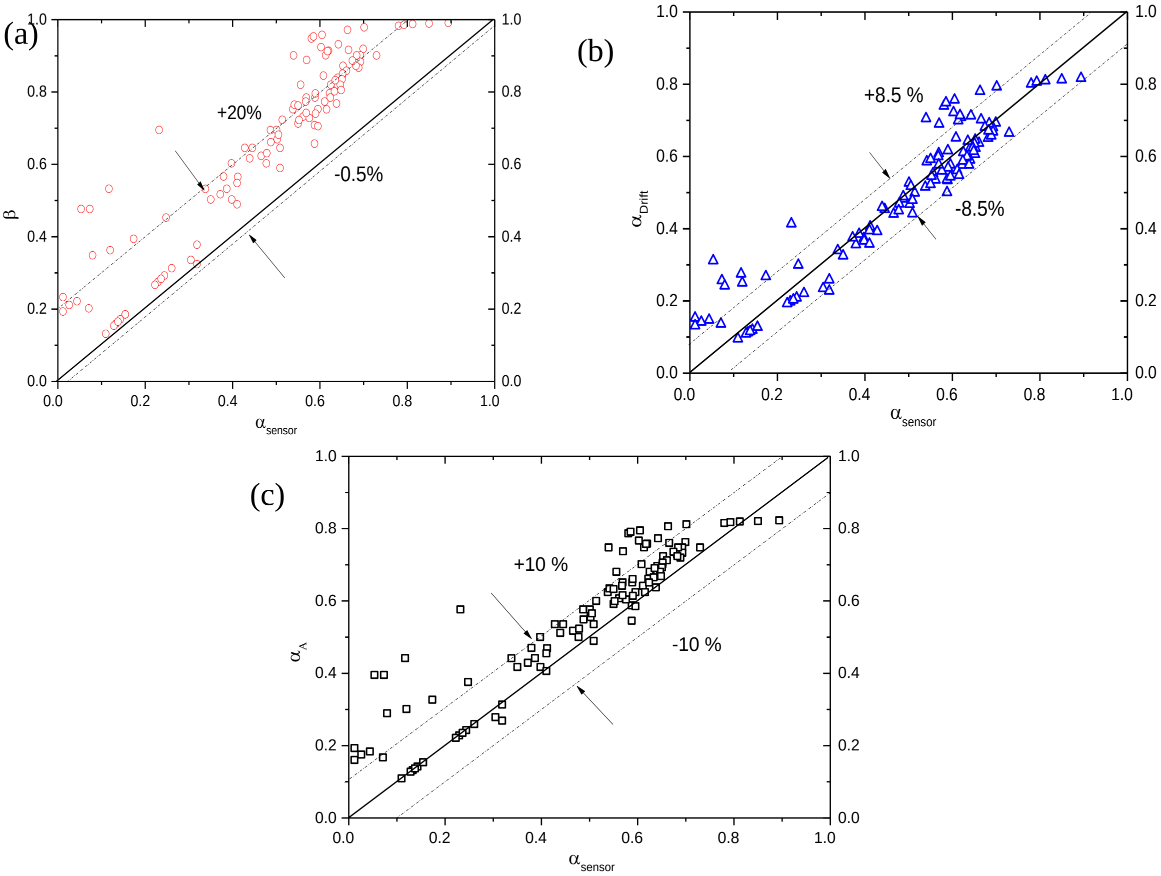

Figure 6. 10: Comparison of sensor void fraction under flow varied flow conditions with (a) Homogenous correlation (b) Drift flux correlation and (c) Armards correlation

6.4.2. The 880 nm NIOIRS (from Sarkodie et al, 2019).

The optical sensor (880 nm) set up by Sarkodie et, al. (2019) (see chapter 4) was installed on the main flow rig and recalibrated for phase fraction determination based on the same models summarized in Table 4.1 of chapter 4. Figure 6.11 presents a comparison of the responses in the presence of a rising Taylor bubble with entrained bubbles for each sensor, logged at 1000 Hz. It is observed that each sensor has different calibrated responses, indicated for presence of air, water and the interface of air and water.

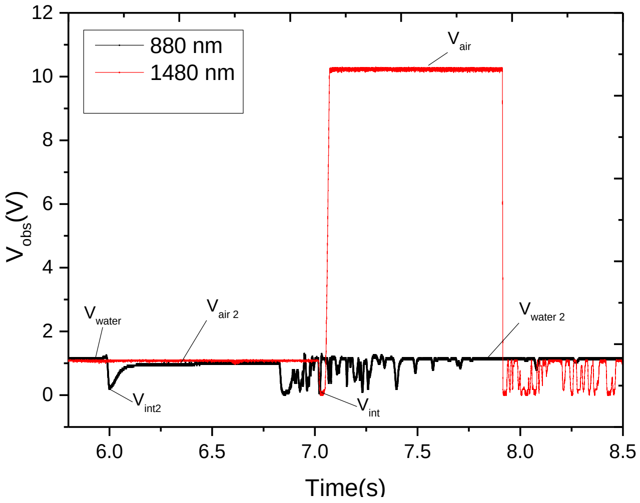

Figure 6.11: Comparison of the sensor responses from the 880 nm sensor from Sarkodie et al, 2019 and the 1490 nm used in the current study for a typical Taylor bubble and entrained bubble.

*The observed calibration responses for air, water and interfaces are also indicated as V_{air}, V_{water}, V_{int}, for the optical sensor 1480 nm sensor (used in the current study) and $V_{air\ 2}$, $V_{water\ 2}$, $V_{int\ 2}$ for the 880 nm sensor. (*Note that the same nomenclature is used for the 880 nm sensor in chapter 4, however for the sake of distinguishing responses, the subscript “2” is used).

The results of the reduction in sensitivity of the 880 nm sensor due to changes in pipe size is presented in figure 6.12 (a) with the percentage drop at each calibrated response also presented in figure 6.12 (b). Theoretically, the overall drop in sensitivity is mainly due to a longer ray path length created by a larger pipe diameter. This further increase ray divergence of the emitted light, causing a reduced intensity of light received at the photodiode. It can be observed that the maximum drop in sensitivity by 82 % at the V_{int} response (table 6.2.) infers a potential for a poor sensor resolution to detect accurately smaller bubbles. The optical sensor used by Keska and BE, (1999) produced a poor performance in delineating phase distributions due to the poor resolution given similar sensitivity ranges as the 880 nm sensor when they used a 32 mm pipe.

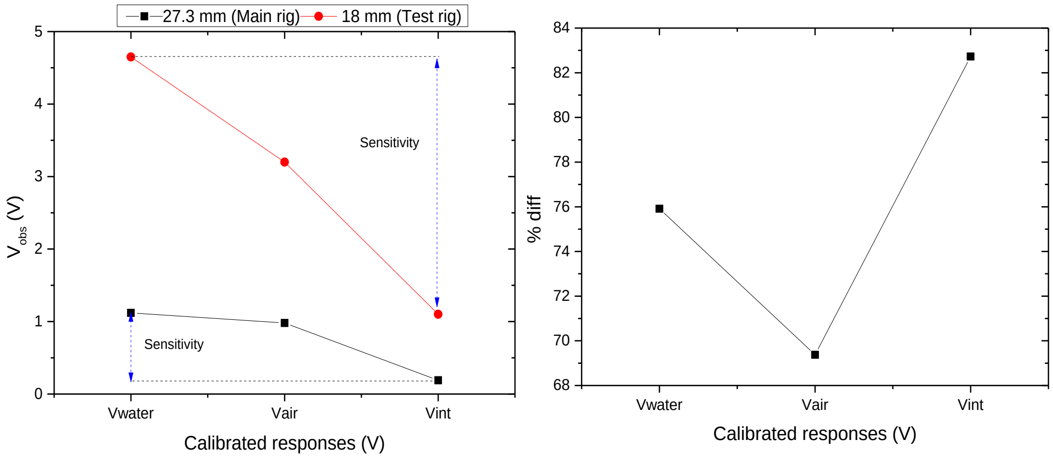

Figure 6.12: The effect of pipe size on the sensitivity of calibrated response of the 880 nm sensor used by Sarkodie et al, (2019) showing (a) two decreasing trends from the test rig of 18 mm (red trend line) and the main rig of 27.3 mm (black trend line) and (b) the percentage drop (% diff) in the sensitivity.

Table 6.2. The variation in calibration responses with sensitivities of the 880 nm sensor due to changes in pipe sizes

Response (V)	Main rig (27.4 mm)	Test rig (18 mm)	ratio	diff	% diff
V_{water}	1.12	4.65	4.15	3.53	75.9
V_{air}	0.98	3.2	3.27	2.22	69.4
V_{int}	0.19	1.1	5.79	0.91	82.7
Sensitivity	0.93	3.55	3.82	2.62	73.8

Figure 6.13 presents evidence of poor performance of the 880 nm sensor as it underestimates the void fraction relative to that derived from photography in the bubble flow regime, followed by significant deviations in the churn flow regime. This performance was expected since the variance in bubble sizes that lead to scattering of light as indicated by the V_{int} response exists. Figure 6.13 presents the results of the void fraction derived from 880 nm sensor to have an overall +/- 5% error margin (based on the maximum void fraction measured), relative to the void fraction derived from photography.

Although, the 880 nm sensor indicates a response that reflects the shape of the Taylor bubble nose and tails, the increase in pipe diameter from 18 mm of the test rig to 27.3 mm of the main rig, led to a reduction in intensity received by the photodiode of the 880 nm sensor as already discussed.

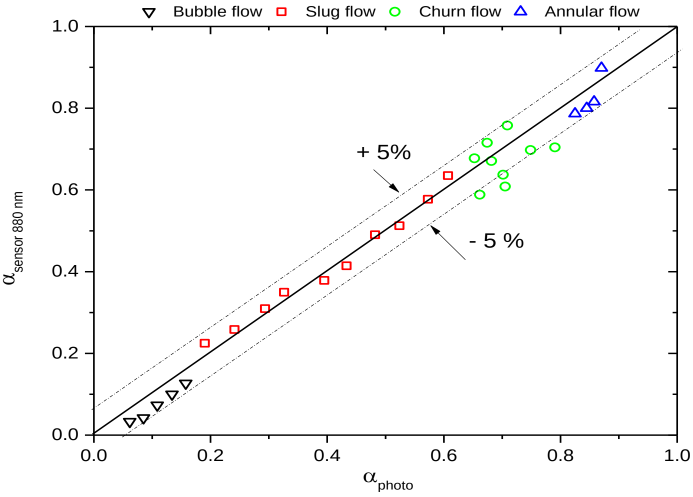

Figure 6.13: Comparison of the 880 nm optical sensor void fraction from Sarkodie et al,2019 with validation results from photography, showing a +/- 5 % error margin.

Based on the comparisons with results from figure 6.6, the 1480 nm sensor has a better measurement accuracy, given that it performed at +/- 1.25 % error margin (based on the maximum value of void fraction measured) obtained from the photography validation. It is also clear that the 1480 nm sensor is adequately amplified to provide a higher sensitivity in the detection of varied flow structures in the flow stream. None the less, in order to improve the performance of the 880 nm sensor, increasing the amplification ratio using the variable resistor from the circuit can be performed, even though there exist a saturation limit on the output. Overall, the accuracy of the 880 nm optical sensor is still adequate compared with other investigations on non-intrusive optical sensors in literature (Keska and BE, 1999; Ruixi *et al.*, 2013, ; Li *et al.*, 2016).(Wang *et al.*, 2016).

6.4.3. Pressure drop sensor measurement

Figure 6.14 shows the relationship between the measured pressure drop extracted from the two absolute pressure transducers and superficial gas velocities. At $v_{sl} = 0.43$ m/s and $0 < v_{sg} < 0.89$ m/s. It is observed that increase in the gas flow rates leads to corresponding decrease in the measured pressure drop given a reduction in the liquid fraction relative to increases in gas fraction in the pipe. In effect, this creates a significant reduction in the hydrostatic component of the total pressure drop created a reduction in mixture density. As already discussed in the review of chapter 2, the frictional pressure drops which is as a result of wall shear stresses between the fluids and wall of the pipe was considered negligible for the flow rates of liquid considered. This is evident following a maximum of 3 % variation in the total pressure drop measured at a single-phase flow of liquid for v_{sl} =0.29 m/s, 0.43 m/s and 0.54 m/s. Also, the drop in total pressure drop given in figure 6.14, provides an indication of hydrostatic dominance during the GLF.

However, at higher gas superficial velocities (typically greater than 0.89 m/s) the significance of wall stresses increases (hence increases in the frictional pressure drop) such that the total pressure drop begins to increase, irrespective of the aeration effect on the liquid phase. It is worth noting that the consequence of this occurrence makes the Differential pressure void fraction model unreliable.

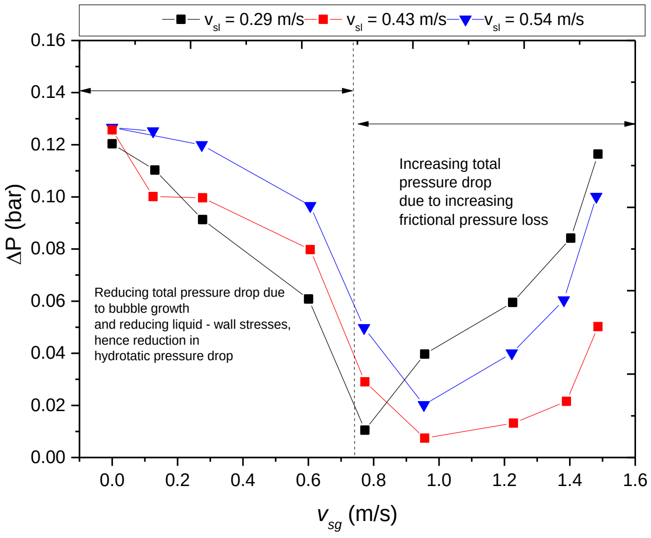

Figure 6.14: Relationship between the measured pressure drop and superficial gas velocities at corresponding superficial liquid velocities

Figure 6.15 presents the corresponding error margins based on the maximum values measured, (defined by the dashed lines) of the flow conditions considered in figure 6.14. At void fractions between 0 – 60%, which covered 65% of the data point, an error margin of +/- 20% is obtained. These data points correspond with the bubble and slug flow regimes, where it is expected that hydrostatic pressure drops dominates the flow. A +/- 30% error margin (deviation from parity) relative to the sensor void fraction was also obtained. The larger deviation at higher void fraction (greater than 60 %) was as a result of increasing frictional pressure drop, mostly corresponding to the slug- churn transitions and the chum flow regimes.

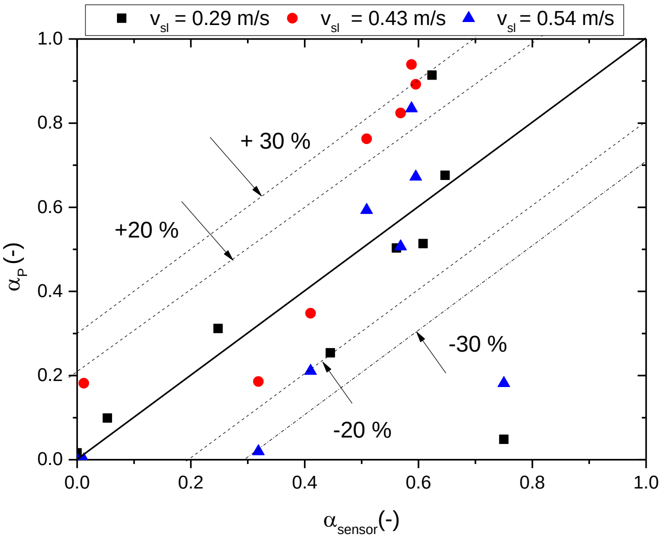

Figure 6.15: Comparison between the sensor void fraction and differential pressure, αP void fraction for at vsl = 0.29 m/s, 0.43 m/s and 0.54 m/s. The error margin of +/- 30 for most of 97% of the data and a +/- 20 for 65% of data points relative to the sensor void fraction, αsensor.

Differential pressure models have been modified to account for frictional pressure drops, with promising results, however they have only been applicable to low flow conditions. For example ,Tang and Heindel, (2006) proposed a wall shear stress void fraction model with significant reductions in error margins compared to the model used in this work. A differential pressure void fraction model was also derived by Jia *et al.*, (2015) (equation 3.3) that accounted for the frictional pressure drop reported a 3% error margin relative to other non-intrusive sensors, however , this accuracy was valid in the range of 0.001 – 0.01 m/s and may not apply to conditions of this work.

Apart from the effect of hydrodynamics on the derived differential pressure void fractions, a key source of error with the pressure sensors is the possibility of bubbles de-wetting the pressure probe causing possible blinding of the sensor to wall pressures. Hence increasing the error margin significantly.

6.5. Determination of Structural characteristics

Given the adequate performance of the void fraction models from the optical sensor, further structural characteristics of the gas liquid flow were determined from the temporal void fraction response via signal analysis methods that provide real time measurement and monitoring capabilities. A validation of results is carried out to establish the accuracy of each signal analysis method. These structural characteristics, include

i. Average Taylor bubble void fraction, α_{TB}
ii. Entrained bubble fraction α_{EB}
iii. Average Liquid film thickness δ_{favg}

6.5.1. Average Taylor bubble and entrained bubble void fractions

In order to determine the average Taylor, bubble and entrained bubble void fractions of a slug flow regime, the percentage counts of the $\alpha(t)$ responses were computed into bin intervals of 0.01 and class widths as, 0.05, 0.10. 020, void fraction. The percentage count of each bin interval was obtained relative to the total number of samples captured, which represents a percentage count distribution of the local void fraction. Figure 6.16 (a-d) presents the percent count distributions for a set of flow conditions given at a constant v_{sl} = 0.11 m/s and of v_{sg} conditions equivalent to 0.13 m/s (figure 6.16 (a)), 0.26 m/s (figure 6.16 (b)), 0.53 m/s (figure 6.16 (c)) and 1.04 m/s (figure 6.16 (d)). Two distinct regions can be identified in of figures 6.16 (a-d). These are the liquid slug and the gas slug regions indicated by the dashed boundaries on all figures.

In the liquid slug region, the peaks that occur at a void fraction of zero infer the detection of only liquid in the liquid slug as captured by the sensor, hence a percentage count represents the average liquid fraction within the slug (α_{LS}). However, figure 6.16 (d) presents an exception, where the disappearance of the liquid peak can be seen. This is due to high gas velocities of v_{sg} = 1.04 m/s which increased entrained bubble clusters, thus masked the detection of liquid fractions in the liquid slug. The percentage peaks that occur in the range $0 < \alpha(t) < 12$ % for all distributions in figure 6.16, infer the average fraction of entrained bubbles in the liquid slug as α_{EB}. This range corresponds to typical bubble sizes $D_b < 0.35D$, which in turn is coherent with the phase fraction model summarized in table 6.1. **The gas slug regions** indicated in figures 6.16 (a-d), occur in the range $80 < \alpha(t) < 100$ % where a single peak occurs at a center bin of approximately 88 % of the void fraction of which the percentage counts corresponds to α_{TB}. Slight deviation from the 88 % due to a varying liquid film thickness around the Taylor bubble.

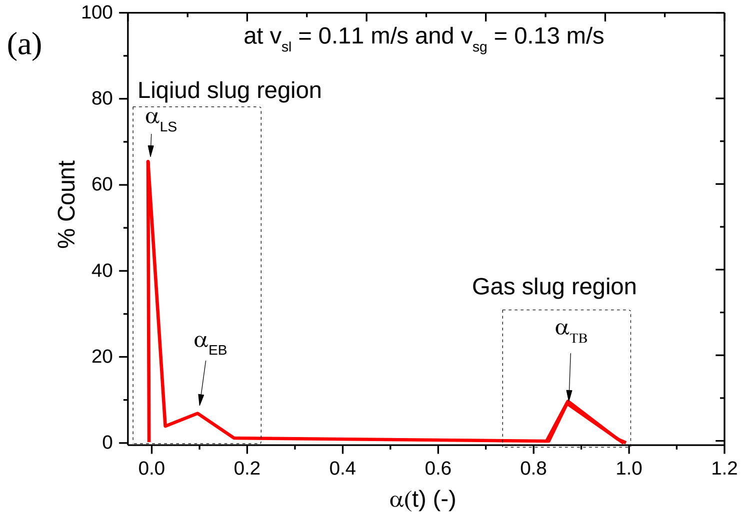
(a)
at v_{sl} = 0.11 m/s and v_{sg} = 0.13 m/s
Liqiud slug region
α_{LS}
α_{EB}
Gas slug region
α_{TB}
% Count
0
20
40
60
80
100
0.0
0.2
0.4
0.6
0.8
1.0
1.2
α(t) (-)

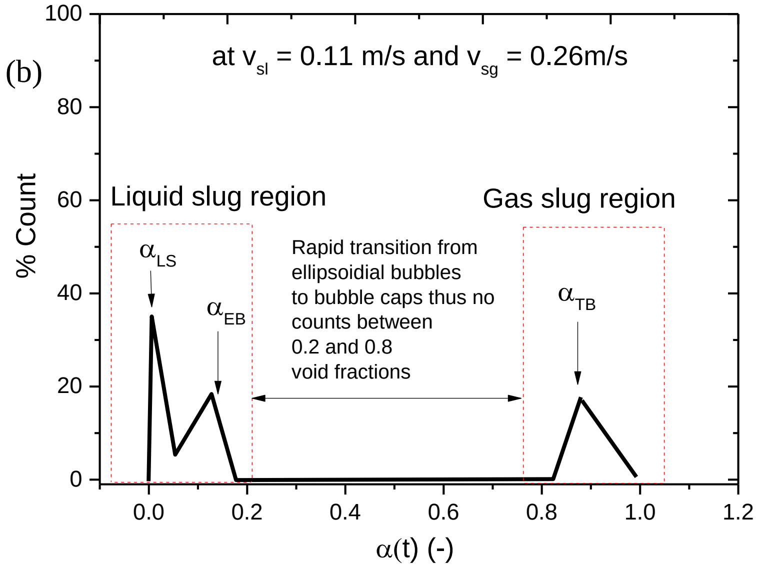
(b)
at v_{sl} = 0.11 m/s and v_{sg} = 0.26m/s
Liquid slug region
Gas slug region
α_{LS}
α_{EB}
Rapid transition from
ellipsoidial bubbles
to bubble caps thus no
counts between
0.2 and 0.8
void fractions
α_{TB}
% Count
0
20
40
60
80
100
0.0
0.2
0.4
0.6
0.8
1.0
1.2
α(t) (-)

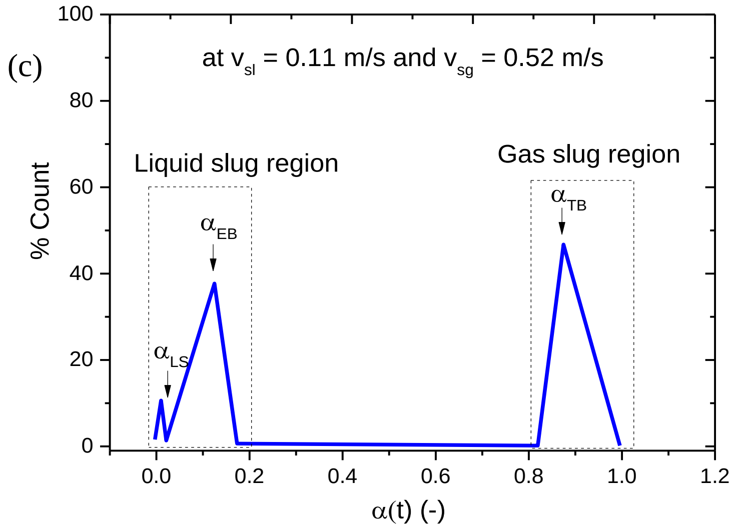
(c)
at v_{sl} = 0.11 m/s and v_{sg} = 0.52 m/s
Liquid slug region
Gas slug region
α_{TB}
α_{EB}
α_{LS}
% Count
0
20
40
60
80
100
0.0
0.2
0.4
0.6
0.8
1.0
1.2
α(t) (-)

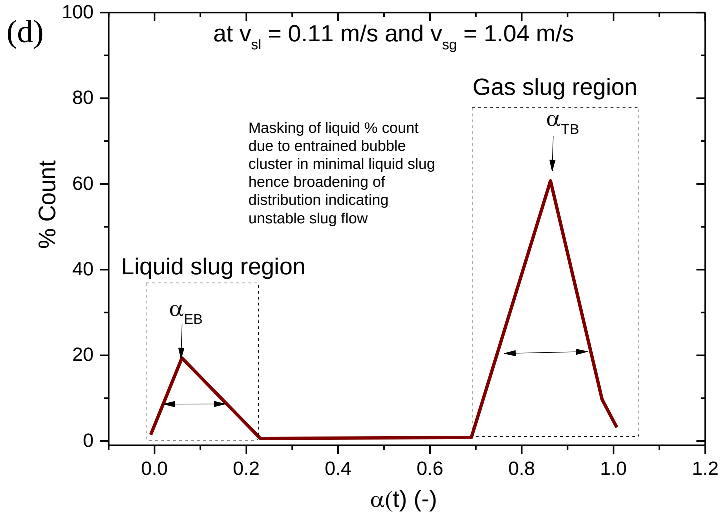

Figure 6.16: The percentage count distributions of temporal void fractions for slug flow development conditions, showing characteristics liquid slug and gas slug regions for a constant vsl = 0.11 m/s and vsg conditions of (a) 0.13 m/s (b) 0.26 m/s (c) 0.52 m/s and (d)1.04 m/s

The observed trends in figures 6.16 (a-d) can further provide relevant understanding on the variations in the void fraction specific to each structure in the slug flow regime, i.e. entrained bubbles, Taylor bubbles and liquid fractions. It is worth noting that the masking effect of entrained bubbles in the liquid slug observed in the void fraction distribution, makes it a challenge to accurately determine the entrained void fraction. Therefore, α_{EB}, can be derived by subtracting the α_{TB}, from α_{sensor}.

Gas and liquid effects on α_{TB} and α_{EB}

The effect of gas and liquid velocities on the derived average Taylor bubble and entrained bubble fractions are presented in figure 6.17 (a) and (b) respectively at constant conditions of v_{sl} = 0.11 m/s, 0.29 m/s, 0.43 m/s and 0.54 m/s, and varied v_{sg} conditions of range 0.13 m/s < v_{sg} < 1.04 m/s. The ranges of flow conditions considered, correspond to the slug flow regime.

Figure 6.17 (a) shows that increases in v_{sg} at constant v_{sl} leads to increases in the average Taylor bubble void fraction. These results are as expected given the fact that increases in gas flow rate provokes bubble growth via bubble coalescence to create Taylor bubble elongation. The average Taylor bubble void fraction also decreases for increases in the v_{sl} conditions at constant v_{sg}. This decrease is attributed to the increase in liquid slug length which means that the spacing between rising Taylor bubble increases, which eventually reduces bubble coalesce and hence inhibits Taylor bubble elongation.

It can be observed from Figure 6.17 (b) that increases in the superficial gas velocities at constant v_{sl} = 0.11 m/s, 0.29 m/s and 0.43 m/s lead to relative decreases in the entrained bubble fraction. This is due to increases in the rate of bubble coalesce instigated by increases in gas volumes in the pipe. The newly formed bubbles (larger sized) in the liquid slug then coalesce with the leading Taylor bubbles, hence, reduces the fraction of bubbles in the liquid slug. It can also be observed that for lower superficial liquid velocities (as mentioned earlier), have a minimal effect on the entrained bubble fraction given the slight increases for increases in the v_{sl} conditions. It is therefore conceivable that variations in the liquid flowrate do not affect the liquid slug length as well as the wake region for a developed slug flow regime.

It is also understood from literature that the stability criterion for a fully developed slug flow occurs at a minimum wake length beyond which there are no Taylor bubble interactions, thus increases in v_{sl} may ever so slightly contribute to the dynamics of the wake region. In their study of the liquid slug content , Guet *et al.*, (2006) presented similar results; when they compared a model based on the turbulent jet effect , with their experimental work of air - water in a slug flow regime. Abdulkadir *et al.*, (2014b) who worked with air and silicone oil also observed no effect of increasing liquids rates on the entrained bubble fraction.

At a higher liquid rate equivalent to v_{sl} = 0.54 m/s (figure 6.17(b)), the α_{EB} increases for increases in v_{sg}. For a slug flow condition, increases in the liquid velocity increases the Taylor bubble velocity which intron creates a higher downward velocity of the liquid film. Increase in the liquid film velocity forms a turbulent jet effect; enough to induce entrainment at the wake region of the Taylor bubble. The induced entrainment then increases the bubble population in the liquid slug which ultimately increases entrained bubble void fraction. Barnea *et al.*, (2013) observed similar behaviour in their experimental work on entrainement rates for air -water flow in vertical pipes, where a mixture velocity limit of 0.4 m/s, inferred a zero entrainement rate.

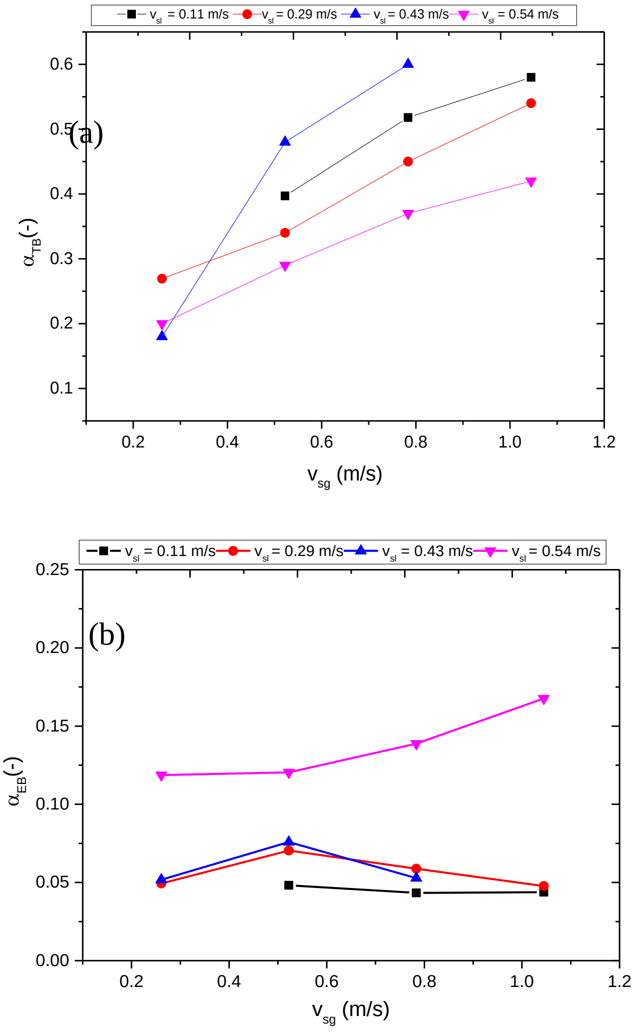

Figure 6.17: The effect of gas flow rates on the (a) Taylor bubble void fraction and (b) entrained bubbles inn the liquid slug.

6.5.2. Average liquid film thickness, δ_{favg} in the slug, churn and annular flow regimes

A liquid film structure exists in the slug flow, (around each Taylor bubble), in the churn flow (around unstable bubbles) and the annular flow (around the rising gas core). The average liquid film thickness $\boldsymbol{\delta_{favg}}$, is thus computed according to the prevailing flow regime. Computation of the liquid film thickness is based on equations 2.22 and 2.23 respectively for the slug, churn and annular flow regimes.

Figure 6.18 (a) shows the plot of the dimensionless average liquid film thickness, $\frac{\delta_{favg}}{D}$ against v_{sg} that correspond to slug and churn flow conditions, under constant v_{sl} = 0.11 m/s, 0.20 m/s, 0.29 m/s and 0.43 m/s. Increases in v_{sg} within the slug flow regime (marked by the dotted boundary line), leads to variations in the liquid film thickness between 0.057 and 0.065 of the pipe diameter for all v_{sl} conditions. The slight variation is due to the presence of ostensibly stable Taylor bubbles (observed to be greater than 1.5D in length). The $\frac{\delta_{favg}}{D}$ also deviates from the 0.06 for increases in v_{sg} due to the turbulence around the liquid film. Further increases in v_{sg} at constant liquid velocities, leads to a general decrease in film thickness for the churn flow region due to further turbulence in the liquid film and increasing Taylor bubble cross sectional area. At v_{sl} = 0.29 m/s increases in v_{sg} causes an undulating liquid film thickness as observed due to the churn effect which causes bubble shape distortion hence the significant variance in the its cross section.

In the annular flow regime, as presented in figure 6.18 (b), further decreases in $\frac{\delta_{favg}}{D}$ are observed for increases in the $\boldsymbol{v_{sg}}$. At the annular flow regime, it is established that a rising gas core is formed with sufficient momentum, to reverse the velocity of the liquid film in the upward direction. The flow reversal mechanism induces wavy disturbances in the liquid film that leads to variations in its thickness. It can be suggested from observation that the severity of the induced disturbances is a strong function of the gas - liquid ratio for an annular flow condition. It can also be observed that increases in the superficial liquid velocity from v_{sl} = 0.11 m/s to 0.43 m/s show increases in the liquid film thickness as expected, as liquid fractions increase in the pipe.

Measurement of the liquid film by a non-intrusive sensor has not been largely considered for specific flow regime. However some researchers mostly considered the slug flow regime (see Abdulkadir *et al.*, (2014b)) and for annular flow (see Liu and Bai, (2017) who investigated the fraction of entrained droplets in the annular flow regime).

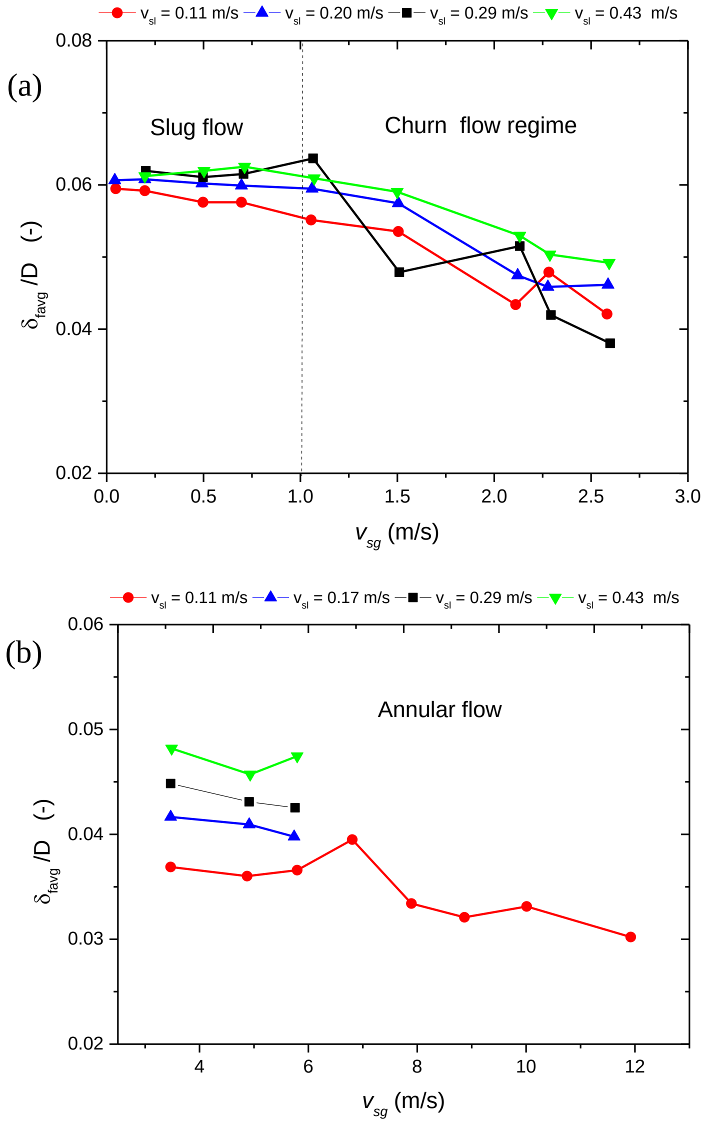

Figure 6.18: Effect of liquid and gas superficial velocities on the average liquid film thickness for (a) slug flow, churn flow and (b) annular flow regimes

6.5.3. Comparison of α_{TB}, α_{EB} and δ_{favg} with photos

A comparison of the sensor derived, average Taylor bubble, average entrained bubble void fractions and average liquid film thickness was made with photos that were processed according to the procedure described in section 3.5.2. It should be noted that the photos were extracted for 10 slug units and averaged per flow condition.

Figure 6.19 (a) presents the parity plot of the sensor derived average Taylor bubble void fraction with photos. It can be observed that an error of +/- 0.5 % is obtained. The error band infers an excellent agreement with photos given the apparent symmetric geometry of the Taylor bubble which almost fills the cross section of the test section. Figure 6.19 (b) presents the parity plot of the sensor average entrained bubbles void fraction with that from processed photos. A general underestimation by the sensor is observed, compared to the photos, given the complexity of light interaction in the presence of a bubble cluster. This amounts to an error of + 5% and / - 10 %, which amounts to an average error of +/- 7.5% based on the maximum entrained bubble fraction. It is however possible to considered in future investigations, a multiple sensor setup that may capture varied chordal orientations of the flow. This is expected to improve the accuracy of entrained bubble measurement in the liquid slug. None the less, the results are acceptable given the complexity of the void distribution in the liquid slug of a slug flow regime.

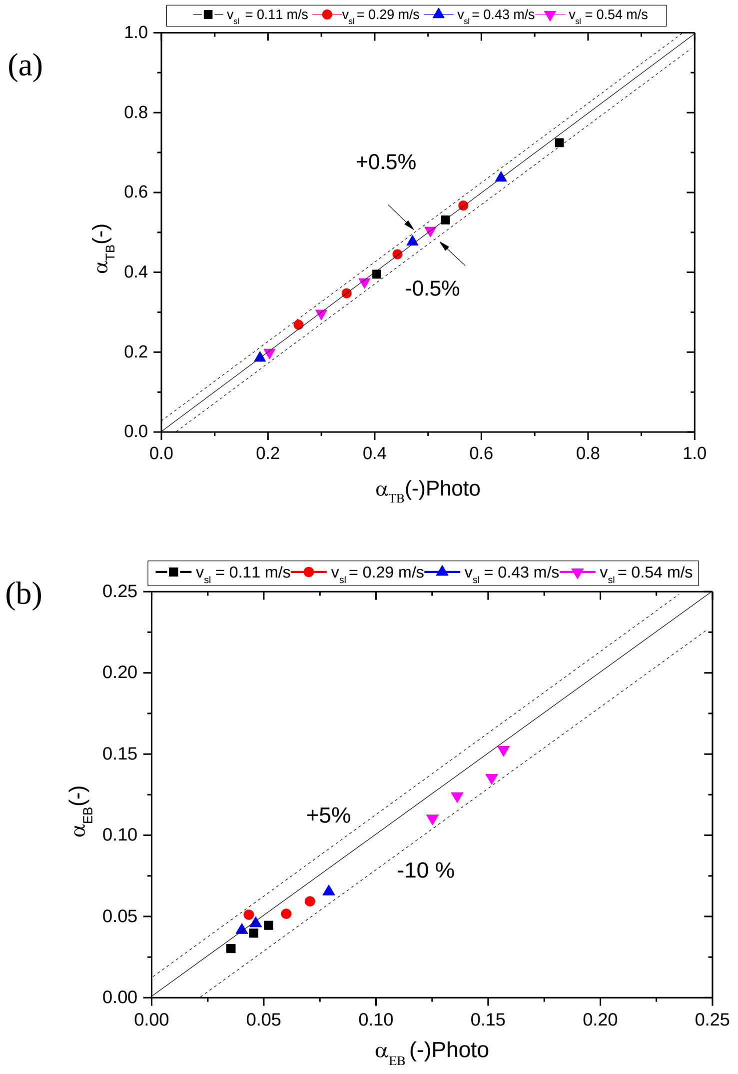

Figure 6.19: Comparison of the sensor average (a) Taylor bubble void fraction and the (b) entrained bubble void fraction for slug flow regime conditions with photographs

The validation results of the dimensionless average liquid film thickness, for conditions corresponding to the slug and churn flow regime and the annular flow regimes with photos is presented in figure 6.20 (a) and figure 6.20 (b) respectively. As observed in figure 6.20 (a), an error band of +/- 15% was obtained for all flow conditions considered. A general over estimation of the liquid film thickness for most data points is evidence of the chaotic nature of the churn flow regime. For instance, the liquid film thickness determined from photos includes the fraction of liquid droplets in the unstable bubbles and entrainment of smaller bubbles in the liquid film which were created during the turbulent flow. For the annular flow conditions, figure 6.20 (b) shows an error band of +/- 6.25% of the maximum dimensionless thickness relative to results from photos. The variation in disturbances waves in the liquid film which leads to droplet entrainment in the gas core and entry of entrained bubbles in the liquid film is cause of the observed error. It is also observed that for the lowest liquid rate (v_{sl} = 0.11 m/s) , an over estimation of δ_{favg}/D occurs , at increasing gas rates. At these conditions, the amplitude of such waves in the liquid film tends to increase.

(a)

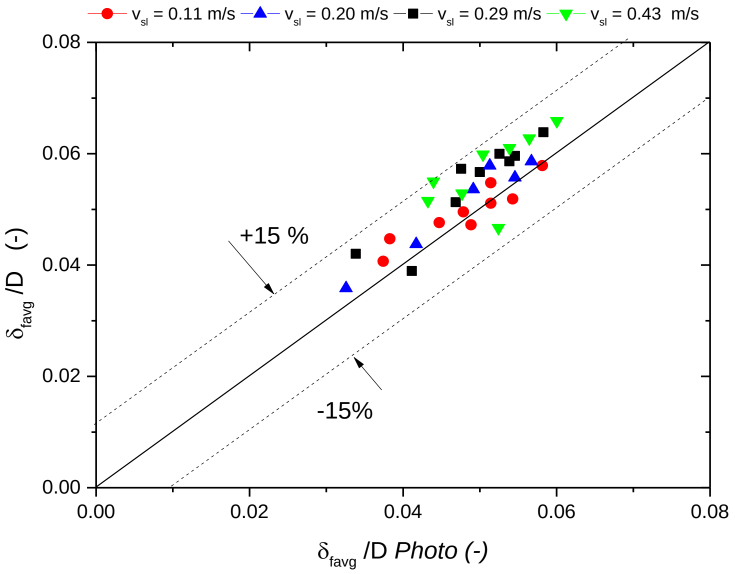

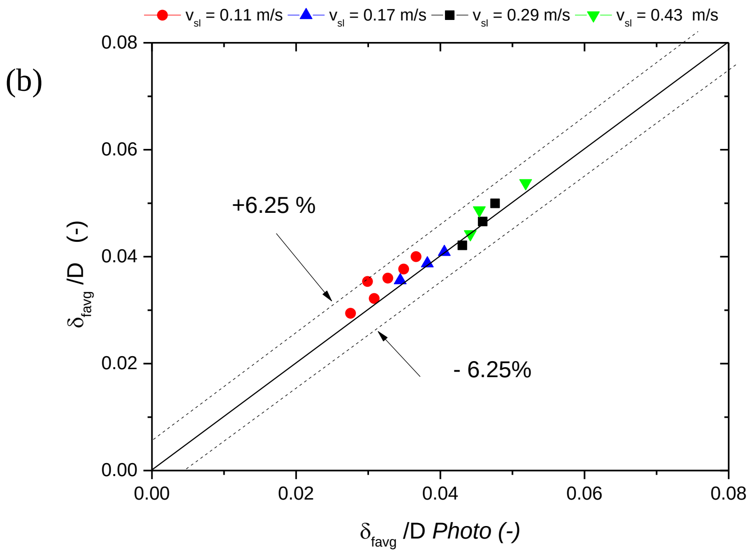

Figure 6.20: Comparison of the sensor derived average liquid film thickness with photos for the (a) slug and churn flow regimes at v_{sl} = 0.11 m/s, 0.20m/s, 0.29 m/s and 0.43 m/s and (b) annular flow condition at v_{sl} = 0.11 m/s, 0.17 m/s, 0.29 m/s and 0.43 m/s

6.6. Summary

Phase fractions were determined from the signal analysis of the 1480 nm NIOIRS response. Using a simple linear interpolation model that accounted for the variation in bubble sizes and shapes, hence corrected for interfacial scattering. The model was used to determine local and time averaged void fractions for a GLF under upward vertical flow conditions. Prior to validation of the model, the estimated stabilization times time of 35 seconds was realized as sufficient for a stabilized void fraction which relates to the flow regime stability. This cumulative time was necessary in comparing the sensor phase fraction with existing correlations.

The accuracy of the derived phase fractions was compared to photos and swell level changes of the liquid due to rising bubbles in the test section with excellent agreements given as +/- 1.25% and +/- 2% deviation from parity plots respectively. Variation in results of the experimental validation was due to the distortion of bubbles, from photos while the swell level method was useful for validating void fractions during the slug flow regime, given that, the rise of smaller bubbles (less than 0.35D) could not provide an observable change in liquid level.

Comparison with the homogenous, Drift flux and Amard correlations was carried out, with deviations from parity relative to the time averaged sensor void fraction of +20 % and -0.5% (homogenous), +/- 8.5% (Drift flux) and +/-10 % (Amard). The homogenous model mainly overestimated the void fraction due to the exclusion non- slip assumption. Amard correlation provided better agreement due to the correction factor of 0.83 on the homogenous correlation with the best agreement by the Drift flux correlation the inclusion of the flow regime parameter and slip velocity effects.

The performance of the 880 nm optical sensor by Sarkodie *et al.,* (2019) gave +/-5 % deviation form parity with the photos. The sensor suffered from low power (emission intensity) since it was tested for a larger test section. It is therefore recommended that sufficient emission intensity be achieved by modifying the amplifier circuit. Further Comparison of the sensor average void fraction with differential pressure method showed poor agreement especially for high liquid flow rates (greater than 0.89m/s) where the frictional component of the pressure drop was significant. Overall, the deviation from parity was +/- 15 %. This further supported recommendations from other authors on the application of pressure method for void fraction to be used under low flow conditions.

A count distribution of the sensor temporal void fraction was used to determine the average Taylor bubble and entrained bubble void fractions, α_{TB} and α_{EB} respectively. Results of the effect of gas and liquid flow rates on the entrained bubble fraction in the liquid slug revealed two mechanisms that controlled the distribution of entrained bubbles in the liquid slug. These mechanisms were described as the bubble coalescence and turbulent jet mechanisms observed by other investigators. The validation of the α_{TB} and α_{EB} from photos showed +/-0.5% and +/- 7.5 % error bands respectively.

Finally, the corresponding average liquid film thickness derived for the slug, chum and annular flow conditions was investigated. A general decrease in liquid film occurred followed by an increase in gas velocities. A local variation due to the churn ad annular flow effects were also observed and in agreement with photos, with a +/-15 % error band for the slug and churn flow and a +/- 6.25% error for the annular flow regime. Overall the measurement accuracy of the 1480nm NIOIRS for phase fraction and intrinsic structures is deemed adequate even though higher error margins are obtained during more chaotic flow regimes such as the churn and annular flow regimes. An extension of this study is made with previous studies to determine phase flow rate. Results are presented in chapter 7 of this work.

Chapter 7

7. Measurement of Phase Velocities and Flowrates

7.1. Introduction

This chapter details the analysis of results of the actual phase velocities and flow rates of gas and liquid, derived from the optical sensor response combined with an adequate calibration model. As summarized in Figure 7.1, the actual gas velocity is determined from the cross correlation of the temporal void fractions of the bottom and top sensor pairs of the 1480 nm sensor setup. The derived velocities are then validated with photos and compared with existing correlations. The sensor average void fraction derived from both sensor pairs is combined with the actual gas velocities and a proposed calibration model to estimate the actual liquid velocity. More so, a validation of the calibration model is carried out by running new test conditions.

The actual phase velocities can then be combined with the phase fractions and pipe diameter to determine the actual volumetric flow rates. The terms of the proposed calibration model include a modified drift velocity term v_{gu} and the distribution coefficient, C_o. A justification for the use of the calibration model is presented with further discussions on possible applications for real time measurements.

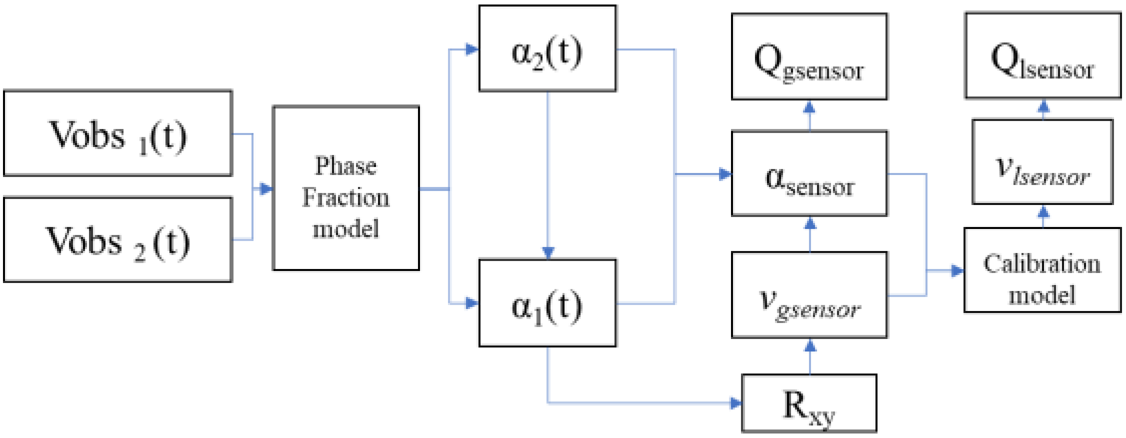

Figure 7.1: Actual phase velocities and flow rates from the sensor response coupled with closure relationships

7.2. Actual gas velocity $v_{gsensor}$, determination

The actual gas velocity $v_{gsensor}$ is determined based on the average lag time τ* which corresponds to a maximum R_{12} and combined with the sensor spacing s. Equations 2.33 – 2.35 are implemented to obtain the average gas velocities. Results of the correlation coefficient and lag times under varied flow conditions are disused as follows;

Figure 7.2 presents a typical result of the cross-correlation coefficient, R_{12} with lag time, τ derived for flow conditions corresponding to bubble flow. It is observed that increases in v_{sl} at a constant v_{sg}= 0.13 m/s leads to shorter average lag times (the average lag time corresponds to the peak R_{12}) as expected, since bubble rise faster at higher liquid rates. At v_{sl} = 0.26 m/s and 0.52 m/s, lower R_{12} values are obtained (0.4 and 0.5, respectively) relative to the R_{12} obtained for the v_{sl} = 0.54 m/s condition. Mathematically it is established that R_{12} infers a degree of similarity between the temporal responses, hence a lower R_{12} infers a variation in bubble sizes, between the measurement points. i.e. the occurrence of structural variations in the bubble flow.

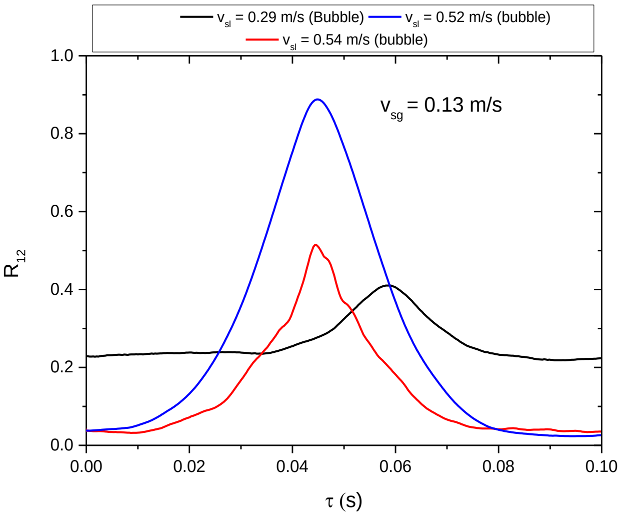

Figure 7.2: Typical cross correlation velocities for the bubble flow regime at constant superficial gas velocity (vsg = 0.13 m/s) and varied superficial liquid velocities (vsl = 0.29 m/s, 0.43 m/s, 0.52 m/s and 0.54 m/s).

Figures 7.3 (a) and (b) present results of R_{12} with τ, for conditions that correspond to the slug and churn flow regimes considered at a constant v_{sl} = 0.43 m/s and 0.54 m/s. In both cases, the slug flow and churn flow conditions show that increases in v_{sg} leads to decreases in τ*, this clearly infers shorter transit times and hence faster mixture velocities of the GLF. For the slug flow conditions, corresponding increases in R_{12} infer an increase in structural coherence and stability, such as flow of stable Taylor bubbles. However, further increase in the superficial gas velocity for the churn flow regime (at v_{sg} = 1.57 m/s) shows a decrease in R_{12}, given the characteristic collapse of slugs, that indicates a disparity in void fraction responses between measurement points.

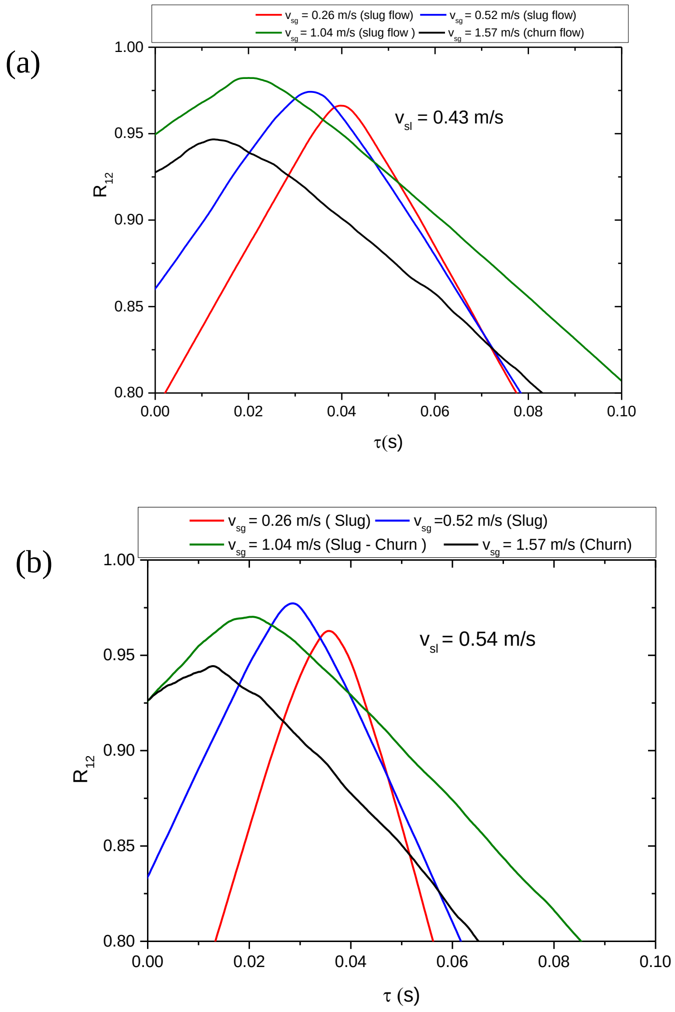

Figure 7.3: The cross correlation of the temporal void fraction responses from the bottom and top sensor (BS) and (TS) pairs respectively, for typical slug and churn flow regimes under vsg = 0.26 m/s, 0.52 m/s, 1.04 m/s, and 1.57 m/s at constant superficial liquid velocities of (a) 0.43 m/s and (b) 0.54 m/s.

The cross-correlation results of the annular flow conditions presented in figure 7.4, shows faster transmit times for increases in superficial gas velocity. This infers that the average velocity in the annual flow regime increases. It is also worth noting that the cross correlation of annular flow conditions is considered valid when there are detectible features, such as, the entrained liquid droplets and significant wave disturbances that rise under the interfacial stresses between the gas core and liquid film.

Investigators have highlighted that disturbance waves and droplet velocities are propagated upwards at the same rate as the interface between the liquid film and the gas core, (see ,Azzopardi, Barry J, Zaidi, 2013; Azzopardi, 1985), hence it can be suggested that the cross correlation velocity in the annular flow is taken as the average velocity of mixture , where gas and liquid rates are equal. Schubring *et al.*, (2010) provided proof of this claim of their validation work of annular flow characteristics using image processing techniques.

The decreases in the peak correlation coefficients for increases in the superficial gas velocities also indicates the complex evolution of the disturbance waves and entrained droplets. The complexity causes a significant variation in detected structures detected between both sensor pairs.

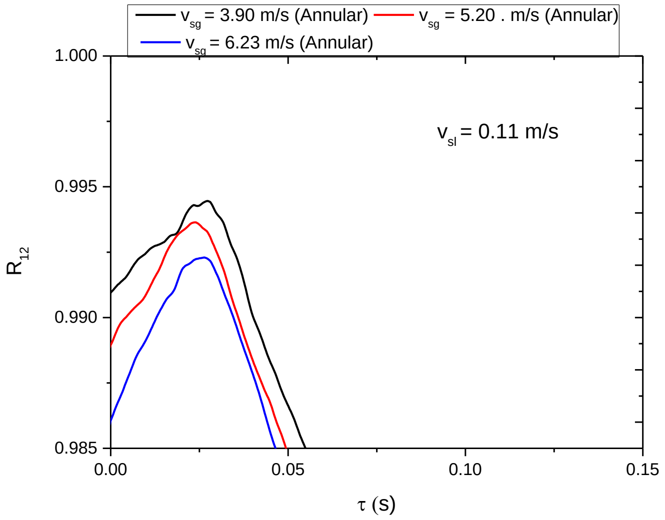

Figure 7.4: Cross correlation of temporal void fraction from bottom and top sensors under typical annular flow regime conditions corresponding to vsl = 0.11 m/s for vsg = 3.90 m/s, 5.20 m/s and 6.23 m/s.

7.2.1. Validation of cross correlation derived velocities with photos.

To assess the accuracy of the cross-correlation method, a validation of the cross-correlation derived velocities from photos and manual inspection of void fraction responses from both sensor pairs was performed. Figure 7.5 presents a parity plot of the velocity from the cross correlation, $v_{gsensor}$ with the average velocity determined from photos v_g photo. The results show +/- 1.5 error band for the bubble and slug flow conditions considered. This error obtained can be considered a good agreement considering the turbulence involved in two phase flows. A broader error band of +/- 3.3 %, is obtained for the churn and annular flow conditions, given the complex nature of these flows as already discussed. The obtained error bands are relative to the maximum velocities measured respective to each considered flow regime.

The accuracy of the cross-correlation method under the churn and annular flow regimes requires careful verification. Given the chaotic nature of flow, the derived error band may also differ for the same flow conditions when tested at different runs. The velocities derived from each flow conditions were carried out 5 times with an average taken. The photos that corresponded to each repeated flow condition is also taken before the comparisons are made.

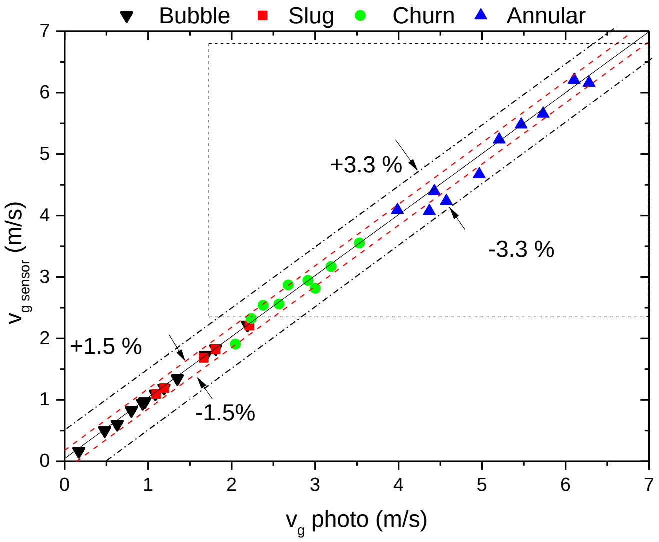

Figure 7.5: Validation of the average gas velocity derived from cross correlation with average velocities derived from photos under typical bubble, slug, churn and annular flow regimes (the dashed box shows the regime of churn and annular flow velocities).

7.2.2. Comparison with correlations

Comparisons of the $v_{gsensor}$ with the gas velocities that correspond to the slug flow conditions with the correlations of Nicklin (1962) and Fernandes *et al.* (1983) are presented in figure 7.6 and 7.7. The sensor derived gas velocities are underpredicted by both correlations. The reasons for the under prediction are disused as follows;

Nicklin’s correlation was developed based on injected isolated Taylor bubbles of air into a flowing liquid of water, where the velocities of bubble noses were determined. The effects that impede the rise velocities of Taylor bubbles such as the entrained bubbles at the wake and front of bubbles created by the turbulent jets were hence ignored.

The correlation of Fernandez *et al.* (1983) was developed based on stable rising slugs which accounts for the effect of trailing and preceding Taylor bubbles. Mao and Dukler, (1985) explained that the discrepancy between with Nicklin’s correlation and that of Fernandez *et al.* (1983) was instrumental to provide understanding of the interaction between the Taylor bubbles and entrained bubbles. However, Fernandez *et al.* (1983) did not account for the effect of surface tension and turbulence that impedes rise velocities in their drift velocity model hence higher predictions are obtained.

It is also evident that the slope represented as the distribution parameter, C_0 differs from that of the linear fit of the sensor as presented in figure 7.6. This line can be modelled as,

$$v_{gsensor} = 1.11v_{mix} + 0.165 \qquad (7.1)$$

Where C_0 is defined as 1.11 and the drift velocity of the Taylor bubbles v_{gu} = 0.165 m/s equivalent a Froude number (Fr) of 0.33 which is well within the observed ranges in literature between 0.328 – 0.37 over varied flow conditions. C_0 and v_{gu} can further be validated to establish a premise for the use of the linear fit (Equation 7.1) to determine the actual liquid velocity under the slug flow regime and bubble flow regimes.

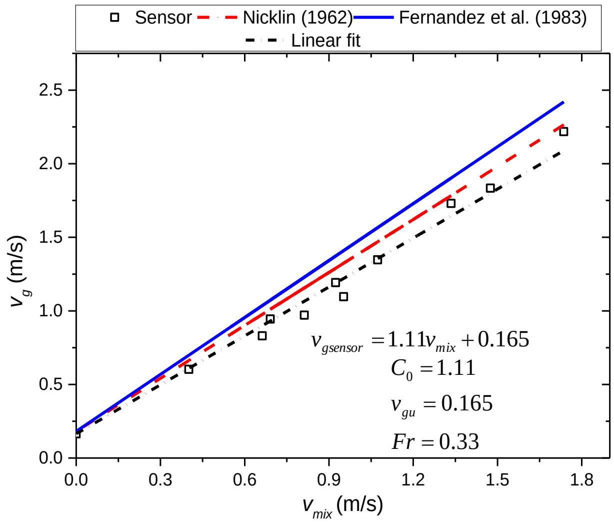

Figure 7.6: Relationship between the mixture velocity vmix and actual gas velocity for slug flow condition at vsl = 0.14 m/s, 0.29 m/s 0.43 m/s, and vsg range between 0 and 1.30 m/s.

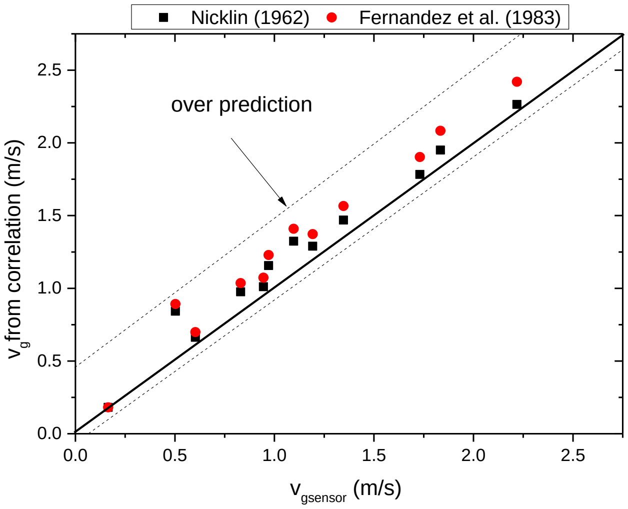

Figure 7.7: Parity plot comparing the performance of the actual gas velocities from cross correlation with the rise velocity correlations of Nicklin, (1962) (black data points) and Fernandes *et al.*, (1983) (red data points), for v_{sl} = 0.14 m/s , 0.29 m/s 0.43 m/s, and v_{sg} range between 0 and 1.30 m/s.

7.2.3. Comparison with gas flow meter derived superficial velocity

According to the established two-phase flow separated model given by equations 7.2 and 7.3 that consider a slip condition between the gas and liquid phases, the relationship between the average actual phase velocities and average phase fractions can be used to predict the superficial gas and liquid velocities as,

$$v_{sg} = \alpha v_g \tag{7.2}$$

$$v_{sl} = (1-\alpha)v_l \tag{7.3}$$

Publications by Shen *et al.*(2014) and Zhang *et al.* (2017) provide strong theoretical support for equation 7.2 and 7.3, where they concluded it to be valid for the slug flow regime. Guet *et al.*, (2006) and Shoham, (2003) also presented experimental evidence on the applicability of the model in equation 7.2 for the prediction of entrained bubble velocities in the liquid slug. It is therefore worthwhile to extend this model to the sensor average void fraction and actual gas velocity, as expressed in equation 7.4,

$$v_{sgsensor} = \alpha_{sensor} v_{gsensor} \tag{7.4}$$

The performance of the model in equation 7.4 is summarized in table 7.1 for a typical set of slug flow conditions. The table presents the computed mean absolute percentage error (MAPE), and percentage standard deviation as 7.01 % and 6.78% respectively, between the derived sensor superficial gas velocities, $v_{sgsensor}$ and that from the gas rotameter as v_{sg} flowmeter. Figure 7.8 further presents the +/- 3.4 % deviation from parity between the measured and predicted superficial gas velocity from the sensor.

Even though the considered flow conditions were measured over the derived stability times for the slug flow condition (see chapter 6), transient effects due to entrained bubbles and variances in the local distribution of the phase (bubble expansion and shape distortion) and velocities is responsible for the deviation in prediction by the sensor. Furthermore, contribution to the deviation is the individual errors propagated from the determination of α_{sensor} and $v_{gsensor}$ by the sensor. The combined error from both measurements is obtained as +/- 2.7 %. The results are however considered to be in an acceptable range considering the complex nature of GLF.

Table 7.1: Typical results of the computed superficial velocity from sensor and that from the gas flow meter, showing the error of prediction

v_{sl} flowmeter (m/s)	v_{sg} flowmeter (m/s)	$v_{gsensor}$ (m/s)	α_{sensor} (-)	v_{sg} sensor (m/s)	Absolute error (%)
0.14	0.261	0.603	0.431	0.260	0.553185
0.14	0.522	0.830	0.589	0.489	6.436913
0.14	0.784	1.192	0.652	0.777	0.855448
0.29	0.261	0.503	0.403	0.203	22.3826
0.29	0.522	0.971	0.502	0.487	6.716896
0.29	0.784	1.347	0.561	0.756	3.497108
0.29	1.045	1.731	0.624	1.079	3.320662
0.43	0.261	0.945	0.319	0.301	15.24504
0.43	0.522	1.097	0.410	0.450	13.84558
0.43	1.045	1.834	0.588	1.078	3.165675
0.43	1.306	2.219	0.595	1.321	1.132261
Mean Absolute Percentage Error (MAPE)					**7.01**
% Standard deviation of absolute error					**6.78**

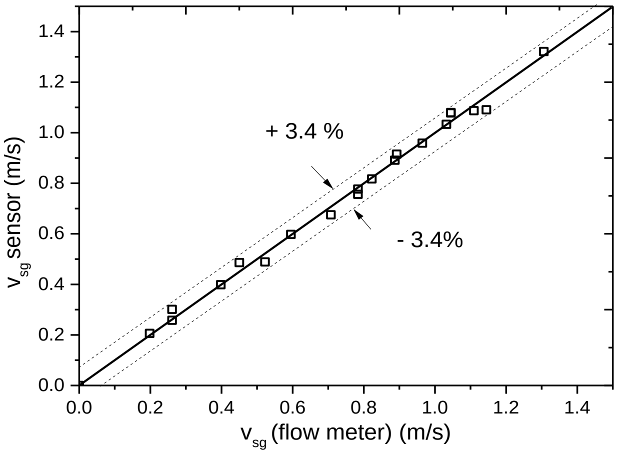

Figure 7.8: Parity between the sensor derived superficial gas velocity and that from the flow meter.

Actual gas velocity and average void fraction

The relationship between the average void fraction and actual gas velocities derived from the sensor under bubble and slug flow conditions is presented in figure 7.9. A nonlinear fit based on a hill function describes this relationship. The trend is a steep rise in void fraction for increases in $v_{gsensor}$ and an apparent saturation trend of the void fraction at higher actual gas velocities. Interestingly, the described trend in figure 7.9 compared to that from figure 6.5 of chapter 6 (which depicts the relationship between v_{sg} and α_{Sensor}) is similar. This provides further confidence on the linear relationship between the superficial gas velocity and actual gas velocity expressed by equation 7.2.

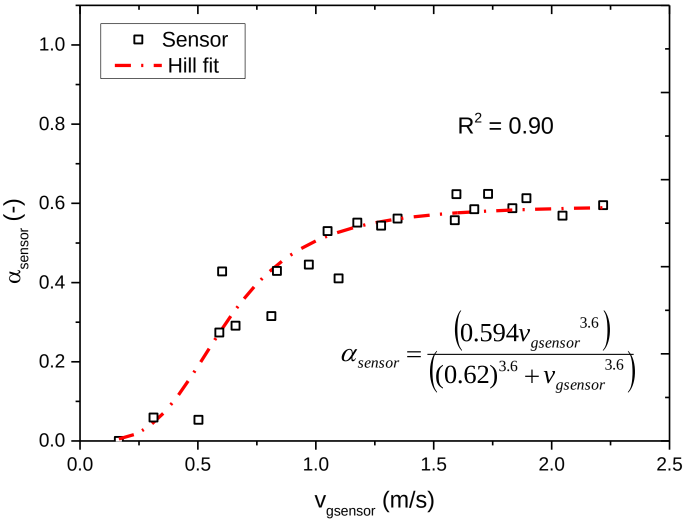

Figure 7.9: Relationship between the average void fraction and the actual gas velocity, which follows a Hill function

7.3. Actual liquid velocity, $v_{lsensor}$ determination

The determination of the actual liquid velocity by the optical sensor $v_{lsensor}$ is performed with proposed the calibration model that represents a modification of the Nicklin's correlation, and the separated models presented by equation 7.2 and 7.3. A calibration model is useful given the absence of local density and mass flow rate measurements of the GLF, which aide the computation of a slip ratio or velocity. The series of equation presented below (equation 7.5 – 7.11), delineates development of the calibration model for actual liquid measurement. Equation 7.5 presents the Nicklin type correlation in terms of the sensor average actual gas velocity, the distribution coefficient parameter *Co*, mixture velocity v_{mix} and the drift velocity, v_{gu}

$$v_{gsensor} = C_o v_{mix} + v_{gu} \tag{7.5}$$

Where v_{gu}, as expressed by Dumitrescu, (1943) to be a function of the pipe size D, and acceleration due to gravity g, and the Froude number, Fr,

$$v_{gu} = Fr\sqrt{gD} \tag{7.6}$$

while the mixture velocity v_{mix}, is further expressed in terms of the superficial phase velocities as

$$v_{mix} = v_{sg} + v_{sl} \tag{7.7}$$

Since it is assumed that there is no prior knowledge of the superficial phase velocities, equation 7.7 needs to be re-written in terms of the separated models presented on equations 7.2. and 7.3 as,

$$v_{mix} = \alpha_{sensor} v_{gsensor} + (1 - \alpha_{sensor}) v_{lsensor} \tag{7.8}$$

The actual liquid velocity $v_{lsensor}$ derived by the sensor can then be expressed as,

$$v_{lsensor} = \frac{v_{mix} - \alpha_{sensor} v_{gsensor}}{1 - \alpha_{sensor}} \tag{7.9}$$

Where v_{mix} is also expressed from by rewriting equation 7.5 as,

$$v_{mix} = \frac{v_{gsensor} - v_{gu}}{C_o} \tag{7.10}$$

Therefore, by combining equation 7.6, 7.9 and 7.10, the modified calibration model for average actual liquid velocity measurement $v_{lsensor}$ can be expressed as,

$$v_{lsesnor} = \frac{v_{gsensor}(1 - \alpha_{sensor} C_o) - F_r\sqrt{gD}}{(1 - \alpha_{sensor}) C_o} \tag{7.11}$$

It then follows that the unknowns, C_o and Fr from v_{gu} are required from calibration to provide an acceptable estimate for $v_{lsesnor}$. These parameters therefore are further investigated under the slug and bubble flow regimes. Discussion of results are presented in the next section.

7.3.1. Slug flow regime

For the slug flow conditions, the *Co* value is already been derived from the linear fit of sensor data as observed in figure 7.6. Therefore, *Co* is taken as the gradient of the linear fit to be 1.11. In addition, the average rise velocity defined by the drift velocity of Taylor bubbles was derived as 0.165 m/s which gives an equivalent Fr value of 0.33. However further investigation is required to determine the deviation of these findings for the slug flow regime.

Isolated bubbles of varied lengths were injected into the test section at stagnant flow liquid conditions. The velocity of an individual bubble was taken as the average of the nose and tail velocities via manual inspection of the sensor responses between the bottom and top sensor pairs. The bubble lengths are then determined as a product of the residence times and velocities of each bubbles from the sensor responses with validation carried out with photos. A total of 56 bubbles with lengths greater than 1.5D are considered as Taylor bubbles, according to literature (see Nigmatulin and Bonetto, 1997).

Figure 7.10 presents the results of bubble lengths with corresponding rise velocities. It can be observed that for increases in Taylor bubble length that a stabilization of rise velocity occurs for lengths greater than 80 mm (equivalent of 2.9D). This stabilization indicates the occurrence of terminal velocities given the balance buoyancy and drag forces. For bubble length less than 80 mm, a significant variation in rise velocities occurs. These bubbles are to be bubble caps which are characterized by instabilities in bubble noses and tails velocities. This instability as observed by other investigators (Bhusan *et al.*, 2009; Mao and Dukler, 1985b, 1985a; Polonsky *et al.*, 1999) is a result of variations in drag and buoyancy force interactions given the dominance of a hemispherical nose. Figure 7.11 (a) presents the bubble length distribution that shows dominant bubble lengths around 80 – 100 mm (2.9D – 3.7D) that contributed to the modal rise velocities of 0.165 m/s presented in figure 7.11 (b). The standard deviation of +/- 0.014 m/s is computed for the data. The modal rise velocity is taken as the drift velocity, v_{gu} under the slug flow regime, which is a confirmation of results derived from the linear fit in equation 7.1.

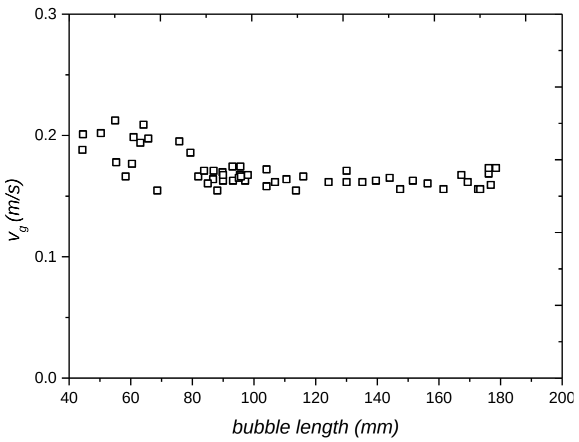

Figure 7.10: The relationship between Taylor bubble length with rise velocity

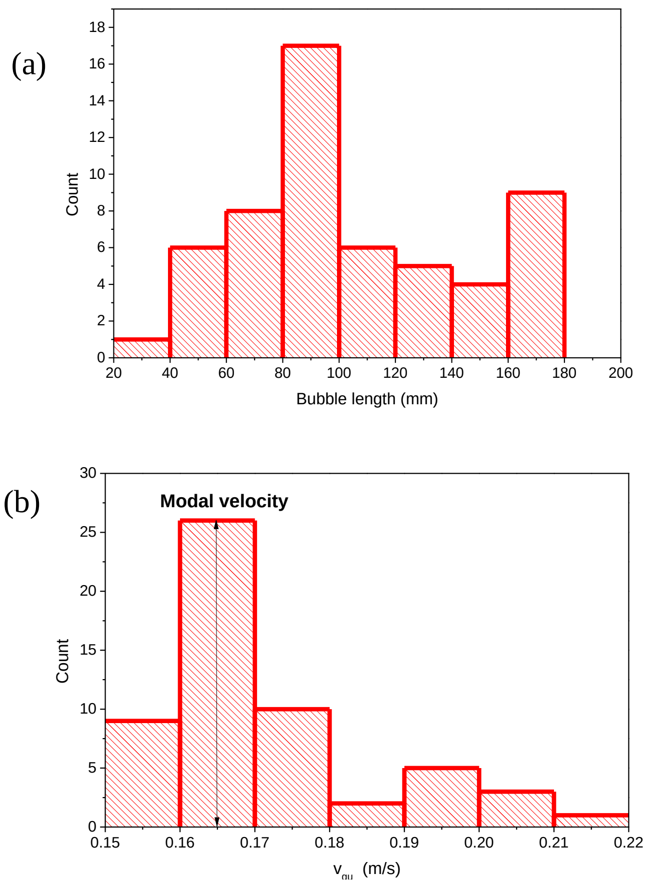

Figure 7.11: Histograms showing distribution of (a) Taylor bubble length distribution and (b) rise velocity with a modal velocity at 0.165 m/s under stagnant liquid conditions

7.3.2. Bubble flow regime

For the bubble flow regime, the injection of smaller bubbles carried similar to the procedure as described in section 7.3.1 to determine the C_o and v_{gu} values. The derived bubble diameters were validated with photos with a relative error of +\ - 4.2 % under a stagnant liquid condition.

Figure 7.12 and 7.13 present the relationship between the derived bubble diameters (spherical and ellipsoidal bubble) and rise velocities up to diameters of 10 mm, for a total of 50 spherical bubbles (figure 7.13 (a) and 32 ellipsoidal bubbles (figure 7.13 (b)). The results indicate variations in the rise velocities for each bubble category to be around an average of 0.21 m/s with standard deviations of +/- 0.019 m/s for the spherical and +/- 0.043 m/s for the ellipsoidal bubbles (see figure 7.13 (b) and (d)). The deviation from the average bubble rise velocities indicates the effect of an imbalance between interfacial tension and buoyancy force acting on each bubble surface. The impact of the imbalance in forces was evident given wobbly, zig zag and spiral motions of the bubbles. The value of the obtained rise velocities agree with results reviewed by Kulkarni and Joshi (2005) and Zhang *et al* .(2017) when they presented the effect of air bubble size on terminal rise velocity in varied water concentrations. In addition, the obtained average rise velocities are 27% higher than that obtained for the Taylor bubbles in this work. This increase in bubble velocity is due to the absence of drag forces contributed by the wall of the pipe. Based on the results of the average rise velocity, equivalent to the drift velocity, v_{gu}, equation 7.6 can then be used to determine an equivalent Froude number in respect of a bubble flow regime as 0.41.

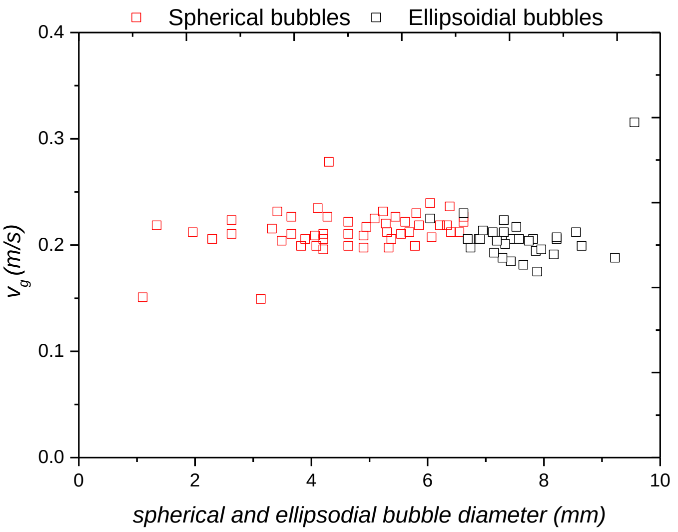

Figure 7.12: The relationship between spherical and ellipsoidal bubble diameter with rise velocity

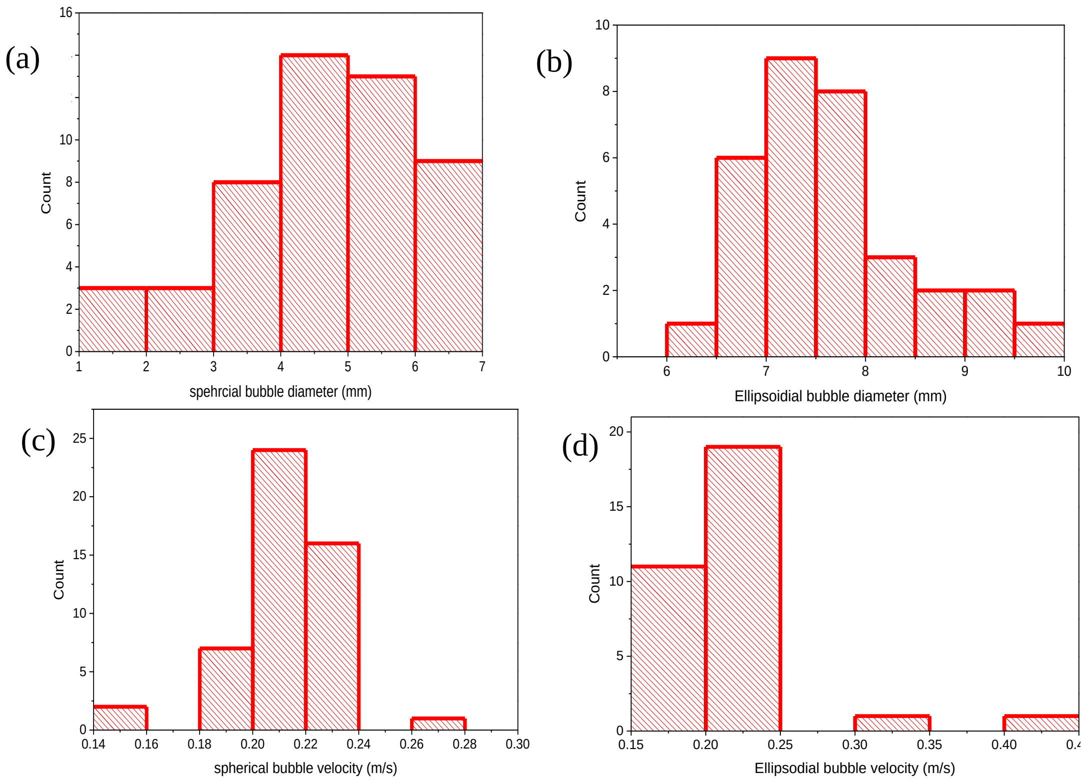

Figure 7.13: Histograms showing the distributions of (a) spherical bubble sizes (b) ellipsoidal bubble sizes (c) spherical bubble velocities and (d) ellipsoidal bubble velocities.

Further consideration is given to bubble caps that were formed as a result of bubble coalescence during the small bubble injection process. As shown in figure 7.14, increases in the cap diameter shows significant variation in the rise velocities between 20 – 32 mm length. The variation has to do with the unstable nature of the transitional phase from bubble to slug flow. According to the classic theory of Stokes, (1851) it is also apparent that the force imbalances exist on the surface of these caps which leads to variation in rise velocity. As a result, an average rise velocity of 0.19 m/s (figure 7.15 (b)) and standard deviation of +/- 0.0239 m/s are obtained. Therefore, the v_{gu} = 0.19 m/s provides an equivalent Froude number equal to 0.37.

For the sake of simplicity and real time measurement, the flow of dispersed phases in the form of small bubbles (spherical and ellipsoidal) and bubble caps are identified in this work as a bubble flow regime. A review of vertical upward flow by Morgado *et al.* (2016) back this claim, when they described the occurrence of a fully developed slug flow to be characterized by the presence of Taylor bubbles with lengths equivalent to 1.5D. It therefore follows that an average of the drift velocities from the small bubbles and bubble caps categories can then be made to represent the bubble flow regime drift velocity to be equivalent to 0.2 m/s.

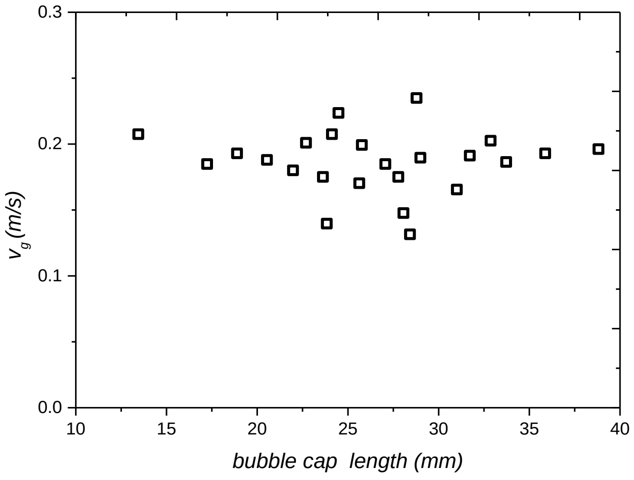

Figure 7.14: Relationship between bubble cap diameter and rise velocities at stagnant conditions of liquid.

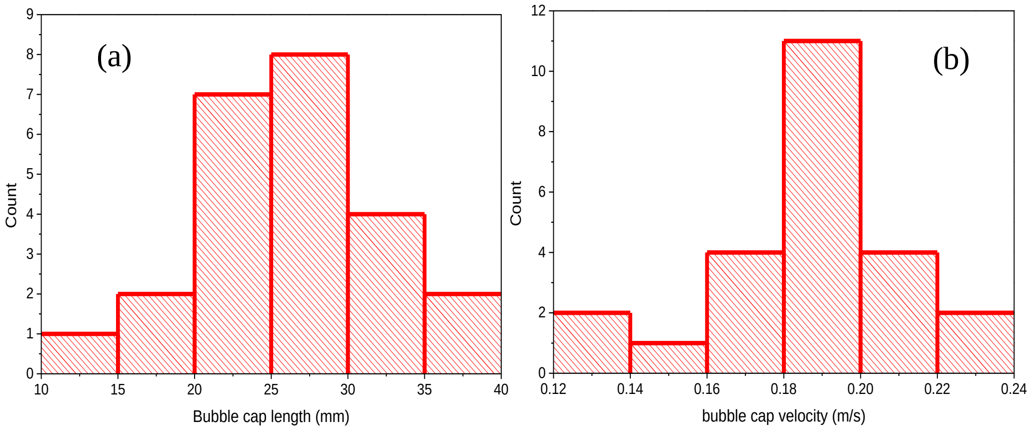

Figure 7.15: Histograms showing the distributions of (a) bubble cap sizes and (a) bubble cap velocities

Comparison of sensor bubble rise velocities with rise velocity correlations

Figure 7.16 presents a comparison of results of bubble rise velocities derived from the sensor and bubble rise correlations (summarized in table 2.2). of Harmathy (1960)., Mendelson (1967), Lehrer (1976) and Davies and Taylor (1950) under stagnant liquid conditions. The effect of bubble size corresponding to spherical bubbles (SB), ellipsoidal bubbles (EB) and bubble caps (BC), on the bubble rise velocities is observed. In the spherical bubble region, the correlations of Lehere (1976) and Mendelson (1967) predict initially high velocities relative to the sensor results (around 0.4 – 0.45 m/s). This was followed by a steep decrease in the velocities for increases in bubble size. More so, the correlation of Davies and Taylor (1950) predicts a rather low velocity with subsequent increases in velocity for increases in bubble size.

The correlation of Harmathy (1960) predicts a constant bubble rise velocity (at 0.24 m/s) for all bubble categories. In comparison, a general cluster of curves in the ellipsoidal bubble region from each correlation and of the sensor is observed, followed by divergence in predictions in the bubble cap region. The variations in trend over each bubble category is indicative of the varied assumptions made in developing each correlation. Bansode and Kulkarni (2015) present a comprehensive review of these correlations and ranges of validity.

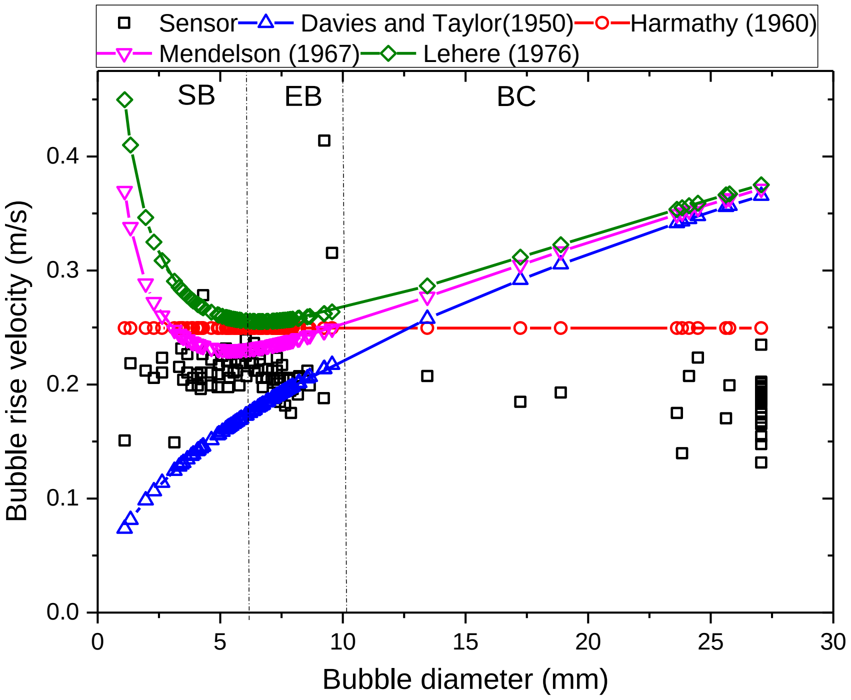

Figure 7.16: Comparison of bubble rise velocities for the sensor and correlations for spherical bubbles (SB) ellipsoidal bubbles (EB) and (BC) showing bubble size variation

Table 7.2 presents a summary of results of the average bubble rise velocities for the bubble flow regime and standard deviation relative to the sensor derived bubble rise velocities. It is observed that the Harmathy (1960) correlation produced the least deviation from the sensor rise velocity of +/-0.03 m/s for all bubble categories considered. Harmathy (1960) correlation was derived for a wide range of bubbles shapes, such as moderately ellipsoidal bubbles, spherical bubbles less and bubble caps, hence the least deviant from experimental results of this work.

Table 7.2. summary of average bubble velocities and standard deviation bubble rise correlations and sensor for the small bubbles under stagnant liquid conditions.

	Sensor	Harmathy	Davies and Taylor	Mendelson	Lehere
v_{gu} (m/s)	0.20	0.25	0.22	0.28	0.30
Standard deviation	0.02	0.03	0.11	0.08	0.07

Distribution coefficient for the bubble flow regime.

The C_0 for the bubble flow regime is determined for a continuous flow of gas and liquid. Figure 7.17 presents the relationship between the v_{mix} and $v_{gsensor}$ for typical bubble flow conditions that correspond to $v_{sl} =$ 0, 0.14, 0.29, 0.43 and 0.54 m/s for a constant v_{sg} = 0.13 m/s. The $v_{gsensor}$ derived represents the average arise velocity of captured bubbles under each flow combination of v_{sl} and v_{sg}. The results show a linear fit that defines a linear trend between v_{mix} and $v_{gsensor}$ with an obtained C_0 value of 1.18 from the slope of the linear fit. The v_{gu} value of 0.20 m/s is also set as the intercept given the results from section 7.3.2. 1. The C_0 obtained agrees with the *Co* of the Drift flux model proposed by Zubar and Findlay (1965).

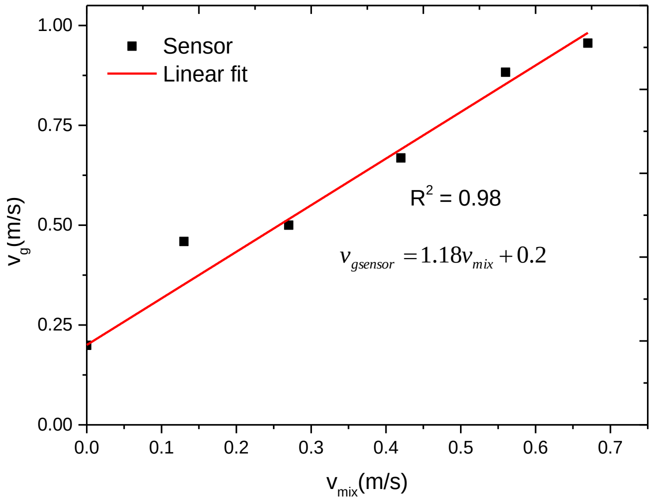

Figure 7.17: The linear fit for the determination of the distribution coefficient C_o under bubble flow conditions.

7.3.3. Summary of calibration model parameters

According to the results obtained for C_o and v_{gu} under the slug (section 7.3.1) and bubble flow regimes (section 7.3.2), the actual liquid velocity can readily be computed based on the calibration model of equation 7.11. Table 7.3 summarizes the calibration model parameters for the bubbles and slug flow regime with associated uncertainties.

Table 7.3. Summary of obtained calibration model parameters with associated uncertainties for the bubble and slug flow regimes.

Flow regime	Co	Uncertainty (-)	v_{gu} (m/s)	Fr	Uncertainty (m/s)
Bubble	1.18	+/- 0.05	0.20	0.41	+/- 0.05
Slug	1.11	+/- 0.01	0.17	0.33	+/- 0.015

7.3.4. Calibration model performance

The validation of the calibration model (equation 7.11) is required to acquire confidence in the actual liquid flow rate measurement and to investigate its performance under the churn and annular flow regimes. Given the complex nature of flow, it was a difficult task to experimentally determine the Co and v_{gu} of a churn and annular flow regimes the slug flow model parameters are assumed to be adequate for the churn flow conditions, while those of the bubble flow regime are assumed for the annular flow conditions. The structural similarities of phase dispersion between the bubble and annular flow and flow intermittences between the slug and churn flow regime are reasons for the assumptions made.

In absence of a gas liquid flow meter installed downstream of the test section, and in proximity with the NIOIRS, it is deemed appropriate to consider a comparison of the liquid flow meter superficial liquid velocity, v_{sl} with that predicted by the calibration model designated as v_{sl*}. Therefore, a re-write of the model expression in equation 7.11 to equation 7.12 is made to compute v_{sl*}, based on measurements of α_{sensor} and $v_{gsensor}$ and designated parameters, $\mathrm{C_o}$ and v_{gu} (to compute F_r) as,

$$v_{sl}{}^{*} = v_{lsensor}(1 - \alpha_{sensor}) = \frac{v_{gsensor}(1 - \alpha_{sensor}C_o) - F_r\sqrt{gD}}{C_o} \qquad (7.12)$$

In this work, new flow conditions are required to validate the calibration model expressed in equation 7.12. Two data sets are considered to achieve the validation process. First, is flow conditions from this work, not used in the derivation of the model parameters (detailed in section 7.3.4.1). The second data set is the experimental data from Shaban and Tavoularis, (2014)used to $v_{sl}{}^{*}$ with v_{sl} derived from their liquid flowmeter (discussions are detailed in section 7.3.5).

Validation from new test data

The new test data consists of flow conditions as indicated in figure 7. 18.. The flow conditions are selected to cover the bubble flow (black dashed box), slug flow (red dashed box), churn flow (green dashed box) and the annular flow (blue dashed box).

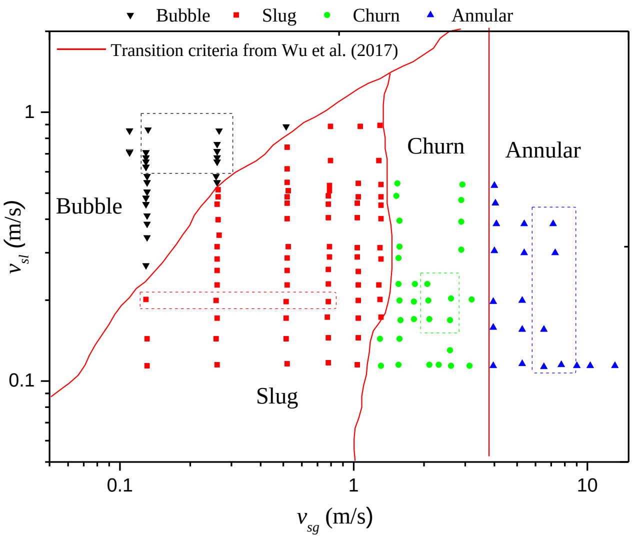

Figure 7.18: Test data conditions (bounded by the red dashed boxes) for the validation of the calibration model.

Figure 7.19 shows that for the data considered, the calibration model predicted the actual liquid velocity within an error band of +/-1.3% relative to maximum equivalent superficial velocity of the liquid flowmeter for the bubble and slug flow regime. An error band of +/- 7.5 % is obtained for the liquid velocity predictions under the churn and annular flow conditions. The deviation from parity was as expected given the chaotic nature of said flow regimes and the choice of model parameters. The model prediction for the bubble and slug flow are adequate within the confines of the flow configuration considered in this work, even though more work is required to improve the accuracy of prediction for the churn and annular flow cases.

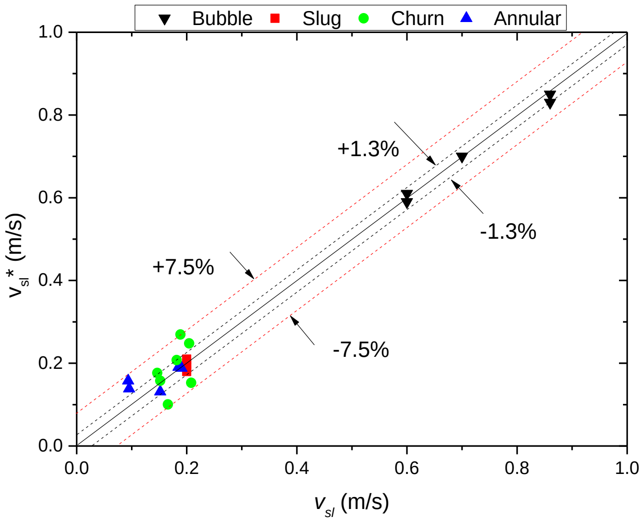

Figure 7.19: Parity between the superficial liquid velocities v_{sl}* derived as a result of equation 7.11 and superficial velocity from liquid flowmeter from the main rig v_{sl} of the current work.

Comparison with the work of Shaban and Tavoularis, (2014)

The selected experimental data from Shaban and Tavoularis, (2014) (see table 7.4) required as input for the calibration model consists of superficial liquid and gas velocities (v_{sl} and v_{sg}) from their single phase flow meter and actual gas velocity (v_{gsaban}) derived from cross correlation of a dual wire mesh sensor spaced at 0.002 m. The dual wire mesh sensors were installed on a 32 mm inner diameter at 75D of a vertical upward section of their air -water flow rig, which is similar to the configuration of this work.

Table 7.4.Selected data from the publication of Shaban and Tavoularis (2014) with calibration model parameters applied to determination of the superficial liquid velocity, v_{sl}*

Data of Shaban and Tavoularis (2014)					**Calibration model parameters used from this work**	
Flow regime	v_{sl} (m/s)	v_{sg} (m/s)	v_{mix}(m/s)	v_{gsaban} (m/s)	Co	v_{gu} (m/s)
Bubble	1.9	0.17	2.07	2.67	1.18	0.2
Bubble	2.3	0.17	2.47	3.08		
Bubble	2.9	0.17	3.07	3.39		
Bubble	2.3	0.1	2.4	2.86		
Bubble	2.3	0.17	2.47	3.08		
Bubble	2.3	0.3	2.6	3.64		
Slug	0.6	0.3	0.9	1.54	1.11	0.17
Slug	1	0.3	1.3	3.33		
Slug	1.4	0.3	1.7	4		
Slug	1	0.3	1.3	1.6		
Slug	1	0.6	1.6	2		
Slug	1	1.6	2.6	2.29		
Churn	0.4	7.4	7.8	8.898	1.11	0.17
Churn	0.7	7.4	8.1	0.24		
Churn	1	7.4	8.4	0.24		
Churn	0.7	5.3	6	0.24		
Churn	0.7	7.4	8.1	0.24		
Churn	0.7	9	9.7	0.24		
Annular	0.2	15	15.2	18.176	1.18	0.2
Annular	0.3	15	15.3	0.24		
Annular	0.6	15	15.6	0.24		
Annular	0.2	11	11.2	0.24		
Annular	0.2	13	13.2	0.24		
Annular	0.2	15	15.2	0.24		

Figure 17.20 presents the parity between the predicted superficial liquid velocity, v_{sl*}, and *that* extracted from Shaban and Tavoularis (2014). An error band of +/- 8.3% is obtained as a deviation from parity for all flow conditions considered. The errors derived can be attributed to bubble nose fragmentation during the wire mesh measurement of the cross-correlation

velocity as reported by Shaban and Tavoularis (2014). They further estimated that the spacing of the dual wire mesh introduced a 4-10% blockage of the cross section of their test section. In addition, this blockage was deemed to cause local distortion of flow which comes as a limitation to intrusive measurements. The associated errors from the drift velocity, void fraction and distribution coefficients from the calibration model used in this study also contribute to the overall error obtained in the prediction of v_{sl^*}. Overall, the calibration model shows a reasonable accuracy for the flow conditions considered, even with the intrusive measurement data used.

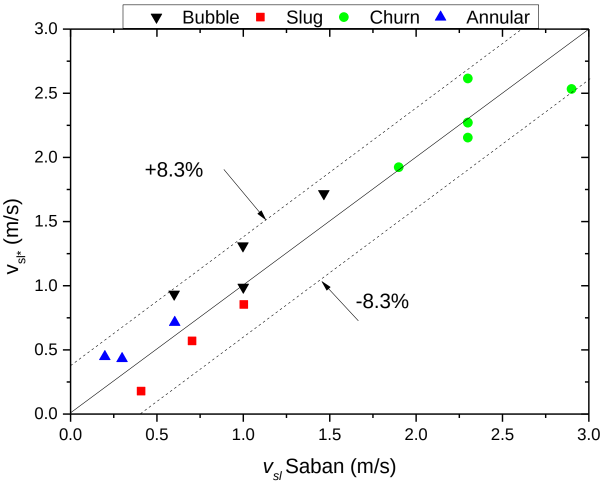

Figure 7.20 : Parity plot showing the effect deviation of predicted superficial liquid velocity v_{sl}* from superficial liquid velocity extracted from Shaban and Tavoularis, (2014), $v_{slsaban}$

7.4. Phase volumetric flow rates

According to the prediction adequacy of flow parameters obtained from the optical sensor, the actual volumetric flow rates of gas and liquid, $Q_{gsensor}$ and $Q_{lsensor}$, for a given cross sectional area A of pipe and known average void fraction can be determined by equation 7.13 and 7.14 respectively as ,

$$Q_{gsensor} = \alpha_{sensor} \, v_{gsensor} \, A \tag{7.13}$$

$$Q_{lsensor} = (1 - \alpha_{sensor}) v_{lsensor} A \tag{7.14}$$

7.4.1. Results of predicted phase flow rates

Figure 7.21 (a) and (b) present results that compare the actual phase flow rates derived from sensor and superficial phase flow rates derived from the liquid and gas flow meters under the flow conditions of 0.11 m/s < v_{sl} < 1 m/s and 0.13 m/s < v_{sg} <13 m/s.

In figure 7.21(a), a good parity between Q_{sl} and $Q_{lsensor}$ can be observed. The parity further confirms the slight compressibility of the liquid with changes related to variations in flow regimes and void fractions. In principle, this suggests that the density of the liquid (water) under atmospheric conditions of flow is slightly altered under the flow conditions considered. It should however be noted that significant variations in the actual liquid flow rate may occur at higher system pressures, which could be considered in future work.

The results presented in figure 7.21 (b) show that the $Q_{gsensor}$ agrees with the Q_{sg} at gas rates less than 50 l/min (from flow meter). For 50 l/min < Q_{sg} < 100 l/min, a decrease in $Q_{gsensor}$ relative to Q_{sg} is a result of the bubble collapse which creates onset of churn flow in the test section. Further increases in Q_{sg} > 100 l /min, shows a significant disparity due to higher $Q_{gsensor}$ at a high gas velocity, the dominance of slip effect between the gas and liquid occurs which is instigated by gas expansion that creates a decrease in gas density downstream of the test section. In theory, for a steady flow condition, where the mass rate is constant in and out of the test section, increases in gas volume must be followed by decreases in the gas density which makes the velocity of gas become greater than that of the liquid. Further discussions on the effect of increasing void fraction on the slip ratio are presented in next section.

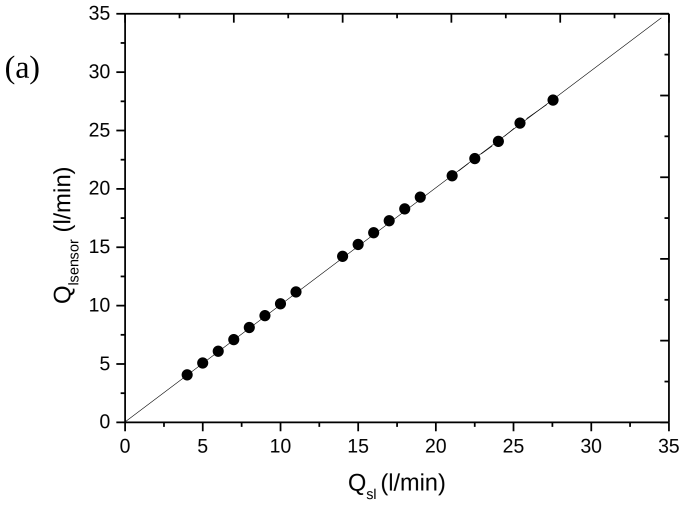

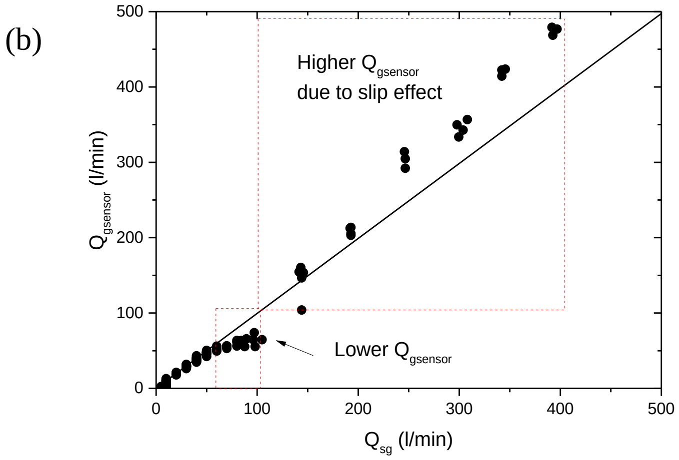

Figure 7.21: Comparison between the superficial and actual flowrates of (a) liquid and (b) gas.

7.4.2. Effects of flow regimes and void fraction on the slip ratio

Figure 7.22 presents results on the effect of the average void fraction on the slip ratio for varied flow regimes. As can be observed in the said figure, increases in void fraction leads to general increases in the slip ratio defined by the actual velocities of the gas and liquid.

For $0 < \alpha_{sensor} < 0.13$ which corresponds to the bubble flow regime, increases in void fraction leads to slight variations in the slip ratio ($S \approx 1.8$). The presence of small bubbles in a developed bubble flow regime have a minimal effect on the overall mixture density, given the fact that $\rho_l \gg \rho_g$. In addition, there is no coalescence of small bubbles which limits bubble growth. The jump in S from 1.8 to 4.0, around $0.13 < \alpha_{sensor} \leq 0.25$ essentially occurs due to the acceleration of small bubbles that lead to coalesce to form bubble caps. This defines the bubble to slug transition.

For $0.25 < \alpha_{sensor} < 0.58$, the occurrence of the slug flow regime is observed with variation in the slip ratio between 1.2 and 3.5. In this region, the occurrence of Taylor bubble growth for increases in void fraction leads to decreases in the mixture density. The decrease in mixture density is expected in principle to cause increases in the bubble rise velocities. However, the drag forces experienced by bubble surfaces in the vicinity of the pipe wall, impede the bubble rise motion, hence the observed variation in slip ratio. A similar transitional jump in the slip ratio is observed at around $\alpha_{sensor} \approx 0.6$. This jump represents a development of unstable Taylor bubbles which accelerate just before collapse to form a gas core.

The observed churn flow conditions correspond to the $0.6 < \alpha_{sensor} < 0.81$. In this region, the slip ratio shows general increases for increases in the void fraction. This increase is constituted by the increase in velocity of distorted bubbles and entrained bubbles created by the flooding mechanism also observed by Govan *et al.*, (1991). Beyond the churn flow conditions, the jump that represents the churn to annular flow, points to an occurrence of a developing gas core which accelerates in turn, to induce a flow reversal on the initial downward motion of the liquid film. At the instance of a flow reversal, it is expected that the liquid film decelerates hence increasing the slip ratio. Beyond the churn – annular transition flow regime conditions i.e., at $\alpha_{sensor} > 0.81$, steady increases in the slip ratio corresponds to increases in the gas core velocity relative to the rising liquid film as characterized by an annular flow regime.

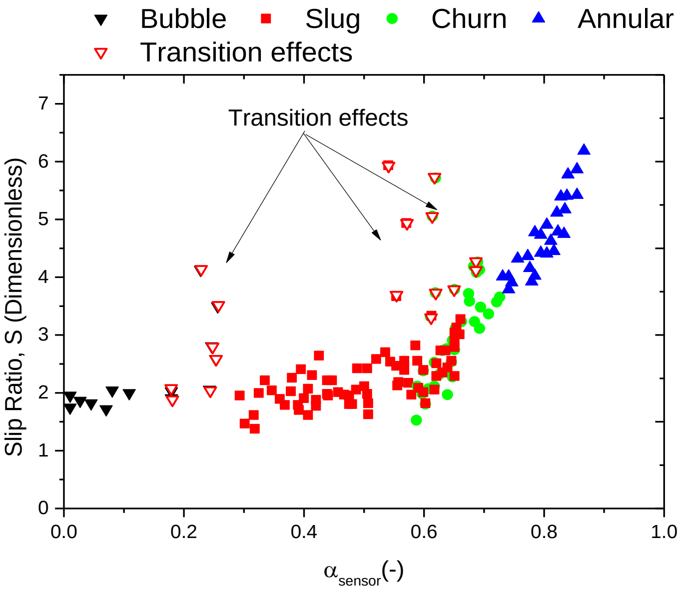

Figure 7.22: The relationship between the average void fraction and the slip ratio under varied flow regimes of a vertical upward flow.

7.4.3. Proposed algorithm for real time phase flow rate measurement.

According to the results from chapter 5 and 6, and the current chapter a real time algorithm can be proposed which enables the non-intrusive optical sensor to operate as a gas liquid flow meter. Key steps are described as summarized in figure 7.23; note the sensor regers to the 1480 nm NIORIS,

a. The sensor detects the GLF under prevailing flow conditions and outputs the results as the observed sensor responses over time as $V_{obs1}(t)$ and $V_{obs2}(t)$ from the BS and TS pair respectively.

b. The polynomial regression model (from chapter 5 equation 5.17) designated as FR model can then be applied to identify flow regimes in real time.

c. Phase fraction models are allocated according to the identified flow regime using the appropriate void fraction models summarized in table 6.1 of chapter 6. This enables the computation of the temporal void fraction for both sensor pairs as $\alpha_1(t)$ and $\alpha_2(t)$.

d. The actual gas velocity $v_{gsensor}$ can be measured by taking the average lag time τ^* of the peak R_{12} derived from the cross correlation of both sensor pairs. τ^* is then combined with the sensor spacing s, to compute $v_{gsensor}$.

e. The actual gas flow rate $Q_{gsensor}$ is computed by combining the α_{sensor}, $v_{gsensor}$ and a known pipe size D.

f. The actual liquid velocity $v_{lsensor}$ can be using the calibration model with inputs from the flow regime dependent Froude number F_r and corresponding distribution parameter Co, combined with α_{sensor} and the $v_{gsensor}$.

g. Finally, the actual gas flowrate, $Q_{lsensor}$ based on the $v_{lsensor}$ and respective sensor average void fraction α_{sensor} and known pipe diameter is then computed.

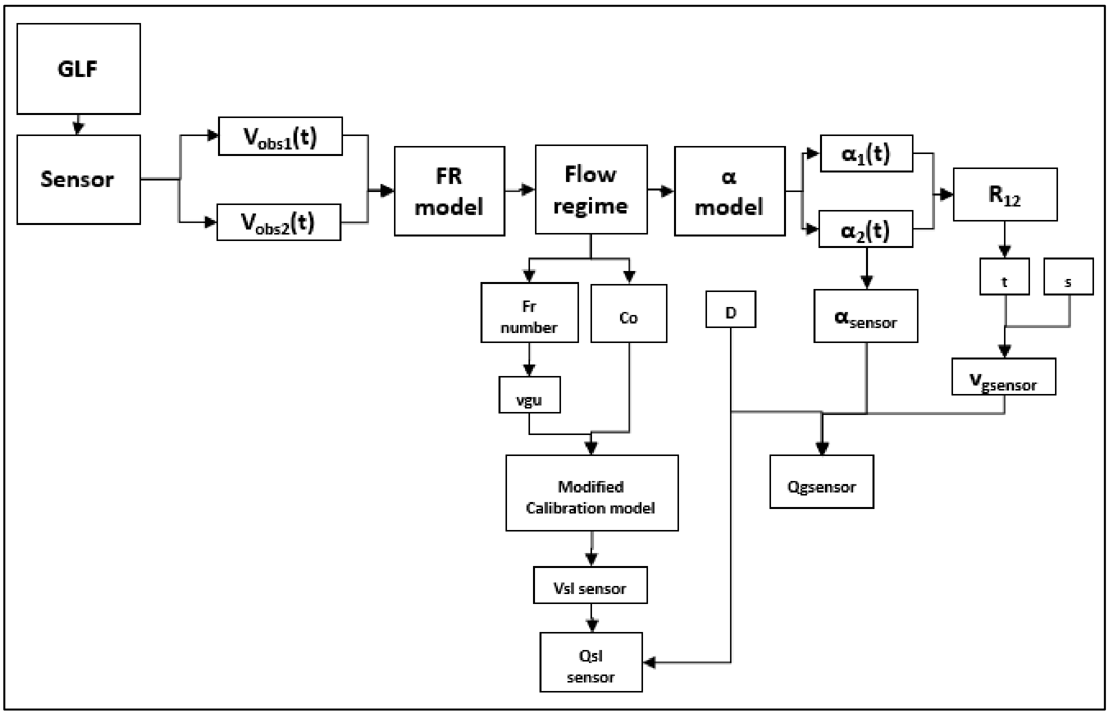

Figure 7.23: Proposed algorithm for real time measurement of gas and liquid flow rates.

7.5. Summary

This chapter has presented results that delineate the capability of a non-intrusive optical sensor to measure actual phase velocities and flow rates for the considered flow conditions. The actual gas velocity has been determined via a cross correlation of the temporal void fraction from each sensor pair. It was observed that the accuracy of the actual gas velocity measurement was flow regime dependent. This was evident when good agreements within an error band of +/- 1.5% relative to photos for the bubble and slug flow regime, were obtained. Under more chaotic flow conditions, such as the churn and annular flow regimes, a broader error band of +/- 3.3% was obtained relative to photos.

The measurement of the actual liquid velocity for the GLF, required the consideration of a calibration model modified from the classic Nicklin (1962) correlation and the separated flow model. The calibration required a modification of the drift velocity and distribution coefficients for the bubble and slug flow regime, which were further validated under the churn and annular flow conditions. A validation of the predicted actual liquid velocity from the calibration in the form of a superficial velocity was performed using test data from this work and that from Shaban and Tavoularis (2014). The predicted results were obtained as +/-1.3 % for bubble and slug flow with +/-7.5% error for the churn and annular flow conditions relative to the equivalent superficial velocities from the flowmeter. The validation using data from Shaban and Tavoularis (2014) gave a prediction error of +/-8.3% for all flow regimes . Apart from the propagated error of the calibration model, a key source of error was attributed to the intrusive nature of measurement used by Shaban and Tavoularis (2014) relative to the flow meters used in their study.

The prediction of phase flowrates using the actual gas velocity, average void fraction and known pipe size was achieved. The predicted actual liquid flow rates showed slight deviation relative to the superficial liquid flow rates from the flow meter. This was related to the slightly compressible state of the liquid at atmospheric conditions. However, the actual gas flowrate predicted, showed significant variations compared with that measured at the gas flow meters. The variation in gas density downstream if the test section led to this observation. More so, the effect of flow regime and void fraction on the slip effect between both phases was studied with results showing significant variations in the slip ratio between 1-7.0. Transitional jumps between flow regimes was observed and was suggested to be due to acceleration and deceleration of bubbles induced by coalescence and flow reversal mechanisms respectively.

Finally, a proposed real time algorithm which enables the optical sensor to operate as a gas liquid flow meter was discussed. This combines the flow regime identification, phase fraction determination, phase velocities and calibrated model parameters to determine the actual flow rates of gas and liquid.

Chapter 8

8. Conclusions and Recommendations

Based on the analysis of results from chapter 4, 5, 6 and 7, the main aim of applying the NIOIRS as a standalone measurement technology combined with adequate signal and statistical analysis has been achieved successfully.

8.1. Conclusions

The following under each objective was achieved and concluded as follows, specific to areas of flow regime identification, phase fraction determination, phase velocity and flow the measurement

8.1.1. Flow regime Identification

For a smaller pipe with less chaotic flow regimes, the use of statistical analysis i.e. counts distribution (PDF) can suffice as an objective identification method combined with the 880 nm NIOIRS response. More so, under larger pipe and chaotic flow regimes such as the churn and annular flow regimes machine learning method can be employed to train and predict adequately the flow regimes.in this work a novel application of supervised for objective flow regime identification has been achieved, where a polynomial regression and probabilistic LDA and QDA were applied to the 1480 nm NIOIRS response, providing excellent results. A real time application is possible using the fast regression model which was based on the established relationship between the average and standard deviation of the sensor response.

8.1.2. Phase fraction determination

The determination of phase fraction was made possible using a flow regime dependent model which accounted for the interfacial effects in a gas liquid flow. The derived models using the 880 nm for the test rig provided information on the potential of this method, even though the 880 nm sensor did not performance as well compared to the 1480 nm on the main rig. It recommended that the power requirements of the sensor may be improved when in larger pipe configurations. Overall, an Improved accuracy of phase fractions using a dual wavelength from both sensor types (880 nm and 1480 nm NIOIRS) was deemed adequate.

8.1.3. Phase velocities and flow rates measurement

Phase velocities and flow rates of gas and liquid were measured using the 1480 nm NIOIRS the accuracy of the gas velocity and gas flow rates using the cross-correlation method form both sensor pairs of the 1480 nm NIOIRS was adequate in the case of an upward vertical GLF. The accuracy of measurement is however dependent on the combined errors propagated from the phase fraction measurement approach.

The liquid velocity and liquid flow rate however were not straight forward measurements given the absence of a slip relationship data. Nonetheless, the application of a modified calibration model that was derived from the Nicklin type correlations and closure relationships made the actual liquid velocity measurement possible with reasonable degree of accuracy. In view of the degree of accuracy, results of the effect of more chaotic flow regimes such as the churn and annular flow regimes were quite reasonable when compared to validation results and data from literature.

8.2. Contributions

Using the NIOIRS as a standalone measurement technology combined with adequate signal processing, the following contributions have been made in this thesis

i. Novel application of a probabilistic approach of LDA and QDA for flow regime identification.

ii. Improved accuracy of phase fractions using flow regime dependent linear interpolation models for a water transmissive and absorbance optical sensor setups (880 nm, and 1490 nm) setup.

iii. A derived modified correlation for liquid rate determination of gas liquid flow. this would be enabling the better measurement accuracy of the multiphase flow metering and monitoring systems without prior knowledge of the superficial velocities.

iv. An elaborate review on existing applications of non-intrusive IR sensing technique to characterize gas liquid flows.

v. Application of a polynomial regression model for real time flow regime identification

vi. Testing the capability of NIOIRS over a full range of flow regimes for a vertical upward flow in 0.018 m and 0.0273 m test section.

vii. Deriving an improved flow regime dependent phase fraction models to account for bubble interfacial scattering.

viii. Determination of entrained bubble fraction in the churn flow regime and validation via image processing.

ix. A proposed algorithm for gas liquid flow metering

8.3. Recommendations

At the end of this work, the following recommendations are made in the specific areas for further extensive work

8.3.1. Improvement on sensor configuration

A new reflective and transmissive configuration to improve liquid film characterization, following the total internal reflectance concept. Consideration of a multiple sensor array with polarization of rays which is expected to improve the chordal measurement across the pipe. F furthermore the. Vassallo *et al.*, (1993) who combined a front and back scatter optical sensor to estimate the liquid velocity, even though they used a dye to locate the fluid vortices, the new improvement can eliminate a contamination of the flow stream by applying advanced analysis of the responses received from the sensor configuration.

8.3.2. Modification of rig setup

Application under higher pressure and temperature systems with the installation of mass flow meters for calibrating and testing for two phase flow measurement. Installation of a 2-phase flow meter downstream to further validate liquid rate measurement.

8.3.3. Improved signal analysis

Application of wavelet analysis to decompose average frequencies into specific frequencies improving accuracy of frequency measurement. The derived regression model will be used in a real time application to allocate valid phase fraction models required ultimately for phase flow rate measurement. LDA can be extended to real time monitoring using the coefficients of a canonical analysis and FDA. The time scales of identifying a stable flow regime in the sensing area needs to be investigated in the case of other pipe sizes and configurations to test the robustness of the derived regression model. The performance of combining the NIORS method with unsupervised learning for flow regime identification is also worth considering.

Development of NIOIRS responses into real time images of the void fraction of phases in the pipe using tomographic visualization techniques is also worth considering for the future.

Appendix A

A.1. Mixture properties

Mixture density (ρm*)* – The mixture density of a gas-liquid flow can be calculated as shown in equation A.1. The density is an important property for the calculation of pressure drops of flow.

$$\rho_m = \alpha\rho_g + (1-\alpha)\rho_l \tag{A.1}$$

Mixture viscosity (μm) – This property represents the resistance to the flow of gas and liquid in the pipe and the fluid interface. The individual viscosities of each phase is averaged based on the phase fractions. It is also an important property for defining the turbulence of the flow mixture via the estimation of the Reynolds number and friction factor. The mixture viscosity of a GLF is calculated as:

$$\mu_m = \alpha\mu_g + (1-\alpha)\mu_l \tag{A.2}$$

Governing Equations

To be able to describe and predict multiphase flows, governing equations which include all physical interactions must be defined. The applications of conservation of mass, momentum energy and mass transfer are the bedrock for modeling MPF. Figure A.1 illustrates a general case for the flow of phase k from N number of phases, in a conduit the area covered by the phase as *Ak* over the total area A, the inlet conditions defined as phase pressure *pk*, phase density *ρk*, phase velocity *vk* over a control axis, *dx*. This concept can be extended to GLF

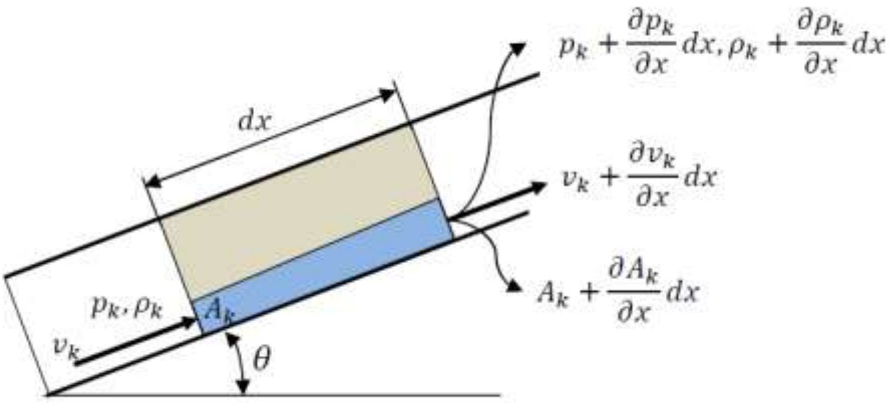

Figure A.1. Compressible multiphase flow (Adapted from Bratland, 2010)

Mass conservation

The mass balance for phase k is defined by equation A.3. Each term from the left-hand side to the right-hand side represents the following respectively

i. accumulated mass,
ii. net mass flow into the control volume,
iii. mass from other phases and $\Gamma_{ki} = \frac{\dot{m}_{ki}}{A\,dx}$
iv. mass from other sources,$\Gamma_{kw} = \frac{\dot{m}_{kw}}{A\,dx}$

$$\frac{\partial(\alpha_k \rho_k)}{\partial t} + \frac{\partial(\alpha_k \rho_k v_k)}{\partial x} - \Gamma_{ki} - \Gamma_{kw} = 0 \tag{A.3}$$

Where α_k is the phase fraction (A_k/A), $\dot{m}_{ki}$ and $\dot{m}_{kw}$ are the mass flows due to mass transfer from other phases and from the wall respectively. Most models neglect the mass transfer components since the overall mass transfer sums up to zero, between phases assuming a closed system, with no pipe perforations

Momentum conservation

The momentum expression is based on Newton's second law, Here of N phases flowing in a conduit interact under varied forces which form a balance. Equation (A.5) describes a general expression of the balance of momentum in the with respect to the phase k.

Mass. Acceleration = Sum of all forces

$$(A\alpha_k \, dx \, \rho_k) . \frac{dv_k}{dt} = \sum F_k \tag{A.4}$$

Where the sum of all forces acting on phase k include,

i. Pressure force due to pressure gradient along the pipe ($F_{kpg} = \alpha_k \frac{\partial p_k}{\partial x}$)
ii. Gravity force along the pipe due to elevation ($F_{kg} = \alpha_k \rho_k g \sin\theta$)
iii. Frictional force from interaction of phase k with other phases (R_{ki})
iv. Friction force from the walls of the pipe (R_{kW})
v. Force due to surface tension from interfaces with other phases (S_{ki})
vi. Forces due to surface tension with the wall of the pipe. (S_{Kw})

$$\begin{aligned} \frac{\partial(\alpha_k \rho_k v_k)}{\partial t} + \frac{\partial(\alpha_k \rho_k v_k^2)}{\partial x} = & -\alpha_k \frac{\partial p_k}{\partial x} + (R_{ki} + R_{kW}) + (S_{ki} + S_{kW}) \\ & + (v_{ki}\Gamma_{ki} + v_{kW}\Gamma_{kw}) - \alpha_k \rho_k g \sin\theta \end{aligned} \tag{A.5}$$

Surface tension has been ignored by most models but could be considered quite significant for discontinuous flows regimes such as bubble flows. The inclusion of mass transfer terms is made to account for phase changes for momentum changes of each phase in the pipe.

Energy conservation

To account for the energy balances in the complex flow, a sum of energies to and from the phase k are considered. The changes that occur in the internal energy (E), work (w) and heat (q) of each phase k in the pipe are considered for situations where transients in temperature are to be modeled. For this work, adiabatic conditions are considered and thus the energy transfer between phases and the wall are not critical. A general energy balance expression is defined in equation (A-6).

$$\frac{\partial E}{\partial t} = \frac{\partial [v(E+p)]}{\partial x} + q + w \tag{A.6}$$

Although these governing equations form the basis of modelling MPF for most fluids. Closure relationships, which refer to fluid property's correlations are required to complete the set of conservation equations. Forces due to surface tension, friction, and phase changes could be determined for varied flow configurations by applying these closure relationships. Also, the conservation assumes a continuous phase flowing in the pipe. This assumption would make modelling bubbles and slugs in the pipe in-accurate and thus a form of averaging is normally used to reduce errors in calculation. Bratland (2010), presents a detailed account of these problems for varied flow regimes. It is also observed that the phase fraction αk is a key parameter in the balance equations. The call for more experimental work to develop better representative correlations for adequate MPF modelling and characterization is vital for the industries

Appendix B

B.1. Experimental flow rigs and data processing

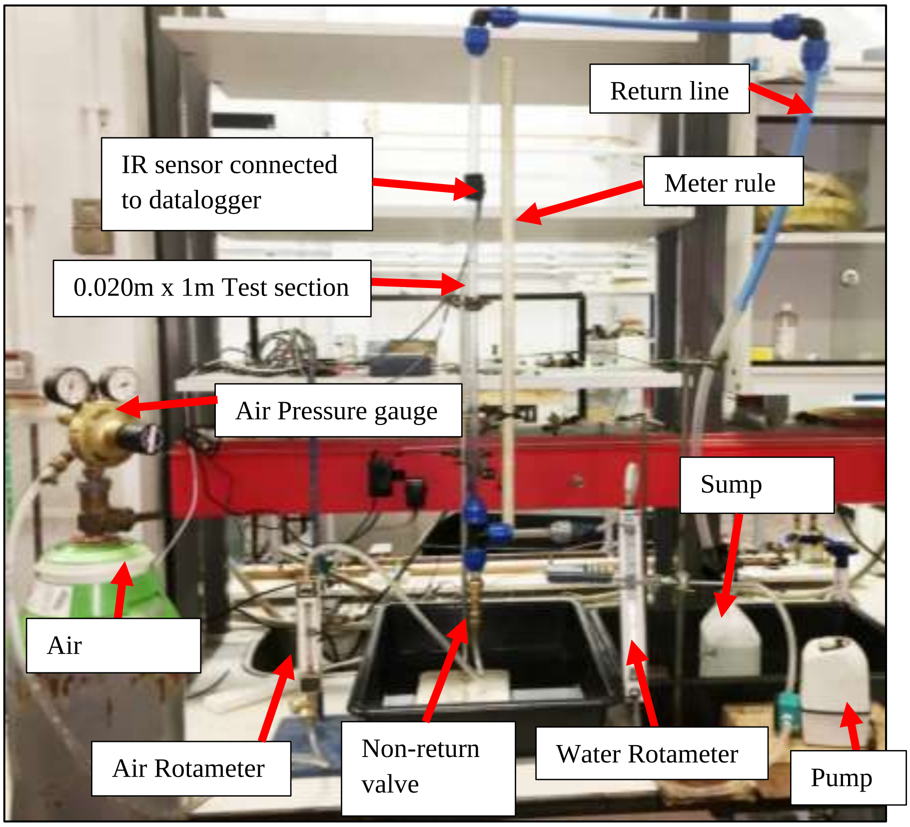

Figure B.1 - Figure Laboratory set up of the Test flow rig

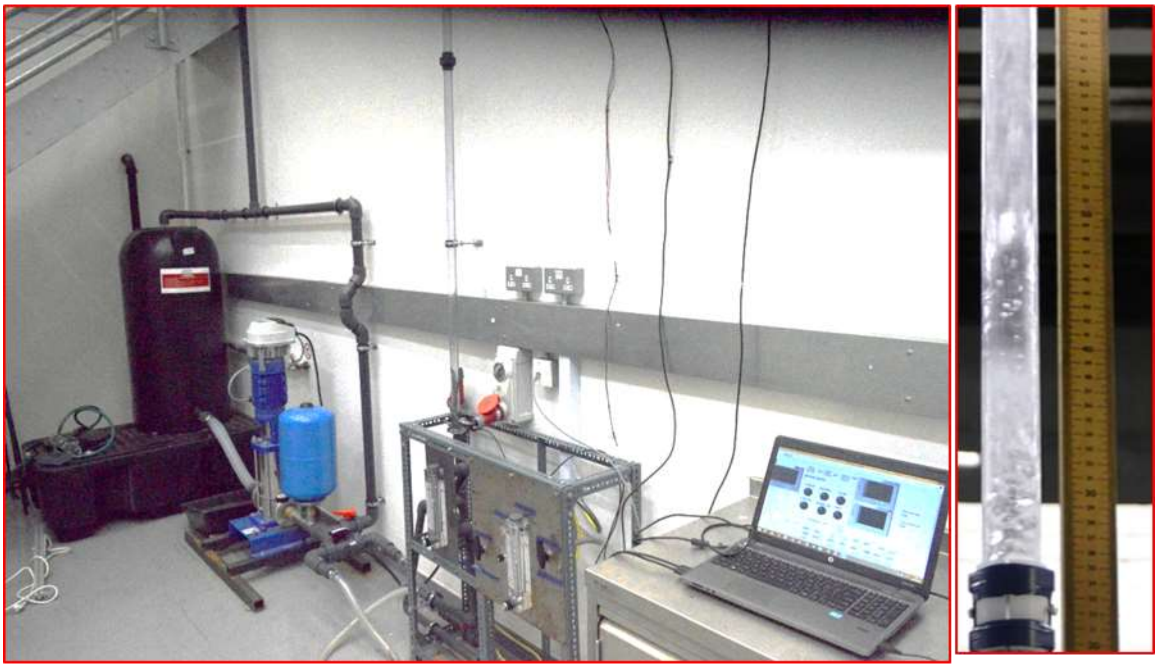

Figure B.2: Picture of the lower level of the (a) 27 mm x 6 m Experimental air water flow rig and (b) close capture of two-phase flow in the test section, installed in the Chemical and Petroleum Laboratory E- 135, London South Bank University.

B.2. Data Analysis tools for the NIOIRS analysis

The table shows the key analysis methods with corresponding software packages used in achieving key results from the air / water Experimental flow rig at the Petroleum and Chemical engineering Laboratory of LSBU.

Analysis	Software package
Data Acquisition	Pico scope 6
Data treatment and storage	Microsoft Excel
Flow regime identification	Origin Lab pro
Error analysis	Origin Lab pro
Velocity Measurement	Origin Lab Pro + Microsoft image editor
Image processing	Origin Lab pro + Microsoft image editor+ Image J
Real time application	National instruments LabVIEW, 2014
Sensor modelling	COMSOL Multiphysics

B.3. Data acquisition and storage

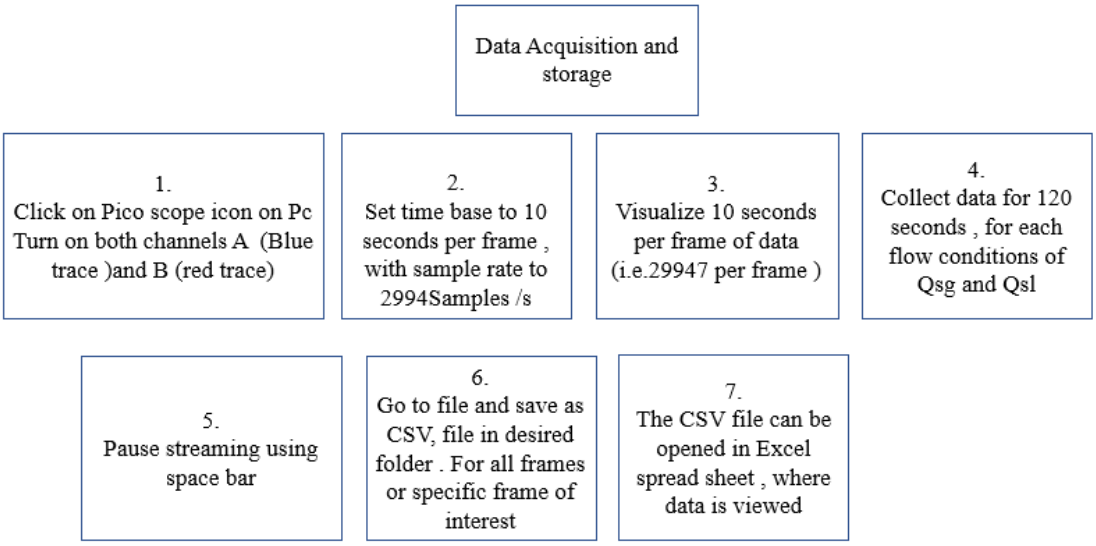

Data Acquisition and storage

1. Click on Pico scope icon on Pc Turn on both channels A (Blue trace)and B (red trace)

2. Set time base to 10 seconds per frame , with sample rate to 2994Samples /s

3. Visualize 10 seconds per frame of data (i.e.29947 per frame)

4. Collect data for 120 seconds , for each flow conditions of Qsg and Qsl

5. Pause streaming using space bar

6. Go to file and save as CSV, file in desired folder . For all frames or specific frame of interest

7. The CSV file can be opened in Excel spread sheet , where data is viewed

Appendix C

C.1. Further results from the 880 nm Optical Sensor On test rig

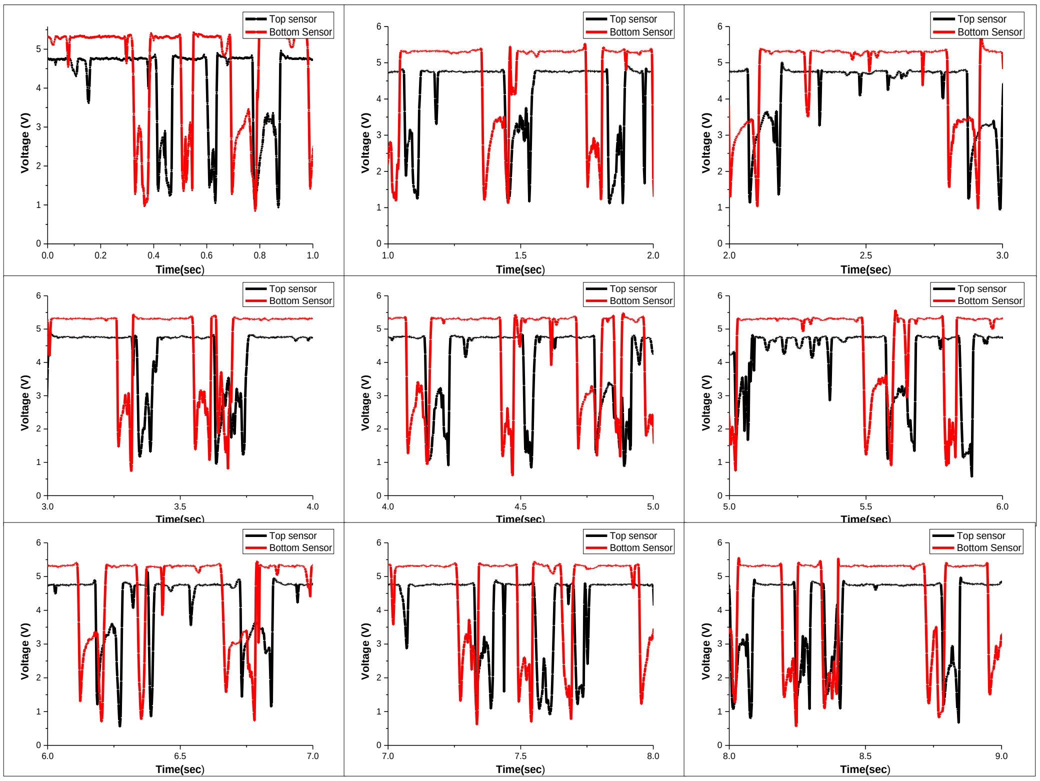

Responses of the top and bottom sensor pair

Appendix D

D.1. Numerical Simulation Results from COMSOL

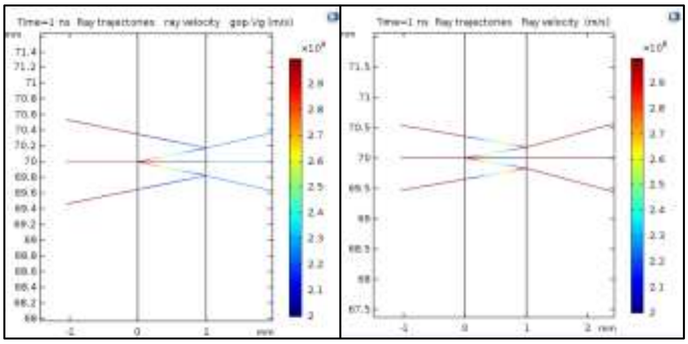

Effect of pipe wall thickness on infrared rays

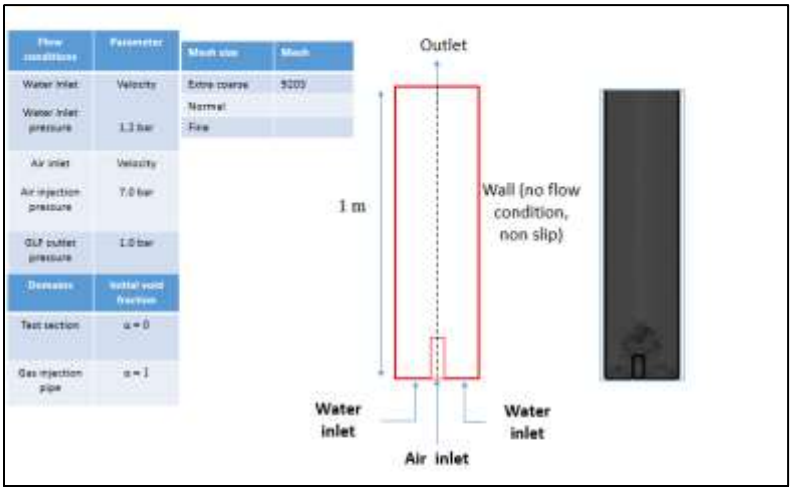

Flow conditions	Parameter
Water inlet	Velocity
Water inlet pressure	1.2 bar
Air inlet	Velocity
Air injection pressure	7.0 bar
GLF outlet pressure	1.0 bar
Domains	**Initial void fraction**
Test section	α = 0
Gas injection pipe	α = 1

Mesh size	Mesh
Extra coarse	9203
Normal	
Fine	

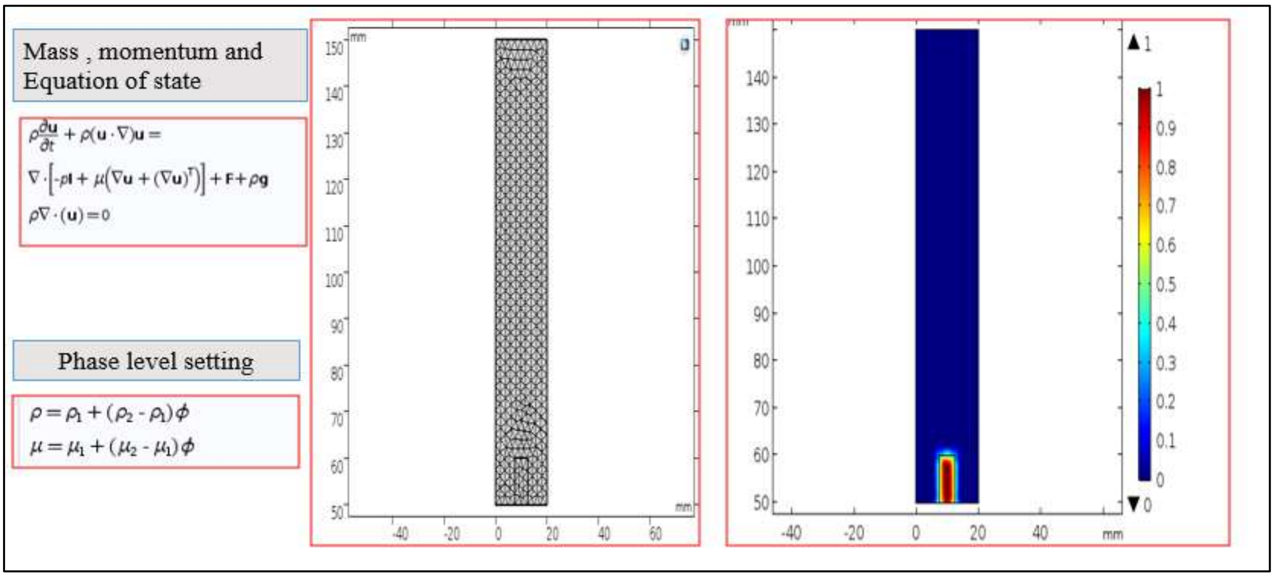

Mass , momentum and Equation of state

$$\rho\frac{\partial \mathbf{u}}{\partial t} + \rho(\mathbf{u}\cdot\nabla)\mathbf{u} =$$
$$\nabla\cdot\left[-p\mathbf{I} + \mu\left(\nabla\mathbf{u} + (\nabla\mathbf{u})^T\right)\right] + \mathbf{F} + \rho\mathbf{g}$$
$$\rho\nabla\cdot(\mathbf{u}) = 0$$

Phase level setting

$$\rho = \rho_1 + (\rho_2 - \rho_1)\phi$$
$$\mu = \mu_1 + (\mu_2 - \mu_1)\phi$$

Level setting method used in COMSOL simulation of air water system.

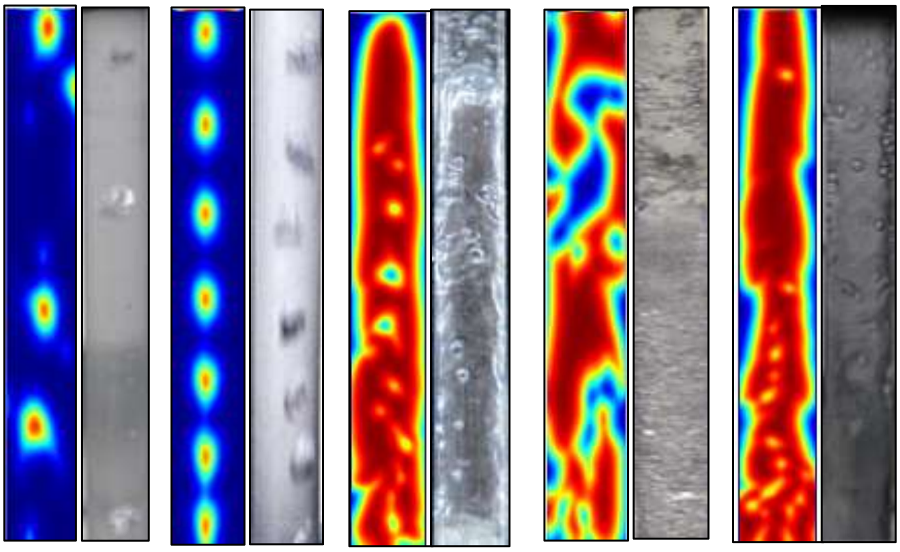

Figure: Effect of increasing gas rates at constant liquid velocity (Main rig)

Appendix E

E.1. Further results on Mahanolobis distances

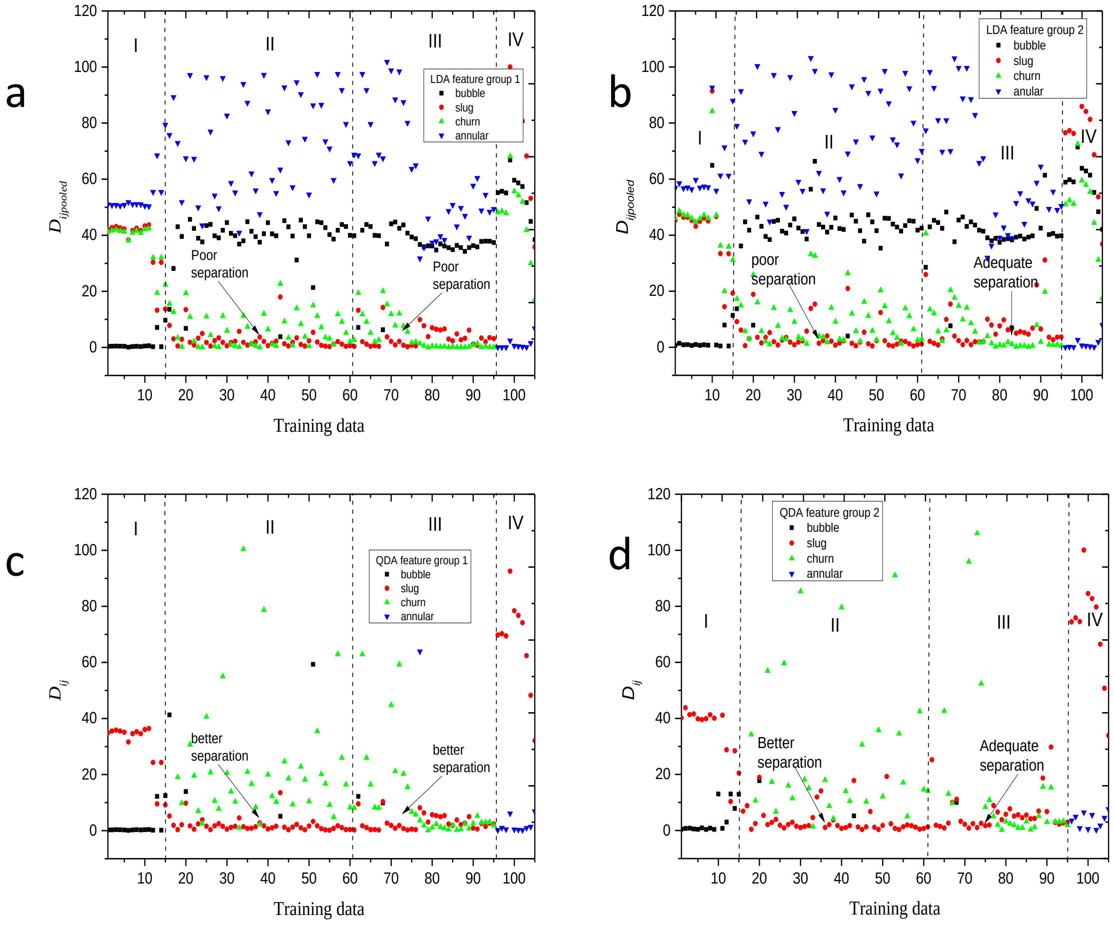

Figure E.1: Computed Maholanobis distances for the Training data.

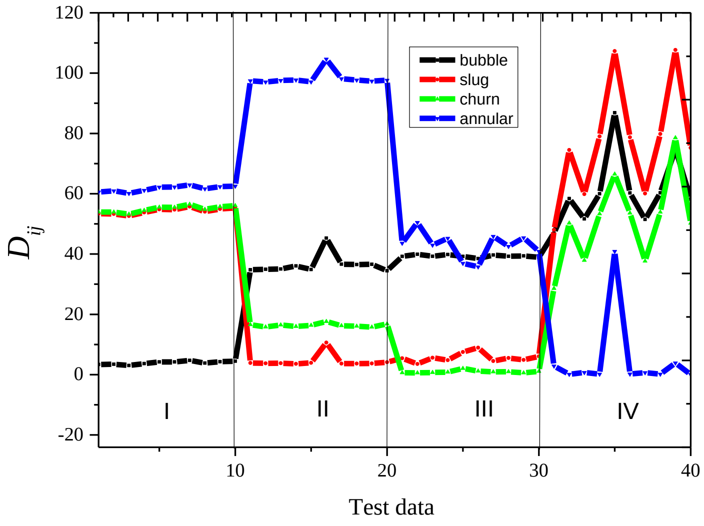

Computed Maholanobis distances for the test data for LDA feature group 2

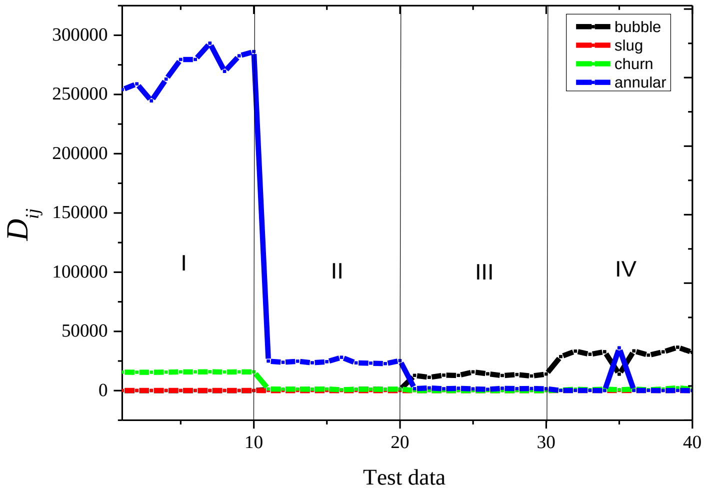

Computed Maholanobis distances for the test data for QDA feature group 2

Appendix G.

G.1. Further Results from the 1480 nm Optical Sensor on Main Rig

Average structural frequency fsavg

The number of passing structures in the form of bubble clusters, slugs or rising waves in the annular flow regimes can be determined using the power spectral density function. An autocorrelation of the Fourier transforms computes the frequency distribution in terms of the power of the sensor response. The frequency corresponding to the peak power of the void fraction trace corresponds with the average frequency of the bubbles past the sensors over time. This method has been compared with manual counting on the trace and represents a good estimation of structural intermittence such as in the slug flow regime. For the bubble flow regime, similar analysis may provide a valid representation of bubble frequency, however the variation in bubble shape and sizes. Applying this approach to the annular flow is expected to capture the peak frequencies of the disturbance waves represented in the void fraction response, which is compared to other works.

At a constant liquid superficial velocity v_{sl} = 0.29 m/s, the results of the frequency distribution (PSD plots) derived from the temporal void fraction responses for typical bubble, bubble – slug, slug flow, slug - churn, churn and annular flow regimes are presented in figures G.1

For the bubble flow regime (at v_{sg} = 0.13 m/s) of figure G.1 (ai and aii), the PSD presents a range of frequencies between 1.0 to 8.3 Hz, with a peak frequency of 1.0 Hz. The obtained spread of frequencies is largely due to the presence of rising bubbles of varied sizes (below 0.35D) that travel upwards at varied velocities (results on the variance in bubble velocities is discussed in section chapter 7). Further to this, Figure G.1(aii) shows a maximum power obtained as $5\text{x}10^{-5}$, $1/\text{Hz}^2$, which is indicative of the variation in α(t), between 0 – 12 %, except for the void fractions at 6.8 and 8.2 s that are around 25% as shown in figure G.1. (ai). The PSD of the bubble – slug flow transition presented in figure 6.16 (bii) shows a general increase in power to a maximum of $1.1\text{x}10^{-3}$ $1/\text{Hz}^2$.

This corresponds to a 20-fold increase compared to the bubble flow PSD results in figure G-1(aii). The increase in power is due to the increases in spectral variance in α(t) marked by the development of bubble caps at v_{sg} = 0.26 m/s. The corresponding frequency range of 1.2 – 7.0 Hz, is further evidence of the presence of a dominant size of bubbles (i.e. bubble caps) compared to the presence of small bubbles in the bubble flow regime.

The PSD presented in figure G.1 (cii) for a fully developed the slug flow regime at v_{sg} = 0.53 m/s shows a single dominant peak with local frequencies of the range 1.0 - 2.9 Hz. The dominant peak frequency at 1.2. Hz was obtained at a power of 3.6 x10^{-2} $1/HZ^2$, which is a 10-fold increase relative to the bubble – slug transition in figure 16.6 (bii). The dominant frequency is mainly due to the rise of Taylor bubbles in the slug flow regime, which represents an average of 1.1 Taylor bubbles per second. This estimation agrees with the corresponding temporal void fraction in figure G.1(ci).

Figure G.1 (di) presents a typical slug – churn transition temporal void fraction series, which corresponds to the PSD in figure G.1 (dii). This shows an increase in frequency range between 0.4 - 4.4 Hz. Two distinct peak frequencies can be observed. The first is the peak frequency which remained at 1.2 Hz which represents fluctuation created by unstable Taylor bubbles. The second peak can be found at 0.8 Hz, which is as a result of collapsing elongated bubbles, which tend to slow down due to the churn effect, hence a lower frequency is observed. A notable reduction in the maximum power to 3.0 $1/Hz^2$ can also be observed due to bubble collapse and formation of smaller bubbles which further cause lower intensity fluctuations in the void fraction. Hossain *et al.*, (2019) recently investigated the frequencies in slug and churn flow regimes for increasing gas superficial velocities, with similar trends in their PSD results.

The PSD corresponding to the developed churn flow regime at v_{sg} = 1.56 m/s in figure G.1 (e. ii) is presented with further variation in the frequencies, however with a general reduction in power compared to the slug – churn transition results in figure 16.6 (dii), can be observed followed by a frequency range of 0.3 - 5.6 Hz. An increase in frequency range indicates the variations in temporal void fractions due to the high gas velocity (v_{sg} = 1.56 m/s). Further to this, according to the bubble coalesce mechanism a high void fraction of entrained bubbles in the liquid slug leads to increases in frequency at a low power of fluctuation. The collapsing elongated bubbles also create a low frequency band with a higher power of fluctuation (see figure G.1. (ei) for fluctuations in void fraction). Results of the PSD can also be compared to the work of Rocha and Simões-Moreira, (2008) who highlighted a similar shift in frequency band for a churn flow regime.

Figure G.1(fi) presents a typical temporal void fraction series for a developed annular flow regime, which indicates varying liquid film effect with 5 and 10 seconds. The corresponding PSD in figure 16.6(fii), presents frequencies, that are mainly due to the disturbance waves of the liquid film in the range 0.3- 5.6 Hz similar to the churn flow condition in figure 16.6(eii).

However, the maximum power of fluctuation ($6.0\text{x}10^{-3}$ $1/HZ^2$) shows an equivalent 10 -fold decrease compared to the churn flow regime case in figure 16.6(eii). This reduction is due to the decrease in void fraction fluctuations, given the presence of a steady gas core, with slight variations in α(t) caused by disturbance waves of the liquid film.

In summary, even though there were no unique frequency band for each flow regime, the results show that the spectral power from the PSD is directly proportional to the variance of the temporal void fraction response relative to the prevailing regimes. Therefore, increases in variance indicate increases in structural dimensions in a two-phase flow condition. In effect, the relationship between the average sensor response and standard deviation in chapter 5 supports this claim, where the signal variance increases for increasing gas fraction up to a maximum indicating the bubble growth from bubble to slug flow regime and then decreases following the bubble break up in the churn and annular flow regimes.

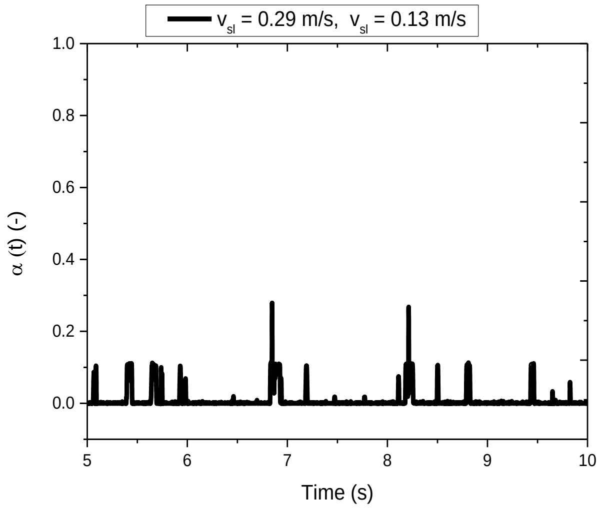

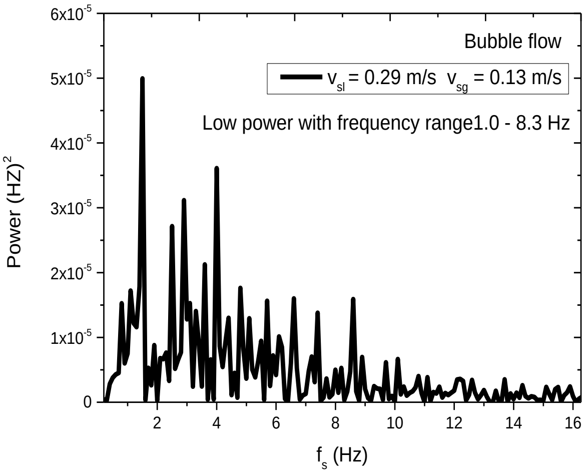

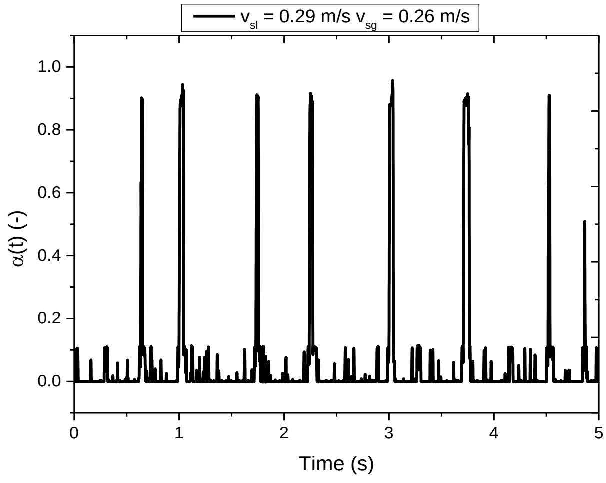

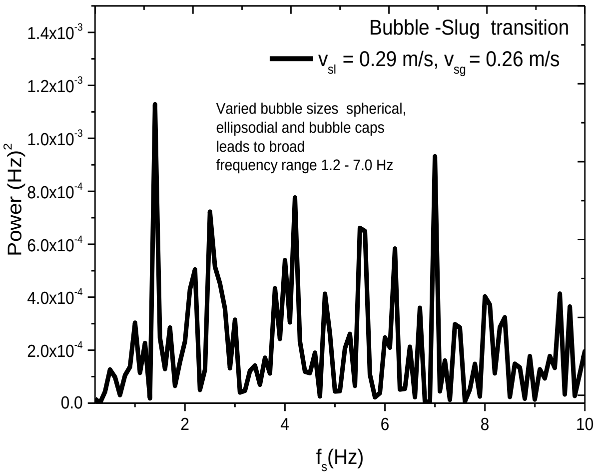

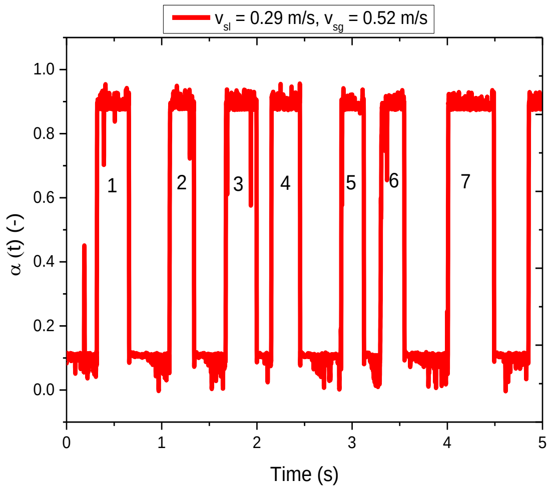
v_sl = 0.29 m/s, v_sg = 0.52 m/s
α (t) (-)
1.0
0.8
0.6
0.4
0.2
0.0
1
2
3
4
5
6
7
0
1
2
3
4
5
Time (s)

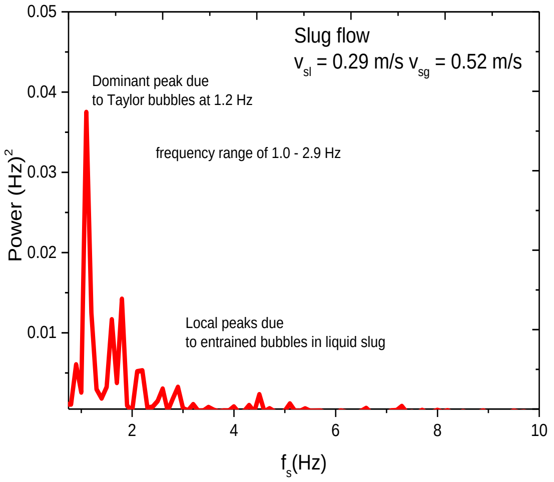
0.05
0.04
0.03
0.02
0.01
Power (Hz)^2
Slug flow
v_sl = 0.29 m/s v_sg = 0.52 m/s
Dominant peak due
to Taylor bubbles at 1.2 Hz
frequency range of 1.0 - 2.9 Hz
Local peaks due
to entrained bubbles in liquid slug
2
4
6
8
10
f_s(Hz)

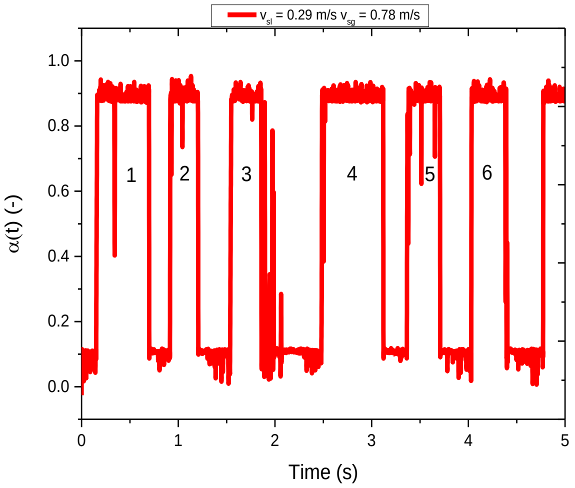
v_sl = 0.29 m/s v_sg = 0.78 m/s
α(t) (-)
1.0
0.8
0.6
0.4
0.2
0.0
1
2
3
4
5
6
0
1
2
3
4
5
Time (s)

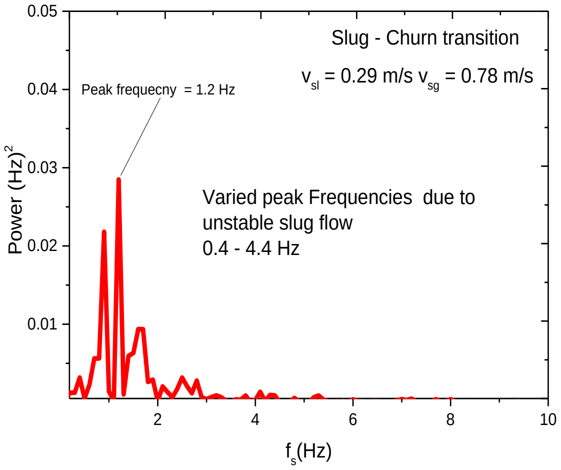
0.05
0.04
0.03
0.02
0.01
Power (Hz)^2
Slug - Churn transition
v_sl = 0.29 m/s v_sg = 0.78 m/s
Peak frequecny = 1.2 Hz
Varied peak Frequencies due to
unstable slug flow
0.4 - 4.4 Hz
2
4
6
8
10
f_s(Hz)

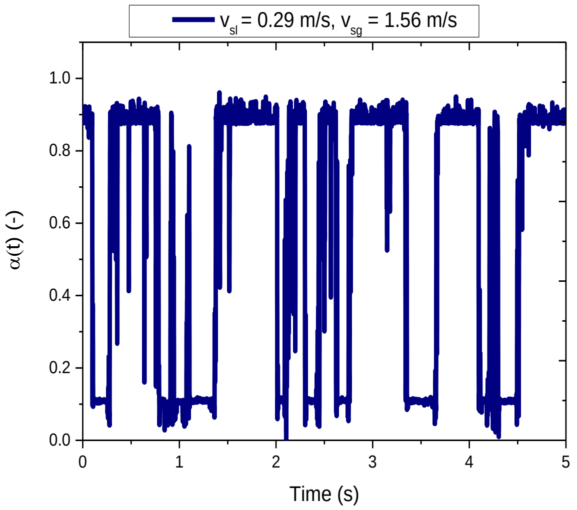
v_sl = 0.29 m/s, v_sg = 1.56 m/s
α(t) (-)
1.0
0.8
0.6
0.4
0.2
0.0
0
1
2
3
4
5
Time (s)

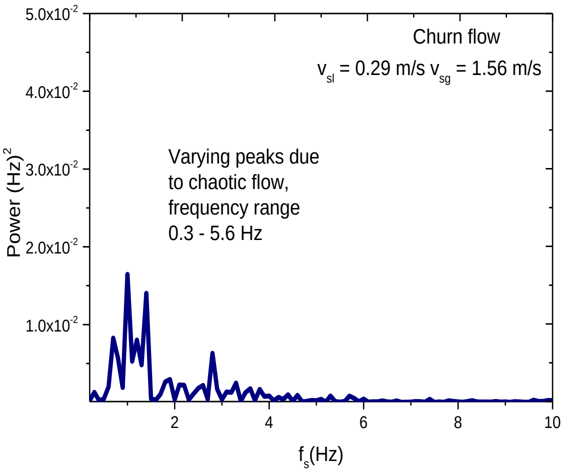
5.0x10^-2
4.0x10^-2
3.0x10^-2
2.0x10^-2
1.0x10^-2
Power (Hz)^2
Churn flow
v_sl = 0.29 m/s v_sg = 1.56 m/s
Varying peaks due
to chaotic flow,
frequency range
0.3 - 5.6 Hz
2
4
6
8
10
f_s(Hz)

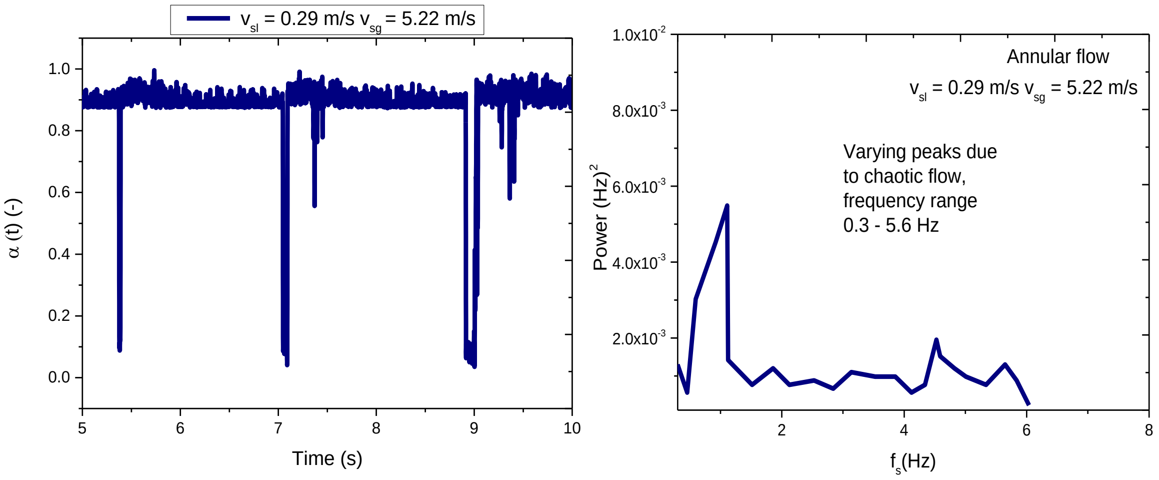

G.1.: Results of the (i) temporal void fractions and (ii) corresponding PSD at constant superficial liquid velocity ,v_{sl} = 0.29 m/s for a typical (a) Bubble flow at v_{sg} = 0.13 m/s (b) bubble – slug transition at v_{sg} = 0.26 m/s (c) slug flow at v_{sg} = 0.53 m/s (d) slug – churn transition v_{sg} = 0.78 m/s (e) churn flow v_{sg} = 1.56 m/s and (f) Annular flow at v_{sg} = 5.22 m/s

Effect of gas and liquid velocities on average structural frequency

The average structural frequency, f_{savg} derived from the PSD for each flow condition was obtained as an average of the range of frequencies f_s where a dominant peak is not observed. In the case of an identifiable dominant peak frequency, such as in the slug flow regime, the dominant peak frequency, f_s is taken as the average structural frequency f_{savg}. The effect of the gas and liquid superficial velocity on the average structural frequency is presented in figure G.2. At all conditions of v_{sl} = 0.11 m/s, 0.29 m/s, 0.43 m/s and 0.54 m/s, a decrease in f_{savg} can be observed, between 0.13 m/s < v_{sg} < 1.0 m/s, due to formation of Taylor bubbles and slug initiation, which corresponds to longer residence times which creates a reduction in the average frequency.

A reduction in the rate of frequency decline is however observed around 1.0 m/s < v_{sg} < 1.04 m/s given a transition from slug to churn flow. An apparent variation followed by a slow increase in frequency is also observed for 5m/s <v_{sg} < 13 m/s due to a churn annular transition with flow reversal effects where the liquid film begin an upward movement at turbulent conditions. Zhao *et al.*, (2013) observed a similar trend when they investigated the growth of disturbance waves in the annular flow regime of a vertical upward flow of air and water for a 0.035 m diameter test section using an electrical sensing set up. They concluded that the disturbance waves in the liquid film tends to reduce in amplitude when a coherence of the transiting disturbance occurs, causing the frequency to eventually become constant in the annular flow. In this work the steady increase in film frequency observed at high velocities is indicative of growth of disturbance waves rather than stabilization at the point of measurement.

The effect of increasing the liquid superficial velocities in successive amounts (vsl = 0.11 m/s, 0.29 m/s, 0.43 m/s and 0.54 m/s) is also observed to lead to substantial increases in the f_{savg} given the fact that ρ_l is >>ρ_g,, the mass and momentum transfer effect is much larger compared to the superficial gas flow effect , hence increasing the overall mixture velocity of the two phase flow. Relevant investigations have proposed empirical correlations which indicate the influence of the superficial liquid velocity on the structural frequency (see, Baba *et al.*, 2017; Barral and Angeli, 2014; Gregory and Scott, 1969; Hernandez-Perez *et al.*, 2010; Zabaras, 2000).

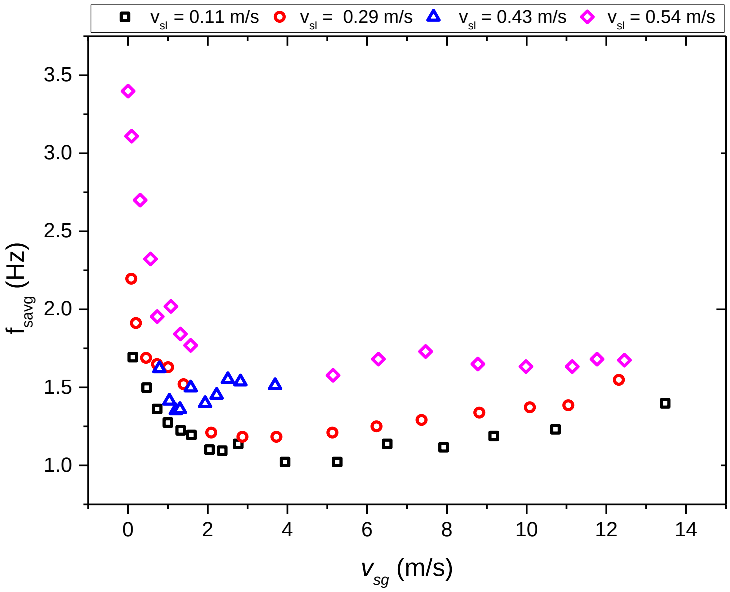

Figure G.2. The effect of superficial gas and liquid velocity on average structural frequencies at v_{sl} =0.11 m/s, 0.29 m/s, 0.43 m/s and v_{sl} = 0.54 m/s.

Validation of average structural frequency with processed images

The accuracy of the PSD analysis of α (t) requires further validation even though results agree well with the manual count of structures (mostly Taylor bubbles) in figure G.1. A manual count from the trace is however limited in choosing the adequate void fraction threshold to count clusters of entrained bubbles, unstable Taylor bubbles that create a churn effect and disturbance waves in the annular flow regime. Therefore, a more convincing validation method was performed via image processing (details provided in chapter 3) of videos frames captured under similar flow conditions as the sensor. Figure G.3, presents results of the parity between the PSD derived f_{savg}, and that from images, for similar flow conditions as described in figure G.2. A deviation from parity of +/- 10 % was obtained for all 64 data points, which is largely due to higher frequency ranges which are attributed to bubble , chaotic churn flow regimes and annular film disturbance waves similarly observed by Vasques *et al.*, (2018) . For 77 % of the data points, a decrease in deviation from parity of +/- 5 % is obtained. This data points corresponded to mid frequency band from 0.8 -1.5 Hz, which corresponded to the slug and slug churn transition conditions. Another source of error emanates from the emitted ray divergence of 7 degrees through the test section, which does not span the entire cross section. This setting may lead to a none detection of small bubble that stray or wobble downstream.

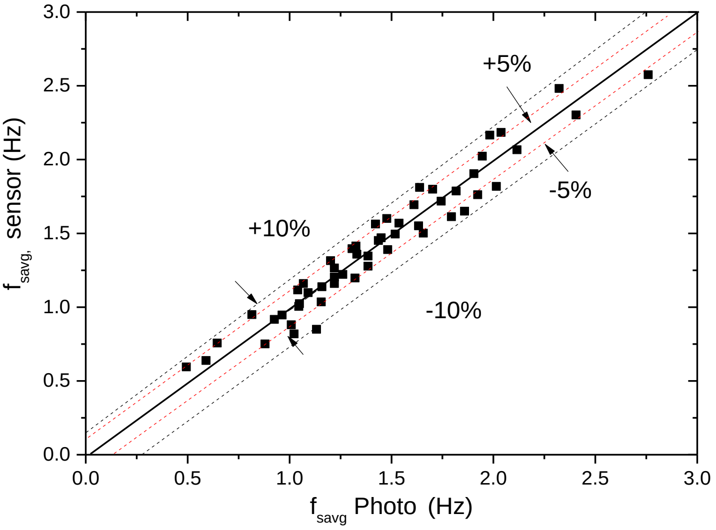

Figure G.3. Validation of the average structural frequency from PSD and average frequency from processed images.

Comparison of average structural frequency with empirical correlations

Figure G.4 presents a comparison between the f_{savg} derived from PSD of α(t) with empirical frequency correlations of Hernandez-Perez *et al.*, (2010) ,Gregory and Scott, (1969) and Zabaras, (1999). A general observation shows that the Hernandez-Perez *et al.*, (2010) correlation is in better agreement with the sensor derived frequency for all v_{sl} conditions considered. This agreement is mainly due to the vertical upward flow data used in deriving their correlation compared to the large disagreement observed for the horizonal flow based correlations of Zabaras, (1999) and Gregory and Scott, (1969).

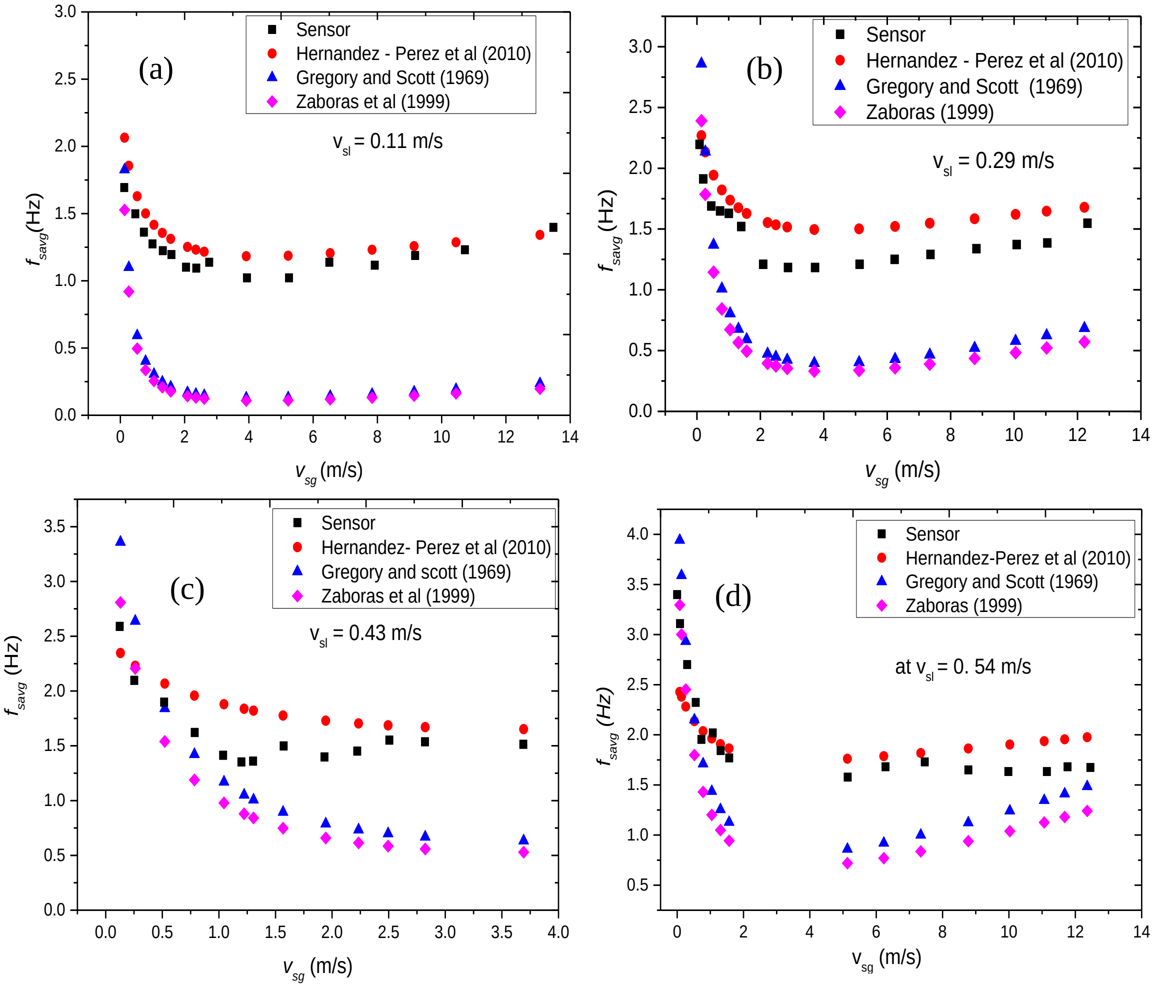

Figure G.4 Comparison of PSD derived average structural frequency with empirical correlation of Hernandez – Perez et al (2010), Gregory and Scott (1969) and Zabaras et al. (1999).

Figure G.5(a – c) presents parity comparisons of the sensor f_{savg} and that from the frequency correlations. The correlation of Hernandez-Perez *et al.*(2010) in figure G.5(a) as already discussed provides the best prediction of the f_{savg} for ranges between 1.0 – 1.5 Hz of which corresponds with the slug flow regime. A significant underestimation of the sensor frequency by Zabaras, (1999) (figure G.5(b)) and Gregory and Scott, (1969) (figure G.5(c)) correlations can however be observed at the same frequency range . At higher frequencies greater than 1.5 Hz, that correlate with the bubble , churn and annular flow regimes, Hernandez-Perez *et al.*(2010) correlation underestimates the sensor frequency given the fact that it was derived from data predominantly for a vertical upward slug flow regime. More so, the structural similarities between the stratified flow for a horizontal flow and that of an annular flow condition in a vertical flow is the reason for the reduction in disagreement from parity for the Zabaras, (1999) and Gregory and Scott, (1969) correlations. None the less, an over estimation can be observed from Gregory and Scott, (1969) correlations with an underestimation by Zabaras, (1999) .

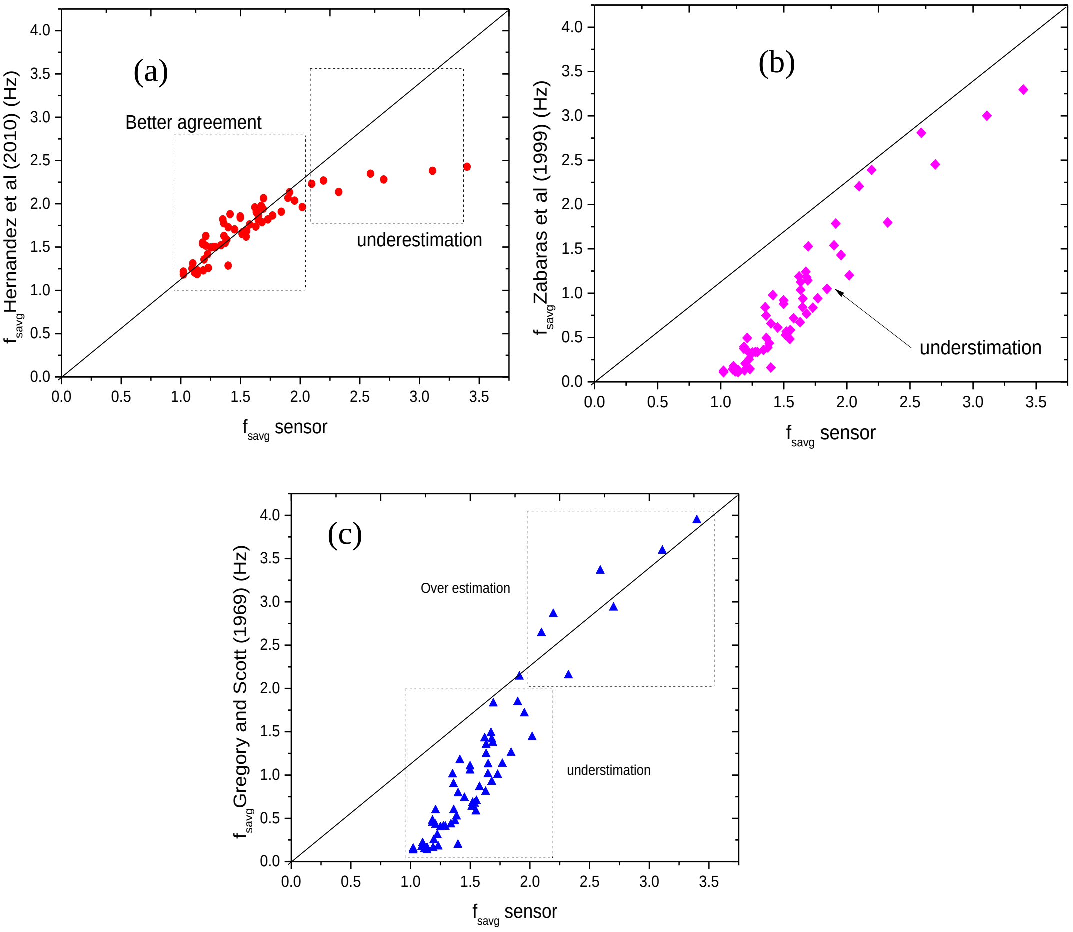

Figure G.5: Comparison between the sensor average structural frequency (PSD derived) with that from correlation of (a) Hernandez – Perez et al. (2010), (b) Zaboras et al. (1999). and (c) Gregory and Scott (1969)

The analysis reported herein fill in a gap in the knowledge that pertains to the variation of structural frequencies specific to all flow regime in a vertical upward flow of gas. A better understanding is thus provided for the development of unified frequency correlations that capture the effects of all flow regimes for the upward vertical flow of gas and liquid.

Summary

According to the performance of the optical sensor considered in this work, average structural frequency fsavg, was determined using the PSD of the temporal void fraction. Validation of the PSD derived f_{savg} with photos gave an error band of +/- 10 % for all flow regimes. Specific to slug flow conditions, +/-5% error band was obtained since the slug flow regime provided dominant frequencies compared to the larger broad band of frequencies obtained for other flow regimes. In comparison with the correlations of Hernandez-Perez *et al.*, (2010) ,Gregory and Scott, (1969) and Zabaras, (1999) similar trends in the average frequencies were observed for all cases. There was however a general underestimation of the PSD frequency compared with the correlations of Gregory and Scott, (1969) and Zabaras, (1999). More so, a better agreement was obtained with the correlation of Hernandez-Perez *et al.*, (2010) given its derivation was based on a slug flow for vertical flow experiments.

References

1. Abdulkadir, M., Hernandez-Perez, V., Lowndes, I. S., Azzopardi, B. J. and Brantson, E. T. (2014a) Detailed analysis of phase distributions in a vertical riser using wire mesh sensor (WMS), *Experimental Thermal and Fluid Science*, 59 DOI:10.1016/j.expthermflusci.2014.07.010.
2. Abdulkadir, M., Hernandez-Perez, V., Lowndes, I. S., Azzopardi, B. J. and Dzomeku, S. (2014b) Experimental study of the hydrodynamic behaviour of slug flow in a vertical riser, *Chemical Engineering Science*, 106. DOI:10.1016/j.ces.2013.11.021.
3. Abuaf, N., Jones, O. C. and Zimmer, G. A. (1978) Optical probe for local void fraction and interface velocity measurements, *Review of Scientific Instruments*, 49 (8), pp. 1090–1094. DOI:10.1063/1.1135524.
4. Adhavan, J., Balachandar, C., Arunkumar, S. and Venkatesan, M. (2017) Determination of Two Phase Flow Slug Velocity and Length Using Infrared Sensor BT - Fluid Mechanics and Fluid Power – Contemporary Research, in: Saha, A. K., Das, D., Srivastava, R., Panigrahi, P. K., and Muralidhar, K. (eds.) New Delhi: Springer India, pp. 1011–1017.
5. Agrawal, A. (2010) Two phase flow patterns and flow maps,
6. Al-Kayiem, H. H., Mohmmed, A. O., Al-Hashimy, Z. I. and Time, R. W. (2017) Statistical assessment of experimental observation on the slug body length and slug translational velocity in a horizontal pipe, *International Journal of Heat and Mass Transfer*, 105, pp. 252–260. DOI:10.1016/j.ijheatmasstransfer.2016.09.105.
7. Almabrok, A. A., Aliyu, A. M., Baba, Y. D., Lao, L. and Yeung, H. (2018) Void fraction development in gas-liquid flow after a U-bend in a vertically upwards serpentine-configuration large-diameter pipe, *Heat and Mass Transfer*, 54 (1), pp. 209–226.
8. Amaral, C. E. F., Alves, R. F., Silva, M. J., Arruda, L. V. R., Dorini, L., Morales, R. E. M. and Pipa, D. R. (2013) Image processing techniques for high-speed videometry in horizontal two-phase slug fl ows, *Flow Measurement and Instrumentation*, 33, pp. 257–264. DOI:10.1016/j.flowmeasinst.2013.07.006.
9. Ameel, B., De Kerpel, K., Caniere, H., T'Joen, C., Huisseune, H. and De Paepe, M. (2012) Classification of two phase flows using linear discriminant analysis and expectation maximization clustering of video footage, *International Journal of Multiphase Flow*, 40, pp. 106–112.

10. Andreussi, P., Di Donfrancesco, A. and Messia, M. (1988) An impedance method for the measurement of liquid hold-up in two-phase flow, *International Journal of Multiphase Flow*, 14 (6), pp. 777–785. DOI:10.1016/0301-9322(88)90074-2.
11. Aoyama, S., Hayashi, K., Hosokawa, S. and Tomiyama, A. (2016) Shapes of ellipsoidal bubbles in infinite stagnant liquids, *International Journal of Multiphase Flow*, 79, pp. 23–30.
12. Armand, A. A. (1946) The resistance during the movement of a two-phase system in horizontal pipes, *Izvestiia Vsesoiuznyi Teplotekhnicheskii Institut*, 1, pp. 16–23.
13. Arunaganesan, S., Adhavan, J., Arunkumar, S. and Venkatesan, M. (2017) Laser-Based Measurement of Gas–Liquid Two-Phase Flows in Micro and Mini Channels using Multiple Photodiode Arrangement, *Chemical Engineering Communications*, 204 (3), pp. 337–347.
14. Arunkumar, S., Adhavan, J., Venkatesan, M., Das, S. K. and Balakrishnan, A. R. (2016) Two phase flow regime identification using infrared sensor and volume of fluids method, *Flow Measurement and Instrumentation*, 51, pp. 49–54.
15. Ashwood, A. C., Vanden Hogen, S. J., Rodarte, M. A., Kopplin, C. R., Rodríguez, D. J., Hurlburt, E. T. and Shedd, T. A. (2014) Reprint of: A multiphase, micro-scale PIV measurement technique for liquid film velocity measurements in annular two-phase flow, *International Journal of Multiphase Flow*, 67 (S). DOI:10.1016/j.ijmultiphaseflow.2014.10.011.
16. Azzopardi, Barry J, Zaidi, S. (2013) Determination of Entrained Fraction in Vertical Annular Gas / Liquid Flow, *Asme*, 122 (March 2000).
17. Azzopardi, Hills, Fabre, Brauner, Bertola, Celata, Mariani, Marchioli, Picciotto, S. (2003) *Modelling and experimentation in two-phase flow*, *Journal of Chemical Information and Modeling*. Vol. 53. DOI:10.1017/CBO9781107415324.004.
18. Azzopardi, B. J. (1985) Drop sizes in annular two-phase flow, *Experiments in Fluids*, 3 (1), pp. 53–59. DOI:10.1007/BF00285271.
19. Azzopardi, B. J., Do, H. K., Azzi, A. and Hernandez Perez, V. (2015) Characteristics of air/water slug flow in an intermediate diameter pipe, *Experimental Thermal and Fluid Science*, 60, pp. 1–8. DOI:10.1016/j.expthermflusci.2014.08.004.
20. Baba, Y. D., Archibong, A. E., Aliyu, A. M. and Ameen, A. I. (2017) Slug frequency in high viscosity oil-gas two-phase flow: Experiment and prediction, *Flow Measurement and Instrumentation*, 54. DOI:10.1016/j.flowmeasinst.2017.01.002.
21. Banowski, M., Beyer, M., Szalinski, L., Lucas, D. and Hampel, U. (2017) Comparative

study of ultrafast X-ray tomography and wire-mesh sensors for vertical gas–liquid pipe flows, *Flow Measurement and Instrumentation*, 53 (Part A), pp. 95–106. DOI:https://doi.org/10.1016/j.flowmeasinst.2016.02.001.

22. Bansode, P. M. and Kulkarni, V. B. (2015) IR and LASER sensors for Newtonian fluids for flow-rate measurement using FPGA, in: *Industrial Instrumentation and Control (ICIC), 2015 International Conference on*. IEEE, pp. 821–824.
23. Barnea, D. (1987) A unified model for predicting flow-pattern transitions for the whole range of pipe inclinations, *International Journal of Multiphase Flow*, 13 (1), pp. 1–12.
24. Barnea, D. and Taitel, Y. (1993) A model for slug length distribution in gas-liquid slug flow, *International Journal of Multiphase Flow*, 19 (5), pp. 829–838.
25. Barral, A. H. and Angeli, P. (2014) Spectral density analysis of the interface in stratified oil-water flows, *International Journal of Multiphase Flow*, 65. DOI:10.1016/j.ijmultiphaseflow.2014.06.005.
26. Barrau, E., Rivière, N., Poupot, C. and Cartellier, A. (1999) Single and double optical probes in air-water two-phase flows: Real time signal processing and sensor performance, *International Journal of Multiphase Flow*, 25 (2), pp. 229–256. DOI:10.1016/S0301-9322(98)00042-1.
27. Batchelor, G. K. (1987) The stability of a large gas bubble rising through liquid, *Journal of Fluid Mechanics*, 184, pp. 399–422.
28. Bello, O. O., Falcone, G. and Teodoriu, C. (2007a) Experimental validation of multiphase flow models and testing of multiphase flow meters: a critical review of flow loops worldwide, in: *4th International Conference on Computational Methods in Multiphase Flow, Italy*. pp. 97–111.
29. Bello, O. O., Falcone, G. and Teodoriu, C. (2007b) Experimental validation of multiphase flow models and testing of multiphase flow meters: A critical review of flow loops worldwide, *WIT Transactions on Engineering Sciences*, 56, pp. 97–111. DOI:10.2495/MPF070101.
30. Bertani, C., De Salve, M. and Malandrone, M. (2010) *State-of-Art and selection of techniques in multiphase flow measurement*.
31. Berthold, J. W., Reed, S. E. and Nash, C. A. (1994) Fibre optic sensor system for void fraction measurement in aqueous two-phase fluids, *Flow Measurement and Instrumentation*, 5 (1), pp. 3–13. DOI:https://doi.org/10.1016/0955-5986(94)90003-5.
32. Bhagwat, S. M. and Ghajar, A. J. (2014) A flow pattern independent drift flux model based void fraction correlation for a wide range of gas-liquid two phase flow,

International Journal of Multiphase Flow, 59. DOI:10.1016/j.ijmultiphaseflow.2013.11.001.

33. Bhusan, S., Ghosh, S., Das, G. and Das, P. K. (2009) Rise of Taylor bubbles through narrow rectangular channels, *Chemical Engineering Journal*, 155 (1–2), pp. 326–332.
34. Biesheuvel, A. and Gorissen, W. C. M. (1990) Void fraction disturbances in a uniform bubbly fluid, *International Journal of Multiphase Flow*, 16 (2), pp. 211–231.
35. Bin, S., Zhang, H., Cheng, L. and Zhao, Y. (2006) Flow Regime Identification of Gas-liquid Two-phase Flow Based on HHT, *Chinese J. Chem. Eng.*, 14 (1), pp. 24–30.
36. Blaney, S. and Yeung, H. (2007) Gamma radiation methods for cost-effective multiphase flow metering, in: *13th International Conference on Multiphase Production Technology*. BHR Group,.
37. Bonilla Riaño, A., Rodriguez, I. H., Bannwart, A. C. and Rodriguez, O. M. H. (2015) Film thickness measurement in oil-water pipe flow using image processing technique, *Experimental Thermal and Fluid Science*, 68. DOI:10.1016/j.expthermflusci.2015.05.004.
38. Bratland, O. (2010) *Pipe Flow 2: Multi-phase Flow Assurance*, *Ove Bratland*. Available from: http://scholar.google.de/scholar?q=ove+bratland+pipe+flow+assurance&btnG=&hl=de&as_sdt=0,5#0
39. Brauner, N. and Barnea, D. (1986) Slug/Churn transition in upward gas-liquid flow, *Chemical Engineering Science*, 41 (1), pp. 159–163. DOI:https://doi.org/10.1016/0009-2509(86)85209-5.
40. Bray, J. H., Maxwell, S. E. and Maxwell, S. E. (1985) *Multivariate analysis of variance*. Sage.
41. Brunton, S. L., Noack, B. R. and Koumoutsakos, P. (2019) Machine learning for fluid mechanics, *Annual Review of Fluid Mechanics*, 52.
42. Chakrabarti, D. P., Das, G. and Das, P. K. (2007) Identification of stratified liquid-liquid flow through horizontal pipes by a non-intrusive optical probe, *Chemical Engineering Science*, 62 (7), pp. 1861–1876. DOI:10.1016/j.ces.2006.11.056.
43. Chen, L. (2006) Flow patterns in upward two-phase flow in small diameter tubes. Brunel University School of Engineering and Design PhD Theses.
44. Chen, L., Tian, Y. S. and Karayiannis, T. G. (2005) Vertical upward flow patterns in small diameter tubes, *6th World Conference on Experimental Heat Transfer, Fluid Mechanics and Thermodynamics, Matsushima, Miyagi, Japan, April 17-21, 2005*.

Available from: http://bura.brunel.ac.uk/handle/2438/3189 [Accessed

45. Cioncolini, A. and Thome, J. R. (2012) Void fraction prediction in annular two-phase flow, *International Journal of Multiphase Flow*, 43, pp. 72–84.
46. Coleman, J. W. and Garimella, S. (1999) Characterization of two-phase flow patterns in small diameter round and rectangular tubes, *International Journal of Heat and Mass Transfer*, 42 (15), pp. 2869–2881. DOI:https://doi.org/10.1016/S0017-9310(98)00362-7.
47. Costigan, G. and Whalley, P. B. (1997) Slug flow regime identification from dynamic void fraction measurements in vertical air-water flows, *International Journal of Multiphase Flow*, 23 (2), pp. 263–282. DOI:10.1016/S0301-9322(96)00050-X.
48. Davies, R. M. and Taylor, G. I. (1950) The mechanics of large bubbles rising through extended liquids and through liquids in tubes, *Proceedings of the Royal Society of London. Series A. Mathematical and Physical Sciences*, 200 (1062), pp. 375–390.
49. De Oliveira, W. R., De Paula, I. B., Martins, F. J. W. A., Farias, P. S. C. and Azevedo, L. F. A. (2015) Bubble characterization in horizontal air-water intermittent flow, *International Journal of Multiphase Flow*, 69, pp. 18–30. DOI:10.1016/j.ijmultiphaseflow.2014.10.014.
50. dos Reis, E. and da Silva Cunha, D. (2014) Experimental study on different configurations of capacitive sensors for measuring the volumetric concentration in two-phase flows, *Flow Measurement and Instrumentation*, 37, pp. 127–134. DOI:10.1016/j.flowmeasinst.2014.04.001.
51. Duda, R. O., Hart, P. E. and Stork, D. G. (2012) *Pattern classification*. John Wiley & Sons.
52. Dumitrescu, D. T. (1943) Strömung an einer Luftblase im senkrechten Rohr, *ZAMM-Journal of Applied Mathematics and Mechanics/Zeitschrift Für Angewandte Mathematik Und Mechanik*, 23 (3), pp. 139–149.
53. Dutra, G., Martelli, C., Da Silva, M. J., Patyk, R. L. and Morales, R. E. M. (2017) Air Flow Detection in Crude Oil by Infrared Light, *Sensors*, 17 (6), pp. 1278.
54. Elperin, T. and Klochko, M. (2002) Flow regime identification in a two-phase flow using wavelet transform, *Experiments in Fluids*, 32, pp. 674–682. DOI:10.1007/s00348-002-0415-x.
55. Falcone, G. (2009) Key multiphase flow metering techniques, *Developments in Petroleum Science*, 54, pp. 47–190.
56. Falcone, G., Teodoriu, C., Reinicke, K. M. and Bello, O. O. (2008) Multiphase-flow

modeling based on experimental testing: An overview of research facilities worldwide and the need for future developments, *SPE Projects, Facilities and Construction*, 3 (3), pp. 11–14.

57. Fernandes, R. C., Semiat, R. and Dukler, A. E. (1983) Hydrodynamic model for gas-liquid slug flow in vertical tubes, *AIChE Journal*, 29 (6), pp. 981–989.
58. Govan, A. H., Hewitt, G. F., Richter, H. J. and Scott, A. (1991) Flooding and churn flow in vertical pipes, *International Journal of Multiphase Flow*, 17 (1), pp. 27–44.
59. Gregory, G. A. and Scott, D. S. (1969) Correlation of liquid slug velocity and frequency in horizontal cocurrent gas-liquid slug flow, *AIChE Journal*, 15 (6), pp. 933–935.
60. Guet, S., Decarre, S., Henriot, V. and Liné, A. (2006) Void fraction in vertical gas–liquid slug flow: influence of liquid slug content, *Chemical Engineering Science*, 61 (22), pp. 7336–7350.
61. Guet, S. and Ooms, G. (2006) Fluid mechanical aspects of the gas-lift technique, *Annu. Rev. Fluid Mech.*, 38, pp. 225–249.
62. Guet, S., Ooms, G. and Oliemans, R. V. A. (2002) Influence of bubble size on the transition from low-Re bubbly flow to slug flow in a vertical pipe, *Experimental Thermal and Fluid Science*, 26 (6–7), pp. 635–641. DOI:10.1016/S0894-1777(02)00172-3.
63. Hamilton, W. G. (2012) Flow Patterns, *The Journal of Arthroplasty*, 27 (8 Suppl), pp. 1. DOI:10.1016/j.arth.2012.04.013.
64. Han, Y. F., Zhao, A., Zhang, H. X., Ren, Y. Y., Liu, W. X. and Jin, N. D. (2016) Differential pressure method for measuring water holdup of oil-water two-phase flow with low velocity and high water-cut, *Experimental Thermal and Fluid Science*, 72. DOI:10.1016/j.expthermflusci.2015.11.008.
65. Harmathy, T. Z. (1960) Velocity of large drops and bubbles in media of infinite or restricted extent, *AIChE Journal*, 6 (2), pp. 281–288.
66. Harvel, G. D., Hori, K., Kawanishi, K. and Chang, J. S. (1996) Real-time cross-sectional averaged void fraction measurements in vertical annulus gas-liquid two-phase flow by neutron radiography and X-ray tomography techniques, *Nuclear Instruments and Methods in Physics Research Section A: Accelerators, Spectrometers, Detectors and Associated Equipment*, 371 (3), pp. 544–552. DOI:https://doi.org/10.1016/0168-9002(95)00807-1.
67. Hastie, T., Tibshirani, R., Friedman, J. and Franklin, J. (2005) The elements of statistical learning: data mining, inference and prediction, *The Mathematical*

Intelligencer, 27 (2), pp. 83–85.

68. Heindel, T. J. (2011) A Review of X-Ray Flow Visualization With Applications to Multiphase Flows, *Journal of Fluids Engineering*, 133 (7), pp. 74001–74016. Available from: http://dx.doi.org/10.1115/1.4004367 [Accessed
69. Hernandez-Perez, V., Abdulkadir, M. and Azzopardi, B. J. (2010) Slugging frequency correlation for inclined gas–liquid flow, *World Academy of Science, Engineering and Technology*, 6, pp. 44–51.
70. Hewitt, G. F. and Roberts, D. N. (1969) *Studies of two-phase flow patterns by simultaneous X-ray and flash photography*. ATOMIC ENERGY RESEARCH ESTABLISHMENT HARWELL (UNITED KINGDOM).
71. Hill, A. V. (1910) The possible effects of the aggregation of the molecules of haemoglobin on its dissociation curves, *J. Physiol.*, 40, pp. 4–7.
72. Hiraoka, K., Hamahira, M., Hidai, K., Mizoguchi, H., Mishima, T. and Yoshizawa, S. (2001) Fast algorithm for online linear discriminant analysis, *IEICE TRANSACTIONS on Fundamentals of Electronics, Communications and Computer Sciences*, 84 (6), pp. 1431–1441.
73. Hossain, M., Chinenye-Kanu, N. M., Droubi, G. M. and Islam, S. Z. (2019) Investigation of slug-churn flow induced transient excitation forces at pipe bend, *Journal of Fluids and Structures*, 91, pp. 102733.
74. Huang, K., Wan, J. W., Chen, C. X., Li, Y. Q., Mao, D. F. and Zhang, M. Y. (2013a) Experimental investigation on friction factor in pipes with large roughness, *Experimental Thermal and Fluid Science*, 50, pp. 147–153. DOI:10.1016/j.expthermflusci.2013.06.002.
75. Huang, S., Xie, C., Lenn, C., Yang, W. and Wu, Z. (2013b) Issues of a Combination of Ultrasonic Doppler Velocity Measurement with a Venturi for Multiphase Flow Metering, *SPE Middle East Oil and Gas Show and Exhibition*, pp. 1–9. DOI:10.2118/164442-MS.
76. Ide, H., Kimura, R. and Kawaji, M. (2007) Optical measurement of void fraction and bubble size distributions in a microchannel, *Heat Transfer Engineering*, 28 (8–9), pp. 713–719.
77. Ioffe, S. (2006) Probabilistic linear discriminant analysis, in: *European Conference on Computer Vision*. Springer, pp. 531–542.
78. Isao, K. and Mamoru, I. (1987) Drift flux model for large diameter pipe and new correlation for pool void fraction, *International Journal of Heat and Mass Transfer*, 30

(9), pp. 1927–1939.

79. Ishii, M. and Mishima, K. (1984) Two-fluid model and hydrodynamic constitutive relations, *Nuclear Engineering and Design*, 82 (2–3), pp. 107–126.
80. Jayanti, S. and Hewitt, G. F. (1992) Prediction of the slug-to-churn flow transition in vertical two-phase flow, *International Journal of Multiphase Flow*, 18 (6), pp. 847–860.
81. Ji, H., Li, H., Huang, Z., Wang, B. and Li, H. (2014) Measurement of gas-liquid two-phase flow in micro-pipes by a capacitance sensor, *Sensors (Switzerland)*, 14 (12), pp. 22431–22446. DOI:10.3390/s141222431.
82. Jia, J., Babatunde, A. and Wang, M. (2015) Void fraction measurement of gas-liquid two-phase flow from differential pressure, *Flow Measurement and Instrumentation*, 41. DOI:10.1016/j.flowmeasinst.2014.10.010.
83. Jones, O. C. and Zuber, N. (1975) The interrelation between void fraction fluctuations and flow patterns in two-phase flow, *International Journal of Multiphase Flow*, 2 (3), pp. 273–306. DOI:https://doi.org/10.1016/0301-9322(75)90015-4.
84. Kaichiro, M. and Ishii, M. (1984) Flow regime transition criteria for upward two-phase flow in vertical tubes, *International Journal of Heat and Mass Transfer*, 27 (5), pp. 723–737.
85. Keerthi Vasan, G. C. and Venkatesan, M. (2017) Determining the Thin Film Thickness of Two Phase Flow using Optics and Image Processing., *Journal of Applied Fluid Mechanics*, 10 (3).
86. Kelessidis, V. C. and Dukler, A. E. (1989) Modeling flow pattern transitions for upward gas-liquid flow in vertical concentric and eccentric annuli, *International Journal of Multiphase Flow*, 15 (2), pp. 173–191. DOI:10.1016/0301-9322(89)90069-4.
87. Keska, J. K. and BE, W. (1999) Experimental comparison of flow pattern detection techniques for air-water mixture flow, *Experimental Thermal Fluid Science*, 19, pp. 1–12.
88. Kulkarni, A. A. and Joshi, J. B. (2005) Bubble formation and bubble rise velocity in gas− liquid systems: a review, *Industrial & Engineering Chemistry Research*, 44 (16), pp. 5873–5931.
89. Kumar, M. K. and Scientist, S. [no date] Multiphase Flow Metering: An Overview.
90. Lau, Y. M., Deen, N. G. and Kuipers, J. A. M. (2013) Development of an image measurement technique for size distribution in dense bubbly flows, *Chemical Engineering Science*, 94. DOI:10.1016/j.ces.2013.02.043.

91. Lehrer, I. H. (1976) A rational terminal velocity equation for bubbles and drops at intermediate and high Reynolds numbers, *Journal of Chemical Engineering of Japan*, 9 (3), pp. 237–240.
92. Li, H., Ji, H., Huang, Z., Wang, B., Li, H. and Wu, G. (2016) A New Void Fraction Measurement Method for Gas-Liquid Two-Phase Flow in Small Channels, *Sensors,* 16 (2), pp. 159. DOI:10.3390/s16020159.
93. Liu, L. and Bai, B. (2017) Generalization of droplet entrainment rate correlation for annular flow considering disturbance wave properties, *Chemical Engineering Science,* 164, pp. 279–291.
94. Lokanathan, M. and Hibiki, T. (2016) Flow regime, void fraction and interfacial area transport and characteristics of co-current downward two-phase flow, *Nuclear Engineering and Design*. DOI:10.1016/j.nucengdes.2016.05.042.
95. Malekzadeh, R. (2012) *Severe slugging in gas-liquid two-phase pipe flow, Ph.D. Dissertation,Univ. of Delft*. Univ. of Delft.
96. Mao, K. and Hibiki, T. (2017) Flow regime transition criteria for upward two-phase cross-flow in horizontal tube bundles, *Applied Thermal Engineering*, 112. DOI:10.1016/j.applthermaleng.2016.10.182.
97. Mao, Z.-S. and Dukler, A. E. (1985a) Rise velocity of a Taylor bubble in a train of such bubbles in a flowing liquid, *Chemical Engineering Science*, 40 (11), pp. 2158–2160.
98. Mao, Z.-S. and Dukler, A. E. (1985b) Rise velocity of a Taylor bubble in a train of such bubbles in a flowing liquid, *Chemical Engineering Science*, 40 (11), pp. 2158–2160. DOI:10.1016/0009-2509(85)87039-1.
99. Mao, Z.-S. and Dukler, A. E. (1991) The motion of Taylor bubbles in vertical tubes—II. Experimental data and simulations for laminar and turbulent flow, *Chemical Engineering Science*, 46 (8), pp. 2055–2064.
100. Matsui, G. (1984) Identification of flow regimes in vertical gas-liquid two-phase flow using differential pressure fluctuations, *International Journal of Multiphase Flow*, 10 (6), pp. 711–719.
101. Maugis, C., Celeux, G. and Martin-Magniette, M.-L. (2011) Variable selection in model-based discriminant analysis, *Journal of Multivariate Analysis*, 102 (10), pp. 1374–1387. DOI:https://doi.org/10.1016/j.jmva.2011.05.004.
102. McQuillan, K. W., Whalley, P. B. and Hewitt, G. F. (1985) Flooding in vertical two-phase flow, *International Journal of Multiphase Flow*, 11 (6), pp. 741–760.
103. Mehdizadeh, P., Marrelli, J. and Ting, V. C. (2002) Wet gas metering: trends in

applications and technical developments, in: *SPE Annual Technical Conference and Exhibition*. Society of Petroleum Engineers,.

104. Mendelson, H. D. (1967) The prediction of bubble terminal velocities from wave theory, *AIChE Journal*, 13 (2), pp. 250–253.

105. Merilo, M., L. Dechene, R. and M. Cichowlas, W. (1977) *Void Fraction Measurement With a Rotating Electric Field Conductance Gauge*, *Journal of Heat Transfer*. Vol. 99. DOI:10.1115/1.3450689.

106. Mithran, N. and Venkatesan, M. (2017) Effect of IR Transceiver orientation on gas/liquid two-phase flow regimes, *Flow Measurement and Instrumentation*, 58, pp. 12–20.

107. Moissis, R. and Radovcich, N. A. (1962) *TWO PHASE FLOW THROUGH A VERTICAL VENTURI. Topical Report No. 4. Report No. 321*. Dynatech Corp., Cambridge, Mass.

108. Morgado, A. O., Miranda, J. M., Ara??jo, J. D. P. and Campos, J. B. L. M. (2016) Review on vertical gas???liquid slug flow, *International Journal of Multiphase Flow*, 85, pp. 348–368. DOI:10.1016/j.ijmultiphaseflow.2016.07.002.

109. Nguyen, N.-T. and Truong, T.-Q. (2005) Flow rate measurement in microfluidics using optical sensors, in: *1st international conference on sensing technology, Palmerston North*.

110. Nicklin, D. J. (1962) Two-phase flow in vertical tubes, Trans, *Inst. Chem. Engr.*, 40 (1), pp. 61–68.

111. Nigmatulin, T. R. and Bonetto, F. J. (1997) Shape of Taylor bubbles in vertical tubes, *International Communications in Heat and Mass Transfer*, 24 (8), pp. 1177–1185.

112. Nnabuife, S. G., Pilario, K. E. S., Lao, L., Cao, Y. and Shafiee, M. (2019) Identification of gas-liquid flow regimes using a non-intrusive Doppler ultrasonic sensor and virtual flow regime maps, *Flow Measurement and Instrumentation*, 68, pp. 101568. DOI:https://doi.org/10.1016/j.flowmeasinst.2019.05.002.

113. Nuryadin, S., Ignaczak, M., Lucas, D. and Deendarlianto (2015) On the accuracy of wire-mesh sensors in dependence of bubble sizes and liquid flow rates, *Experimental Thermal and Fluid Science*, 65. DOI:10.1016/j.expthermflusci.2015.02.022.

114. Objectives, L. (2011) Chapter 6 Continuous Probability Distributions, pp. 1–23.

115. Olerni, C., Jia, J. and Wang, M. (2013) Measurement of air distribution and void

fraction of an upwards air–water flow using electrical resistance tomography and a wire-mesh sensor, *Meas. Sci. Technol. Meas. Sci. Technol*, 24 (24), pp. 35403–9. DOI:10.1088/0957-0233/24/3/035403.

116. Oliveira, J. L. G., Passos, J. C., Verschaeren, R. and Van Der Geld, C. (2009) Mass flow rate measurements in gas–liquid flows by means of a venturi or orifice plate coupled to a void fraction sensor, *Experimental Thermal and Fluid Science*, 33 (2), pp. 253–260.

117. Omebere-Iyari, N. K. and Azzopardi, B. J. (2007) A Study of Flow Patterns for Gas/Liquid Flow in Small Diameter Tubes, *Chemical Engineering Research and Design*, 85 (2), pp. 180–192. DOI:http://dx.doi.org/10.1205/cherd05059.

118. Oshinowo, T. and Charles, M. E. (1974) Vertical two-phase flow part I. Flow pattern correlations, *The Canadian Journal of Chemical Engineering*, 52 (1), pp. 25–35.

119. Owen, D. G. (1986) An experimental and theoretical analysis of equilibrium annular flows. University of Birmingham.

120. Polonsky, S., Shemer, L. and Barnea, D. (1999) The relation between the Taylor bubble motion and the velocity field ahead of it, *International Journal of Multiphase Flow*, 25 (6–7), pp. 957–975.

121. Rezkallah, K. S. and Zhao, L. (1995) A flow pattern map for two-phase liquid-gas flows under reduced gravity conditions, *Advances in Space Research*, 16 (7), pp. 133–136.

122. Rocha, M. S. and Simões-Moreira, J. R. (2008) Void Fraction Measurement and Signal Analysis from Multiple-Electrode Impedance Sensors, *Heat Transfer Engineering*, 29 (11), pp. 924–935. DOI:10.1080/01457630802186015.

123. Ruixi, D., Da, Y., Haihao, W., Jing, G., Ying, L., Tong, Z. and Lijun, Z. (2013) Optical method for flow patterns discrimination, slug and pig detection in horizontal gas liquid pipe, *Flow Measurement and Instrumentation*, 32, pp. 96–102. DOI:10.1016/j.flowmeasinst.2013.03.001.

124. S A Abouelwafa, M. and J M Kendall, E. (2000) *The measurement of component ratios in multiphase systems using γ-ray attenuation*, *Journal of Physics E: Scientific Instruments*. Vol. 13. DOI:10.1088/0022-3735/13/3/022.

125. Salehi, S. M., Karimi, H., Moosavi, R. and Dastranj, A. A. (2017) Different configurations of capacitance sensor for gas/oil two phase flow measurement: An experimental and numerical study, *Experimental Thermal and Fluid Science*, 82

(November), pp. 349–358. DOI:10.1016/j.expthermflusci.2016.11.027.

126. Sardeshpande, M. V., Harinarayan, S. and Ranade, V. V. (2015) Void fraction measurement using electrical capacitance tomography and high speed photography, *Chemical Engineering Research and Design*, 94. DOI:10.1016/j.cherd.2014.11.013.

127. Sarkodie, K., Fergusson-Rees, A., Makwashi, N. and Diaz, P. (2019) Slug Flow Monitoring in Pipes Using a Novel Non-Intrusive Optical Infrared Sensing Technology.

128. Schreier, P. (2011) *Handbook of Chinese Medicinal Plants: Chemistry, Pharmacology, Toxicology W. Tang, G. Eisenbrand Vols. I+II Wiley-VCH, Weinheim, 2011, pp. 1150 ISBN: 978-3-527-32226-8.*, *Molecular nutrition & food research*. Vol. 55. DOI:10.1002/mnfr.201190015.

129. Schubring, D., Shedd, T. A. and Hurlburt, E. T. (2010) Studying disturbance waves in vertical annular flow with high-speed video, *International Journal of Multiphase Flow*, 36 (5), pp. 385–396. DOI:https://doi.org/10.1016/j.ijmultiphaseflow.2010.01.003.

130. Semiconductors, V. and Drawings, S. [no date] *Vishay Semiconductors Application of Optical Reflex Sensors Vishay Semiconductors Optoelectronic Sensors*.

131. Shaban, H. (2015) *Experimental Investigations of Internal Air-water Flows*. Available from : http://www.ruor.uottawa.ca/handle/10393/32952

132. Shaban, H. and Tavoularis, S. (2014a) Identification of flow regime in vertical upward air-water pipe flow using differential pressure signals and elastic maps, *International Journal of Multiphase Flow*, 61, pp. 62–72. DOI:10.1016/j.ijmultiphaseflow.2014.01.009.

133. Shaban, H. and Tavoularis, S. (2014b) Measurement of gas and liquid flow rates in two-phase pipe flows by the application of machine learning techniques to differential pressure signals, *International Journal of Multiphase Flow*, 67. DOI:10.1016/j.ijmultiphaseflow.2014.08.012.

134. Shaban, H. and Tavoularis, S. (2014c) The wire-mesh sensor as a two-phase flow meter, *Measurement Science and Technology*, 26 (1), pp. 15306.

135. Shaban, H. and Tavoularis, S. (2015) The wire-mesh sensor as a two-phase flow meter, *Measurement Science and Technology*, 26, pp. 015306. DOI:10.1088/0957-0233/26/1/015306.

136. Shaban, H. and Tavoularis, S. (2016) On the accuracy of gas flow rate measurements in gas-liquid pipe flows by cross-correlating dual wire-mesh sensor

signals, *International Journal of Multiphase Flow*, 78. DOI:10.1016/j.ijmultiphaseflow.2015.10.001.

137. Sheers, A. M. and Noordhuis, B. R. (1999) Multi-phase and wet gas flow measurement, in: *IBC Annual Multiphase Metering Conference, Aberdeen*. pp. 22–23.

138. Shemer, L., Gulitski, A. and Barnea, D. (2007) Movement of two consecutive taylor bubbles in vertical pipes, *Multiphase Science and Technology*, 19, pp. 99–120. DOI:10.1615/MultScienTechn.v19.i2.10.

139. Shen, X., Schlegel, J. P., Chen, S., Rassame, S., Griffiths, M. J., Hibiki, T., *et al.* (2014) Flow Characteristics and Void Fraction Prediction in Large Diameter Pipes, in: Cheng, L. (ed.) *Frontiers and Progress in Multiphase Flow*. Springer, pp. 50.

140. Shoham, O. (2003) Mechanistic modeling of gas-liquid two-phase ow in pipes.

141. Sowiński, J., Dziubiński, M. and Fidos, H. (2009) Velocity and gas-void fraction in two-phase liquid-gas flow in narrow mini-channels, *Archives of Mechanics*, 61 (1), pp. 29–40.

142. Stokes, G. G. (1851) *On the effect of the internal friction of fluids on the motion of pendulums*. Vol. 9. Pitt Press Cambridge.

143. Sulthana, S. A., Marieswaran, T., Braghadesh, N., Mithran, N. and Venkatesan, M. (2018) Slug-bubble regime identification in a square channel using a IR Sensor, in: *MATEC Web of Conferences*. EDP Sciences,172, pp. 1002.

144. Taitel, Y., Bornea, D. and Dukler, A. E. (1980) Modelling flow pattern transitions for steady upward gas-liquid flow in vertical tubes, *AIChE Journal*, 26 (3), pp. 345–354.

145. Taitel, Y., Vierkandt, S., Shoham, O. and Brill, J. P. (1990) Severe slugging in a riser system: experiments and modeling, *International Journal of Multiphase Flow*, 16 (1), pp. 57–68. DOI:10.1016/0301-9322(90)90037-J.

146. Tang, C. and Heindel, T. J. (2006) Estimating gas holdup via pressure difference measurements in a cocurrent bubble column, *International Journal of Multiphase Flow*, 32 (7), pp. 850–863.

147. Tharwat, A. (2016) Linear vs. quadratic discriminant analysis classifier: a tutorial, *International Journal of Applied Pattern Recognition*, 3 (2), pp. 145–180.

148. Tharwat, A., Gaber, T., Ibrahim, A. and Hassanien, A. E. (2017) Linear discriminant analysis: A detailed tutorial, *AI Communications*, 30 (2), pp. 169–190.

149. Thome, J. R. (2005) Void Fractions in Two-Phase Flows, *Engineering Data Book III*, pp. 1–33.

150. Thome, J. R. (2007) Two-Phase Flow Patterns, *Engineering Data Book III*, pp. 1–34.

151. TT electronics plc (2016) Fluid and Bubble Sensing -OPB350, pplication Bulletin 235, *Optek Technology*, pp. 1–2. Available from: www.ttelectronics.com

152. TUV NEL (2013) an Introduction To Multiphase Flow Measurement, *Tuv Nel Ltd.*, pp. 14. Available from: http://www.tuvnel.com/_x90lbm/An_Introduction_to_Multiphase_Flow_Measurement.pdf [Accessed

153. Vaitsis, E., Chadwick, D. and Alpay, E. (2004) Slug flow hydrodynamics in the presence of catalyst rods, *Chem. Eng. Res. Des.*, 82 (May), pp. 653–658. DOI:10.1205/026387604323142711.

154. Van Dijk, P. (2005) *Acoustics of Two-Phase Pipe Flows*.

155. Vasques, J., Cherdantsev, A., Cherdantsev, M., Isaenkov, S. and Hann, D. (2018) Comparison of disturbance wave parameters with flow orientation in vertical annular gas-liquid flows in a small pipe, *Experimental Thermal and Fluid Science*, 97, pp. 484–501.

156. Vassallo, P. F., Trabold, T. A., Moore, W. E. and Kirouac, G. J. (1993) Measurement of velocities in gas-liquid two-phase flow using laser Doppler velocimetry, *Experiments in Fluids*, 15 (3), pp. 227–230. DOI:10.1007/BF00189890.

157. Velasco Peña, H. F. and Rodriguez, O. M. H. (2015) Applications of wire-mesh sensors in multiphase flows, *Flow Measurement and Instrumentation*, 45. DOI:10.1016/j.flowmeasinst.2015.06.024.

158. Wahab, Y. A., Rahim, R. A., Rahiman, M. H. F., Aw, S. R., Yunus, F. R. M., Goh, C. L., Rahim, H. A. and Ling, L. P. (2015) Non-invasive process tomography in chemical mixtures–A review, *Sensors and Actuators B: Chemical*, 210, pp. 602–617.

159. Wallis, G. B. (1969) One-dimensional two-phase flow.

160. Wang, C., Zhao, N., Fang, L., Zhang, T. and Feng, Y. (2016) Void fraction measurement using NIR technology for horizontal wet-gas annular flow, *Experimental Thermal and Fluid Science*, 76, pp. 98–108. DOI:https://doi.org/10.1016/j.expthermflusci.2016.03.014.

161. Woldesemayat, M. A. and Ghajar, A. J. (2007) Comparison of void fraction correlations for different flow patterns in horizontal and upward inclined pipes, *International Journal of Multiphase Flow*, 33 (4), pp. 347–370. DOI:10.1016/j.ijmultiphaseflow.2006.09.004.

162. Wolffenbuttel, B. M. A., Nijhuis, T. A., Stankiewicz, A. and Moulijn, J. A. (2002) Novel method for non-intrusive measurement of velocity and slug length in two- and three-phase slug flow in capillaries, *Measurement Science and Technology*, 13 (10), pp. 1540. DOI:10.1088/0957-0233/13/10/305.

163. Wu, B., Firouzi, M., Mitchell, T., Rufford, T. E., Leonardi, C. and Towler, B. (2017) A critical review of flow maps for gas-liquid flows in vertical pipes and annuli, *Chemical Engineering Journal*, 326, pp. 350–377. DOI:10.1016/j.cej.2017.05.135.

164. Wu, W., Mallet, Y., Walczak, B., Penninckx, W., Massart, D. L., Heuerding, S. and Erni, F. (1996) Comparison of regularized discriminant analysis linear discriminant analysis and quadratic discriminant analysis applied to NIR data, *Analytica Chimica Acta*, 329 (3), pp. 257–265. DOI:https://doi.org/10.1016/0003-2670(96)00142-0.

165. Xia, G., Cui, Z., Liu, Q. and Hu, M. (2009) A model for liquid slug length distribution in vertical gas-liquid slug flow, *Journal of Hydrodynamics*, 21 (4), pp. 491–498.

166. Xiaoming, L., Quanke, F., Qincheng, B. and Tingkuan, C. (2004) Experimental Study on Undisturbed Measurement of Gas Bubble Rising Velocity Using Infrared Emitting Diode and Photodiode [J], *Journal of Xi'an Jiaotong University*, 11, pp. 3.

167. Xie, C., Stott, A. L., Plaskowski, A. and Beck, M. S. (1999) *Design of capacitance electrodes for concentration measurement of two-phase flow, Measurement Science and Technology*. Vol. 1. DOI:10.1088/0957-0233/1/1/012.

168. Xue, T., Yang, L., Ge, P. and Qu, L. (2015) Error analysis and liquid film thickness measurement in gas–liquid annular flow, *Optik*, 126 (20), pp. 2674–2678. DOI:https://doi.org/10.1016/j.ijleo.2015.06.072.

169. Yan, H., Liu, Y. H. and Liu, C. T. (2004) Identification of flow regimes using back-propagation networks trained on simulated data based on a capacitance tomography sensor, *Measurement Science and Technology*, 15 (2), pp. 432.

170. Yanjun, Z. (2015) A Novel Identification Method of Two Phase Flow Based on LDA Feature Extraction and GRNN in ERT System, in: *5th International Symposium on Knowledge Acquisition and Modeling (KAM 2015)*. Atlantis Press,.

171. Yu, S. C. M., Tso, C. P. and Liew, R. (1996) Analysis of thin film thickness determination in two-phase flow using a multifiber optical sensor, *Applied Mathematical Modelling*, 20 (7), pp. 540–548.

172. Zabaras, G. J. (2000) Prediction of slug frequency for gas/liquid flows, *SPE Journal*, 5 (03), pp. 252–258.

173. Zhai, L. S., Jin, N. D., Gao, Z. K., Zhao, A. and Zhu, L. (2014) Cross-correlation velocity measurement of horizontal oil-water two-phase flow by using parallel-wire capacitance probe, *Experimental Thermal and Fluid Science*, 53. DOI:10.1016/j.expthermflusci.2013.12.021.

174. Zhang, M., Pan, L., Ju, P., Yang, X. and Ishii, M. (2017) The mechanism of bubbly to slug flow regime transition in air-water two phase flow: A new transition criterion, *International Journal of Heat and Mass Transfer*, 108, pp. 1579–1590. DOI:10.1016/j.ijheatmasstransfer.2017.01.007.

175. Zhao, Y., Markides, C. N., Matar, O. K. and Hewitt, G. F. (2013) Disturbance wave development in two-phase gas-liquid upwards vertical annular flow, *International Journal of Multiphase Flow*, 55. DOI:10.1016/j.ijmultiphaseflow.2013.04.001.

176. Zhu, M. and Hastie, T. J. (2003) Feature extraction for nonparametric discriminant analysis, *Journal of Computational and Graphical Statistics*, 12 (1), pp. 101–120.

177. Ziegenhein, T., Lucas, D., Besagni, G. and Inzoli, F. (2018) The Bubble Shape in Contaminated Bubbly Flows: Results for Different NaCl Concentrations in Purified Water, *ChemEngineering*, 2 (2), pp. 18.

178. Zubar, N. and Findlay, J. (1965) Average Volumetric Concentration in Two-Phase Flow System, *Trans. ASME, J. Heat Transfer Ser. C*, 87, pp. 453.